DEPARTMENT OF PHYSICS
UNIVERSITY OF JYVÄSKYLÄ
RESEARCH REPORT No. 7/2011

The ion-optical design of the MARA recoil separator and absolute transmission measurements of the RITU gas-filled recoil separator

by

Jan Sarén

Academic Dissertation
for the Degree of
Doctor of Philosophy

To be presented, by permission of the
Faculty of Mathematics and Science
of the University of Jyväskylä,
for public examination in Auditorium FYS-1 of the
University of Jyväskylä on December 9, 2011
at 12 o'clock noon

Jyväskylä, Finland
December 2011

Preface

The work reported in this thesis has been carried out during the years 2004–2011. While the work concerns modelling and design of recoil separators the author had the priviledge of participating in the research of the nuclear structure during the years.

I wish to express my most sincere thanks to my supervisors, prof. Matti Leino and Dr. Juha Uusitalo, for their guidance during these years and for giving me the opportunity to do my PhD thesis work in the RITU group. They have read the manuscript of this thesis very carefully through and have given valuable comments but still leaving me the freedom to fulfil myself. I would like to thank Prof. Rauno Julin who has valued my work sometimes more than I do myself and Prof. Juha Äystö for supporting my work related to the FAIR project and this thesis study.

I thank Ulrika Jakobsson and Dr. Cath Scholey for many common years we have spent around the RITU focal plane. I would like to thank Ulrika also for numerous fascinating conversations about work and free time. Taneli Kalvas I would like to thank for our long common journey in the physics wonderland. I thank Taneli and Dr. Olli Tarvainen for great lunch times and especially the highly analytic chat we have had.

Physics is usually much easier than the bureaucracy or the administrative tasks. I would like to express my gratitude to Soili Leskinen, Marjut Hilska, Anna-Liisa Blå and Ritva Väyrynen for making my life easier.

Outside the topic of the thesis work and the research group, I would like to thank my long-time friends for whole-hearted relationships. With you I can simply be myself. I want to express my gratitude to my parents for all the support and encouragement. I thank my wonderful children, my daughter Iida and my son Altti. You have given me a great insight into humanity. Finally, I thank my loving wife Raisa for both understanding me during the years of the PhD studies and pushing me to write this book.

Abstract

Sarén, Jan
The ion-optical design of the MARA recoil separator and absolute transmission measurements of the RITU gas-filled recoil separator
Jyväskylä: University of Jyväskylä, 2011, 190 p.
Department of Physics Research Report No. 7/2011
ISSN: 0075-465X; 7/2011
ISBN: 978-951-39-4511-4 (paper version)
ISBN: 978-951-39-4512-1 (electronic version)
Diss.

In this thesis work, the use of two complementary recoil separators for studies of nuclear structure via fusion-evaporation reactions are discussed. The design and the main ion-optical properties of the vacuum-mode recoil-mass separator MARA, intended for studies of nuclei with $N \approx Z$ close to the proton drip-line, are presented. MARA (*Mass Analysing Recoil Apparatus*) consists of a magnetic quadrupole triplet followed by an electrostatic deflector and a magnetic dipole. The working principle of MARA is discussed and the reasons for the choice of the optical parameters of the elements are given. The performance of MARA for different kind of fusion reactions has been studied with Monte Carlo simulations. The results of a sensitivity analysis especially of the electrostatic deflector are reported. The requirements for the instrumentation are discussed.

The absolute transmission values of the RITU gas-filled recoil separator have been measured for several fusion evaporation products in the mass region $A = 170$–190 using different reaction asymmetries. It was observed that the angular distribution of products after the target and the angular acceptance of RITU determine the transmission value accurately. The effects of filling-gas pressure on the average charge state and focal plane image properties as well as on transmission values have been studied experimentally. The transmission probability for ^{254}No synthesized in the ^{48}Ca+^{208}Pb reaction has been calculated and is in agreement with the experiment. Simulations of transportation of ^{186}Hg fusion products through RITU have been carried out. The simulated behaviour of transmission and image properties agrees well with an experiment.

Keywords: ion optics, recoil separator, gas-filled recoil separator, recoil-separator modelling

Author's address Jan Sarén
Department of Physics
University of Jyväskylä
Finland

Supervisors Prof. Matti Leino
Department of Physics
University of Jyväskylä
Finland

Dr. Juha Uusitalo
Department of Physics
University of Jyväskylä
Finland

Reviewers Dr. Teng Lek Khoo
Argonne National Laboratory
9700 S. Cass Avenue
Argonne, IL 60439
USA

Dr. Maurycy Rejmund
GANIL
Bd Henri Becquerel
BP 55027 - 14076 CAEN Cedex 05
France

Opponents Prof. Gottfried Münzenberg
GSI
Planckstraße 1
64291 Darmstadt
Germany

Contents

Chapter 1

Modelling of an in-flight recoil separator

In this chapter working principles and modelling aspects of in-flight recoil separators, vacuum and gas-filled ones, are discussed. The concept *recoil* is used throughout the text to describe a product of interest from a nuclear reaction. Focus has been set on separators which are at zero degrees and meant mainly for studies of heavy isotopes produced in fusion evaporation reactions. Therefore the main task of such a device is to physically separate the intense primary beam from the interesting products. Additionally to this primary beam suppression, a recoil separator can provide further identification of products.

The working princinple of an in-flight recoil separator is based on the particles' magnetic and electric rigidities which define the trajectory of a particle in a magnetic or an electric field, respectively. The magnetic ridigity is proportional to the momentum of an ion while the electric rigidity is proportional to the energy. In-flight recoil separators are very fast compared to any other separation methods and thus can be used to study short living ($t_{1/2} \gtrsim 1$ µs) isotopes. The working of an in-flight separator is also independent on particles' chemical properties.

Gas-filled recoil separators are used in many laboratories to study heavy elements produced in fusion evaporation reactions. The charge of an ion travelling in a gas-filled separator is changed relatively often by charge-exchange reactions and thus the transmission of the ion is independent on the initial charge state. Additionally to this, the magnetic rigidity of an ion is in first order independent on velocity. As a result the gas-filled recoil separators enable high transmission for fusion evaporation residues. However, the primary beam cannot be

suppressed enough if the fusion reaction is symmetric or if inverse kinematics is used. The use of such reactions are required to study many of the neutron deficient species having $Z \lesssim 60$.

The magnetic rigidities of a primary beam and fusion products overlap or are too close to each other also without the filling gas. This problem can be overcome by adding an electric field to the device since the electric rigidities of primary beam and fusion products differ much more from each other than magnetic rigidities. In addition to primary beam suppression, the device employing electric and magnetic sector fields can provide physical mass separation of products. This can be used for further identification or tagging of a reaction and is useful when the counting rate of a focal plane detector needs to be limited.

An overview of optics of charged particles is given without detailed derivation of results. Also the most common ion-optical elements used in in-flight separators are introduced. The detection and identification probability for the product under study depends greatly on initial energy and angular distributions of the products after a target foil. In order to achieve reasonably realistic energy and angular distributions for performance studies of the RITU [Lei95] and MARA separators, a computer programme utilizing Monte-Carlo method has been constructed and will be introduced. The methods of ion-optical calculations used for MARA design will also be described.

1.1 Basic concepts of the optics of charged particles

Beams of charged particles, i.e. heavy ions in this thesis study, can be bent and focused via electromagnetic fields as the light beams can be transferred and shaped by lenses and prisms in light optics. For example magnetic quadrupoles can be used for defocusing and focusing (lenses in light optics) and homogenous magnetic fields for achromatic bending of charged particles with different momenta (prisms in light optics).

1.1.1 About ion optical simulation methods

Ion optical systems can be studied and calculated nowadays easily with the aid of modern computers. There are two main methods for this: transfer matrices and ray tracing. In the former every optical element is described by a *transfer matrix* and the total transfer matrix can be obtained by multiplying each matrix together in right order. The transfer-matrix method is very fast and

is suitable for devices which are built from standard electromagnetic elements such as dipoles and quadrupoles. In the *ray-tracing method* the equation of motion is integrated for every single particle which makes it slow for a large set of particles. The ray-tracing method can be more suitable if special elements are used or if for example the space charge has to be taken into account or if other phenomena like scattering or energy losses occur inside an element. The ray-tracing method requires also detailed knowledge of the electromagnetic field.

In this study the transfer-matrix formalism has been adopted and the text below is more focused into that direction. The ray-tracing method has been utilized in the design of the electrostatic deflector for the MARA separator (see section 2.5.3). The matrix formalism can be used also in situations where the particles interact inside an optical element since the total matrix representing the element can be divided into matrices representing fringing fields and multiple ones representing small parts of an ideal element. The weakness of this aproach is of course the interactions occurring in fringing field section. The method of divided transfer matrices can be employed for example in modelling of a gas-filled separator.

In some cases the best strategy for the ion optical simulation might be a mixture of both ray tracing and matrix formalism. The measured or calculated field map of an element can be used directly for integration of a transfer matrix representing an entire element or part of it. If the system is deterministic inside the element then a ray traced ensemble of particles can be used to fit the transfer matrix.

1.1.2 Coordinate system

In this thesis study a three dimensional curvilinear coordinate system has been used where the z-axis is along a continuous and curved *optical axis* and is increasing in the direction where particles are flying. In every position on the z-axis the euclidean xy-plane is perpendicular to the z-axis. The xy-plane attached to optical-axis position z_i is a *profile plane*. If the optical system is bending charged particles only in horizontal direction the y-axes of different profile planes are parallel to each other. The right handed coordinate system is visualized in figure 1.1.

The spatial coordinates, x_i and y_i on the profile plane i at z_i are not sufficient alone to describe fully the state of a particle. Two other coordinates are needed to define the direction of the particle at the profile plane. A widely used definition of such inclination angles α and β is

$$\tan\alpha = \frac{p_x}{p_z} \quad \text{and} \quad \tan\beta = \frac{p_y}{p_z}, \tag{1.1}$$

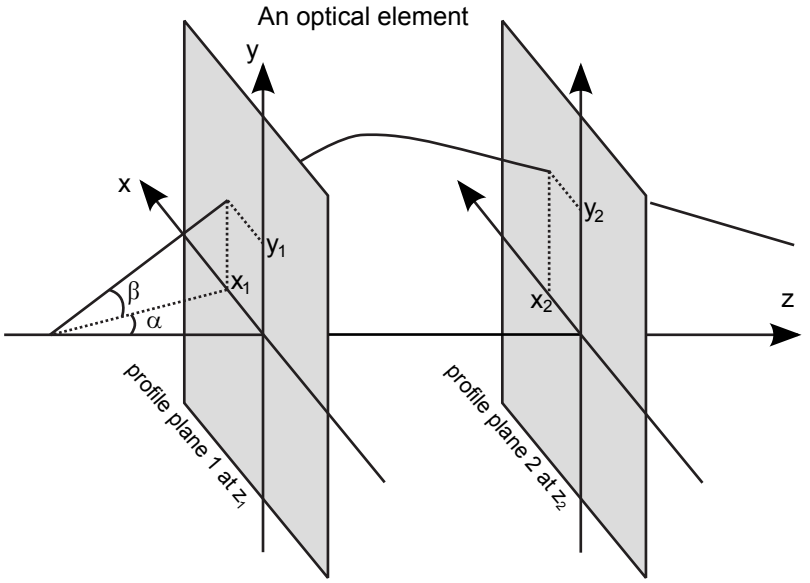

Figure 1.1: The right handed curvilinear coordinate system showing track of an imaginary particle through an optical element confined by two profile planes.

where p_x, p_y and p_z are components of the momentum $\boldsymbol{p}$ of the ion in horizontal, vertical and longitudinal direction, respectively. This is a practical choice since in a *drift region* (absent of electromagnetic fields) between two profile planes, 1 and 2, the ion will be shifted horizontally a distance $\Delta x = x_2 - x_1 = x_1 + v_x \Delta t = x_1 + \Delta z \tan(\alpha)$ if the effects from special relativity are not concerned. In the transfer matrix formalism the inclination-angle coordinates are defined as

$$\begin{aligned} a \equiv a_{\text{nonsymplectic}} &\equiv \frac{p_x}{p_z} = \tan(\alpha) \\ b \equiv b_{\text{nonsymplectic}} &\equiv \frac{p_y}{p_z} = \tan(\beta) \end{aligned} \tag{1.2}$$

if the *nonsymplectic* coordinate system has been adopted.

Some codes like GICOSY [GICOSY] use a different coordinate system for angles. Inclination angles in this *symplectic* coordinate system are defined as

$$\begin{aligned} a_{\text{symplectic}} &\equiv \frac{p_x}{p_0} = \frac{(1+\delta_p)\tan\alpha}{\sqrt{1+\tan^2\alpha+\tan^2\beta}} \\ b_{\text{symplectic}} &\equiv \frac{p_y}{p_0} = \frac{(1+\delta_p)\tan\alpha}{\sqrt{1+\tan^2\alpha+\tan^2\beta}} \end{aligned} \tag{1.3}$$

where the $p_0 = (1+\delta_p)^{-1}|\boldsymbol{p}|$ is the momentum of a reference particle. The user can change the output coordinate system of GICOSY code to nonsymplectic but the symplectic convention is still used internally by the code.

The maximum angular acceptances in x- and y-direction (maximum angle relative to z-axis) of in-flight separators or spectrometers are typically between ± 30 mrad (1.7°) to ± 100 mrad (5.7°). These are rather small angles and the small angle approximation, $\tan(\alpha) \approx a$ can be adopted. However, the momentum distribution of the products can be order of 10% wide and therefore in the symplectic coordinate convention (1.3), the absolute value of angular coordinate $a_{\mathrm{symplectic}}/b_{\mathrm{symplectic}}$ can deviate significantly from the corresponding angle α/β. This is the main reason for the adoption of the nonsymplectic convention in this study.

The transfer-matrix computer code [GICOSY] used throughout this work doesn't have the particle's charge explicitly in the transfer matrices but the charge is taken implicitly into account via mass and energy variables. The particle's mass per charge (m/q) and energy per charge (E_k/q) ratios can be calculated from mass m_0, kinetic energy $E_{k,0}$ and charge q_0 of a reference particle as

$$\frac{m}{q} = \frac{m_0}{q_0}(1+\delta_m) \quad \text{and,} \tag{1.4}$$

$$\frac{E_k}{q} = \frac{E_{k,0}}{q_0}(1+\delta_K), \tag{1.5}$$

where the δ_m and δ_K are coordinates expressing the relative difference of m/q or E_k/q ratios to ones of the reference particle.

The time coordinate can be defined in several ways. The GICOSY code allows using of absolute and scaled times or lengths as a time coordinate. If the time (length) option is used the matrix elements give an absolute time (length) the particle has used to travel up to the current position. The scaling of these coordinates means that the time/length coordinate is divided by the time/length of the reference particle. The fifth option for time coordinate is the length which the particle is behind the reference particle if started simultaneously from the beginning of a system.

Since all the coordinates are expressed as deviations from ones of a reference particle it is also practical to express the time coordinate δ_t as

$$\Delta t = \Delta t_0(1+\delta_t), \tag{1.6}$$

where Δt and Δt_0 are the time of flight (ToF) of a particle and the reference particle, respectively.

1.1.3 Interplay between δ_m, δ_K and δ_t

For non-relativistic particles the kinetic energy can be expressed as

$$E_k = \frac{ms^2}{(\Delta t)^2}, \tag{1.7}$$

where Δt is the time needed by the mass m to travel the path length s. Dividing both sides of (1.7) by the charge, q, and substituting equations (1.4), (1.5) and (1.6) the equation

$$(1+\delta t)^2 = \frac{1+\delta_m}{1+\delta_K} \tag{1.8}$$

can be derived. Thus measuring two of these the third one can be calculated. In the case of recoil mass separators where the ions are physically separated according to δ_m, an additional measurement of velocity at the focal plane enables the estimation of δ_K. If also the kinetic energy is recorded then the charge can be calculated as

$$q = \frac{E_k q_0}{E_{k,0}(1+\delta_K)}. \tag{1.9}$$

1.1.4 Lorentz force and the rigidity of a charged particle

The force acting on a charged particle in the combined electric and magnetic field is described by the Lorentz force

$$\boldsymbol{F} = \frac{d(m\boldsymbol{v})}{dt} = q\boldsymbol{E} + q\boldsymbol{v} \times \boldsymbol{B}, \tag{1.10}$$

where $\boldsymbol{E}$ is an electric field and $\boldsymbol{B}$ is a magnetic field. Its strength is directly proportional to the charge q of the particle.

Let us suppose that only a homogenous magnetic field is present and the velocity of a particle is perpendicular to the magnetic field. Since the force (1.10) is always perpendicular to the velocity the particle must be in circular motion with radius ρ. The Lorentz force acts as a centripetal force. The angular velocity of the rotation is $\omega = d\theta/dt = v/\rho$ and the centripetal acceleration is $a = \omega^2\rho = v^2/\rho$. By substituting a with $a = qvB/m$ from (1.10) the definition of the particle's magnetic rigidity becomes

$$\chi_B = B\rho = \frac{mv}{q} = \frac{p}{q}. \tag{1.11}$$

The magnetic rigidity is a property of a particle which describes how easily the trajectory of a particle can be bent. The radius of curvature is usually fixed in the recoil separators and thus the magnetic fields needed in the magnetic elements are proportional to the rigidity of the particle.

The velocity of the fusion evaporation residue (recoil) is usually less than a few percent of the velocity of light. Therefore classical formulas for kinetic energy and momentum can be used. The magnetic rigidity can be then written as

$$\chi_B = \frac{p}{q} = \frac{\sqrt{2E_k m_0}}{q}, \tag{1.12}$$

where E_k is the kinetic energy of an ion having mass m. From this equation one can observe the very important fact that in vacuum separators employing only magnetic field elements the spatial mass resolution is strongly dependent on the kinetic energy spread of the products. The non-relativistic magnetic rigidity equation (1.12) can be further converted to practical form if the unit of the kinetic energy is expressed in MeV, mass in atomic mass units, u, and charge of a particle in elementary charges:

$$\chi_B = 0.1018 \frac{\sqrt{E_k\,[\mathrm{MeV}] \cdot m_0\,[\mathrm{u}]}}{q\,[\mathrm{e}]} \cdot \mathrm{Tm}. \tag{1.13}$$

For the derivation of the electric rigidity let us suppose an electric field to be perpendicular to the velocity of a particle. Then the force is perpendicular to the velocity and the particle is in circular motion and the electric field part of the Lorentz force acts as a centripetal force $F = mv^2/\rho = qE$ which leads to the definition of the electric rigidity

$$\chi_E = E\rho = \frac{pv}{q}. \tag{1.14}$$

For non-relativistic velocities (1.14) can be written in terms of kinetic energy E_k and charge q as

$$\chi_E = E\rho = \frac{2E_k}{q} = \frac{2E_k\,[\mathrm{MeV}]}{q\,[\mathrm{e}]}\,\mathrm{MV}. \tag{1.15}$$

If there is an electric field component parallel to the velocity then the magnitude of the particle's velocity will change. However, the change in the electric rigidity following from the change in velocity depends only on field strength and change in position but not on the properties of a particle. Therefore, two particles with equal electric rigidity entering the same electric field will travel along the same trajectory.

1.1.5 Transfer matrices

Let us consider the coordinate vector

$$\boldsymbol{\xi}_i = \{x_i, y_i, a_i, b_i, \delta_m, \delta_K\} \tag{1.16}$$

in a configuration space which describes fully the location, direction and the chromatic properties of an ion at the profile plane i. All the spatial (x_i, y_i,a_i and b_i) and chromatic (δ_m, δ_K) coordinates are zero, if and only if the ion is the so called *reference particle*. The reference particle travels through an optical system along the *optical axis*. The electromagnetic fields in the system are

smooth and do not vary in time. Since the system is deterministic there must exist a set of functions which transform $\boldsymbol{\xi}_i$ to the new coordinate vector $\boldsymbol{\xi}_{i+1}$ for the next profile plane $i+1$. A natural step is to use a Taylor (MacLaurin) power series of these functions. For example x_2 in first order approximation can be expressed as

$$\begin{aligned} x_2 = (x_2|x_1)x_1 + (x_2|a_1)a_1 + (x_2|y_1)y_1 + (x_2|b_1)b_1 \\ +(x_2|\delta_{m1})\delta_{m1} + (x_2|\delta_{K1})\delta_{K1} + \mathcal{O}(2), \end{aligned} \tag{1.17}$$

where the $(x_2|*)$ are *transfer coefficients*. From the equation (1.17) one can see the origin of matrix usage. Clearly, the coordinate vector at the next profile plane can be calculated as

$$\boldsymbol{\xi}_{i+1} = \mathbf{M}_{i\to i+1}\boldsymbol{\xi}_i \tag{1.18}$$

where $\mathbf{M}_{i\to i+1}$ is the *transfer matrix* having transfer coefficients as matrix elements. The coordinates are therefore represented by a column vector. This matrix formalism can be easily expanded to higher orders. For example, in second order matrices and coordinate vectors the columns and rows are added for $x^2, xa, ..., x\delta_K, ..., aa, ay, ..., a\delta_K, ..., \delta_K^2$. Since a transfer matrix images the coordinates from a profile plane to the next over an optical element the matrix representing multiple subsequent elements can be obtained simply by multiplying the corresponding matrices together in corresponding order.

The electromagnetic separators usually employ a mechanical symmetry where the magnets and electrostatic devices are symmetric about the xz-plane (dipoles, quadrupoles and higher order multipoles). This leads to a magnetic field symmetry: $B_x(x,y,z) = -B_x(x,-y,z)$. Specifically, this states that the field is perpendicular to the xz plane. The same mechanical symmetry holds for elements employing electric fields leading to $E_y(x,y,z) = -E_y(x,-y,z)$. Due to these symmetries the transfer coefficients $(x|y^m b^n)$ and $(y|x^m a^n)$ vanish when the sum of integer powers $m+n$ is odd. This means that $(x|y) = (x|b) = (y|x) = (y|a) = 0$ and the transfer matrices in horizontal and vertical direction can be separated. [Eng79]

The position and the momentum of a particle in the six-dimensional *phase space* are $\boldsymbol{r}$ and $\boldsymbol{p}$, respectively. The Liouville's theorem states that the particle density $\rho(\boldsymbol{r},\boldsymbol{p})$ in the phase space is constant over time for a set of particles. Thus only the shape of the set can be changed but not its volume. In the first order approximation the horizontal and vertical directions are independent on each other and thus the area representing a set of particles is conserved specially in (x,p_x) and (y,p_y) subspaces independently if the particles are not accelerated. Therefore, the submatrices of $\mathbf{M}_{i\to i+1}$ representing the tranformations of (x,a) and (y,b) must have a determinant value of unity. If the symplectic coordinate definition (1.3) is used then a plot of $(x, a_{\text{symplectic}})$ has the same form as plot (x,p_x) since $p_x = p_0 a_{\text{symplectic}}$. In nonsymplectic convention the angular coordinate must be multiplied by the particle's momentum in z-axis direction. The

Liouville's theorem in the case of ion optics is discussed in detail in reference [Wol87a].

Let us consider a situation where a particle travels first in a field free region before entering an optical element where it feels the Lorentz force. Of course, mathematically the magnetic or electric field changes continuously from close to zero to the value inside the element. In order to use the transfer-matrix method it is convenient to split the element transfer matrix to the part covering the *effective optical length* where the field can be approximated as *ideal* and two *fringing field* matrices taking the effects of changing fields into account. The distance between the profile planes attached to a fringing field matrix is usually zero. This leads to small errors in calculations of a particle's coordinates close to element boundaries. The ideal field is the field of a corresponding infinitely long element.

Drift length

The simplest element in a electromagnetic system is a drift-length region which means that there are no electric or magnetic fields present and an ion is just drifting in volume. The first order transfer matrix representing a drift length of l is simply

$$\mathbf{T}_l = \begin{pmatrix} (x|x) & (x|a) \\ (a|x) & (a|a) \end{pmatrix} = \begin{pmatrix} 1 & l \\ 0 & 1 \end{pmatrix}, \tag{1.19}$$

for both column vectors (x, a) and (y, b). If relativistic effects are not taken into account the matrix (1.19) is correct in all orders while in symplectic coordinates already the second order terms like $(x|a\delta_m)$ and $(x|a\delta_K)$ are nonzero.

Thin lens

Thin lens describes a lens which is infinitely thin and where the ray of light or a charged particle is deflected towards or away from the optical axis. In a thin lens the bending angle $\Delta\alpha$ is directly proportional to the distance from the optical axis. This causes all rays parallel to the optical axis to be focused at the *focal point* after a *focal length* f. The transfer matrix representing a thin lens is

$$\mathbf{F_f} = \begin{pmatrix} 1 & 0 \\ -1/f & 1 \end{pmatrix}, \tag{1.20}$$

where f is the focal length. The focal length is negative for a defocusing lens.

1.1.6 Properties of an ion-otical system and aberrations

The matrix elements of a system transfer matrix can be used to get useful information about the system. When the system is to be designed, various properties like point-to-point focusing for the system are normally required. This and other properties can be analysed from the system transfer matrix. In the first order calculations the solutions can be found even analytically with a pen and a piece of paper. However, in the large solid angle devices the second and higher order effects cannot be neglected and thus the use of computer codes is necessary in order to find a set of parameters minimizing the values to be optimized.

The most common requirement in optical design of an in-flight separator is the vanishing of certain first order matrix elements. Since the determinant of the first order matrix is unity for a system preserving particle energy (i.e. in x-direction one obtains $(x|x)(a|a) - (x|a)(a|x) = 1$) at the most two matrix elements can vanish simultaneously. Usually the disappearance of two elements simultaneously is not required. In figure 1.2 vanishing of the first order geometrical transfer coefficients is shown schematically. In the case (a) the $(x|a) = 0$ and the system is *point-to-point focusing*, case (b) is *parallel-to-parallel* ($(a|x) = 0$) and cases (c) ($(x|x) = 0$) and (d) ($(a|a) = 0$) represent *parallel-to-point* and *point-to-parallel focusing*, respectively. In a point-to-point focusing system (a) the relation

$$\mathcal{M}_x \equiv (x|x) = (a|a)^{-1} \tag{1.21}$$

between $(a|a)$ and the *magnification*, $\mathcal{M}_x \equiv (x|x)$, must be fulfilled. This very powerful result means that the magnification increases if the focal length is decreased. Also the signs of these coefficients must be the same.

Resolving power

The first order *mass resolving power* of a point-to-point (at least in x-direction) focusing system with energy focus can be calculated easily from the system transfer matrix. It reads

$$\mathcal{R}_m = \frac{(x|\delta_m)}{|(x|x)|\Delta x_0} = \frac{\mathcal{D}_m}{|\mathcal{M}_x|\Delta x_0}, \tag{1.22}$$

where $\mathcal{D}_m \equiv (x|\delta_m)$ is the *mass dispersion*, $\mathcal{M}_x \equiv (x|x)$ is the *magnification* in the x-direction and Δx_0 is the initial full width of the image before the system [Eng79]. The dispersion is produced in a dipole field. The dispersion can be increased by increasing the bending angle. However, that results in to shorter focal length which translates to increased magnification (1.21) and as a net effect the resolving power will not be enhanced. In general, the resolving

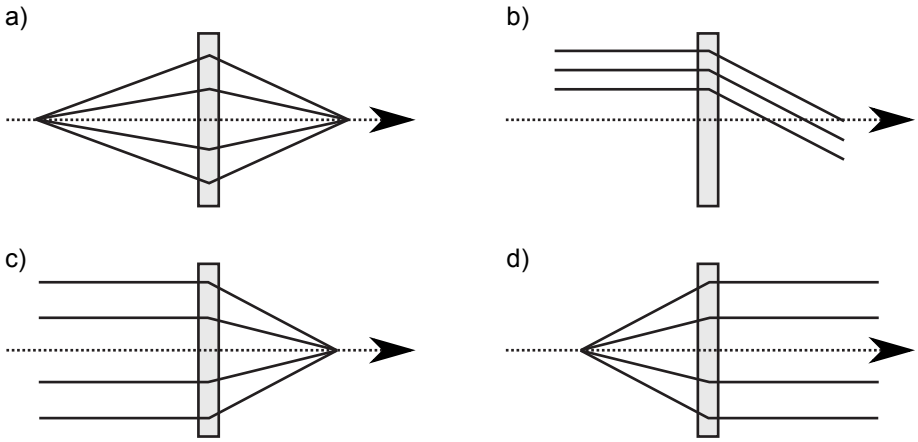

Figure 1.2: Vanishing of a) $(x|a)$, b) $(a|x)$, c) $(x|x)$ and d) $(a|a)$ matrix elements.

power can be enhanced by maximizing the area in xz-plane used by the particles in a dipole magnet. The area can be increased by increasing the physical size of the magnet and/or by using suitable focusing elements around the dipole. [Wol87a]

Aberrations

Aberrations of an ion-optical system are described by the higher order matrix elements which blur the image at the focal plane and make the image wider degrading the real mass resolving power. The aberrations are either *chromatic*, *geometrical* or a mixture of them. A geometric aberration shifts particles by Δx at the focal plane according to initial position and angle coordinates (x_0, y_0, a_0, b_0) and the corresponding matrix elements are $(x|x^k a^l y^m b^n)$ where $\{k, l, m, n\} \in 0, 1, 2, \ldots$ and $k + l + m + n \geq 2$. Transfer coefficients like $(x|\delta_K^2)$ and $(x|\delta_K \delta_m)$ represent pure chromatic aberrations.

In recoil mass spectrometers the most harmful aberrations which are usually minimized in the ion-optical design are $(x|a^2)$, $(x|a\delta_K)$ and $(x|\delta_K^2)$. The effects caused by these are typically discussed in a publication describing a new recoil mass spectrometer (see for example [Spo85] and [BDav05]. These aberrations set restrictions to horizontal angular acceptance and energy acceptance of an in-flight spectrometer. Since the $(x|a^n \delta_K^m)$ aberrations are usually those which limit the mass resolution it is clear that, when required, the mass resolution can be improved by limiting the angular and energy acceptance of the spectrometer.

The so called *mass focal plane* is usually not perpendicular to the optical axis at the angular focal plane ($z = z_{\mathrm{fp}}$). This means that the masses deviating

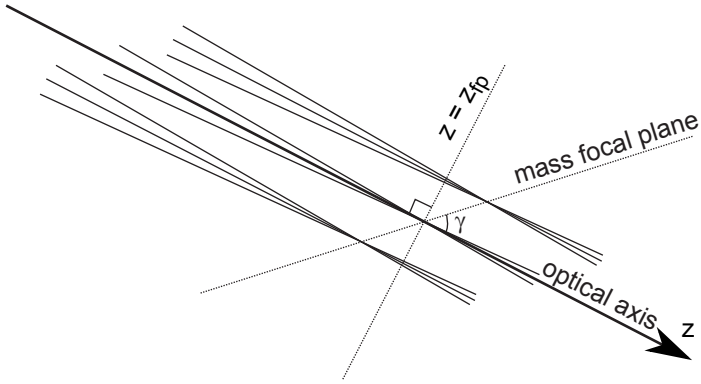

Figure 1.3: A schematic representation of mass focal plane at an angle γ relative to optical axis.

from that of a reference particle are focused at the profile planes located before or after z_{fp}. This is clarified in figure 1.3 which shows schematically three different masses focused along the line which makes an angle γ relative to the optical axis. The tilted focal plane is a second order effect. The third order calculation would add additional curvature to the mass focal plane.

Angle γ can be shown to be related to the *angular magnification* $(a|a)$, mass dispersion $\mathcal{D}_m$ and second order transfer coefficient $(x|a\delta_m)$ as [Eng79]

$$\tan\gamma = -\frac{(a|a)\mathcal{D}_m}{(x|a\delta_m)}. \tag{1.23}$$

Usually in the case of mass spectrometers it is advisable to have the mass focal plane perpendicular to the optical axis since the particle detectors placed at the focal plane usually give better results if ions approach a detector surface perpendicularly. The required width of the detector is also minimized when $\gamma = 90^\circ$. Equation (1.23) tells us that either angular magnification has to be maximized or the coefficient $(x|a\delta_m)$ has to be minimized if a perpendicular mass focal plane is desired. The former means strong horizontal angular focusing just before the focal plane and the latter requires an addition of a hexapole correction element after the dipole magnet which separates the masses. However, the correction element should be relatively far from the dipole exit and would require possibly other hexapole element(s) at other location(s) for compensation of increased second order aberrations induced by the hexapole added first.

1.2 Ion optical elements used in a recoil separator

Usually electromagnetic fields in a separator and in beam transport lines are constructed from pure multipoles or elements where different multipoles are combined. The cartesian components of the magnetic field of a 2n-pole at the xy-plane (names for $n = 1, 2, 3, \ldots$ poles are dipole, quadrupole, hexapole, octupole, etc.) are

$$B_{n,x}(r,\phi) = C_n \left(\frac{r}{R_{ref}}\right)^{n-1} \sin\left[(n-1)\phi - n\alpha_n\right] \quad (1.24a)$$

$$B_{n,y}(r,\phi) = C_n \left(\frac{r}{R_{ref}}\right)^{n-1} \cos\left[(n-1)\phi - n\alpha_n\right] \quad (1.24b)$$

where r is the distance from the optical axis, ϕ is the angle in xy-plane, α_n is the angular orientation of the field and R_{ref} is a reference distance with maximum field of C_n. It can be shown that in a current free region, any magnetic field can be represented as a sum of multipole components: $\boldsymbol{B}(\boldsymbol{r}) = \boldsymbol{B}_1(\boldsymbol{r}) + \boldsymbol{B}_2(\boldsymbol{r}) + \boldsymbol{B}_3(\boldsymbol{r}) + \ldots$ with suitable amplitudes C_n and phase angles α_n. This is called a multipole expansion. Magnets used in separators and beam lines have typically $\alpha_n = 0$. Corresponding electrostatic elements have $\alpha_n = \pi/(2n)$.

Homogenous magnetic and electric fields are created by two opposing parallel pole faces and electrodes, respectively. These dipoles ($2n = 2$) are used to separate particles according to their magnetic and electric rigidities. Clearly, these elements bend the ion-optical axis. In addition to dipoles, focusing elements are usually needed in order to achieve desired foci in horizontal and vertical directions. One can think that the bending of the optical axis is a zeroth order effect (all trajectories regardless of particle properties are bent). Dispersion is a first order effect (aberration) of a dipole. The quadrupoles ($2n = 4$) can be used to change first order coefficients like magnification but they also introduce second and higher order aberrations. In general, a 2n-pole is used to adjust the transfer coefficient values of order $(n-1)$ and they give rise to aberrations of order n and higher.

In the recoil separators operating at Coulomb barrier energies magnetic quadrupoles are used exclusively for focusing since the electrostatic devices cannot provide the required field strengths. In the applications where ions have lower rigidities also electrostatic quadrupoles or Einzel lenses are widely used.

1.2.1 Magnetic dipole

A magnetic dipole is certainly one of the most important elements used in recoil separators since it bends particle trajectories according to the particle's magnetic rigidity. If the horizontal direction is chosen to be the dispersive direction then in the dipole the magnetic field lines are perpendicular to the horizontal plane. The magnetic field in a pure dipole is constant across the active region.

In some cases it is advantageous to implement a quadrupole component to a dipole field which means approximately that the field magnitude is proportional to the x coordinate (in the coordinate system adopted here). This can be done by tilting the pole shoes symmetrically about the zx-plane so that the gap between the shoes is proportional to x. As an example, in the abandoned plan of a new gas-filled separator at JYFL the design included a dipole magnet with a strong quadrupole component created by a radially changing gap [Enq03]. Smaller quadrupole components can be created also with surface coils. Figure 2.30 shows a photo of the dipole magnet of the MARA separator which is equipped with surface coils. The strips of the surface coils have equal width, they are parallel to the optical axis and carry the same current. According to Ampère's law the current inside a closed integration path increases linearly as a function of x. Therefore the magnetic flux density generated by the surface coils is directly proportional to x.

Most of the magnetic dipoles include other kind of quadrupole and hexapole corrections implemented as inclined and rounded effective field boundaries, respectively, at the entrance and exit of the dipole. For example, in the case of an inclined field boundary the z-coordinate, when a particle enters a dipole, depends on its x-coordinate. Hence the focal length of a dipole can be altered by changing the inclination angle. This is illustrated in figure 1.4. The left subfigure shows a dipole with field boundaries perpendicular to the optical axis. In such cases the focus point after the dipole is on the line connecting the focus before the dipole and the center of curvature. [Wol87a]

If the field boundaries are perpendicular to the optical axis then the first order transfer matrix of a dipole to be applied to coordinate vector $\{x, a, \delta_m, \delta_K\}$ in the dispersive direction can be written as

$$\mathbf{D}_{\mathrm{M},x} = \begin{pmatrix} \cos(\phi_0) & \rho_0 \sin(\phi_0) & \frac{d\rho}{2}\left[1-\cos(\phi_0)\right] & \frac{d\rho}{2}\left[1-\cos(\phi_0)\right] \\ -\frac{1}{\rho_0}\sin(\phi_0) & \cos(\phi_0) & \frac{1}{2}d\sin(\phi_0) & \frac{1}{2}d\sin(\phi_0) \\ 0 & 0 & 1 & 0 \\ 0 & 0 & 0 & 1 \end{pmatrix} \tag{1.25}$$

where ρ_0 is the bending radius, ϕ_0 is the deflection angle and $d = \pm 1$ is the direction. $d = 1$ and $d = -1$ correspond to bending towards negative and posi-

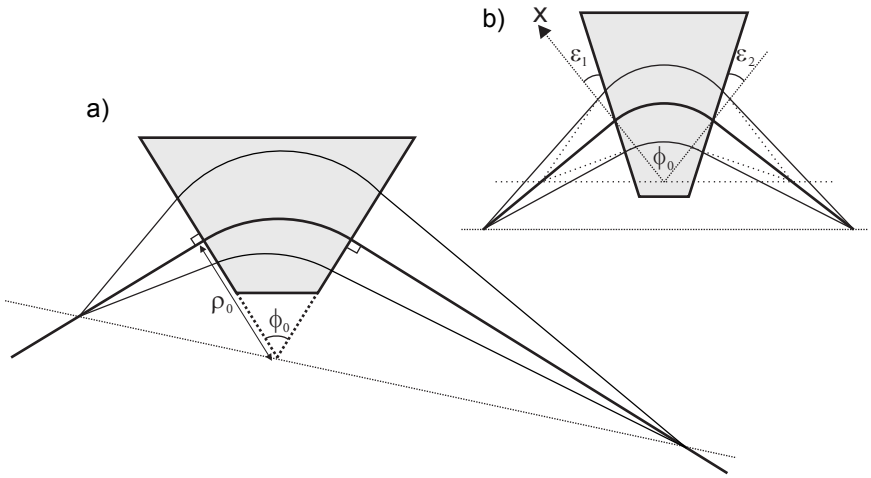

Figure 1.4: Focusing of the dipole in the dispersive plane. a) Field boundaries are perpendicular to the optical axis. The center of curvature is on the line connecting two focus points (Barber's rule). b) Inclined field boundaries at the entrance and the exit.

tive x-axis, respectively. The matrix has been adopted from reference [Wol87a] by neglecting the corrections of the theory of relativity. In the y-direction there are no electromagnetic forces acting on a particle and the corresponding transfer matrix is simply the drift length of the equation (1.19) with optical axis length $l = \phi_0\rho$.

If the effective field boundary (EFB) has an angle ε with respect to the direction perpendicular to the optical axis (see figure 1.4 for definition of positive ε) then focusing or defocusing action can be observed in both x- and y-directions. For positive angles there is defocusing action in horizontal and focusing action in vertical direction. For negative angles these actions are opposite. For the inclination angle ε the (de)focusing action can be described by a thin lens at the EFB having a focal length

$$f_y = -f_x = \rho_0 \tan(\varepsilon), \tag{1.26}$$

where ρ_0 is the radius of curvature of the magnet. The matrix representation of a thin lens having a focal length f is given in equation (1.20). The matrix representing a dipole with inclined EFBs can be obtained as multiplication $\mathbf{F}_{f(\varepsilon_2)}\mathbf{D}_{\mathrm{M},x}\mathbf{F}_{f(\varepsilon_1)}$.

1.2.2 Electric dipole (electrostatic deflector)

A charged particle can be deflected also by an electric field which has a nonzero component perpendicular to the particle's velocity. The radius of curvature in the perpendicular electric field is defined by the electric rigidity of equation (1.14). The simplest device which creates such a field consists of two opposing parallel plates at different electric potentials. This kind of element is not very much used in mass spectrometers since the optical axis through the element is neither straight nor an arc of a circle and the coupling of such an element to a magnetic dipole is presumably more difficult. However, such parallel plate electrodes are used in some separators which do not have mass resolution. These are for example the velocity filter SHIP [Mün81] and the electric rigidity separator VASSILISSA [Yer94].

In those in-flight recoil mass separators which employ both electric and magnetic fields the electrodes of the deflectors form a cylindrical condensor where the electrodes are arcs of a concentric circles with a constant gap between. Usually the electric potentials are set so that the optical axis, which is also an arc of a circle, is at ground potential. As in the case of magnetic dipole, quadrupole components can be added also to an electric dipole. Similar effect to the inclined field boundaries in a magnetic dipole can be implemented by adding a curvature to the plates in the yz-plane in the entrance or exit of a deflector. Toroidal or spherical electrodes in a deflector are analogous to an inhomogeneous magnetic field in a magnetic dipole. A quadrupole component introduced by toroidal electrodes or curved entrance/exit can be used to add focusing in non-dispersive vertical direction. Nevertheless, the electrodes of all the recoil mass separators in active use have cylindrical electrodes. This is probably due to increasing cost and difficulty in the manufactoring of such high precision and tailor-made elements. Therefore, the discussion in the following is focused on cylindrical deflectors.

Let R_1 be the radius of the inner electrode and R_2 that of the outer electrode. Let the potentials in the electrodes be V_1 and V_2, respectively. In a *symmetric setup* the anode and cathode have equal but opposite potentials, $V_1 \equiv -V$ and $V_2 \equiv V$. In the symmetric setup the optical axis lies in the middle of the electrodes and hence has the radius $R_{oa} = (R_1 + R_2)/2$. The analytic equation for the strength of the electric field between two concentric and infinitely tall cylindrical electrodes can be derived from the Gauss law $\oint \boldsymbol{E} \cdot \boldsymbol{dA} = Q/\varepsilon_0$ and from the boundary conditions $V(R_i) = V_i$ to be

$$E(r) = \frac{V_2 - V_1}{\ln(R_2/R_1)} \frac{1}{r} = \frac{2V}{\ln(R_2/R_1)} \frac{1}{r} \tag{1.27}$$

in a general arrangement and in the symmetric arrangement of the cylindrical electrodes, respectively. Thus, the potential as a function of radius can be

obtained to be

$$V(r) = \frac{V_2 - V_1}{\ln(R_2/R_1)} \ln(r/R_1) + V_1 = V \left(\frac{2\ln(r/R_1)}{\ln(R_2/R_1)} - 1 \right) \tag{1.28}$$

for both arrangements by integrating the electric $E(r)$ field over the radius r.

By substituting the electric field from the definition of electric rigidity, $\chi_E^* = E\rho$, to the equation (1.27) the electric potential required to bend a particle with radius of curvature of $r = \rho$ and parallel to the electrodes can be solved to be

$$V(\chi_E^*) = \frac{1}{2} \ln \frac{R_2}{R_1} \chi_E^* \tag{1.29}$$

for the symmetric case. It's worthwhile to notice that the radius of curvature cancels out and the same voltage works for all parallel trajectories independently on radius as far as the rigidity is χ_E^*. The potential energy of an particle, $U(r) = V(r)q$, is however a function of the radius which leads to different rigidities inside the deflector (marked with *) while the rigidity of the particles would be the same in the field free region before the deflector. This effect is usually negligible along the optical axis but can be several per cent for particles close to the electrodes. For non-relativistic velocities one can express the rigidity, χ_E^*, as a function of kinetic energy, E_k^*, (see equation (1.15)) and then the symmetric voltage simplifies to a practical formula

$$V(E_k^*) = \ln \left(\frac{R_2}{R_1} \right) \frac{E_k^* \text{ [MeV]}}{q \text{ [e]}} \text{ MV}. \tag{1.30}$$

Here, the rigidity and the kinetic energy are marked with * in order to address the change in kinetic energy due to different electric potential.

The first order transfer matrix for a cylindrical condensor in a symmetric setup in horizontal direction is [Wol87a]

$$\mathbf{D}_{\mathrm{E},x} = \begin{pmatrix} \cos(\sqrt{2}\phi_0) & \frac{\rho_0}{\sqrt{2}} \sin(\sqrt{2}\phi_0) & \frac{\rho d}{2}(1 - \cos(\sqrt{2}\phi_0) & 0 \\ -\frac{\sqrt{2}}{\rho_0} \sin(\sqrt{2}\phi_0) & \cos(\sqrt{2}\phi_0) & \frac{d}{\sqrt{2}} \sin(\sqrt{2}\phi_0) & 0 \\ 0 & 0 & 1 & 0 \\ 0 & 0 & 0 & 1 \end{pmatrix} \tag{1.31}$$

where ρ_0 is the radius of curvature of the optical axis, ϕ_0 is the deflection angle and $d = \pm 1$ defines whether the bending is towards negative ($d = 1$) or positive ($d = -1$) x-axis. In the equation non-relativistic velocities are assumed. The matrix elements of (1.31) with the relativistic correction can be found in reference [Wol87a]. In the vertical direction the transfer matrix, $\mathbf{D}_{\mathrm{E},y}$, is simply the drift length matrix of the equation (1.19) with length $l = \phi_0 \rho_0$.

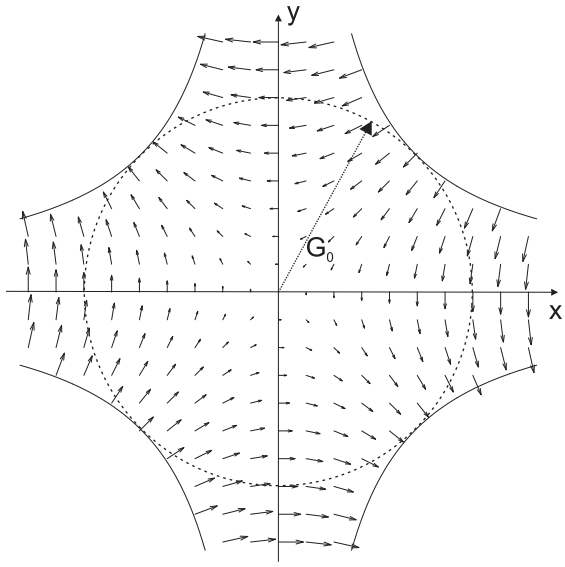

Figure 1.5: A schematic cross-sectional view of a magnetic quadrupole. Arrows show the direction of the B-field at the point and the lengths of the arrows are proportional to the strength of the field. $|\boldsymbol{B}| = B_T$ at radius G_0.

1.2.3 Magnetic quadrupole

Both electrostatic and magnetic quadrupoles are the often most used elements for ion-beam focusing. Electrostatic quadrupoles are restricted to be used with ions having low energy due to limits in high voltage and therefore they are not applicable to recoil separators. An ideal magnetic quadrupole consists of four hyperbolic poles in four-fold symmetry. A schematic view of a cross section of a magnetic quadrupole having inside radius of G_0 is presented in figure 1.5. The figure shows also magnitude and direction of the B-field. The magnitude $|\boldsymbol{B}|$ is proportional to r and has a value of B_T at pole tips at $r = G_0$. An electric quadrupole is similar to the magnetic one but the hyperbolic electrodes are rotated by 45°. Hyperbolic poles are rather difficult to fabricate and often they are replaced by round or facetted poles.

By substituting $\sin(\phi) = y/r$, $\cos(\phi) = x/r$ and $r = \sqrt{x^2 + y^2}$ to the multipole expansion (1.24) with $n = 2$ and $\alpha_n = 0$ one obtains the magnetic field inside a magnetic quadrupole to be

$$\boldsymbol{B}(x, y, z) = -g_B y\hat{\boldsymbol{x}} - g_B x\hat{\boldsymbol{y}} \tag{1.32}$$

where $g_B = C_n/R_{\text{ref}} = B_T/G_0$ is the gradient of the magnetic field.

From figure 1.5 or equation (1.32) one can see the operation of a magnetic

quadrupole. Let us study the quadrupole presented in the figure. If a positively charged ion is flying towards the paper having velocity $\vec{v} = v_z\hat{\boldsymbol{z}}$ it feels a force $\vec{F} = qg_Bv(x\hat{\boldsymbol{x}} - y\hat{\boldsymbol{y}})$ which is focusing in x-direction and defocusing in y-direction for positive g_B. The strength of the bending in both directions is proportional to the distance from the optical axis independently for x and y. Focusing in both directions can be achieved by using multiple quadrupoles in focusing-defocusing-focusing... structure. By changing the polarity of the poles one can swap the focusing and defocusing axes.

The first order transfer matrices describing a magnetic quadrupole focusing in x-direction are

$$\mathbf{Q}_x = \begin{pmatrix} \cos(kw) & k^{-1}\sin(kw) \\ -k\sin(kw) & \cos(kw) \end{pmatrix} \quad \text{and} \tag{1.33a}$$

$$\mathbf{Q}_y = \begin{pmatrix} \cosh(kw) & k^{-1}\sinh(kw) \\ k\sinh(kw) & \cosh(kw) \end{pmatrix}, \tag{1.33b}$$

where the constant k can be calculated from $k^2 = |g_B|q/(mv_z) \approx |B_T|/(G_0\chi_B)$. For vertically focusing quadrupole matrices $\mathbf{Q}_x$ and $\mathbf{Q}_y$ must be swapped.

1.3 Charge state distributions

Heavy atoms having kinetic energy up to few tens of keV are typically single or doubly charged or even neutral when they are emitted from solid foils or are travelling in a gas volume. The developments in accelarator techniques over 50 years ago enabled the acceleration of heavy ions to velocities where a larger fraction of electrons are removed from the atom. This raised a need to estimate the most probable charge state and width of the charge state distribution as a function of projectile velocity and proton number. An extensive compilation of measured charge states, charge-exchange cross sections and various formulae has been published by Betz in 1972 [Bet72]. After that, new parametrizations have been invented and better fits to the measured data have been achieved. Knowing of the average charge state and the width of the distribution is important among others in the design process of an in-flight separator and for example planning of the experiments to be run using a recoil mass spectrometer.

The symbol q is used for both *charge* and *charge state*. The explicit charge is used only in the connection with the Lorentz equation. Otherwise, the symbol q means charge state which is a bare number and which tells how many electrons is removed from the neutral atom. In some contexts the unit of charge cancels out.

The formulae used to estimate the average charge state, $\bar{q}$, after a solid foil

or in a gas are (semi)empirical. It seems that the underlying physics of electron captures and losses mixed with atomic shell effects is too complicated for that one simple, theory based, equation could be invented. Development of computer codes aiming for microscopic description of charge-exchange processes have been started. They calculate the charge-state distribution taking into account electron capture and loss processes in atomic subshells and in principle are not restricted to the equilibrium condition. One promising code is ETACHA [Roz96] developed in GANIL. In 2001 the code was extended to calculate projectiles with up to 60 bound electrons in order to be usable in a lower energy region. The aim is to be able to utilize ETACHA also for ions like 1 MeV/u Sn in the context of the S^3 separator project [Roz09].

The *average charge state* is defined as

$$\bar{q} = \sum_{q=0}^{Z} qF(q), \tag{1.34}$$

where q runs over charge states and $F(q)$ is the equilibrium charge-state fraction. The width, $d_{\bar{q}}$, of the charge state distribution is defined as

$$d_{\bar{q}} = \sqrt{\sum_{q=0}^{Z} (q - \bar{q})^2 F(q)}. \tag{1.35}$$

The charge state of an ion changes in a *charge-exchange collision*. The cross sections for the *electron-capture* and *electron-loss* reactions define the statistical width, $d_{\bar{q}}$, of the charge state distribution. In principle, the charge-state fractions, $F(q)$, and the average charge state, $\bar{q}$, can be calculated from the charge-exchange cross sections. However, these cross sections are very poorly known for fast heavy ions. Also the cross section of multiple electron loss events cannot be ignored in all cases. The other difficulty in the cross section approach is that the probability to change the number of bound electrons depends also on atomic excitation which is caused by interactions between the electron clouds of an ion and a medium. The high velocity or short mean free path between collisions leave less time for atomic de-excitation processes and can effect the average charge state. This phenomenon is called the *density effect*. The exact description of the charge-state fractions or the average charge state would therefore require knowing of capture and loss cross sections for each charge state and excited state combination.

The mean free paths between atomic collisions are much shorter in solid media than in a gas which is the major reason that the equilibrium charge state is much higher in the solid media. The differencies between charge-exchange cross sections in gaseous and solid targets are discussed for example in [Woo84].

1.3.1 Solid targets

Let us consider solid iron which represents here a typical target. The density of iron atoms in a target is about 85 $(\mathrm{nm})^{-2}$. If a fusion product has a velocity of 4% of speed of flight it advances 1 nm in $8.3{\cdot}10^{-17}$ s. This is clearly less than the time needed for atomic de-excitation and thus the atomic excitation can accumulate and high charge states can be produced. One complication follows from the accumulated vacancies in the first principal shells. When such vacancies are filled by electrons from outer shells the energy released can generate an Auger electron or many of them which ionizes the projectile even more. Thus the charge state inside the solid target can be smaller than after the target. The converted de-excitations of long-living nuclear states can also produce Auger electron cascades and increase the average charge state after the target foil [Ulf78].

One of the most often used formulae for estimating the average charge state of heavy ion after a C-foil is

$$\bar{q} = Z\left[1 + \left(\frac{v}{Z^{\alpha}v'}\right)^{-1/k}\right]^{-k}, \tag{1.36}$$

where $k = 0.6$, $\alpha = 0.45$ and $v' = 3.6 \cdot 10^6$ m/s, developed by Nikolaev and Dmitriev [Nik68]. In the same reference, the equation

$$d_{\bar{q}} = d_0\sqrt{\bar{q}\left[1 - (\bar{q}/Z)^{1/k}\right]} \tag{1.37}$$

is given for the width of the charge-state distribution.

Schiwietz and Grande have analysed a large experimental data set of equilibrium charge states after a solid target (and also gaseous targets) [Sch01] and have developed the formula

$$\bar{q} = Z\frac{12x + x^4}{0.07x^{-1} + 6 + 0.3x^{1/2} + 10.37x + x^4}, \tag{1.38}$$

where x is defined as

$$x = \left(0.595v/v_0 Z^{-0.52} Z_t^{-0.019Z^{-0.52}v/v_0}\right)^{1+1.8/Z}. \tag{1.39}$$

In the formula Z_t is the proton number of a target and $v_0 = 2.19 \cdot 10^6$ m/s is the Bohr velocity. According to the reference, the equation is reported to have absolute uncertainty of $\Delta\bar{q} = 0.54$ e and relative uncertainty of $\Delta\bar{q}/Z = 2.3\%$. They give also the following equation for the reduced with of the distribution:

$$w = d_{\bar{q}}\, Z^{-0.27} Z_t^{0.035-0.0009Z} f(\bar{q}) f(Z - \bar{q}), \tag{1.40}$$

where $f(x) = \sqrt{(x + 0.37Z^{0.6})/x}$. The parameter w has a value typically between 0.6 and 0.9. The values of w are plotted against the number of bound electrons $(Z - \bar{q})$ in the reference for experimental data.

Both equations (1.36) and (1.38) as well as many other similar equations not presented here reproduce the general trends of experimental data reasonably well and can be used in the design of a recoil mass spectrometer or in simulations of fusion evaporation reactions when charge-state distributions are concerned. The major deviations of the formulae occur in average charges representing a change in principal electron shell. These shell effects are evident in figures shown in [Sch01] for both $\bar{q}$ and $d_{\bar{q}}$. This so called *shell effect* is discussed in detail by Shima et al. [Shi89]. In the reference [Shi92] Shima et al. tabulate charge-state fractions of projectiles in the range Z =4–92 emerging from a carbon foil having energy range E=0.02–6 A MeV.

The proton number of the target medium affects the charge state slightly. This has been taken into account in (1.38). However, a carbon foil is practically always used downstream from the target to reset the charge states which can be exceptionally high due to an Auger-electron cascade occurring after a converted de-excitation from an isomeric nuclear state.

1.3.2 Gaseous targets

The gaseous targets differ from solid targets mostly in respect to the charge-exchange collision rate. In a gas volume a projectile has typically time enough for Auger-electron emission between collisions and the excitation is not accumulated as in the case of solids. By measuring the charge distribution of Cl, Br and I ions with 4–15 MeV kinetic energies after H and He gases with variable pressure Ryding, Betz and Wittkower have observed clear evidence of the density effect in gas [Ryd70]. Their main conclusion was that the electron capture cross section decreases as a function of collision frequency but the electron loss cross section remains constant. The density effect in gaseous media has been observed also by J. Sarén et al. (see the article included in chapter 3).

The simplest theoretical equation for the average charge state in gas is

$$\bar{q}_1 = (v/v_0)Z^{1/3}, \tag{1.41}$$

where v is the ion velocity, $v_0 = 2.19 \cdot 10^6$ m/s is the Bohr velocity and Z is the proton number of the ion. The equation can be derived from the Bohr stripping criterion [Boh40] when applied to the Thomas-Fermi atomic model. Substituting this average charge state to equation (1.11) the magnetic rigidity becomes velocity independent. The gas-filled recoil separators take advantage of this important property. The Bohr stripping criterion states that all the electrons of the projectile which have lower orbiting velocity than the velocity

of the projectile travelling in the gas volume are stripped. This criterion is practically the only physical input for the average charge state formulae. The criterion is discussed in detail in reference [Bet72].

Equation (1.41) can be obtained as a first order approximation from the parametrization

$$\bar{q}_2 = Z\left[1 - C_1 \exp\left(-C_2(v/v_0)Z^{-2/3}\right)\right], \tag{1.42}$$

of Betz [Bet72] by choosing $C_0 = C_1 = 1$. Ghiorso et al. [Ghi88] deduced the values of $C_1 = 1.04$ and $C_2 = 0.91$ from a fit to experimental data. Let us label this equation with these fitted coefficients as $\bar{q}_3$. Based on the measurements carried out in Dubna, Oganessian et al. have reported for the case of He gas the following parametrization [Oga91]

$$\bar{q}_4 = \begin{cases} 0.394(v/v_0)Z^{1/3} + 1.65 & \text{if } v/v_0 < 9.13Z^{-1/3} \\ 0.723(v/v_0)Z^{1/3} - 1.18 & \text{if } v/v_0 > 9.13Z^{-1/3} \end{cases}, \tag{1.43}$$

which resembles the first order approximation of equation (1.42). Later, using a larger data set the formula

$$\bar{q}_5 = 0.00871(v/v_0)^{1.54}Z^{1.10} + 2.05. \tag{1.44}$$

was constructed in Dubna [Lei04]. The equations (1.43) and (1.44) have been found to be generally in agreement with magnetic rigidity values measured in RITU experiments. Similar equations with different coefficient values exist for hydrogen filling gas also.

Probably the most general semiempirical formula was published by Schiwietz in 2001 [Sch01]

$$\bar{q}_6 = Z\frac{376x + x^6}{1428 - 1206x^{0.5} + 690x + x^6}, \tag{1.45}$$

with reduced parameter

$$x = \left(v/v_0\, Z^{-0.52} Z_t^{0.03-0.017Z^{-0.52}v/v_0}\right)^{1+0.4/Z},$$

where Z_t is the proton number of the target atom.

Gregorich et al. [Gre05] have implemented the empirical charge state formula

$$\bar{q}_7 = mx + b + d\sin\left\{\frac{2\pi}{32}\left[Z - (mx + b) - f\right]\right\} \tag{1.46}$$
$$x = \frac{v}{v_0}Z^{1/3} \quad (\text{valid for } Z \gtrsim 45)$$

for heavy ions travelling in dilute He gas. It has the same linear trend as a function of velocity ($vZ^{1/3}$) as in the equations (1.41) and (1.43). In addition

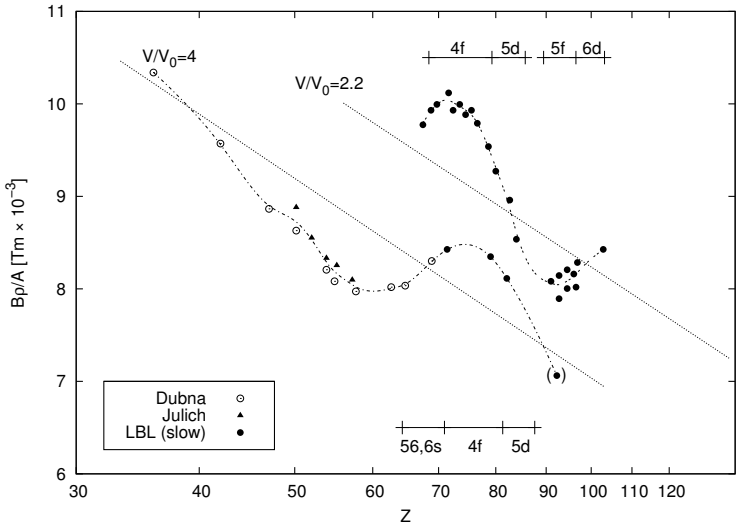

Figure 1.6: Example of electron shell effects to the average charge state. The points represent experimental data and the dot-dashed lines are for helping the eye. The datapoint in parentheses has $v/v_0 = 3.33$. The straight lines are fits to data and show the linear $Z^{-1/3}$ trend. The datapoints and other information have been adopted from a similar figure in [Ghi88].

to these, the formula introduces a sinusoidal correction which takes the atomic shell effects into account. In the publication, values of $m = 0.641$, $b = -0.235$, $d = 0.517$ and $f = 74.647$ have been reported as a result from a global fit. An example of shell effects is shown in figure 1.6 where the magnetic rigidities divided by mass number are plotted against the proton number of the projectiles.

The width of the charge distribution, $d_{\bar{q}}$, in gas is close to the width after solid targets. The shell effects affect also $d_{\bar{q}}$ and based on obvious reasons the distribution should be narrower if the equilibrium charge state is low or close to Z. In the reference [Bet72] the estimation

$$d_{\bar{q}} = 0.27\sqrt{Z} \tag{1.47}$$

is given for gases and solids. However, the essential observation is that the $d_{\bar{q}}$ is practically independent on velocity.

The above average charge-state equations ($\bar{q}_{1,3\text{–}6}$) have been compared against the experimental equilibrium charge states measured as a side result of the RITU transmission studies and discussed in the article included in chapter 3.

Charge-exchange cross sections

Schlachter et al. [Schla83] have found an empirical scaling rule for the electron-capture cross section applicable to highly charged ions in gas. According to their work, the reduced cross section, $\tilde{\sigma}$, as a function of the reduced energy, $\tilde{E}$, can be expressed as

$$\tilde{\sigma} = \frac{1.1 \cdot 10^{-8}}{\tilde{E}^{4.8}} \left(1 - e^{-0.037\tilde{E}^{2.2}}\right) \left(1 - e^{-2.44 \cdot 10^{-5}\tilde{E}^{2.6}}\right). \tag{1.48}$$

The definitions of reduced quantities are

$$\tilde{\sigma} = \sigma Z_t^{1.8}/q^{0.5} \quad \text{and} \tag{1.49a}$$

$$\tilde{E} = E/\left(Z_t^{1.25} q^{0.7}\right), \tag{1.49b}$$

where σ is the real cross section in cm^2 and E is the kinetic energy in keV/u.

If a Gaussian shape is assumed for a charge-state distribution then the charge-state fractions are

$$F(q) = (d_{\bar{q}}\sqrt{2\pi})^{-1} e^{-(q-\bar{q})^2/(2d_{\bar{q}}^2)}, \tag{1.50}$$

where $d_{\bar{q}}$ is the standard deviation of the distribution centered at $\bar{q}$. Let us further assume that the charge state evolves in the charge-exchange collisions via single electron capture or loss and the cross sections of such events can be approximated with the exponential functions

$$\sigma_c(q) = A_c e^{b_c(q-\bar{q})} \quad \text{and} \tag{1.51a}$$

$$\sigma_l(q) = A_l e^{b_l(\bar{q}-q)}, \tag{1.51b}$$

where symbols with subscripts c and l refer to capture and loss events, respectively. If the assumptions hold then the coefficients of the exponential cross-section curve for electron loss can be solved from the width of the charge state distribution and the coefficients of the capture curve as [Bet83]

$$b_l = 1/d_{\bar{q}}^2 - b_c \quad \text{and} \tag{1.52a}$$

$$A_l = A_c e^{(b_c - b_l)/2}. \tag{1.52b}$$

The empirical formulae for the average charge state in gas and width of the distribution (obtained with (1.47) or interpolated from experimental data) can be used together with the Schlachter scaling rule (1.48) for the capture cross section in order to calculate the cross section for an electron loss event. The mean free path between the charge-exchange collisions in gas having a molecular density n is then

$$l_{qq'} = \frac{1}{n(\sigma_c + \sigma_l)}. \tag{1.53}$$

1.4 Fusion evaporation reactions

The valley of beta stability bends towards neutron rich nuclei when the number of protons is increased. Up to nickel the lightest stable isotope of a given element is relatively close to the $N = Z$ line (especially for even Z). The heaviest stable $N = Z$ nucleus is ^{40}Ca. The heavier elements have more and more neutrons than protons. Thus the isotopes on the β^+ active side of the valley of β stability can be studied via fusion reactions. In contrast, the study of the super heavy elements and the lighter neutron rich isotopes (β^- side of the valley of stability) are difficult to access via fusion due to lack of neutrons in a reaction.

After a fusion of two distinct nuclei the nuclides are interacting and moving towards a minimum in potential energy. In the time scale of $\cdot 10^{-22}$ s after the collision the projectile and target nuclei are still partly separated. At this point the system can undergo either fast fission or a formation of the *compound nucleus*. After the compound nucleus is formed the system reaches an equilibrium where it has no information about the colliding nuclei anymore. At about 10^{-19} s after the collision the compound system cools down by evaporating light particles (neutrons, protons, alphas) and at 10^{-15} s the de-excitation process continues by emission of statistical γ rays.

1.4.1 Fusion barrier

Before the fusion reaction the projectile and target atom feel the repulsive Coulomb barrier generated by protons in both nuclei. If a sufficient amount of kinetic energy is available in the collision to bring the nuclei in the range of the strong interaction the nuclei can fuse and form the compound nucleus. The minimum energy needed to reach this small distance is called the *interaction barrier*.

The height of the interaction barrier of projectile ($^{A_p}Z_p$) and target ($^{A_t}Z_t$) nuclei can be calculated quite precisely with the classical Bass model [Bas74]. The Bass interaction barrier is

$$B_{int} = \frac{Z_p Z_t e^2}{4\pi\varepsilon_0 R_{12}} \left[\frac{R_{12}}{R_{12} + d_{int}} - \frac{1}{x} \frac{d}{R_{12}} \exp\left(\frac{-d_{int}}{d} \right) \right], \tag{1.54}$$

where

$$x = \frac{e^2}{4\pi\varepsilon_0 a_s} \frac{Z_1 Z_2}{A_p^{1/3} A_t^{1/3} R_{12}}$$

is the ratio of the Coulomb force to the nuclear force at the point of contact $r = R_{12} = r_0(A_p^{1/3} + A_t^{1/3})$. The constant $a_s = 17.23$ MeV is the surface-term

constant of the liquid-drop model. The interaction barrier corresponds to the kinetic energy needed in center-of-mass reference frame to bring the nuclei at the distance $R_{12} + d_{int}$, where R_{12} is the sum of the radii of the nuclei and d_{int} is the interaction distance. According to [Bas74] the values $d = 1.35$ fm and $d_{int} = 2d = 2.70$ fm are good for heavy projectiles and targets if $r_0 = 1.07$ fm is adopted.

1.4.2 Kinematics

The kinetic energy of the approaching projectile and target atoms in the center-of-mass reference frame, E_{CM}, as a function of the projectile kinetic energy, $E_{\mathrm{p,lab}}$, is

$$E_{\mathrm{CM}} = \frac{m_{\mathrm{t}}}{m_{\mathrm{p}} + m_{\mathrm{t}}} E_{\mathrm{p,lab}}, \tag{1.55}$$

where m_{p} and m_{t} are the masses of the projectile and target, respectively.

After a fusion of two distinct nuclei, the protons and neutrons form a compound nucleus ($^{\mathrm{A_p+A_t}}(\mathrm{Z_p + Z_t})$). The collision is perfectly inelastic since the colliding particles stick together. The velocity of the compound nucleus, v_{c}, can be derived from the conservation of momentum and becomes

$$v_{\mathrm{c}} \equiv v_{\mathrm{c,lab}} = \frac{m_{\mathrm{p}}}{m_{\mathrm{p}} + m_{\mathrm{t}}} v_{\mathrm{p,lab}} \tag{1.56}$$

as a function of the projectile velocity $v_{1,\mathrm{lab}}$ and masses of the nuclei. Therefore the kinetic energy of the compound nucleus in the laboratory frame is

$$E_{\mathrm{c,lab}} = \frac{m_{\mathrm{p}}}{m_{\mathrm{p}} + m_{\mathrm{t}}} E_{\mathrm{p,lab}}. \tag{1.57}$$

Since the total momentum in the CM reference-frame is zero the compound nucleus will be at rest in the CM system. Clearly, the kinetic energies of the projectile and the target nuclei will end up in the excitation energy of the compound. The binding energy of the compound is typically different from the sum of the binding energies of the colliding nuclei and thus the change in binding energy contributes to the excitation energy also. The change in binding energy is the *Q-value* of the reaction and is defined as

$$Q = (m_{\mathrm{initial}} - m_{\mathrm{final}})c^2 = (m_{\mathrm{t}} + m_{\mathrm{p}} - m_{\mathrm{c}}), \tag{1.58}$$

where m_{c} is the mass of the compound nucleus. The Q-value tells how much energy is released in the reaction. Taking the Q-value into account the excitation energy becomes

$$E^* = E_{\mathrm{CM}} + Q. \tag{1.59}$$

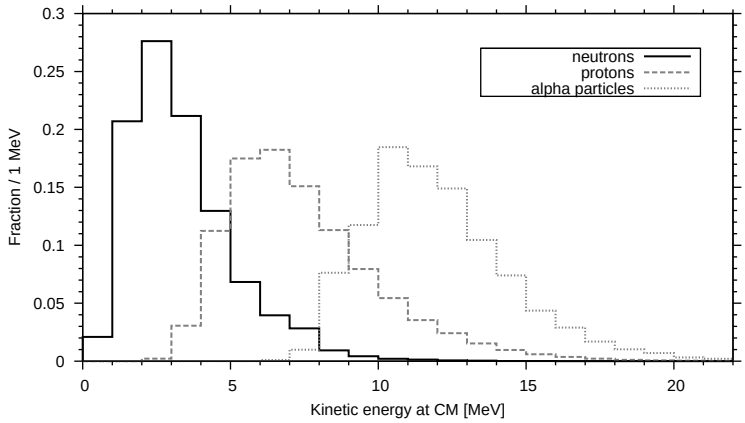

Figure 1.7: Kinetic energies of evaporated light particles (neutrons, protons and alphas) in the center-of-mass reference frame after the symmetric fusion reaction ^{40}Ca(115 MeV in lab.) + ^{40}Ca calculated with PACE4.

1.4.3 Evaporation of light particles and cooling down

Right after the formation the compound nucleus has a large amount of excitation energy and typically also high angular momentum. In the first stage (at $t \approx 1 \cdot 10^{-19}$ s) the nucleus cools down by evaporating light particles—neutrons (n), protons (p) and alpha particles (α). These particles have kinetic energies ranging from neutrons of a 1–2 MeV up to alphas of around 20 MeV in the center-of-mass frame. Typical CM-energy spectra of emitted particles are shown in figure 1.7. The spectra, calculated with the PACE4 evaporation code [Gav80], are taken from a reaction where ^{40}Ca target atoms are bombarded by $E_{\mathrm{p,lab}} = 115$ MeV ^{40}Ca projectiles. As can be seen, the energy spectra have the shape of the Maxwell-Boltzmann distribution. It's worthwhile to note that the energy spectra do not vary much between different fusion reactions and reasonably good estimations of recoil angular distributions can even be achieved by using discrete center-of-mass energies of about 2, 7 and 12 MeV for n, p and α, respectively.

The evaporation of neutrons is isotropic in the center-of-mass frame and the subsequent emissions are independent of each other since the neutrons carry only little angular momentum. Alpha particles can carry more angular momentum and thus subsequent α emissions can have a strong angular correlation (see for example [Col00] and references therein). In practice, for the purposes of nuclear structure studies, the assumption of isotropic emission is adequate especially when the nuclei of interest are produced via neutron and proton evaporation.

After the formation of a compound nucleus the center-of-mass reference-frame is moving forward with velocity v_c and the compound is at rest in the CM frame. Let the first evaporated particle have mass $m_{\mathrm{e},1}$ and velocity $\boldsymbol{u}_{\mathrm{e},1}$ in the CM frame. The conservation of momentum yields

$$\boldsymbol{u}_{\mathrm{r},1} = -m_{\mathrm{e},1}/m_{\mathrm{r},1}\boldsymbol{u}_{\mathrm{e},1} \tag{1.60}$$

for the recoil velocity in CM frame. The velocity of the recoil in the laboratory frame is simply $\boldsymbol{v}_{\mathrm{r},1} = \boldsymbol{v}_{\mathrm{c}} + \boldsymbol{u}_{\mathrm{r},1}$. In the next evaporation step the recoil velocity from the previous step is taken to be the new CM velocity. The final recoil velocity after all evaporations is therefore

$$\boldsymbol{v}_{\mathrm{r}} = \boldsymbol{v}_{\mathrm{c}} + \sum_i \boldsymbol{u}_{\mathrm{r},i} = \boldsymbol{v}_{\mathrm{c}} - \sum_i \frac{m_{\mathrm{e},i}}{m_{\mathrm{r},i}}\boldsymbol{u}_{\mathrm{e},1}. \tag{1.61}$$

The maximal change in residue angle is obtained approximately when the light particle is emitted to the angle of $\theta_{\mathrm{e,CM}} = 90^\circ$. If the non-relativistic formulae are used then one can obtain the estimate

$$\theta_{\mathrm{r},1} \approx \frac{u_{\mathrm{r},1}}{v_{\mathrm{c}}} = \frac{m_{\mathrm{c}}}{m_{\mathrm{c}} - m_{\mathrm{e},1}}\sqrt{\frac{m_{\mathrm{e},1}}{m_{\mathrm{p}}}}\sqrt{\frac{E_{\mathrm{e,1,CM}}}{E_{\mathrm{p,lab}}}} \tag{1.62}$$

for the change in evaporation residue angle in the laboratory frame of reference. To get some idea about the recoil effect caused by the evaporation of a light particle, let us consider the fusion reaction ^{40}Ca + ^{40}Ca as an example. For n, p and α energies of 2, 7 and 12 MeV the equation (1.62) yields results of 0.021, 0.040 and 0.110 (rad) for $u_{\mathrm{r},1}/v_{\mathrm{c}}$, respectively. From this, one can observe that in the case of an evaporation channel including an α particle the recoils are easily outside of the acceptance of an in-flight separator if the emission of the α particle occurs at angles around $\theta_{\mathrm{e,CM}} = 90^\circ$. It should be noted that in isotropic emission these angles are also the most probable ones. The recoil effect is illustrated in figure 1.8 for the reaction ^{40}Ca(115 MeV) + ^{40}Ca in three cases: a) single α evaporation with $E_{\mathrm{e,CM}} = 12$ MeV, b) single α evaporation using the energy distribution shown in figure 1.7 and c) evaporation of an α followed by a proton (αp) using the energy distributions. The left column shows horizontal and vertical angles and reveals a clear ring in all cases. The right column shows the energy of the recoil (E_{r}) versus recoil angle (θ_{r}).

If a very thin target is used and only one particle is evaporated then the circle roughly at a radius given by (1.62) in the (a_0, b_0) plot could be observed. Figure 1.7 (b) illustrates this for the α channel in the case of the target having negligible thickness. Evaporation of multiple particles and variation of the depth of the reactions in the target leading to variable energy losses and scattering of projectiles and recoils dissolves the ring in the figure and thus in most of the reactions the most probable (a_0, b_0) value is at the origin. However, the energy and angle distribution of the events accepted by a separator may still

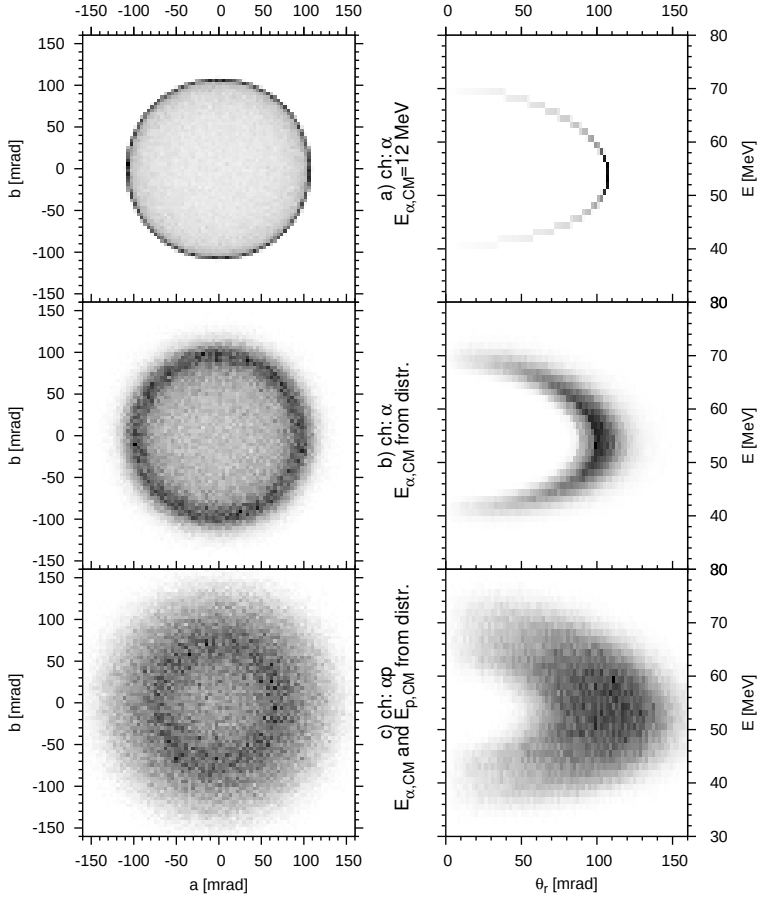

Figure 1.8: The recoil effect in the case of the reaction ^{40}Ca(115 MeV)+^{40}Ca. The energy losses and scattering in the target are ignored. The angle and energy of a fusion evaparation residue after an isotropic evaporation of a) $E_{\alpha,\mathrm{CM}} = 12$ MeV α particle, b) α with the energy distribution and c) α and proton with the energy distribution. The energy distributions in (b) and (c) are shown in figure 1.7. The data are calculated with the JIonO code (see section 1.5).

differ from Gaussians due to the recoil effect. Largest deviations are expected for channels α, p, αn and αp.

One should consider also what happens to charged particles emitted to the forward direction inside the acceptance of an in-flight separator. The CM velocities of evaporated protons and alphas are larger than the velocity of the CM frame and therefore it is enough to consider a forward emission in the CM frame. If non-relativistic equations are used for kinetic energies then the equation

$$E_{\mathrm{e},1,\mathrm{lab}} = E_{\mathrm{e},1,\mathrm{CM}} \left(1 + \frac{m_{\mathrm{e},1} m_{\mathrm{p}}}{m_{\mathrm{c}}^2} \frac{E_{\mathrm{p,lab}}}{E_{\mathrm{e},1,\mathrm{CM}}} + 2 \frac{\sqrt{m_{\mathrm{e},1} m_{\mathrm{p}}}}{m_{\mathrm{c}}} \sqrt{\frac{E_{\mathrm{p,lab}}}{E_{\mathrm{e},1,\mathrm{CM}}}} \right) \quad (1.63)$$

gives the energy of the evaporated particle emitted at zero angle. In the case of the reaction ^{40}Ca + ^{40}Ca one obtains 12 and 27 MeV for such a proton and α, respectively. These numbers correspond to magnetic rigidities of $\chi_B(p)$ =0.5 Tm and $\chi_B(\alpha)$ =0.75 Tm. It seems that in some cases it is possible that these charged particles are transported through the magnetic separator. The electrostatic rigidites for both are more than $\chi_E = 20$ MV which is much higher than that of the recoil and thus an electrostatic deflector should give a strong suppression for evaporated charged particles.

After the evaporation of light particles the nucleus has excitation energy below the evaporation threshold. Now in a timescale of 10^{-15} s the nucleus emits statistical E1 γ-rays which reduces energy but not much angular momentum. After this step the nuclear excitation energy consists mostly of rotational energy ($E \propto I(I+1)$) and it is close to the *yrast line* which is defined by excited states having lowest energy for given angular momentum I. Around time being about 10^{-12} s the nucleus starts slowing down the rotation by emitting E2 γ-rays.

1.4.4 Elastically scattered target atoms

The background particles entering an in-flight separator in an experiment utilizing a fusion evaporation reaction consists of neighbouring fusion-evaporation channels, scattered beam, elastically scattered target atoms and products of transfer reactions and of evaporated charged particles. In a transfer reaction a few nucleons are transferred between a projectile and a target nucleus and therefore the products of such reactions are either target-like or primary-beam like nuclei having properties close to the elastically scattered target or beam particles, respectively.

In an elastic collision the target atom gains momentum towards the beam direction. The equation for kinetic energy of the target atom after the elastic collision can be derived from conservation of momentum and kinetic energy

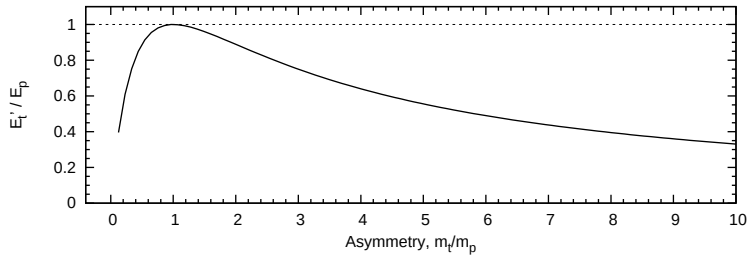

Figure 1.9: The energy of a target atom relative to energy of a projectile after an elastic head on collision between them as a function of the reaction asymmetry.

and is

$$E'_{\mathrm{t}}(\theta'_{\mathrm{p,CM}}) = \frac{2m_{\mathrm{p}}m_{\mathrm{t}}}{(m_{\mathrm{p}}+m_{\mathrm{t}})^2}\left[1-\cos(\theta'_{\mathrm{p,CM}})\right]E'_{\mathrm{p}}, \tag{1.64}$$

where $\theta'_{\mathrm{p,CM}}$ is the angle of the projectile atom after the collision in CM frame. The maximal value of (1.64) is achieved in the case of back scattering ($\theta'_{\mathrm{p,CM}} = \pi$). The angle of the target atom in the laboratory frame is given by

$$\theta'_{\mathrm{t}} = (\pi - \theta'_{\mathrm{p,CM}})/2. \tag{1.65}$$

The factor $1-\cos(\theta'_{\mathrm{p,CM}})$ in (1.64) can be expressed as $1+\cos(2\theta'_{\mathrm{t}})$ which is very close to 2 for small angles. Thus the kinetic energy of the elastically scattered target atom in forward directions ignoring the energy losses in the target is approximately given by

$$E'_{\mathrm{t}} \approx \frac{4m_{\mathrm{p}}m_{\mathrm{t}}}{(m_{\mathrm{p}}+m_{\mathrm{t}})^2}E_{\mathrm{p}} = 4\frac{m_{\mathrm{t}}/m_{\mathrm{p}}}{(1+m_{\mathrm{t}}/m_{\mathrm{p}})^2}, \tag{1.66}$$

where $m_{\mathrm{t}}/m_{\mathrm{p}}$ is the asymmetry of the reaction. The graph is shown in figure 1.9.

In the case of a symmetric reaction the elastic scattering of target atoms should not be a problem since these particles have rigidities similar to that of the primary beam which needs to be suppressed in any case. In a typical RITU experiment the elastically scattered target particles are usually seen but the rates are not too high. It has been observed that the amount of target like nuclei is increasing towards higher asymmetry. Rigidities for elastically scattered target atoms in the case of a vacuum-mode spectrometer are shown in table 2.8 for five fusion reactions.

1.5 JIonO—code for in-flight separator modelling

A Computer code, called *JIonO*, has been developed mainly to help design of the MARA separator. It has been found to be useful also for RITU transmission calculations which are discussed in chapter 3. Although the code has been valuable it is based on quite staightforward use of equations given in this thesis work and other codes like GICOSY [GICOSY], TRIM [Zie04] and PACE4 [Gav80]. The principles of the code are discussed in the following sections mostly from the physics point of view.

The JIonO code offers calculation routines in different categories related to the simulation of in-flight separators. These are

- Calculation of fusion-evaporation reactions across a target and taking care of energy losses and scattering of projectiles and products,
- Generation of various test distributions to be transported and charge state distribution calculations,
- Transportation of particles throught an optical system using matrices calculated with the GICOSY code either in vacuum or in gas (gas-mode routines are partly under development),
- Visualization of information across the optical system (for example cross-sectional view of beam profiles and trajectories),
- Apertures and collimators and
- Degraders based on interpolation of user given data and automatic use of the TRIM code.

In order to get the maximal advantage of the code for various purposes it has been developed as a library and not as a compact programme. This approach enables the flexible use of its routines in other programmes. Actually, the user is always required to write a programme in order to use JIonO. The JIonO library has been written in an object-oriented way using the C++ language. For typical purposes JIonO provides a skeleton of calculation via a set of abstract base classes. The user programme implements suitable classes inherited from the abstract base classes or uses ready-made classes provided by the library. As an example the user can implement a class which calculates ion interactions in a target medium and pass this for a fusion-evaporation routine. The main methods utilized in the JIonO library are presented in next sections and a brief comparison to other codes is given in section 1.5.4 except that the other implementations for gas-filled systems are discussed in section 1.5.3.

The ion-optical calculation in the case of in-flight spectrometers is straightforward in the sense that after the ions have been created they are transported through successive optical elements typically without any feedback. The natural structrure for a programme which models such a successive chain of operations is to represent the target, optical elements, apertures, detectors and degraders as blocks which take the data (set of particles) in and transform it for the input of the next block. The order in which the blocks are executed is naturally the order they are "existing" in a real optical system along the optical axis. In JIonO the classes representing the mentioned actions are derived from a common base class and can be packed to a container object which executes them in given order.

1.5.1 Simulation of fusion-evaporation reactions and ion interactions in a target

The simulation of a fusion evaporation reaction and an ion interaction inside a target can be divided into three steps: 1) energy loss and angular scattering of a projectile ion to the depth of the reaction, 2) evaporation of particles using user provided CM-energy spectra and 3) energy loss and scattering of the evaporation residue (recoil) out of the target. The user programme can implement a handler for evaporation information (location, interaction energy, emitted particles and their velocities and resulting recoil velocity) which is called after every fusion reaction. This informations can be used for example to model a charged particle veto detector located at the target position.

Before modelling interactions or evaporations in the target the code samples N projectiles using a given distribution or a user defined class. The N projectiles are then distributed to B bins with equal width over the target having a total thickness of d_t. The normalized weight $w_{\mathrm{b},j}$ is attached to every bin j and the number of fusion reactions to be calculated in the bin j is about $w_{\mathrm{b},j}N$. The proportions $w_{\mathrm{b},j}N$ are divided for bins in random order since N cannot be always divided for bins exactly according to the weights. Let the number of reactions in bin j be N_j. Additionally, it has been ensured that all bins having $w_{\mathrm{b},j} > 0$ get at least one projectile. The destination depths of the N_j projectiles inside bin j are randomly sampled from a flat distribution and the corresponding fractional position of the reaction i is labeled as $l_{\mathrm{r},i}$ where $l_\mathrm{r} = 0$ ($l_\mathrm{r} = 1$) represents upstream (downstream) edge of the target. The weights and bins have been realized because in some cases, depending on excitation function of the fusion channel, they can enable better statistics with a smaller number of reactions.

The number of reactions to be calculated, N, corresponds to primary beam intensity I which can be defined by the user. If I is set to be the projectile rate

on target the JIonO simulation will yield the correct rates for recoils assuming the right cross-section curves have been given. After the evaporation of defined light particles a weight

$$w_i = \frac{I}{N_j}\frac{n_\mathrm{t}}{B}\sigma(E_{\mathrm{p},i}), \tag{1.67}$$

where n_t is the particle density of the target atoms, is attached to recoil i. The weight is therefore the number of recoils the simulated recoil, i, represents. This approach assumes that the intensity of the projectiles does not change along the target meaning that the cross sections for reactions must be small and losses due to interaction in the target can be ignored.

Angular scattering and energy losses in target

The fusion evaporation object in JIonO samples first the N projectiles having kinetic energies $E_{0,i}$ before the target. In the next step these projectiles are transported to the sampled depths, $l_{\mathrm{r},i}$, into the target. JIonO can automatically simulate this by using the TRIM code. Alternatively, the user programme can implement a class which can be used to sample the energy loss and scattering for projectiles and recoils separately. One of the simplests distributions for sampling of the kinetic energy of the projectile i at the moment of the fusion reaction is

$$E_i \sim E_{0,i} + \frac{l_{\mathrm{r},i}d_\mathrm{t}}{d_\mathrm{s}}\overline{\Delta E} + \mathcal{G}\left(\sqrt{\frac{l_{\mathrm{r},i}d_\mathrm{t}}{d_\mathrm{s}}}\sigma_{\Delta E}\right), \tag{1.68}$$

where $\overline{\Delta E}$ and $\sigma_{\Delta E}$ are the average energy loss and the standard deviation of an energy loss distribution, respectively, measured for a sample having a thickness of d_s. The function $\mathcal{G}(\sigma)$ represents a Gaussian distribution having standard deviation σ.

Correspondingly, the direction of the compound nucleus can be sampled in horizontal direction (replace $a \to b$ for vertical direction) as

$$a_i \sim a_{0,i} + \mathcal{G}\left(\sqrt{\frac{l_{\mathrm{r},i}d_\mathrm{t}}{d_\mathrm{s}}}\sigma_{\Delta a}\right), \tag{1.69}$$

where $a_{0,i}$ is the direction of the projectile entering the target and $\sigma_{\Delta a}$ is the standard deviation of the horizontal angle distribution for the sample.

After the fusion reactions the energy loss and scattering of the recoils can be sampled in a similar way as for projectiles except the target thickness in equations (1.68) and (1.69) to be penetrated is now $(1 - l_{\mathrm{r},i})d_\mathrm{t}$.

Evaporation of light particles

The fusion evaporation class evaporates light particles in given order. In RITU and MARA simulations α particles are typically evaporated first before protons, and the neutrons are emitted lastly. The class samples the center-of-mass energies of the evaporated particles by using a class provided by the user programme. The following classes for this purpose are realized in the library: 1) evaporation in single discrete energies defined by user, 2) energies according to user defined distribution and 3) energies sampled and interpolated from distributions read from PACE4 output files for the reaction. The built-in classes (1) and (2) have been used to produce data for figure 1.8.

The recoil velocity after the reaction, $\boldsymbol{v}_r$, is calculated by adding the recoiling velocities $\boldsymbol{u}_{r,i}$ of each evaporation step to a compound nucleus velocity of equation (1.56) as described in equation (1.61). The light particles are emitted isotropically and independently of each other. The direction of a particle is sampled using the `gsl_ran_dir_3d()` function provided by *Gnu Scientific Library* [GSL].

The independence of subsequent evaporation steps and sampling of the energies from distributions which does not take into account the change in excitation energy in an evaporation chain is of course an approximation. In principle, it is possible, although unlikely, that this method produces some recoils having negative excitation energy. To validate this approximation a comparison of recoil energies and angles in evaporation channels of a) 3p b) α2p and c) 4n has been made between JIonO and PACE4. The results are shown in corresponding subfigures of figure 1.10. The cases (a) and (b) are calculated for the reaction ^{40}Ca(115 MeV)+^{40}Ca and the case (c) for the reaction ^{40}Ar(170 MeV)+^{150}Sm. The numbers of reactions calculated with JIonO are much higher and the contours are therefore smoother. The contours represent constant fractions relative to the total number of counts (not maximum) and can be compared to each other. For channels 3p and 4n the differences are very small. For the channel α2p the angular distribution from JIonO is extending a little further and seems to be a little bit more peaked at the top while the PACE4 distribution has steeper slopes in angular direction but has a more flattened top. However, the differences are small and it can be assumed that the simple method used by JIonO is sufficient to be used for modelling recoil distributions for in-flight separators.

1.5.2 Transfer matrices

The main task of JIonO is to transport ions through an optical system consisting of drift spaces, dipoles, quadrupoles etc. Since the first order matrices

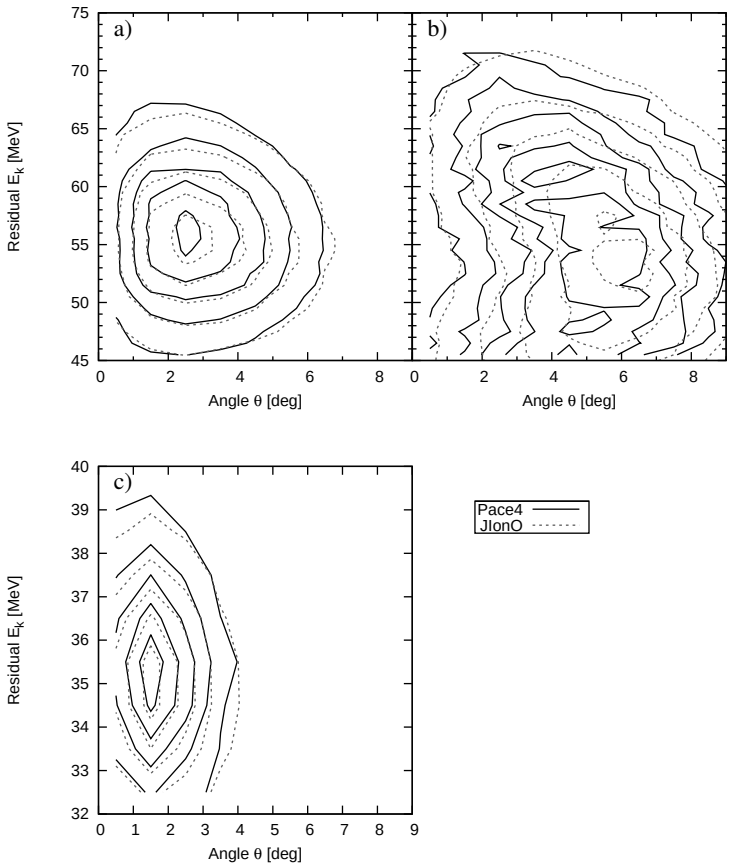

Figure 1.10: Kinetic energy vs. angle distributions of fusion evaporation residues after evaporation of a) 3 protons, b) alpha and 2 protons and c) 4 neutrons according to PACE4 results and JIonO simulation which is partially based on PACE4. The reaction in top figures a) and b) is ^{40}Ca+^{40}Ca with a beam energy of 115 MeV. The reaction used for figure c) is ^{40}Ar+^{150}Sm with an argon beam energy of 170 MeV.

introduced earlier in this chapter are not realistic enough for accurate simulations, JIonO calculates higher order matrices (up to 5th order) with an external programme, GICOSY [GICOSY]. GICOSY is a shell programme which reads an ascii input file and produces ascii files as output. It can be used to calculate transfer matrices with "standard" fringing fields for most common optical elements. The JIonO library includes an interface which communicates with GICOSY and hence decreases the number of steps in a calculation. JIonO is not currently able to run any minimization of optical parameters which enforces one to use for example GICOSY directly in a design process of an optical system.

JIonO acquires matrices from GICOSY with matrix output format "`NONSYMPLECTIC ENERGY TIME NONSCALED`" which is passed to GICOSY command "`OUTPUT COORDINATES`". In JIonO the matrices are stored rather in a polynome format than as a two-dimensional array of numbers. Most of the transfer coefficients are zero due to symmetries and in the polynome format such coefficients are not used at all which speeds up the multiplication procedure. The multiplication has been optimized so that for example the third order factor x^2a is calculated as a product $x^2 \cdot a$ saving one multiplication since the x^2 is already calculated.

The set of ions to be transported is represented as a table where row i is assigned to the ion with number i. The columns are named and represent properties and coordinates of an ion. The user programme can freely add, erase and copy columns apart from a few standard columns which cannot be modified. The user programme can add a built-in column-copying object to the block sequence containing typically target, apertures, optical elements, etc. This object copies for example the current x-coordinate column (called "`X`") to a column with the name "`Xsomething`". These copied columns can be used later for making 2D or 3D histograms which combine for example spatial coordinates from different profile planes. The mass and energy related coordinates G and D, respectively, used by the GICOSY matrices are defined by equations (1.4) and (1.5). These need to be recalculated if the mass, energy or charge of an ion have changed.

For many purposes, like trajectory drawing, the transfer matrix representing the whole optical element is too long. For such cases the maximum length of the transfer matrix can be given which enforces JIonO to construct an element from several GICOSY matrices. The code starts from a full-length matrix. If the length is too long the matrix of half length will be calculated. This halving is continued until the length becomes shorter than required. However, this approach fails in fringing fields since they cannot be split as GICOSY does not provide any method for that. This can be a problem in a case when the properties of an ion are changed (for example due to charge-exchange collisions) in the vicinity of an effective field boundary.

1.5.3 Transporting particles through a gas-filled separator

The principle of the calculation of a gas-filled system in JIonO follows the method described by Paul et al. [Pau89] with the main exception that in JIonO transfer matrices are used instead of a direct integration of the equation of motion based on Lorentz force. Ninov et al. [Nin95] have used almost the identical approach to Paul et al. except they have used interpolated and/or extrapolated experimental equilibrium charge-states and electron capture and loss cross-sections instead of semi-empirical formulas. Apparently, these codes are not in any use nowadays. Subotic et al. have built a code called ANAMARI [Sub02, Sub08] which seems to be used actively for optimizing parameters of the Dubna Gas-Filled Separator, DGFRS. According to the publications, the ANAMARI code describes well the experimental observations of recoil distributions after DGFRS, and the separator acceptance. However, the methods of how the charge-exchange collisions are implemented in ANAMARI are not described well in the literature. ANAMARI integrates also the equation of motion (Lorentz force) directly and takes into account the scattering and energy loss in gas.

The operation of the gas-filled mode in the VAMOS spectrometer [Pul08] in GANIL has been tested recently and the ANAMARI code has been reported to be used for calculations of magnetic rigidities of primary beam, elastically scattered target and recoils but not for recoil transport through VAMOS [Schmitt10]. According to the publication, the transportation of the recoils has been carried out by the ray-tracing technique but not taking the charge-exchange collisions into account at a microscopic level. It seems that a recoil trajectory has been determined from the initial velocity with the average charge state calculated by (1.42) with constants based on the work of Ghiorso et al. [Ghi88]. This approach seems to be adequate for that purpose but is not applicable for longer mean free paths.

In the gas mode, JIonO transports one ion at a time through an element. An optical element is divided to 2^n parts where n is the smallest integer satisfying the equation $l_{\mathrm{eff}}/2^n < l_{\mathrm{min}}$ where l_{min} is a user-defined parameter. The halving procedure described earlier produces a set of matrices with effective lengths $\{l_{\mathrm{eff}}, l_{\mathrm{eff}}/2, l_{\mathrm{eff}}/4, ..., l_{\mathrm{eff}}/2^n\}$. Before moving the ion forward, JIonO calculates cross sections for electron capture (σ_c) and loss (σ_l) events and the corresponding mean free path for the charge-exchange collisions ($l_{qq'}$) using current properties of the ion and the molecular density of the gas. In the next step the longest matrix is chosen with the condition that the probability for multiple charge-exchange is negligible. The matrix is used first to calculate only the accurate path length (l). Then the length is passed to an algorithm which samples the positions of charge-exchange collisions within the length l according to exponential distribution having mean $l_{qq'}$. If one or more collisions

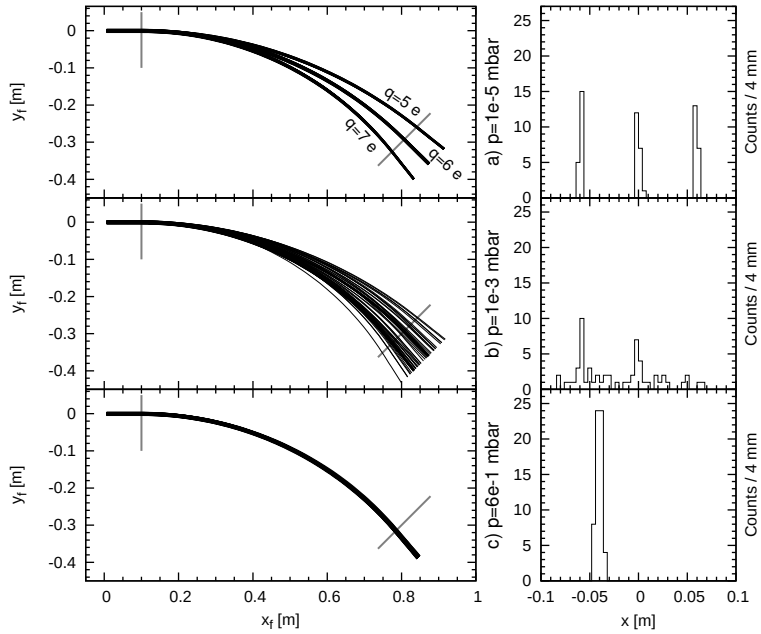

Figure 1.11: Effect of the charge-exchange collisions at pressures a) $1 \cdot 10^{-5}$ hPa, b) $1 \cdot 10^{-3}$ hPa and c) 0.6 hPa in a dipole magnet having parameters $\rho_0 = 1.0$ m and $\phi_0 = 45°$ for ^{186}Hg ions with kinetic energy of $E_k = 31$ MeV. Trajectories represent 60 ions with initial charges of $q_0 = \{5, 6, 7\}$ e (20 trajectories per charge). Energy losses or scattering has not been taken to account.

occur the effective charge for the length l is calculated as a weighted average $q_{\text{eff}} = \sum l_i q_i / l$ where l_i is the path length along which the ion had the charge q_i. Now, the particle is transported again with the matrix over the length l using the effective charge q_{eff}. After this a user-defined class is used to sample the energy loss and angular straggling for the length l. This class can use the information of sampled q_i and l_i in addition to the properties of the ion. This procedure continues until the ion is transported out from the element.

As in the references [Pau89] and [Nin95], JIonO assumes a Gaussian shape (1.50) for an equilibrium charge-state distribution and an exponential behavior for electron capture and loss cross-sections (1.51). The constants for the exponential capture curve are calculated from the value and slope of the capture cross section given by the (Schlachter et al.) scaling rule (1.48) at the point $q = \bar{q}$ where $\bar{q}$ is calculated with (1.44). The constants of the electron-loss cross-section curve are obtained with (1.52) using a user-defined standard deviation, $d_{\bar{q}}$.

The effects of different mean free path lengths between charge-exchange collisions with helium filling-gas on trajectories in a system consisting of a 45° bending dipole and 10 cm drift lengths before and after the magnet are shown in figure 1.11 for a set of 31 MeV ^{186}Hg ions consisting of three initial charge states ($q \in \{5, 6, 7\}$) at the helium pressure a) $1 \cdot 10^{-5}$ hPa, b) $1 \cdot 10^{-3}$ hPa and c) 0.6 hPa. The subfigures in the right hand column show the position spectra after the system. The trajectories have been calculated with JIonO and the path lengths (l) described by one matrix were about 1.2 cm. Energy loss and angular straggling are not taken into account. The average charge state according to (1.44) is $\bar{q} = 6.7$ and the mean free paths are around 0.4, 0.9 and 1.4 mm at $p = 0.6$ hPa pressure for the ion being in the charge state 5, 6 and 7, respectively. In the simulation $d_{\bar{q}} = 0.8$ has been assumed.

The equations (1.68) and (1.69) can be used to sample the energy loss and the angular scattering of a recoil between charge-exchange collisions if values of $\overline{\Delta E}$, $\sigma_{\Delta E}$ and $\sigma_{\Delta a}$ are known. Another approach is to use semiempirical or theoretical formulae for multiple scattering and energy loss. The implementation of these in JIonO has been considered.

Assumptions in the simulation of gas-filled systems

Most of the critical assumptions in the simulation of a gas-filled system are related to charge-exchange collisions and angular straggling of the ions in a filling gas. Since the length of the mean free path is essential in the modelling, the knowledge of the equilibrium charge state distribution is not sufficient and thus it is important to have an accurate model for charge-exchange collision cross sections. It is also evident that the cross sections of such collisions for ions in atomic ground state are not enough for detailed simulation due to the existence of the density effect which is not taken into account either in JIonO or in the codes mentioned above.

All the known codes using charge-exchange cross sections assume a Gaussian shape for the equilibrium charge distribution. However, the distribution can be skewed for example due to events of multiple electron loss. A careful comparison of a recoil distribution as a function of the filling-gas pressure to the Monte-Carlo simulation enabling free parametrization of the cross-section curves could be valuable.

In the JIonO and [Pau89] the recoil scattering and energy loss in a filling-gas is taken into account at each vertex where the charge is changed. In the code described by [Nin95] the cross section for multiple scattering can be separately given. Also in JIonO the maximum length between applying of multiple scattering and energy loss can be set. The approach used in these three codes may give errors when the number of charge exchanges along the particle flight path

is low because the charge-exchange collision may correlate with scattering or energy loss which is not taken into account in the adopted statistical model.

A set of JIonO calculations has been performed for the RITU separator in the case of the reaction ^{150}Sm(^{40}Ar,4n)^{186}Hg. The results, discussed in section 3.3, are in qualitative agreement with the experimental data.

1.5.4 Other computer programmes for separator modelling

The JIonO code is certainly not the only programme which can be used to simulate in-flight separators. As JIonO, the code MOCADI [Iwa97] also uses transfer matrices from the GICOSY programme. MOCADI is heavily used in GSI and together with the code LISE++ [Tar08] they are focused more on reactions high above Coulomb barrier. They include several subprogrammes to calculate reaction mechanisms and beam interaction with matter. LISE++ is still using first order matrices and is not applicaple for the MARA design for example.

An extension, MOCADI_FUSION [Maz08], to MOCADI has been developed for simulations of fusion kinematics and it has been tested in the case of the velocity filter SHIP [Mün81]. MOCADI_FUSION uses PACE for Monte-Carlo calculation of evaporation steps and TRIM (or ATIMA) for energy loss and scattering of beam and recoils in a target. Contrary to JIonO, MOCADI_FUSION uses fixed interaction energy of the primary beam over the target.

A Monte-Carlo code to model fusion reactions and trajectories of the recoils through the HIRA spectrometer has been developed in India [Nat07]. This code calculates the evaporation steps using a Maxwell-Boltzmann distribution calculated from the Fermi-gas prescription. However, this programme is reported in the publication to calculate the trajectories using first order matrices only which limits its usability.

1.6 Angular acceptance and transmission

The main parameter that defines the transmission through a separator is the *solid angle acceptance* of the separator. The bigger the solid angle, the larger the proportion of the reaction products that can be collected and transported to the focal plane. When the angles are relatively small, the solid angle, S, defined by a rectangular aperture, can be calculated from *angular acceptances*

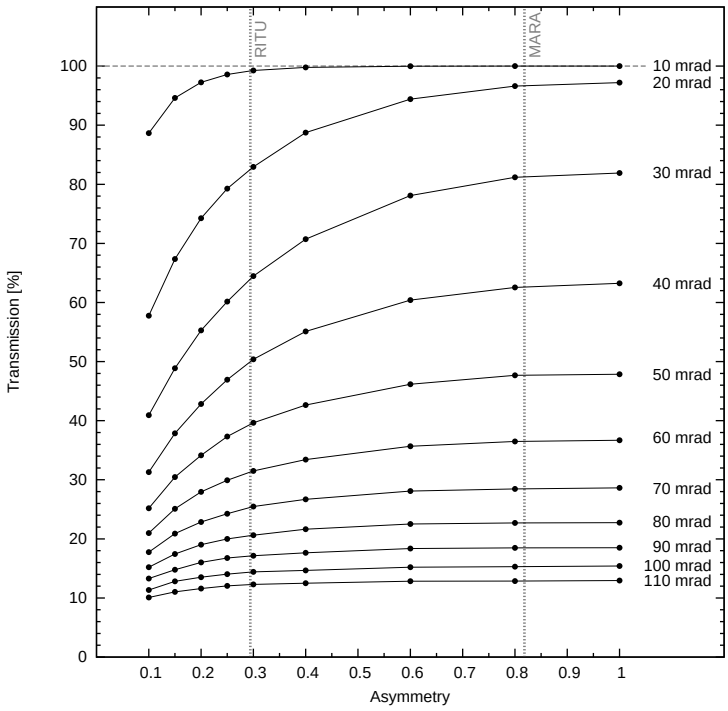

Figure 1.12: Transmission of Gaussian distributions with variable widths (standard deviation) as a function of the angular-acceptance asymmetry for a solid angle acceptance of $S = 10$ msr. The real RITU transmission is smaller than indicated here since $S_{\mathrm{RITU}} \approx 8.5$ msr. MARA is a vacuum-mode recoil mass spectrometer under construction in JYFL and is introduced in chapter 2.

in horizontal ($\pm\alpha_{0,\mathrm{max}}$) and in vertical ($\pm\beta_{0,\mathrm{max}}$) directions as

$$S = 4\alpha_{0,\mathrm{max}}\beta_{0,\mathrm{max}}. \tag{1.70}$$

The factor 4 should be replaced by π if the limiting aperture is elliptical. The beam tubes through the focusing quadrupoles are usually round which would suggest one to use π instead of factor 4. However, in the case of quadrupole multiplets the acceptance is naturally limited by different quadrupoles for horizontal and vertical directions and thus the factor 4 should be used.

It is quite meaningless to compare transmissions of separators by using just solid angles, because the transmission depends also, among others, on the asymmetry of the horizontal and vertical acceptances, $\alpha_{0,\mathrm{max}}/\alpha_{0,\mathrm{max}}$. This is shown in figure 1.12 where the transmission of recoils having different angular distributions is plotted against acceptance asymmetry. In the figure, a total solid angle

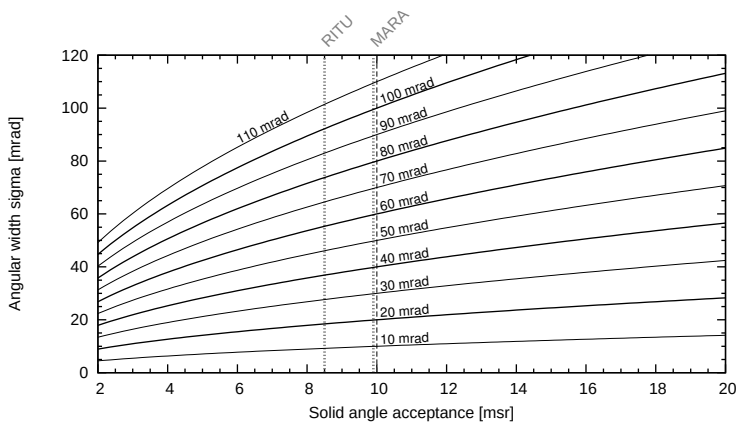

Figure 1.13: Scaling of the transmission curves shown in figure 1.12 as a function of solid angle and real angular width (standard deviation) of the recoils. The labels represent real width only in the case of $S = 10$ msr and otherwise should be treated as connecting names between this figure and 1.12.

of 10 msr is assumed and the widths expressed for the symmetric angular distribution are standard deviations of angular distributions in either horizontal or vertical direction. The transmission of RITU is less than indicated in the figure because its solid angle acceptance is about $S = 8.5$ msr.

The transmission can be read graphically for solid angles other than 10 msr by using figure 1.13. The corresponding width curve in the 10 msr case can be found in the intersection of the solid angle acceptance (x-axis) and the real angular width of the recoils (y-axis) meaning that the labels of the curves in both figures should be treated as names.

Transmission through the separator depends also on the chromatic properties of the products to be transported. Since the average charge state is achieved almost immediately after the target in a gas-filled separator and the magnetic rigidity is also independent of velocity in the first order approximation, the transmission is expected to be mainly prescribed by the angular acceptance. In the vacuum-mode recoil separators only a few charge states can typically be collected which represents about 30% of all products ($\varepsilon_q \approx 0.3$). In addition, the recoil mass spectrometer has a limited energy acceptance which will add an additional efficiency factor of about $\varepsilon_E = 0.9$–1.0.

Chapter 2

Vacuum-mode mass separator MARA

In the early years of the 21st century more requirements for the new recoil separator were presented at the Accelerator Laboratory of the University of Jyväskylä (JYFL). The gas-filled recoil separator RITU (*Recoil Ion Transport Unit*) had been used successfully in the heavy element research programme (see for example [Lei03] for an overview of gas-filled separators and their use in nuclear structure studies) but some research activity was also targeted at fusion evaporation products in the mass region below lead. The MARA (*Mass Analysing Recoil Apparatus*) project, standing for the design and construction of a new recoil mass spectrometer, started around year 2004 to answer these requirements. At the present moment, the HV-supplies for the electrostatic deflector, all the magnets including the quadrupole triplet and the dipole and their power supplies have been purchased and are waiting for the installation. The last ion-optical part, the electrostatic deflector, has been ordered and is supposed to arrive at JYFL in late summer in 2012.

MARA will be a compact recoil mass spectrometer for studies of fusion evaporation residues at the $N \approx Z$ line close to the proton drip-line. Its ion-optical configuration is QQQED which stands for a quadrupole triplet followed by an electrostatic and a magnetic sector field. It has an energy focus at a fixed distance from the magnetic dipole in addition to the stigmatic focus. At the focal plane, a typical first order resolving power of 300 is achieved according to ion-optical calculations. An artistic view of MARA is shown in figure 2.1. Figure 2.2 shows the more detailed two dimensinal drawing of MARA with the names of the ion optical elements as well as the possible locations of vacuum valves, adjustable collimaters, slit system and focal plane detectors.

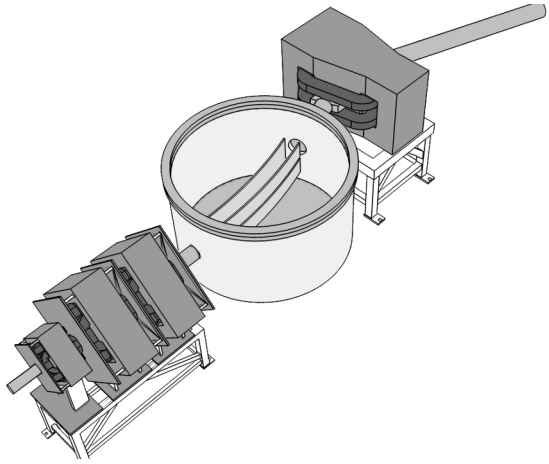

Figure 2.1: An artistic view of the MARA separator. The optical elements from left to right are: the quadrupole triplet, the electrostatic deflector and the magnetic dipole. The focal plane is in the upper right corner.

In this chapter a brief history of MARA and the motivation to build such a separator are given. Other recoil separators comparable to MARA are listed and their typical parameters are discussed. The main focus of the chapter is to describe the working principle and the design reasoning of MARA. A sensitivity analysis including imperfections in electromagnetic fields and physical misplacement of optical devices is carried out. The performance of the chosen optical layout is studied carefully with a few test reactions representing different kind of reactions and possibilities of MARA.

2.1 Motivation to build MARA

The idea of building a new recoil separator complementary to the RITU gas-filled separator was born around eight years ago. The RITU separator had been already then a success story in research of the heavy (trans-lead) neutron deficient isotopes produced in fusion evaporation reactions but a lot of research interest was pointed also to the lighter mass region. In order to produce isotopes above tin with fusion reactions of a stable projectile and target, asymmetric reactions have to be used, since the valley of β stability bends towards the neutron rich side as a function of increasing proton number. This is not the case below tin and these lighter isotopes have to be produced in more symmetric reactions.

A gas-filled recoil separator suppresses the primary beam excellently in the

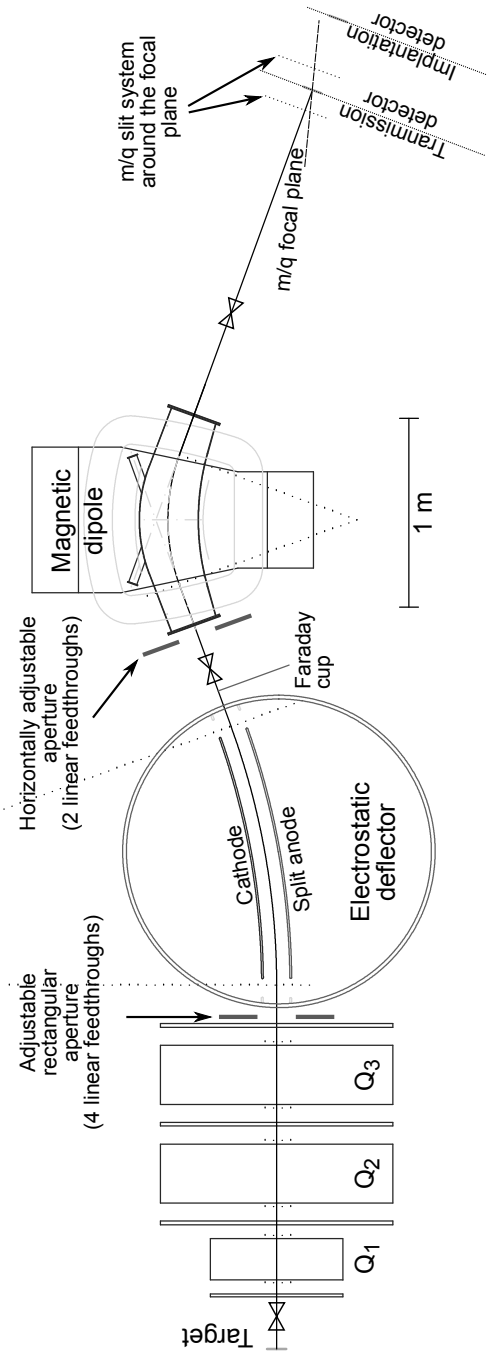

Figure 2.2: Sketch of MARA element layout viewed from top including qualitative disposition of gate valves, apertures and m/q slits. The dimensions of the quadrupoles, dipole and the dipole chamber are in the scale. The dimensions of the deflector may differ from the figure.

case of the asymmetric reactions but lacks mass resolving power. However, gas-filled separators have some important advantages over vacuum-mode mass separators. The operation of a gas-filled separator is much simpler due to non-existing high-voltage elements, and the requirements for the quality of the ion-optics are less stringent. Probably the most important feature is the high transmission due to velocity and charge focusing caused by the charge-exchange collisions. Other important aspects of the research of the heavy nuclei are the strongly diminished overall fusion cross section due to fission competition and the characteristic alpha decays that can be used for the identification of a product. As a conclusion the main task of the gas-filled separator is to suppress the primary beam. For example in studies of transfermium isotopes, most of the counting rate of the RITU focal-plane implantation-detector comes from recoils under interest and scattered target-like nuclei. The typical total counting rate in transfermium studies varies from a few Hz up to a few tens of Hz for the primary-beam intensity being about $1 \cdot 10^{12}$ 1/s and the observation probability of a fusion product being around 30%. The properties of the RITU separator are discussed in detail in the chapter 3.

The studies of medium-heavy (A up to around 150) fusion products with RITU starts to be challenging although RITU has been utilized for studies of as light as arsenic nuclei. Not only does the beam suppression get worse but also a better mass resolution would be highly desirable in order to cut the focal-plane rate due to other fusion channels and for getting better identification. In symmetric reactions the total fusion cross section is usually several hundreds of mb even at Coulomb-barrier energies, whilst that of the interesting channel can be in the order of nb. The number of open channels in the heavier mass region is greatly diminished by the high fission probability of a cooling heavy nucleus.

Before ending up with starting a project aiming to build a vacuum-mode mass separator, two other options were considered. The insertion of an additional 8° dipole magnet at the end of RITU and the shortening of the separator was studied in the master thesis [Sar04]. These modifications would have increased the RITU dispersion by about 8% and improved the primary beam suppression. For instance, at FLNR in Dubna, there were some plans to build a new gas-filled separator resembling RITU with an additional 8° dipole magnet at the end [Yer08]. The second solution was to build a totally new gas-filled separator having the configuration DQQ [Enq03]. In that design the bending angle of the dipole was doubled compared to RITU and additionally the dipole would have included a relatively strong quadrupole component (field index $B_n \approx 3$). These two solutions would have answered only needs in primary-beam separation, hence not being optimal solutions.

About ten years ago Andrej Popeko described a plan for a vacuum-mode separator, which was intended to be built in Bratislava, to Matti Leino. After

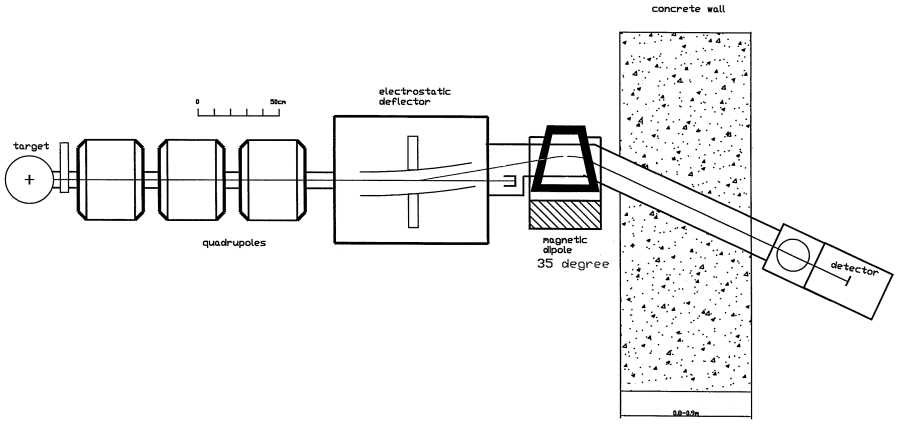

Figure 2.3: Layout of the Bratislava separator plan. Courtesy of A. Popeko.

this it was realized that a vacuum-mode separator could be built also in JYFL which was a real beginning of the MARA project. The configuration of the "Bratislava" separator was QQQEM and the original layout drawing of the separator can be seen in figure 2.3. The parameters of the elements were the following: The quadrupoles had an effective length of 35 cm, half gap of 5 cm and max gradient of 5 T/m. The electrostatic deflector had a bending radius of $\rho = 4$ m, deflection angle of $\phi = 10°$, gap of $2G_0 = 12$ cm between electrodes and maximum field of ± 150 kV. The magnetic dipole had corresponding parameters of $\rho = 1$ m, $\phi = 35°$ and $2G_0 = 10$ cm. The maximum magnetic field was designed to be 1 T. Contrary to MARA operation, the Bratislava separator does not separate masses physically but the masses can be extracted from the trajectory tracking data collected at the focal plane. However, this was suitable since the separator was aimed to be used in the heavy region without needs of physical cutting of the other fusion channels at the focal plane.

2.2 Existing and planned recoil separators employing electric and magnetic fields

Quite many recoil mass spectrometers exist or are under construction all over the world. Some of them are listed in the table 2.1. Most of the separators are longer than MARA will be, because they employ two electrostatic deflectors symmetrically around the magnetic dipole. The advantage of that layout is that the energy dispersion vanishes totally (in first order) after the second deflector which gives the freedom to change the mass dispersion of the separator by moving the focal plane. In MARA the energy dispersion vanishes only at a

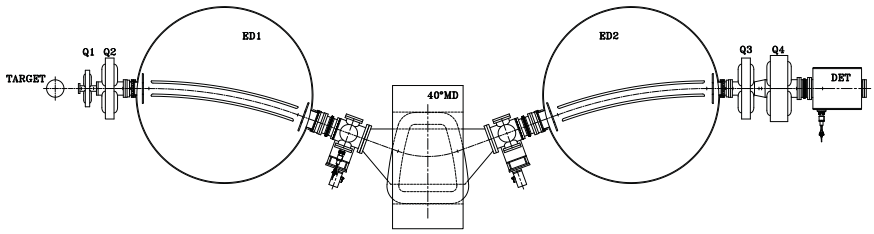

Figure 2.4: The layout of the EMMA mass spectrometer at TRIUMF. Courtesy of B. Davids.

fixed distance after the magnetic dipole and therefore the mass dispersion is also fixed although the quadrupole component introduced by surface coils on the dipole can be used to move the focal plane somewhat. The advantage of MARA is then that it is shorter, less expensive and hopefully easier to set up.

The EMMA recoil separator [BDav05] which is under construction at TRIUMF in Canada, represents the typical EME-configuration for mass spectrometers and is shown in figure 2.4.

2.3 Ion optics and the working principle

The MARA separator consists of three main parts: a quadrupole triplet followed by an electrostatic deflector and a magnetic dipole. The operation of the elements can be seen from figure 2.5 which shows trajectories with different starting angles and kinetic energies in the laboratory-coordinate system (u, v) and in the coordinate system (x, y) perpendicular to the curvilinear optical axis, z. Details of the figure are described in the caption. The main optical properties of the separator are collected in table 2.2. The optical parameters of the quadrupoles and the bending elements and also the drift lengths between the elements are given in table 2.3.

The role of the quadrupole triplet is to focus divergent products from the target position spatially to an area as small as possible in both directions at the focal plane (stigmatic focus). Additionally, the triplet focuses ions from point to parallel to the entrance of the dipole. The first requirement for the electrostatic deflector and the magnetic dipole and their placements is to achieve an energy focus (i.e. vanishing of the $(x|\delta_K)$ coefficient) at the focal plane with a convenient distance after the dipole. This means that the magnetic dipole focuses the particles which were defocused by the deflector but additionally creates the mass dispersion needed to resolve masses.

Table 2.1: Some existing and in construction phase recoil separators using electric and magnetic dipoles. In addition to configurations listed here, most of the separators include also hexapole or higher order correction elements.

Separator and configuration	Length [m]	Electrostatic deflector				Magnetic dipole				Ref.
		ϕ [°]	ρ [m]	Gap [cm]	χ_{max} [MV]	ϕ [°]	ρ [m]	Gap [cm]	χ_{max} [Tm]	
FMA, USA *QQEMEQQ*	8.2	20	4.0	10	18	40	1.0	12	1.0	[CDav89]
EMMA, Canada, *QQEMEQQ*	9.04	20	5.0	12.5	25	40	1.0	12	1.0	[BDav05]
HIRA, India *QQEMEQQ*	8.8	16	5.0	15	15	36	0.86	8	1.0	[Sin94]
CAMEL, Italy *QQEME*	∼7.5	20	4.0	15	12	40	1.0	12	1.0	[Spo85]
JAERI RMS, Japan *QQEMEQQ*	9.4	25	4.0	12	20	50	1.0	12	1.0	[Ike97]
CARP, Japan *QMEQ*	7.34/ 8.64	32	3.0	36	7.5	55	1.0	9	1.0	[Mor92]
MARA, Finland *QQQEM*	6.85	20	4.0	14	14.2	40	1.0	10	1.0	

Table 2.2: Main optical properties of the MARA separator with nominal quadrupole fields.

Total length along the optical axis	6.85 m
Angular acceptance (horiz., vert.)	45 mrad, 55 mrad
Energy acceptance	-15 – +20%
First order resolving power	250
Dispersion	8.1 mm/(% in mass)
Magnification (horiz., vert.)	-1.6, -4.7
First order resolving power with ±1 mm horizontal beam spot	250
Mass focal plane angle from optical axis	13°

Table 2.3: Optical properties of the quadrupoles and the sector fields and the drift lengths between the elements. The abbreviation *EFB* stands for effective field boundary.

Quadrupole triplet	$\mathbf{Q}_1$	$\mathbf{Q}_{2,3}$
Optical length	25 cm	35 cm
Bore diameter	10 cm	15 cm
Maximum field gradient	10 T/m	10 T/m
Nominal field relative to $B\rho$	0.4698 T/$B\rho$	0.5859, 0.2387 T/$B\rho$
Sector fields	**Electrostatic**	**Magnetic**
Radius of curvature, ρ	4.000 m	1.000 m
Bending angle, ϕ	20°	40°
Vertical gap	14 cm	20 cm (active)
Horizontal gap	10 cm (active)	10 cm
Maximum rigidity	14.2 MV	1 Tm
Inclination of EFB (entrance and exit)		8°
EFB curvature radii (entrance and exit)		2.0 m
Height of the gap in the anode	1.5 cm (extending from ∼10° to ∼19°)	
Drift lengths	**Length [cm]**	
Target – Q_1	35.0	
Q_1 – Q_2	14.0	
Q_2 – Q_3	16.0	
Q_3 – Deflector EFB	30.0	
Deflector EFB – Dipole EFB	80.0	
Dipole EFB – Focal plane	205.8	

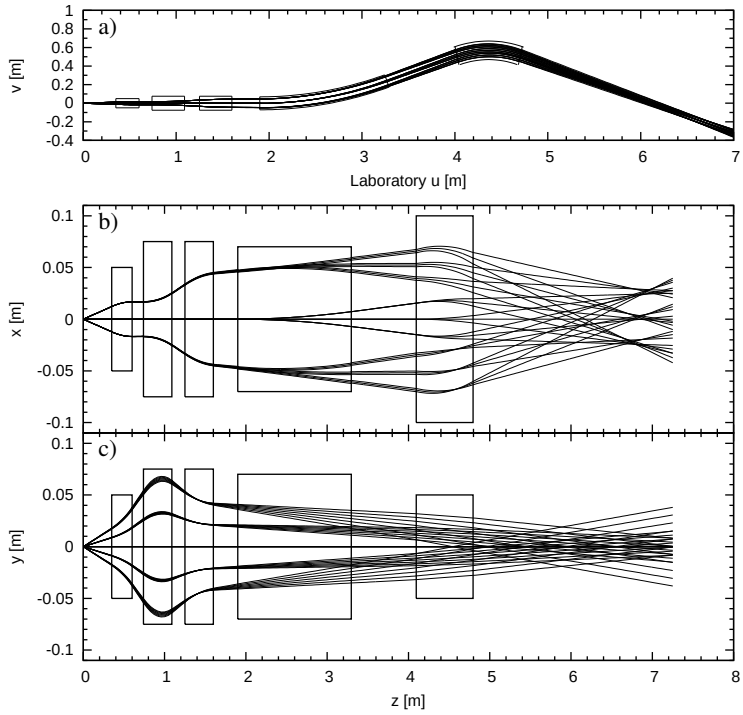

Figure 2.5: Trajectories of ions viewed a) from top in the laboratory coordinate system, b) from top with the straightened optical axis and c) from side with straightened optical axis. The elements are named in figure 2.2. The trajectories have been drawn for all combinations of $a \in \{0, \pm 40\}$ mrad, $m \in \{97, 100, 103\}$ u and $E_k \in \{97, 100, 103\}$ MeV in the case of (a) and (b). In (c) the particles had properties $b \in \{0, \pm 25, \pm 50\}$ mrad and $E_k \in \{94, 95, \ldots, 106\}$ MeV.

The test distribution and the reference particle

The MARA separator is used for relatively slow reaction products. Since the velocities are only a few percent of the speed of light the transfer matrices are approximately the same for all products and reference particles and the deviations from a reference particle are enough to describe the trajectory of an ion. Therefore MARA's ion-optical properties can be described by using one reference particle. A particle having

$$\begin{cases} m_0 & = 100 \text{ u} \\ E_{k,0} & = 100 \text{ MeV} \\ q_0 & = 26 \text{ e} \end{cases} \tag{2.1}$$

has been adopted throughout this chapter as a reference. This choice is favourable for many reasons and is used also in literature. For example the magnitudes of mass dispersion and energy dependent aberrations of a system are easy to deduce from suitable spectra of ion distributions around the reference particle (2.1). Actually, the values in (2.1) are not unrealistic since they are close to the values of ^{100}Sn recoils created in a slightly inverse fusion reaction.

The energy and angular distributions depend substantially on the reaction and especially on its asymmetry. Therefore, choosing a distribution which represents all reactions is not possible. This means, for instance, that only a first order mass resolving power (depends only on dispersion, magnification and beam spot size) can be given but does not tell the real resolving power since it depends strongly on the angular and kinetic energy spread of the products due to aberrations. A better overview of the limitations of MARA optics can be obtained from realistic simulations of different type of reactions which is the goal of section 2.7.

The test distribution used throughout this chapter, excluding section 2.7, is the following. The initial spatial coordinates x_0 and y_0 and the corresponding inclination angles a_0 and b_0 have been randomly sampled in such way that

$$\begin{gathered} x_0 \sim \mathcal{N}(0, x_{00}),\ a_0 \sim \mathcal{N}(0, a_{00}),\ y_0 \sim \mathcal{N}(0, y_{00}),\ b_0 \sim \mathcal{N}(0, b_{00}), \\ \delta_K \sim \mathcal{U}(-0.1, 0.1), \\ (x_0/x_{00})^2 + (a_0/a_{00})^2 < 1, \\ (y_0/y_{00})^2 + (b_0/b_{00})^2 < 1, \\ (x_0/x_{00})^2 + (y_0/y_{00})^2 < 1, \\ \text{with } x_{00} = 0.001,\ a_{00} = 0.045,\ y_{00} = 0.0015 \text{ and } b_{00} = 0.055, \end{gathered} \tag{2.2}$$

where $\mathcal{N}(x_0, \sigma)$ is the normal distribution having x_0 as the mean and σ as the standard deviation. $\mathcal{U}(r_1, r_2)$ is the uniform distribution between values r_1 and r_2. This distribution seems to be approximately the same as the type 2 distribution selectable in the phase-space-plot command in the GICOSY code.

2.3.1 Fixed energy focus with electrostatic deflector and magnetic dipole

In the first step of the optical design the quadrupole triplet can be ignored since the first goal is to achieve an energy focus for particles which enter the deflector on the optical axis but have varying energies. In the next step the quadrupole fields need to be adjusted in order to fulfill the requirement of the stigmatic focus. After these two steps, higher order aberrations should be analysed and the minimization of the most critical ones has to be carried out by applying higher order corrections. One of the most used third order corrections in mass spectrometers is to introduce a curvature to the effective field boundary (EFB) of a magnetic dipole. In the case of MARA, the radius of EFB is 2 m which is twice the radius of curvature of the dipole. This correction is discussed in section 2.3.4.

According to a general rule (see [Wol87a] for example) the area inside the magnetic field, A_B, filled by ion trajectories should be maximised in order to get the maximum mass-resolving power. According to table 2.1, a typical dipole magnet in recoil mass separators has a radius of curvature of $\rho_B = 1.0$ m and a deflection angle around $\phi_B = 40^\circ$. The effective field boundaries (i.e. radius and inclination angle) are also symmetrical at entrance and exit. The area covered is maximised if the system has a focusing close to the point-to-parallel ($(a|a) = 0$) from the target to the entrance of the dipole. The parameters of the deflector and the dipole are based on this assumption. Clearly, because the dipole is the last element in MARA, it must create a condition of parallel-to-point focus ($(x|x) = 0$) from its entrance to the focal plane. The MARA dipole is relatively short which leads to a small $(x|x)$ coefficient of the dipole and thus the horizontal area of the beam envelope in the dipole can be approximated as

$$A_B \approx 2(x|a)_{\text{target-dipole entr.}} a_0 \rho_B \phi_B, \tag{2.3}$$

where a_0 is the maximum horizontal angle of the monochromatic ion distribution and ρ_B and ϕ_B are the bending radius and the bending angle of the dipole in radians, respectively.

The condition $(a|a) = 0$ at the dipole entrance can be fulfilled if the trajectories are slightly diverging at the deflector entrance since the deflector changes the horizontal angle, a, only little if the electric rigidity is same as the reference particle has (equation (1.31) gives $(a|a) = 0.88$ for a 20° bending deflector). Therefore, the coefficient $(x|a)$ of the system matrix does not change much over the deflector and thus the horizontal area inside the beam envelope in the deflector is approximately

$$A_E \approx 2(x|a)_{\text{target-defl.entr.}} a_0 \rho_E \phi_E. \tag{2.4}$$

For non-relativistic particles the mass resolving power is maximized in an achro-

matic system employing one magnetic and electric sector fields if the assertion [Wol87a]

$$A_B/(2\rho_B) = A_E/\rho_E \tag{2.5}$$

holds. By inserting equations (2.3) and (2.4) to it and approximating with $(x|a)_{\text{target-defl.entr.}} \approx (x|a)_{\text{target-dipole entr.}}$ one obtains simply $\phi_E = \phi_B/2$. The MARA deflector has a bending angle of 20° and thus (2.5) is fulfilled.

The simplest layout to achieve the energy focus is to place the electric and magnetic fields so that the ions are bent to opposite directions in the sector fields since the radius of curvature increases as a function of kinetic energy. As discussed above, the optical system up to the dipole entrance is point-to-parallel focusing in horizontal direction ($(a|a) = 0$). The electric field of the deflector introduces energy dispersion (1.31): $(x|\delta_K) \approx -0.24$ and $(a|\delta_K) \approx -0.34$. Therefore the ions with larger (smaller) rigidity will drift towards the negative (positive) x values where the path inside the magnetic field is shorter (longer) and thus the ions will be deflected less (more) than the nominal deflection angle of 40°. Since $(a|a) = 0$ was required at the dipole entrance the angles are there proportional to the electric rigidity solely. It is worthwhile to note here that in principle the total energy focusing does not require that the ions in the inner radius have also higher magnetic rigidity because the focusing due to incident angle a can be made stronger than defocusing action due to rigidity. In practice, this is not possible in the case of MARA because it would mean too massive dipole, potentially decreased acceptance and need of focusing elements after a dipole.

If only the ion optics of the fusion products are concerned then the ordering of the sector fields is insignificant. For many reasons it is advisable to place the electrostatic field first (configuration EM). The difference of electric rigidities between a primary beam and a fusion-reaction product is larger than the difference between magnetic rigidities (see section 2.7 describing simulated test reactions and [Sin94] for example). If the deflector precedes the dipole the beam can be separated earlier from the products and a smaller background level originating from the scattered beam is expected. The MARA deflector will also be equipped with a split anode which reduces the amount of the scattered beam from the deflector plate. Because of the vertically divergent primary beam and the finite gap of the split, the deflector should be placed as close as possible to the target. In contrast, the recoil separator CARP at RCNP [Mor92] has a magnetic dipole preceding the electrostatic deflector (ME). CARP has also a split anode in its deflector but the height of the split gap is about 5 cm which is very much compared to the corresponding height of 1.5 cm in MARA. If larger mass dispersion is required at the focal plane the order of the elements adopted in CARP can be advisable.

A relatively long drift length is needed after the magnetic dipole in order to separate the masses at the focal plane. The equation (1.25) gives $(a|\delta_m) \approx$

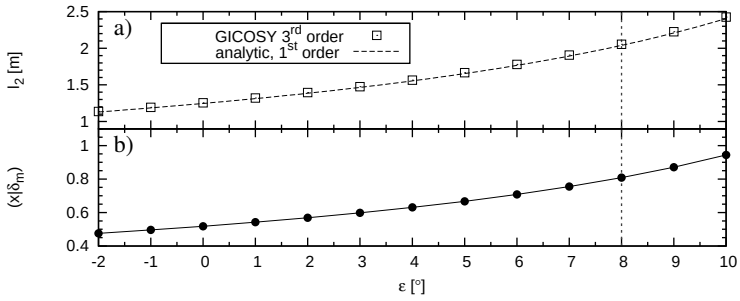

Figure 2.6: a) The drift length between the dipole and the focal plane and b) the mass dispersion as a function of symmetric dipole EFB inclination angle. The mass dispersion is calculated with GICOSY and the data points are connected with lines.

$\sin(\phi_0)/2 \approx 0.32$ as the change in angle induced by the mass difference δ_m for the MARA dipole. At the exit of the dipole the separation due to the mass difference is $(x|\delta_m) \approx 0.12$ according to (1.25). This means roughly that after a drift length of 2.0 m the ions differing by 1% in mass from each other will be separated by $0.01(0.32 \cdot 2.0 + 0.12) \cdot 10^3$ mm = 7.6 mm. This is a reasonable dispersion up to mass region $A = 150$ if the spatial resolution of the focal plane detector is around 1 mm.

According to the discussion in section 1.1.6 the increasing of this drift length does not improve the mass resolving power since the magnification of the system, $\mathcal{M}_x = (x|x)$, increases alongside the decreasing angular magnification, $(a|a)$, which is a consequence of the increasing focal length. To achieve a drift length of 2 m, the effective field boundaries of the dipole need to be inclined. By multiplying the transfer matrices of the deflector (1.31), the dipole (1.25) with inclined boundaries (1.26) and the drift lengths one can solve the latter drift length, l_2, as a function of the EFB inclination angle, ε, as follows

$$l_2 = \frac{0.486651 + 0.325786 \tan\varepsilon}{0.390509 - 0.874908 \tan\varepsilon - 0.325786 \tan^2\varepsilon}, \tag{2.6}$$

when the drift length of $l_1 = 0.800$ m has been adopted between the deflector and the dipole. The equation is plotted in figure 2.6 (a) with the data points given by a third order GICOSY calculation. The differences between the first order analytic and higher order fitted solutions are negligible. The equation results in $l_2 = 2.039$ m for $\varepsilon = 8^\circ$ (the MARA dipole) while the GICOSY fit results in 2.055 m. The value of l_2 depends only weakly on l_1 since the first order calculation gives $\partial l_2/\partial l_1 = 0.014$ at $l_1 = 0.8$ m. The curvature of the dipole EFBs, R_{EFB}, does not affect l_2.

The lower panel (b) of figure 2.6 shows the corresponding mass dispersion as a function of ε calculated with GICOSY. The choice $\varepsilon = 8^\circ$ gives a dispersion of

$\mathcal{D}_m = 0.81$ which is close to the one estimated above for $l_2 \approx 2$ m.

The MARA dipole has the same inclination angle, ε, in both sides symmetrically. This was chosen in order to preserve the option that MARA could be extended by a second deflector in future if for example the background conditions require it. The optical system with asymmetrical EFBs has not been studied.

Magnetic dipole surface coils

The magnetic dipole is equipped with a pair of surface coils which can be used to add a quadrupole component to the magnetic field. The action of this component is equivalent to the inclined effective field boundaries and it can be used to adjust the drift length between the dipole exit and the focal plane. A brief technical specification of the surface coils is given in the section 2.5.2.

The magnetic field profile in mid plane ($y = 0$) along the x-axis can be expressed as [GICOSY manual]

$$B(x, y = 0) = B_0[1 - n_1(x/\rho_0) - n_2(x/\rho_0)^2 - ...], \tag{2.7}$$

where B_0 is the field defined by a reference particle and coefficients n_i specify the values of the multipole elements. The maximum change in the magnetic field introduced by the surface coils of the MARA dipole is 1% of B_0 at the distance of ± 10 cm from the optical axis. Since $\rho_0 = 1$ m the maximum value for the quadrupole coefficient is $n_{1,max} = 0.1$. A negative value corresponds to increasing field with radius which translates to shortened focal length.

The effects of the surface coils on the focal length, dispersion, quadrupole triplet settings and various aberrations are shown in figure 2.7. The data points shown have been calculated with GICOSY in third order. A stigmatic focus at the focal plane and $(x|a) = 1.5$ at the dipole entrance were required for the fitting of the quadrupole settings (nominal quadrupole triplet settings for MARA). According to the figure, the quadrupole triplet field values need only slight adjustment (up to 2%) compared to the case of unenergised surface coils. It can be seen that the maximally powered coils enable around 30 cm shortening and 40 cm lengthening of the focal distance corresponding to values $n_1 = -0.1$ and $n_1 = 0.1$, respectively. The magnification (curve "X" in the bottom panel) is changing between -1.4 and -1.9 which keeps the mass resolution as constant for increased dispersion (curve "G" in the bottom panel). The change in the first order mass resolving power is 1.6%. According to the bottom panel, the behaviour of the most critical aberrations $a_{00}^2(x|a^2)$, $a_{00}\delta_{K0}(x|a\delta_K)$ and $a_{00}b_{00}^2(x|ab^2)$ are almost linear as a function of n_1. The evolution of aberrations suggests that the spatial separation of masses is quite independent on n_1 since the sum of the aberrations is roughly a constant fraction of the mass

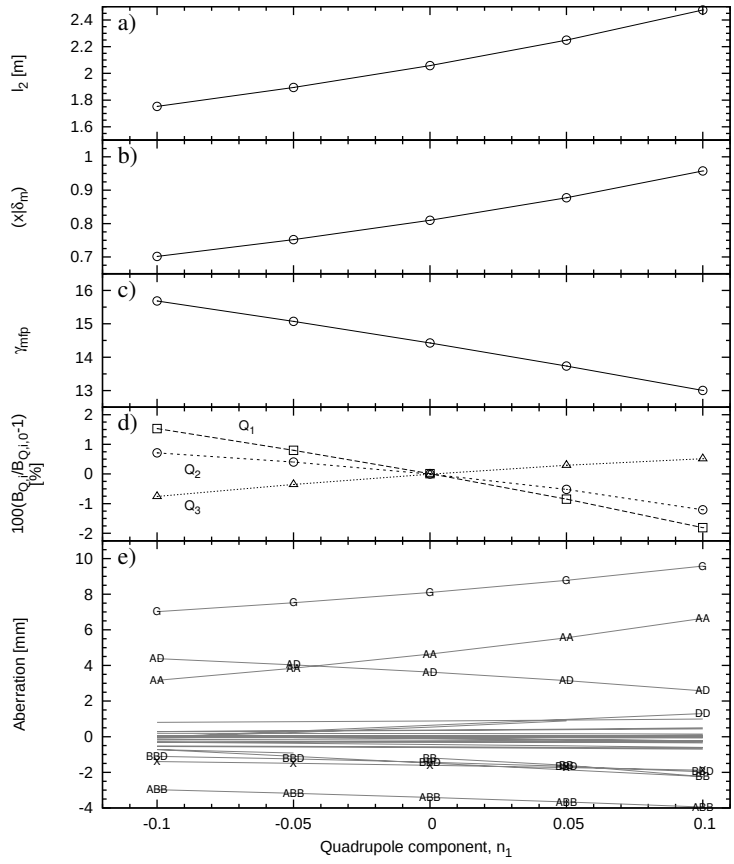

Figure 2.7: Effect of the energised surface coils on a) the focal distance, b) mass dispersion, c) angle of mass focal plane, d) field values of the quadrupole triplet and e) aberrations as a function of quadrupole coefficient, n_1. The aberration curves are: $G \leftrightarrow \delta_{m0}(x|\delta_m)$, $AA \leftrightarrow a_{00}^2(x|a^2)$, $AD \leftrightarrow a_{00}\delta_{K0}(x|a\delta_K)$, $ABB \leftrightarrow a_{00}b_{00}^2(x|ab^2)$ etc. where the initial values of $x_{00} = 1.0$ mm, $a_{00} = 45$ mrad, $y_{00} = 1.5$ mm, $b_{00} = 55$ mrad, $\delta_{m0} = 0.01$ and $\delta_{K0} = 0.07$ have been used.

dispersion. However, an advised limitation of angular acceptance of MARA can easily change this picture and the decreasing $(x|a\delta_K)$ aberration can be a useful property.

2.3.2 Quadrupole triplet

A quadrupole triplet is needed in front of the sector fields in order to achieve some of the overall goals set for the MARA separator. These are relatively large symmetric angular acceptance and a variable mass resolving power depending on the requirements set by an experiment. MARA can be driven also in higher transmission mode if the separation of masses is not required. This mode is achieved by the inversion of the polarities of the quadrupoles which corresponds to a reversal in the direction of the current in the coils. In the normal mode the first and third quadrupole are both focusing in horizontal (dispersive) direction and the quadrupole in the middle is defocusing. This is shown in figure 2.5. In the vertical direction the actions of these elements are opposite.

Regardless of the reference particle used in an experiment the quadrupole triplet needs to produce the same angular magnification from the target to the deflector entrance in both directions. As discussed in section 1.2.3 the trajectories in the quadrupoles are defined by the constant $k^2 \approx |B_T|/(G_0\chi_B)$. From this, one can see that the magnetic field flux density at a pole tip, B_T, must be scaled in proportion to magnetic rigidity which means that the current in the quadrupoles is directly proportional to the current in the magnetic dipole. The nominal values of the magnetic field flux densities in the quadrupoles are given in table 2.3.

The use of a quadrupole doublet instead of the triplet in front of MARA was studied using a trial-and-error method in the beginning of the project. Actually, with a quadrupole triplet the beam can be shaped and it can be kept rounder in the plane perpendicular to the optical axis which is difficult for a doublet. The latter is an important property since the coefficients $(x|a)$ and $(y|b)$ are approximately equal at the deflector as can be seen in figure 2.5. If the doublet had been chosen then the requirement of the stigmatic focus over the separator would have already fixed the fields of both quadrupoles and therefore the flexibility to change the transfer coefficient $(x|a)$ at the deflector entrance would have been lost. However, the doublet preceding a deflector is a typical solution in the EME-type separators (see configurations given in table 2.1), but in those systems the doublet produces a point-to-parallel, $(a|x) = 0$, and a point-to-point, $(y|b) = 0$, focus in the horizontal and vertical directions at the middle of the magnetic dipole, respectively. In MARA the requirement is different since the first (and only) vertical focus is at the focal plane.

Scans over the all sensible field settings with normal and inverted polarities

in quadrupoles have been performed with a script programme utilising the GICOSY code. In each execution of the script the field of the first quadrupole (Q_1) was gradually increased and the corresponding fields of the quadrupoles Q_2 and Q_3 were fitted in order to achieve the stigmatic focus. Additionally to the found field values, the coefficient $(x|a)_{\text{dipole entrance}}$, angular acceptance, first order resolving power and various aberrations were extracted. These are shown, in this order, in figure 2.8. For the case of the inverted polarities the curves are shown in figure 2.9. The scans were extended beyond the nominal maximum field of the first quadrupole. This is sensible, because these high values can be used if the rigidity of a reference particle is less than the maximum 1 Tm which is relatively high compared to the typical rigidity of a fusion evaporation residue. The solutions giving the stigmatic focus were found over the range of field values applied to the first quadrupole.

Let us consider first the case of normal polarities. The absolute field of Q_2, B_{Q2}, increases as Q_1 is increased until $B_{Q1}/\chi_B \approx 0.60$ m^{-1}. After that B_{Q2} starts to decrease rapidly. B_{Q3} is very stable over the normal Q_1 field range up to $B_{Q1}/\chi_B \approx 0.70$ m^{-1}. Its absolute value also begins to decrease with increasing Q_1 field. The largest absolute value needed in the last quadrupole over the range is quite low, only $B_{Q3,\max}/\chi_B \approx 0.26$ m^{-1}. This is about one third of the maximal field it can produce. This translates to low currents in its coils especially when the product has low magnetic rigidity.

The first order resolving power (1.22) shown in figure 2.8 (d) is directly proportional to the B_{Q1}. This reflects the change in horizontal magnification resulting from the change in the angular magnification. A solution with small B_{Q1} gives a resolving power close to 500 but especially the geometric aberration $a_{00}^2(x|a^2)$ has double the value of the dispersion (curve "G"). However, the horizontal acceptance is almost halved compared to the nominal solution and thus the effect of the coefficient $a_{00}^2(x|a^2)$ is decreased almost to one fourth of the value shown by the curve "AA". For the solution $B_{Q1}/\chi_B = 0.10$ m^{-1} the value of $a_{00}^2(x|a^2) \approx 4.5$ is obtained. The increase in the resolving power can be exploited only if the acceptance is further constricted.

Figure 2.9 shows that the total angular acceptance is higher in the inverted mode compared to the normal mode but the aberrations (bottom panel of the figure), especially $a_{00}\delta_{K0}(x|a\delta_K)$ (curve labeled as "AD") and the ones including vertical angles squared (curve "BB"), have values even exceeding the dispersion (curve "G"). It is clear that this mode cannot be used to separate masses spatially.

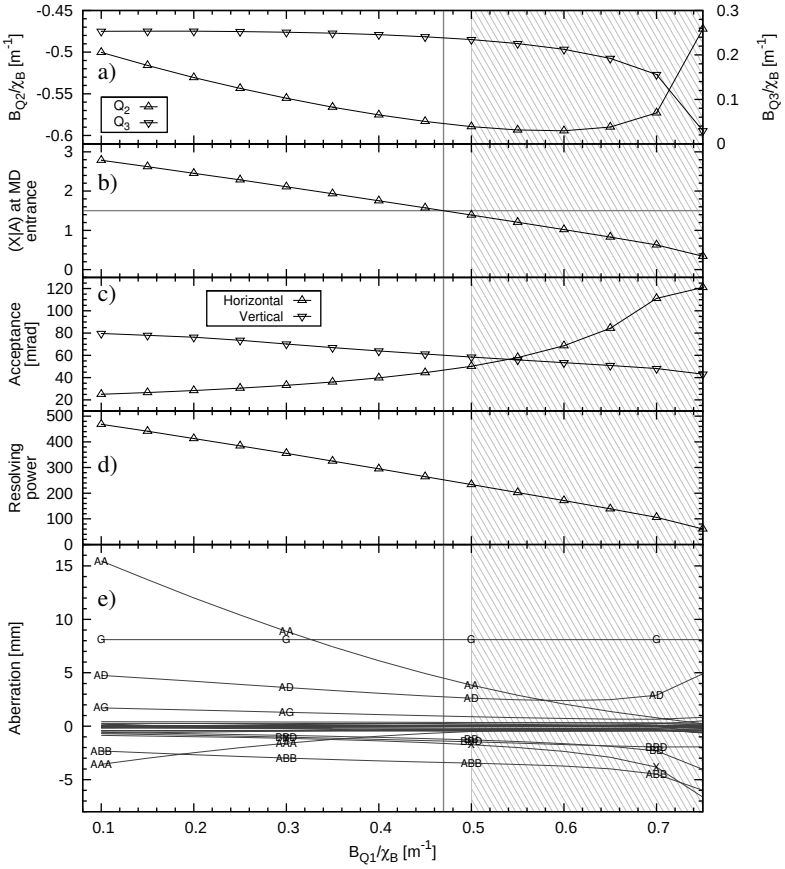

Figure 2.8: Results from a scan over all practical values of pole-tip fields of the quadrupole triplet as a function of the Q_1 field. The shaded area represents Q_1 field values which can be used only if the rigidity is lower than 1 Tm. See explanation of the aberration curves from the caption of figure 2.7.

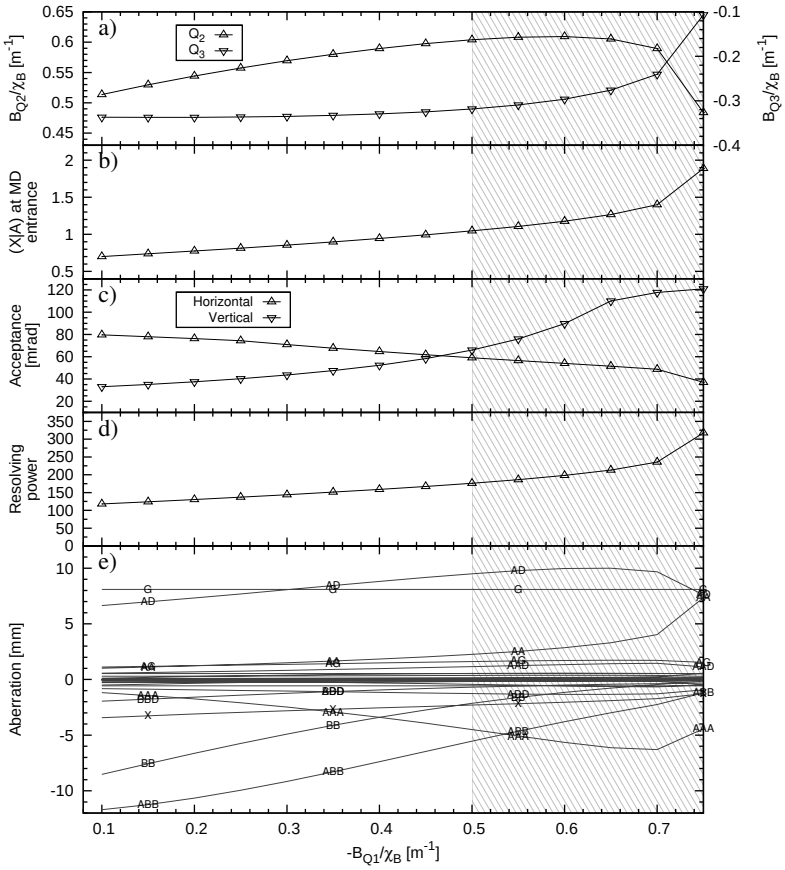

Figure 2.9: Results from a scan over all practical values of pole-tip fields of the quadrupole triplet as a function of the Q_1 field with inverted quadrupole polarities. The shaded area represents Q_1 field values which can be used only if the rigidity is lower than 1 Tm. See explanation of the aberration curves from the caption of figure 2.7.

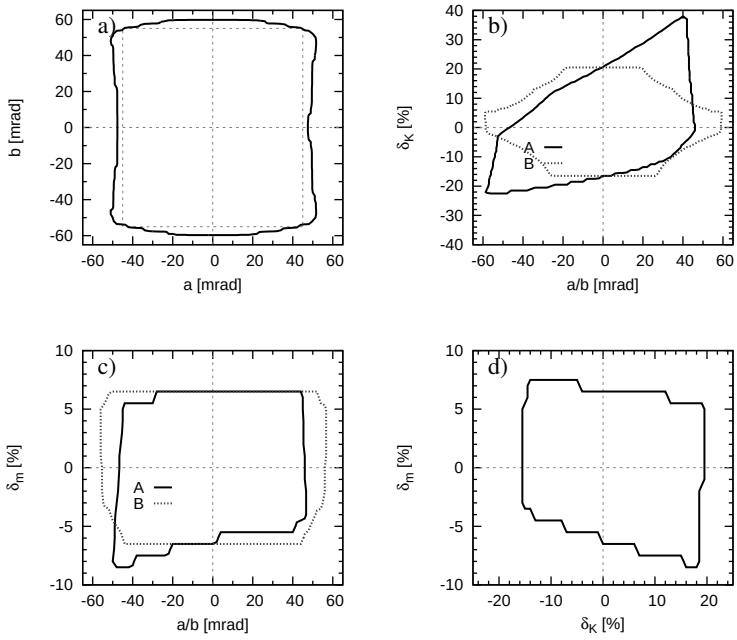

Figure 2.10: The transmission through MARA for various pairs of nonzero starting parameters. The areas enclosed by the contours represent ions that will be transmitted to an implantation detector of size $120 \cdot 60$ mm^2 (width·height).

2.3.3 Transmission

Figure 2.5 showing trajectories through MARA with different starting angles and energies reveals the elements which limit the angular and energy acceptance. The horizontal acceptance and the energy acceptance are limited by the gap between deflector electrodes. In the vertical direction the angular acceptance is first cut by the aperture of the second quadrupole. The vertical acceptance is cut also by the dipole gap since the focal length of the triplet in y-direction depends quite strongly on the rigidity of an ion. As noted in the previus subsection, the ratio between horizontal and vertical acceptances can be changed by choosing different solutions of the triplet as shown in figures 2.8 and 2.9.

The transmission as a function of the horizontal angle, vertical angle and kinetic energy deviation have been studied with the JIonO code. In figure 2.10 the transmission is shown for coordinate pairs (a, b), (a, δ_K), (b, δ_K), (a, δ_m), (b, δ_m) and (δ_K, δ_m). All the other initial coordinates except the mentioned ones were set to zero. In the calculation the natural apertures of the quadrupoles and the

bending elements were used with an additional horizontal aperture of ±10 cm through the magnetic dipole. In the quadrupole triplet the vacuum tube thickness of 2 mm was assumed and taken into account. This affects only marginally the vertical acceptance. Additionally, vertical apertures of ±33.5 mm were added to the entrance and exit of the magnetic dipole in order to model the vacuum chamber height. A round plate with 1 cm radius and centred at $(x = -0.07, y = 0)$ cm was placed 20 cm upstream from the entrance EFB of the deflector in order to obstruct ions from travelling to the non optimal electric field region caused by the split anode. The final size of this obstacle is to be defined experimentally after MARA has been constructed. The size of the implantation detector was assumed to be $120 \cdot 60$ mm^2 (width·height) and it was assumed to be located 40 cm downstream from the focal plane.

The limited width of the implantation detector will cut predominantly only mass acceptance since the system has stigmatic and energy focus at the focal plane and the horizontal cone at the focal plane is around ±55 mrad (see transfer coefficients in appendix A) which translates to a width of ±2 cm. According to figure 2.5 (c) the focal length in the y-direction is increased for ions having larger rigidity and thus the energy acceptance will be lowered for extreme vertical angles by the vertical dipole gap. For the lower rigidities the focal length is shortened and the energy acceptance is cut by the height of the detector.

The substitution of the nominal values $\alpha_{0,\max} \approx 45$ mrad and $\beta_{0,\max} \approx 55$ mrad, determined by the outermost trajectories in horizontal and vertical directions, respectively, in the equation (1.70) gives $S_{\text{total}} \approx 9.9$ msr as the solid angle acceptance. Figure 2.10 (a) validates the numbers and shows that the horizontal and vertical acceptances are practically independent of each other. It should be noted that the solid angle acceptance changes alongside the solution of the quadrupole triplet. The acceptance curves of figure 2.8 (c) give for example the solid angle acceptances of 12 msr and 19 msr for the solutions having $B_{Q1}/\chi_B = 0.56$ m^{-1} and $B_{Q1}/\chi_B = 0.70$ m^{-1}, respectively. However, these solutions could be used only if the magnetic rigidities are less than 0.9 Tm or 0.7 Tm, respectively.

As a reference, the reported acceptance of the HIRA separator [Sin94] is 10 msr. Solid angle acceptance of the EMMA separator [BDav05] is around 16 msr, which is double compared to FMA [CDav89]. The solid angle acceptance of MARA and of most of the EME-type separators is almost symmetric.

Comparison to RITU

The gas-filled separator RITU is an example of a device having quite asymmetric acceptance ($S_{\text{RITU}} \approx 4 \cdot 25 \cdot 85$ mrad$^2 \approx 8.5$ msr). The asymmetries and

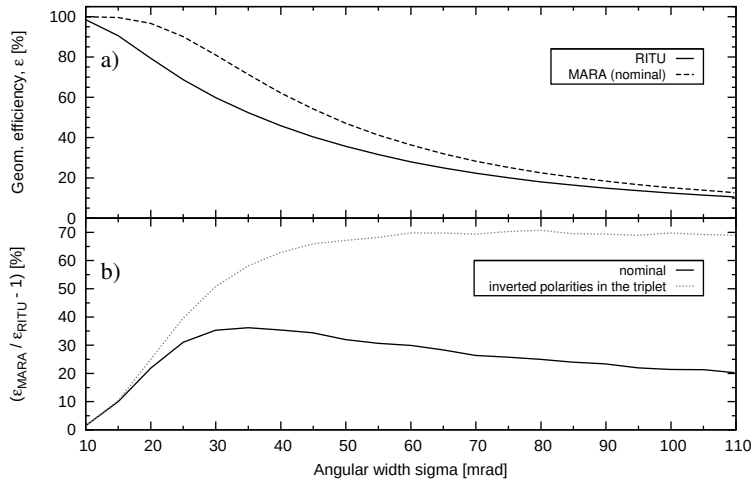

Figure 2.11: a) Geometrical transmission/efficiency of the RITU and MARA separators as a function of the standard deviation of the Gaussian angular distribution. b) Relative enhancement of the MARA transmission compared to RITU in the cases of nominal MARA settings and when the polarities of the quadrupoles are inverted ($B_{Q1}/\chi_B = 0.50$ m^{-1}).

total solid angle acceptances are marked in figures 1.12 and 1.13 for RITU and MARA. In figure 2.11 (a) the geometrical efficiency (i.e. geometrical transmission) is shown for these two as a function of the standard deviation of the Gaussian angular distribution. The relative enhancement of the geometrical transmission of MARA compared to RITU is shown also in (b) for the nominal mode and for the "high transmission mode" with inverted quadrupole polarities. In the high transmission mode the angular acceptances of $\alpha_{0,\max} \approx 55$ mrad and $\beta_{0,\max} \approx 65$ mrad yielding $S_{\mathrm{total,HT}} \approx 14$ msr were used as suggested by figure 2.9 with $B_{Q1}/\chi_B = 0.50$ m^{-1}. As in the case of normal polarities, a larger solid angle will be obtained if a solution which requires a smaller magnetic rigidity than 1 Tm, is used.

The geometrical transmission value of MARA is higher for all angular distribution widths. The largest difference of about 35% is located at 30 mrad which is a consequence of the low horizontal acceptance (~ 25 mrad) of RITU. In the case of the largest angular cones the difference between RITU and MARA is mainly due to solid angle. The geometrical transmission of the high transmission mode of MARA has a linearly increasing enhancement over RITU until around 35 mrad where it reaches the constant enhancement of 60%. In most cases, the real transmission is less than discussed above for MARA since only two or three charge states can be collected at the maximum. Two or three most

abundant charge states after a C-foil represent from 20% up to 40% of the total (see for example figures 2.45 (a) and 2.54 (a)). Therefore, the transmission in the normal mode is typically less than 40% of the RITU transmission if the transmission of these charge states is not cut by the energy acceptance. In some cases the RITU transmission can be achieved. MARA allows the use of a more symmetric fusion reaction or even one with inverse kinematics for the production of an isotope under study compared to an experiment with RITU. This type of reaction would have a smaller angular cone translating to an increased transmission value. In addition, the higher velocity generates smaller separation between neighbouring charge states due to the increased avarage charge which may allow more ions to be collected at the focal plane.

2.3.4 Image aberrations

The most common image aberrations in the dispersive direction in the recoil separators comparable to MARA are those related to the transfer matrix coefficients $(x|a^2)$, $(x|a^3)$, $(x|a\delta_K)$ and $(x|\delta_K^2)$. The first two are purely geometrical and nonzero for dipole magnets without hexapole component [Wol99]. These aberrations can be corrected partially by curved effective field boundaries which is a widely adopted solution and for example is used in all the separators listed in table 2.1. The curved effective field boundary is a second order correction and is equivalent to a magnetic hexapole at the vicinity of the EFB. Such a second order correction affects mainly the second order transfer coefficients but can introduce higher order aberrations which needs to be taken into account. Additionally to the curved EFB, the usage of additional hexapoles with MARA and the effects of the tilted mass focal plane are studied in the following.

Curved boundaries of the poles of the dipole

Figure 2.12 shows the aberrations as a function of the radius of curvature divided by the EFB radius (ρ_0/R_{EFB}), set symmetrically for entrance and exit. The field boundary radius affects mainly the coefficients $(x|a^2)$ and $(x|a\delta_K)$. Both are inversely proportional to R_{EFB} with positive and negative proportionality constants, respectively. The absolute values of the constants of proportionality are almost the same. Thus the sum of these is practically constant. The value of $R = 2$ m has been adopted for MARA since this value gives relatively straight distributions in the xa-plane at the focal plane for typical angular and energy distributions. This is illustrated in figure 2.13 which shows the horizontal phase space distribution for masses $m = \{99, 100, 101\}$ u and charge states $q = \{25, 26, 27\}$ without curvature in the EFB (top panel) and with the value adopted (the second panel from top). The initial distribution defined by (2.2) has been used in the figure. By comparing these plots, it can

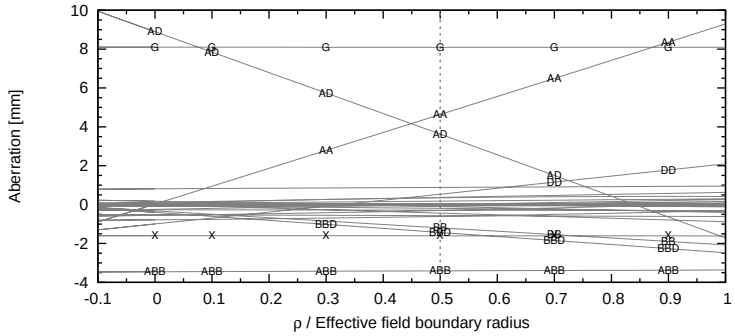

Figure 2.12: Sizes of the aberrations at the MARA focal plane as a function of the dipole bending radius $\rho_0 = 1$ m divided by the radius of the effective field boundary, set symmetrically for the entrance and exit. The line $\rho_0/R_{\mathrm{EFB}} = 0.5$ shows the value adopted in MARA. The positive (negative) values represent a convex (concave) EFB. For an explanation of the aberration curves and the initial values used see the caption of figure 2.7.

be seen that the value $\rho_0/R_{\mathrm{EFB}} = 0.5$ yields much better spatial separation of neighbouring masses.

Main aberrations of MARA

The transfer matrix coefficients listed in appendix A and suitable initial values (x_0, a_0, y_0, b_0 and δ_{K0}) can be used to calculate the size of the aberrations. As shown in figure 2.12 the most critical second order aberrations are $(x|a^2)$ and $(x|a\delta_K)$. The value of the third order aberration $(x|ab^2)$ is also relatively high. However, the sizes of the third order aberration may be different in the real system. It should be noted that the real fringing fields may differ from the ones used in the GICOSY calculations which may lead to slightly different aberrations. Also the electric field distortion due to the split anode is expected to be reflected in some aberrations involving coordinates a, δ_K and b.

In order to get a better conception of the two most important aberrations, $(x|a^2)$ and $(x|a\delta_K)$, alongside the dispersion and magnification, a graph showing how the initial (x, a) phase-space ellipses are imaged to the focal plane for different energies has been produced and is shown in figure 2.14 for all combinations of $E_k = \{90, 100, 110\}$ MeV, $m = \{99, 100, 101\}$ u and $q = \{25, 26, 27\}$. The intial phase space ellipses were not tilted and had $x_{0,\max} = \pm 1$ mm and $a_{0,\max} = \pm 45$ mrad as major and minor radii. All the ellipses are transformed to paths having a banana shape which open to the right. This is due to the $a_0^2(x|a^2)$ aberration which is positive for all initial angles ($(x|a^2) \approx 2.3$). The

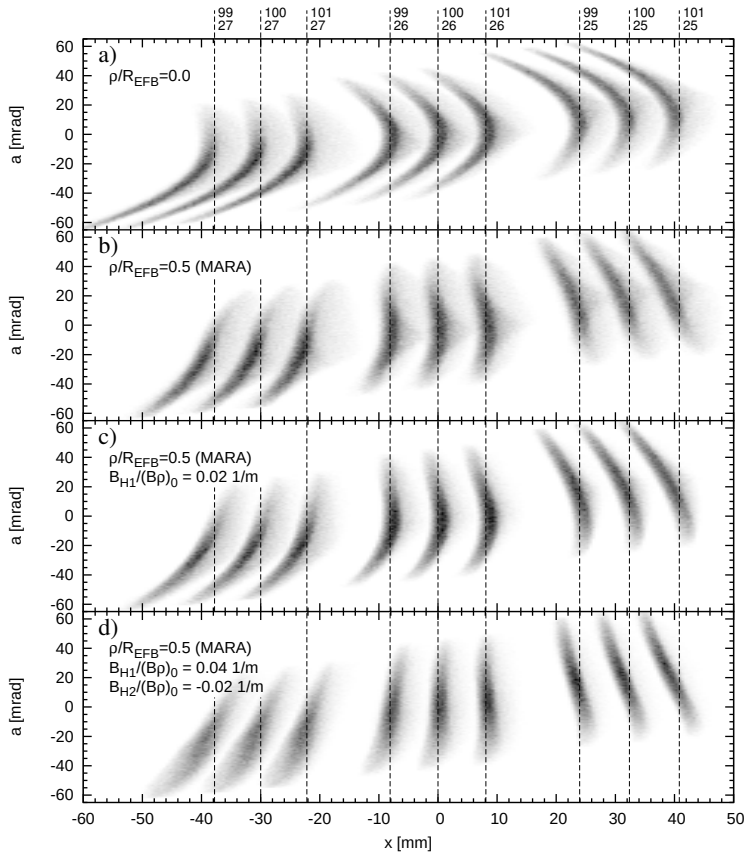

Figure 2.13: The effect of second order corrections on the horizontal phase space image at the focal plane a) without any corrections and b) in the case of rounded EFB in the dipole (the nominal MARA setup). Additionally to the nominal setup of (b), the effect of one and two hexapoles correcting mostly aberrations related to $a_0^2(x|a^2)$ and $a_0\delta_K(x|a\delta_K)$ are shown in (c) and (d), respectively. The masses and charge states are given in the labels attached to the vertical lines.

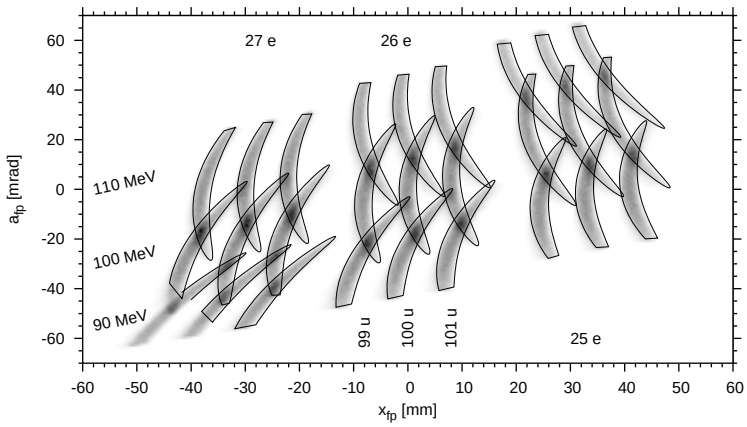

Figure 2.14: Horizontal phase space images at the focal plane of initial phase space ellipses at the target with varying mass, charge and energy (given in the figure). The particle with 100 u, 26 e and 100 MeV has been used as a reference. The intensity matrix represents random particles sampled from the test distribution (2.2) using the same masses, energies and charges.

horizontal angle at the focal plane, a_{fp}, depends mostly on initial angle and energy. This dependence is shown in figure 2.19.

The $a_0\delta_{K0}(x|a\delta_K)$ aberration can have either a positive or a negative value ($(x|a\delta_K) \approx 1.15$) depending on the sign of the initial angle (in the context of figure 2.14). Since the energy is constant in a path and the coefficient $(a|a)$ is negative the $(x|a\delta_K)$ aberration shears the banana-shaped paths horizontally.

All the other aberrations which include any coordinates other than a or δ_K are visualised as well in the figure by an intensity matrix drawn behind the curves. The intensity matrix represents a set of random particles sampled from the test distribution defined in (2.2). The gray color is black for maximum counts per pixel and white for pixels without any counts and linear in between. Only a faint trace of intensity lies outside the curves with maximum change in x_{fp} being around 3 mm. These are caused by the "negative" aberrations including b_0^2 shown in the bottom of figure 2.12.

The main aberrations are represented also in figure 2.15 in which the contours of the constant horizontal deviation at the focal plane are drawn as a function of the initial horizontal angle and the relative kinetic energy difference. This graph used in conjunction with a known separation between neighbour masses is practical when estimating the needed sizes of adjustable apertures which can be used to reduce the horizontal angular acceptance. By neglecting the other aberrations one can read that for example the masses 100 u and 101 u can be

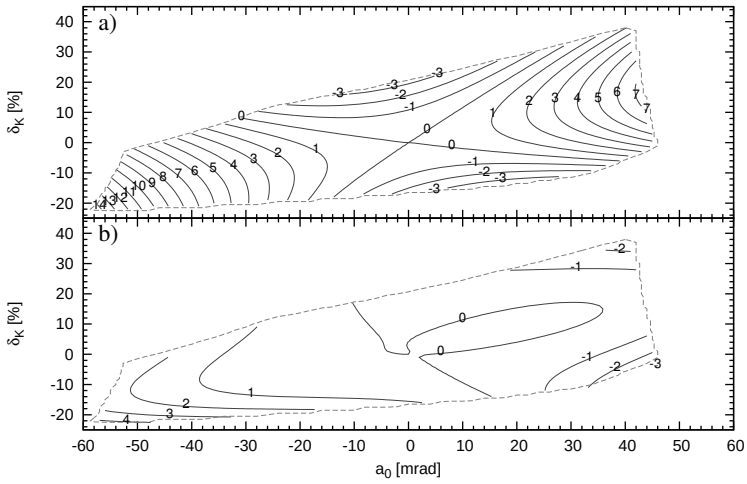

Figure 2.15: Horizontal deviation at the focal plane as a function of the initial horizontal angle, a_0, and the relative kinetic energy difference, δ_K for a) nominal MARA setup and for b) nominal setup with two additional hexapoles. All the other initial coordinates have been set to zero.

separated physically without any overlap if the horizontal acceptance is limited to $\sim \pm 30$ mrad (Dispersion is about 8 mm/1% in mass). A similar graph was constructed by P. Spolaore et al. [Spo85] for CAMEL. The comparison between these graphs shows that the aberration due to the incident angle is a little bit larger in MARA for positive angles and for negative angles it is almost double the value given for CAMEL. The aberrations due to energy seem to be a little smaller in MARA.

Correcting main aberrations by hexapole element(s)

Let us consider the aberration $a_0^2(x|a^2)$ in detail. By analysing the trajectories of different horizontal incident angles, one can observe that the ones having high positive angles are over focused by sector fields and the trajectories with negative initial angles are correspondingly under focused. If this is meant to be corrected then a hexapole element should be added at the position where the beam width is maximised due to the initial angle. The obvious place, according to figure 2.5, is between the Q_3 and the deflector. In the hexapole field the trajectories with large $|x|$ are bent in the same direction and thus the over and under focusing mentioned above can be corrected. This hexapole is marked as H_1 throughout the text.

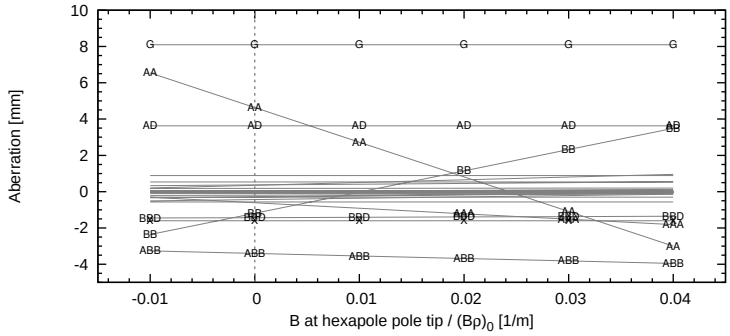

Figure 2.16: Aberrations $(x|*)$ as a function of the magnetic field at the pole tip of a hexapole element ($l_{\text{eff}} = 15$ cm, $G_0 = 7.5$ cm) placed between the quadrupole triplet and the deflector.

Figure 2.16 shows how the aberrations $(x|*)$ evolve as a function of the hexapole field of H_1 placed 5 cm after the triplet. The optical parameters of $l_{\text{eff}} = 15$ cm and $G_0 = 7.5$ cm were adopted for the hexapole. For example the pole-tip field of $B_{H1}/\chi_B = 0.02$ m^{-1} seems to be reasonable if such a correction element would be added alone. Then the $a_0^2(x|a^2)$ aberration would be reduced to around 1 mm (for $a_0 = 45$ mrad). With higher B_{H1} values the $b_0^2(x|b^2)$ aberration would became larger than around 1 mm. The horizontal phase-space plot at the focal plane for this configuration is shown in figure 2.13 (c).

As given in the table 2.3, the optical distance between the last quadrupole and the deflector is only 30 cm. The field clamp at the exit of the Q_3 extends about 11 cm downstream from the effective field boundary and thus the real position of H_1 should be more downstream. As the vacuum chamber of the deflector also needs some space, the drift length between the triplet and the deflector needs to be increased approximately 10 cm if a 15-cm long hexapole is to be added. However, this length had not been extended in the simulations since the effects are expected to be small. One option is to move the deflector closer to the dipole without increasing the total optical length of MARA. This has been studied briefly by moving the deflector 10 cm downstream. It was found that the movement had very small impact on resolving power even if the quadrupole fields were kept untouched. In any case, if the hexapole element is proposed then more detailed simulations are recommended. The safe solution would be to reserve enough space for the hexapole before the construction because moving the deflector forward changes the placement of the downstream elements.

Figure 2.16 shows that the hexapole H_1 can be used to change the $(x|a^2)$ transfer coefficient while the $(x|a\delta_K)$ remains constant. As discussed earlier and suggested by figure 2.12, both of these coefficients can be changed si-

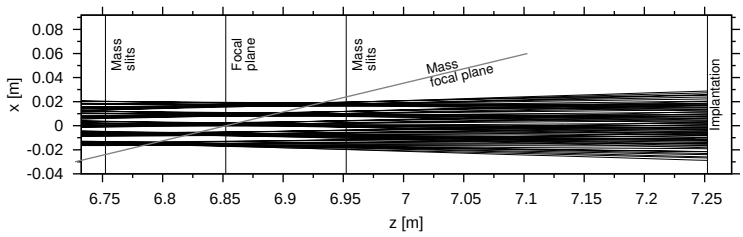

Figure 2.17: Trajectories of ions having masses $m \in \{98, 99, 100, 101, 102\}$ u in the vicinity of the focal plane. For all masses all the combinations of kinetic energies and horizontal starting angles of $E_k \in \{98, 100, 102\}$ MeV and $a \in \{\pm 30, \pm 20, 0\}$ mrad are used.

multaneously by introducing curvature in the dipole EFB which acts like a hexapole. Therefore, let us consider a second hexapole, H_2, with parameters $l_{\text{eff}} = 15$ cm and $G_0 = 10$ cm, placed 30 cm downstream from the deflector. Now the hexapole fields can be adjusted so that both of the aberrations are reduced simultaneously. For example the values of $B_{H1}/\chi_B = 0.04$ m^{-1} and $B_{H2}/\chi_B = -0.02$ m^{-1} have been found to give a reasonable balance between these aberrations and others. The largest aberration would be then $a_0 b_0^2 (x|ab^2)$ according to the GICOSY calculations. The horizontal phase-space distribution at the focal plane for these hexapole fields is shown in figure 2.13 (d). The addition of such hexapoles in order to correct the worst aberrations is reasonable if better physical separation is required for example to cut focal plane counting rates because neighbouring masses are leaking through. However, this is not so straightforward since the tilted mass focal plane of MARA complicates this in any case.

The tilted mass focal plane

The angular magnification of MARA is $(a|a) = -0.624$ which is relatively small. This is of course a direct consequence of the long drift length preceding the focal plane. The other transfer coefficient contributing to the mass focal plane angle, γ_{mfp}, is $(x|a\delta_m) = 1.96$. With these values substituted to equation (1.23) one obtains $\gamma_{\text{mfp}} = 14.4^\circ$.

The trajectories of five masses with different energies and initial horizontal angles have been calculated with the JIonO code through MARA and are shown in figure 2.17 around the focal plane. Also the mass focal plane with the above calculated $\gamma_{\text{mfp}} = 14.4^\circ$ has been drawn. It can be seen that the equation (1.23) is enough to describe the position of the best focus for given mass. Due to this tilted focal plane a more advanced slit system is needed around the main focal

plane detector. This is discussed in detail in section 2.8.4

It is practically impossible to change either coefficient affecting the γ_{mfp}. The value will increase only slightly (about 1°) if the drift length preceding the focal plane is shortened (changing the value of $(a|a)$) the maximum 30 cm allowed by the surface coils. This is shown in figure 2.7 (c). The different solutions for quadrupoles suggested by figure 2.8 have also been tested with the GICOSY code. The effect turned out to be negligible. The value of the other coefficient, $(x|a\delta_m)$, cannot be altered significantly in the MARA configuration since it would require a hexapole in a place where the dispersion is large.

2.4 MARA performance

The aberrations of MARA, at least according to the ion optical simulations, are about the same order than in other recoil mass spectrometers like FMA, CAMEL and HIRA. In any recoil-mass separator the m/q ratio of a particle arriving at the focal plane is obtained from the horizontal coordinate, x_{fp}. Due to small the mass focal plane angle, γ_{mfp}, in MARA the ability to track incoming particles has been set as one of the main requirements of its focal-plane detector system in order to improve the m/q resolution by software. The ions having m/q ratios smaller than the reference m_0/q_0 value are focused before the focal plane (see figure 2.17), thus represented by a horizontal phase-space distribution that has a negative horizontal angle a_{fp} for smaller x_{fp} and positive a_{fp} for larger x_{fp}. Corresponding distributions for larger-than-reference m/q are tilted in the opposite fashion and will be focused behind the focal plane. The tilting can be seen in all panels of figure 2.13 and especially in (d) where the additional hexapoles remove most of the aberrations which affect the shape of the mass distributions in the phase-space plot excluding $(x|a\delta_m)$.

The relationship between the angle and position can be used, within the limits of the detector resolutions, to gain back the mass resolving power diminished due to the tilted focal plane. This is clearly the main correction the tracking is needed for. The simplest practical equation for the mass deviation (including charge) is $\delta_m = \mathcal{D}_m^{-1} x_{\mathrm{fp}} + c_{\mathrm{ma}} x_{\mathrm{fp}} a_{\mathrm{fp}}$, where x_{fp} and a_{fp} are the recorded horizontal position and angle coordinates at the focal plane, respectively, and c_{ma} is a constant which can be calculated from the transfer matrices or can be fitted into the data. Clearly, to obtain the incoming angle, two position sensitive detectors are required. The first, located at the focal plane, should be as thin as possible in order to avoid beam spreading and loss of information about incoming angle. These detectors should also have a good timing resolution which can be used to obtain a time of flight and the velocity. Additionally, if the second detector can provide a recoil energy signal then a very rough charge state estimate can be calculated. The focal plane setup of MARA is discussed

in the section 2.8.5 and more technical details can be found therein.

When the knowledge about the MARA ion optics is combined to the focal plane tracking information even more properties of an ion or event can be calculated in software. For example the corresponding beam pulse which created the observed recoil can be identified. Some estimation of the initial angle of the recoil can be made as well.

2.4.1 Observed quantities of an ion

In addition to the main observable—which is the horizontal position—at the focal plane, also time of flight, energy and incoming angle of an ion can be measured. In some cases also a time of flight over the MARA spectrometer can be recorded if a fusion reaction event which has created the ion can be observed at the target position via prompt γ radiation or charged-particle emission. The following information about the ion travelling through MARA can be obtained with suitable detectors:

- $x_{\mathrm{fp}}, y_{\mathrm{fp}}$, the horizontal and vertical positions at the focal plane. Resolutions of around $\sigma = 0.6$ mm can be achieved [Dro07] if a secondary electron detector (SED) is to be used.
- $a_{\mathrm{fp}}, b_{\mathrm{fp}}$, the horizontal and vertical angles at the focal plane. To obtain these, a second position sensitive detector behind the focal plane detector is required. Most probably this will be a double-sided Si-strip detector (DSSD). A resolution around 5–10 mrad can be expected (assumed 1 mm position resolution in the detectors separated by a distance of 40 cm and some scattering in the first detector).
- Δt_1, the time of flight from target position to the focal plane. Due to the high intensity of the stable primary beams it is not possible to use a start detector. However, an RF pulse (beam pulse) time (length around 5–11 ns) or a detector observing prompt γ radiation or evaporated charged particles can be used. The clover Ge-detectors used in the Jurogam II array have a time peak FWHM around 6 ns [Duc99]. If a fast scintillator is used at the target then a sub-ns ToF resolution could be easily reached.
- Δt_2, the time of flight between the transmission detector at z_{fp} and the implantation detector. Time peak widths of σ =0.4–0.5 ns can be achieved (for SED $\sigma = 0.13$ ns and for DSSD $\sigma = 0.4$ ns).
- E_k, the energy deposited into the implantation detector (probably DSSD). The FWHM value of 3% can be achieved with a DSSD and 1% with an ionization chamber (IC).

Probably the most convenient method to estimate for example the ToF over MARA (Δt_1) from $x_{\rm fp}$, $a_{\rm fp}$ and Δt_2 is to develop a Taylor polynome up to reasonable order: $\Delta t_1 \approx \sum_i c_i x_{\rm fp}^l a_{\rm fp}^m (\Delta t_2)^n$ where l, m and n are natural numbers and $1 < l+m+n \leq N$. N is the order of the polynome. In this study the coefficients c_i have been fitted numerically using the *Gnu Scientific Library* [GSL] and its `gsl_multifit_linear` function. The data used for fits were calculated with JIonO library. In the calculations input distributions which fill the energy and rigidity acceptance of MARA completely were used. In principle, such polynomes can be derived also from matrix elements but that approach does not take finite detector resolutions into account. Because the fit tries to minimize the sum of deviations squared, the values of c_i should optimally depend on detector resolutions. Generally, in the case of the higher detection accuracy the higher order polynomes can be utilized.

2.4.2 Time of flight from the target to the focal plane, Δt_1

The non-relativistic formula for kinetic energy gives $v_{\rm ref} = 1.389 \cdot 10^7$ m/s as the velocity of the reference particle having $E_k/m = 1$ MeV/u. In a nominal setup described in tables 2.2 and 2.3 the length along the optical axis from target to the focal plane is $l_{\rm ref} = 6.852$ m. The time of flight for the reference particle is thus $t_{1,\rm ref} = 493.3$ ns (the relativistically correct time of flight would be 493.7 ns).

The path length of an ion has been calculated as a function of initial coordinates x_0, y_0, a_0, b_0 and mass and energy deviations δ_m, δ_K with the GICOSY programme. The maximum absolute values of $x_0 = 1$ mm, y_0 =1.5 mm, a_0 =45 mrad, b_0 =55 mrad, $\delta_m = 0.05$ and $\delta_K = 0.3$ have been utilized to calculate the maximum absolute contribution of different transfer matrix coefficients. If only the coefficients which contribute more than 0.1% (=6.9 mm) are taken into account the equation for the path length is

$$l_1 = 6.852 - 0.3336\delta_K + 0.8696 a_0 \delta_K + 0.4729\delta_K^2 - 0.6011\delta_K^3. \qquad (2.8)$$

According to this, the flight-path length depends strongly on the energy but only weakly on the initial horizontal angle. The energy is not constant over the deflector and thus (2.8) is not perfectly valid to be used as a product of the observed Δt_1 and velocity. The time of flight has been calculated directly in similar manner and is

$$t_1 = (493.68 + 248.55\delta_m - 270.48\delta_K + 62.65 a_0 \delta_K - 125.54\delta_m\delta_K + 231.00\delta_K^2 - 223.45\delta_K^3)\ \text{ns}. \qquad (2.9)$$

The initial angle, a_0, dependence of the equation (2.9) is also weak and the time of flight, t_1, is essentially a function of δ_m and δ_K (see also discussion in

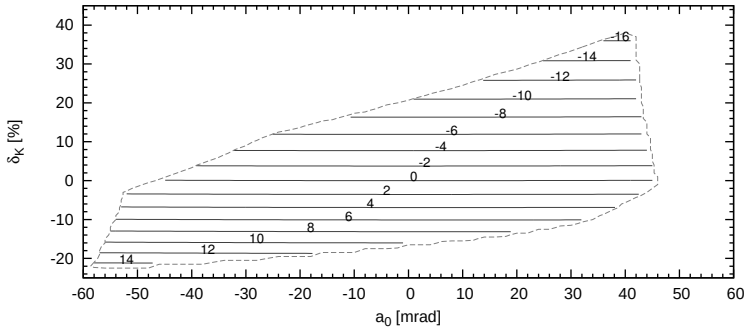

Figure 2.18: Relative change in flight time over MARA in per cents as a function of the initial horizontal angle a_0 and energy deviation δ_K. The standard reference particle has been used. A Change of 1% in t_1 corresponds to about 4.9 ns for this reference particle.

section 1.1.3). Figure 2.18 shows the relative change in t_1 as a function of a_0 and δ_K for central mass including all transfer coefficients up to 3rd order. The figure and the equation suggest that the time of flight measurement together with δ_m from the hit position at the focal plane, x_{fp}, can be used to obtain the δ_K.

2.4.3 The focal plane position and angles

In the first order approximation the horizontal position, x_{fp}, where the ion arrives depends only on δ_m which is the relative difference in the m/q ratio compared to a reference particle, and on the initial coordinate x_0. Aberrations of second and third order degrade the mass spectrum as discussed earlier. According to the transfer matrix (see appendix A) the equation

$$\begin{aligned} x_{\mathrm{fp}} = &-1.604x_0 + 0.8096\delta_m + 2.289a_0^2 + 1.963a_0\delta_m + 1.151a_0\delta_K - 0.3947b_0^2 \\ &- 0.6075\delta_m^2 - 0.8106\delta_m\delta_K + 0.1094\delta_K^2 + 4.774a_0^2\delta_K - 25.04a_0b_0^2 \\ &- 0.8099a_0\delta_K^2 - 6.838b_0^2\delta_m - 7.157b_0^2\delta_K + 0.9404\delta_m\delta_K^2 - 0.2925\delta_K^3 \end{aligned} \quad (2.10)$$

can be obtained. The terms which are not included contribute less than 1 mm with the maximum initial coordinates used above for the equation (2.8). The effect of a_0 and δ_K on x_{fp} has been shown earlier in figure 2.15.

As suggested by figure 2.5 the horizontal angle of an incoming ion (a_{fp}) depends mostly on the initial horizontal angle (a_0) and the energy deviation (δ_K). The

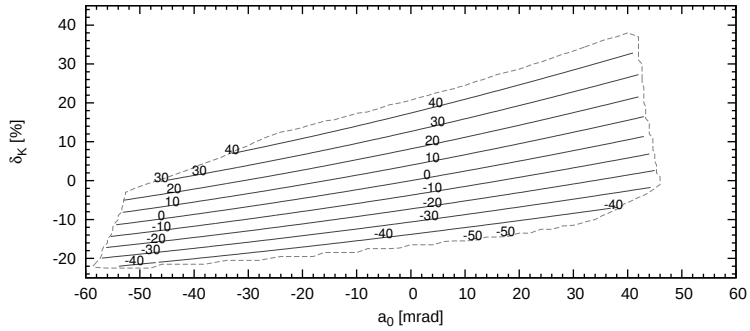

Figure 2.19: Horizontal inclination angle at the focal plane in units of mrad as a function of the initial horizontal angle and energy deviation.

3rd order calculation gives the equation:

$$a_{\mathrm{fp}} = -0.6236a_0 + 0.3369\delta_m + 0.2595\delta_K - 0.5141a_0\delta_K - 0.3176\delta_m\delta_K - 0.2029\delta_K^2 \quad (2.11)$$

where only terms having a maximum effect of more than 4 mrad have been included. Figure 2.19 illustrates the equation (2.11) as a function of a_0 and δ_K. The figure suggests that if δ_K is known (from time of flight for example) the initial angle can be calculated in some precision. This estimate of the initial angle can be further used to correct the a_0-related aberrations in δ_m. As indicated by equation (2.11) the horizontal end angle has some δ_m dependence. The first order term suggests a change of 3.4 mrad per change of 1% in mass. The maximum effect of the second order term $-0.3176\delta_m\delta_K$ is around 1 mrad for 1% change in mass.

When adopting only the terms contributing more than 1 mm to the vertical position at the focal plane the following equation can be obtained.

$$\begin{aligned} y_{\mathrm{fp}} = {} & -4.702y_0 - 2.315a_0b_0 + 6.282b_0\delta_m + 7.432b_0\delta_K \\ & - 73.99a_0^2b_0 - 22.29a_0b_0\delta_m - 24.46a_0b_0\delta_K - 336.2y_0b_0^2 \\ & + 16.85y_0\delta_K^2 - 85.88b_0^3 + 7.305b_0\delta_m\delta_K + 3.627b_0\delta_K^2. \end{aligned} \quad (2.12)$$

The maximum contribution of the first order term including y_0 (the vertical magnification) according to the equation is around 7 mm. The effects of $b_0^n\delta_K^m$ terms of the equation are illustrated in figure 2.20 (a). The terms including a_0 and δ_m (zero in the figure) can contribute from a few mm up to 1.8 cm ($a_0b_0\delta_K$) in maximum. However, the value of y_{fp} is dominated by values of b_0 and δ_K for realistic recoil distributions.

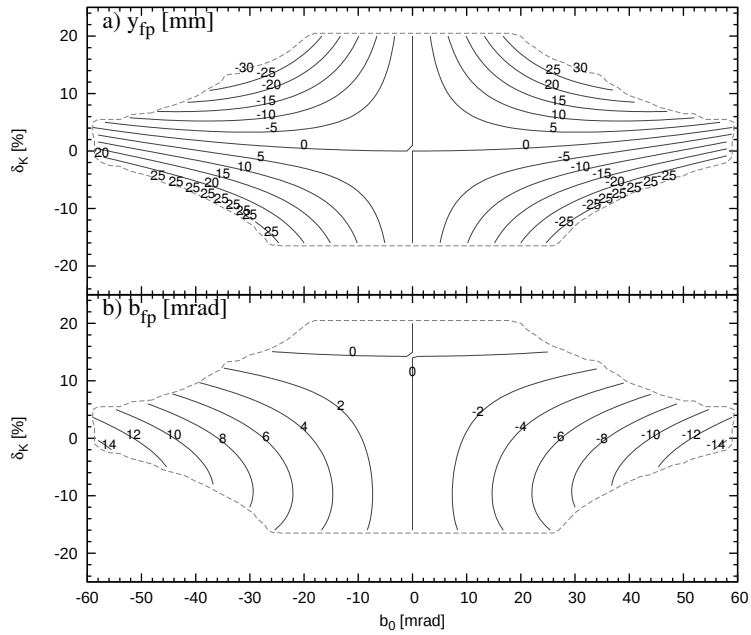

Figure 2.20: a) Vertical position, y_{fp}, and b) vertical inclination angle, b_{fp}, at the focal plane as a function of the initial vertical angle b_0 and the energy deviation δ_K.

The equation

$$b_{\mathrm{fp}} = -0.2127 b_0 + 1.087 b_0 \delta_K - 10.54 a_0 b_0 \delta_K + 5.68 b_0 \delta_m \delta_K + 3.912 b_0 \delta_K^2 \quad (2.13)$$

can be extracted for the vertical inclination angle at the focal plane from the coefficients contributing more than 4 mrad. The effects of $b_0^n \delta_K^m$ terms are visualized in figure 2.20 (b). In any case, only a coarse estimate of the initial vertical angle, b_0, can be made from measured b_{fp} and δ_K since the value of b_{fp} is relatively small compared to the precision of the angle measurement which is mainly due to scattering in the first detector.

2.4.4 Estimating Δt_1 from focal plane information

According to the approximate equation (2.9), the time of flight over MARA is essentially a function of δ_m and δ_K. The parameter δ_m can be obtained directly from x_{fp} and the parameter δ_K from δ_m and Δt_2 (time of flight between focal plane detectors) by using equation (1.8). Clearly, there should be a Taylor polynome which can be used to estimate the ToF over MARA from the focal plane information.

Altogether 120000 ions sampled from the initial distribution of

$$\begin{aligned} &x_0 \sim \mathcal{U}(-1,1)\ \text{mm}, \quad a_0 \sim \mathcal{U}(-60,60)\ \text{mrad},\\ &y_0 \sim \mathcal{U}(-2,2)\ \text{mm}, \quad b_0 \sim \mathcal{U}(-80,80)\ \text{mrad},\\ &m \sim 100+\mathcal{U}(2,2)\ \text{u},\ E_k \sim 100+\mathcal{U}(-10,10)\ \text{MeV},\ q \sim 26+\mathcal{U}(-1,1) \end{aligned} \tag{2.14}$$

were transported through MARA and the vector $\{x_{\text{fp}}, \Delta x_{\text{fp}}, \Delta t_2\}$ was recorded for every transmitted ion. The Δx_{fp} is the difference of horizontal positions in the subsequent focal plane detectors. The realistic detector resolutions were taken into account by adding random numbers obeying Gaussian distributions ($\sigma(x_{\text{fp}}) = 0.6$ mm, $\sigma(a_{\text{fp}}) = 4$ mrad and $\sigma(\Delta t_2) = 0.4$ ns) to the simulated quantities. In addition to these, the width of 1 mm for the DSSD strips was taken into account. The distance of 40 cm between the detectors was used. Using the GSL library the following first order function for the relative difference in Δt_1 was fitted:

$$\begin{aligned} T_{\text{est}} &\equiv \Delta t_1/\Delta t_{1,\text{ref}} - 1\\ &\approx 0.1567 x_{\text{fp}} - 0.5631 \Delta x_{\text{fp}} + 0.8103(\Delta t_2/\Delta t_{2,\text{ref}} - 1), \end{aligned} \tag{2.15}$$

where Δt_2 and $\Delta t_{2,\text{ref}}$ are the observed and the reference flight times between the detectors, respectively. For the distribution (2.14) itself the standard deviation of the fit is $\sigma(T_{\text{est}}) = 0.013$ and the distribution of the deviations is very close to a Gaussian. The suitability of the equation (2.15) was tested for discrete mass and charge combinations with the test distribution (2.2) expanded with neighbouring masses and charges, namely $m \in= \{96, 97, ..., 104\}$ u and $q \in \{25, 26, 27\}$. The distribution of deviations was Gaussian with the same standard deviation $\sigma(T_{\text{est}}) = 0.013$. In the case of the reference particle, this standard deviation corresponds to $\sigma(\Delta t_1) = 6.4$ ns and therefore 95% of ions are inside 26 ns which is less than the time between subsequent primary beam pulses hitting a target (RF pulses). The energy spread of ±10% yields alone a ToF spread of about ±24 ns. The RF frequency range of the K130 cyclotron of the Accelerator laboratory at Jyväskylä is 10–20 MHz corresponding to a 100–50 ns period in time structure. The length of the beam pulse is around 10 ns. According to these numbers the correct beam pulse in which the product has been created can be identified at least in the case of the standard reference particle.

The fit has been performed for different resolutions of detecting x_{fp}, a_{fp} and Δt_2. The effect of the observation precisions is presented in figure 2.21. As expected the precision of the Δt_1 estimate depends mostly on the precision of Δt_2. The change in the position resolution or scattering in the first detector have very marginal effect. According to the figure, $\sigma(\Delta t_2) = 0.2$ ns yields $\sigma(T_{\text{est}}) \approx 0.0075$ and $\sigma(\Delta t_2) = 0.8$ ns yields $\sigma(T_{\text{est}}) \approx 0.02$.

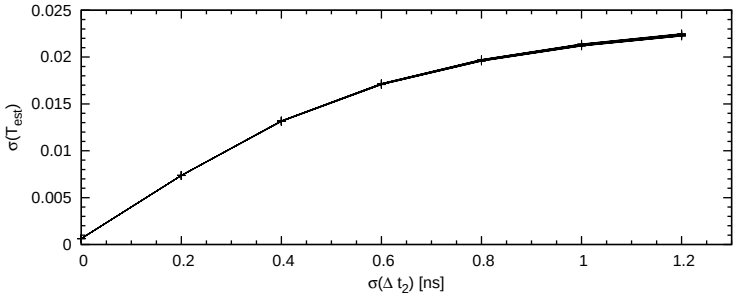

Figure 2.21: Standard deviation of the estimate of the relative flight time through MARA, T_{est}, as a function of the standard deviation of the measured fligth time between the focal plane detectors, Δt_2. Additionally to this, the lines with all 9 combinations of $\sigma(x_{\mathrm{fp}}) = \{0.4, 0.6, 0.8\}$ mm and $\sigma(a_{\mathrm{fp}}) = \{4, 5, 6\}$ mrad have been drawn. Since these lines are not separated the effect of $\sigma(x_{\mathrm{fp}})$ and $\sigma(a_{\mathrm{fp}}) = \{4, 5, 6\}$ on $\sigma(T_{\mathrm{est}})$ is insignificant.

2.4.5 Estimating the initial horizontal angle (a_0)

The initial horizontal angle affects the focal plane angle and position. According to the equation (2.11), approximately half of the value of the focal plane horizontal angle is contributed by the initial horizontal angle while the energy deviation δ_K contributes the second half. By using the equation (1.8) the δ_K value can be calculated from time of flight and δ_m given by x_{fp}. Thus a_0 should be calculable from the observation set of $\{x_{\mathrm{fp}}, \Delta x_{\mathrm{fp}}, \Delta t_2\}$. If Δt_1 (ToF through MARA) can be observed for an event then the resolution of the estimated a_0 can be enhanced by using an observation set of $\{x_{\mathrm{fp}}, \Delta x_{\mathrm{fp}}, \Delta t_1\}$. These expectations are confirmed by the results of the 1st and 2nd order Taylor polynome fits to the simulated observations of input distribution (2.14). The standard deviations of the estimate of the initial angle in the case of 1st order fit are shown in figure 2.22 as a function of either $\sigma(\Delta t_1)$ or $\sigma(\Delta t_2)$ and for different focal plane resolutions and standard deviation of the scattering in the medium of the first detector. As expected the use of Δt_1 provides better resolution. The dependence of the estimation precision on the detection resolution of x_{fp} is weak but as suggested by equation (2.11) the scattering at the first detector has a stronger effect. The improvements of the second order fits were found to be negligible.

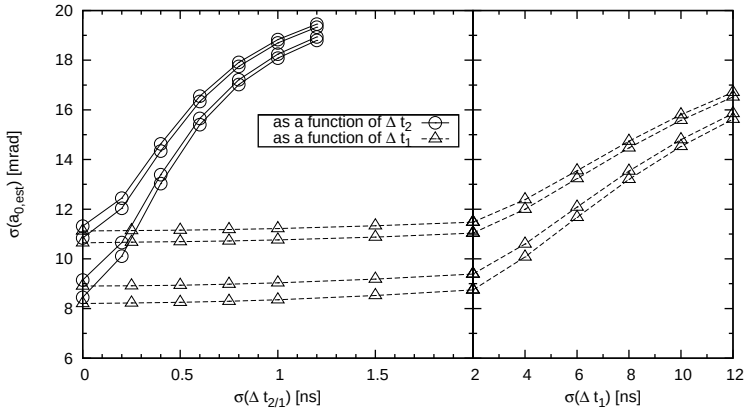

Figure 2.22: The accuracy of the estimate of the initial angle (a_0) by a first order Taylor polynome as a function of either $\sigma(\Delta t_2)$ (ToF between focal plane detectors) or $\sigma(\Delta t_1)$ (ToF through MARA) with different resolutions in x_{fp} and Δx_{fp}. The lines from bottom to top correspond to ($\sigma(x_{\mathrm{fp}})$ [mm], $\sigma(a_{\mathrm{fp}})$ [mrad]) pairs of $\{(0.4, 4), (0.8, 4), (0.4, 6), (0.8, 6)\}$, respectively. Note the change in x-axis scale.

2.4.6 Estimating δ_K and charge q

The relative energy per charge deviation compared to the reference particle (δ_K) can be calculated from δ_m and ToF quite accurately. As in section 2.4.5, better accuracy can be reached if a ToF through MARA (Δt_1) is measured. The effects of the ToF and the position resolutions and the scattering at the focal plane on δ_K resolution have been studied as in the preceding sections with first and second order Taylor polynomes fitted to distribution (2.14). As a result $\sigma(x_{\mathrm{fp}})$ and $\sigma(a_{\mathrm{fp}})$ have been found to have negligible impact on $\sigma(\delta_K)$. In figure 2.23 $\sigma(\delta_K)$ is shown as a function of the ToF resolutions (as a function of both ToFs). It seems that only in the case where a fast detector observes the reaction event at the target position (i.e. $\sigma(\Delta t_1) < 1$ ns) the second order polynome should be used.

If the kinetic energy of a recoil is measured at the focal plane in addition to the calculated δ_K then equation (1.9) can be used to obtain the recoil charge. This has been tested for discrete mass and charge combinations with the test distribution (2.2) expanded with neighbouring masses ($m \in \{96, 97, ..., 104\}$ u) and charge states ($q \in \{25, 26, 27\}$) and using the second order Taylor polynome fit $\delta_K(x_{\mathrm{fp}}, \Delta x_{\mathrm{fp}}, \Delta t_1)$. In the fit, the values of $\sigma(x_{\mathrm{fp}}) = 0.6$ mm, $\sigma(a_{\mathrm{fp}}) = 5$ mrad and $\sigma(\Delta t_1) = 1$ ns have been used. The resulting charge spectra with combinations of ToF resolutions $\sigma(\Delta t_1) \in \{1, 3\}$ ns and energy resolutions $\sigma(E_k) \in \{0.6, 1.2, 1.8\}$ MeV are shown in figure 2.24. The figure suggests that

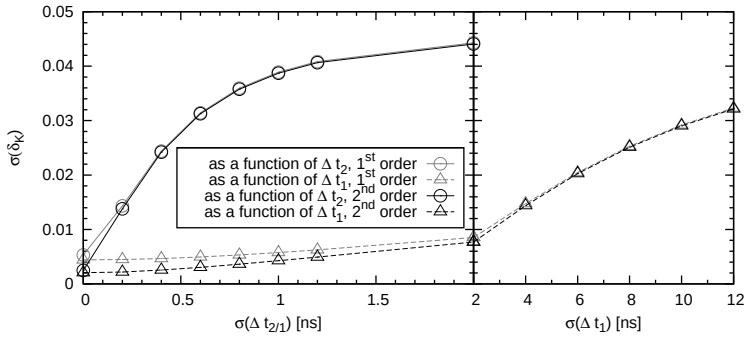

Figure 2.23: The accuracy of the estimate of δ_K by first and second order Taylor polynomes as a function of either $\sigma(\Delta t_2)$ or $\sigma(\Delta t_1)$. The position resolution of $\sigma(x_{\mathrm{fp}}) = 0.6$ mm and scattering with $\sigma(a_{\mathrm{fp}}) = 5$ mrad have been adopted.

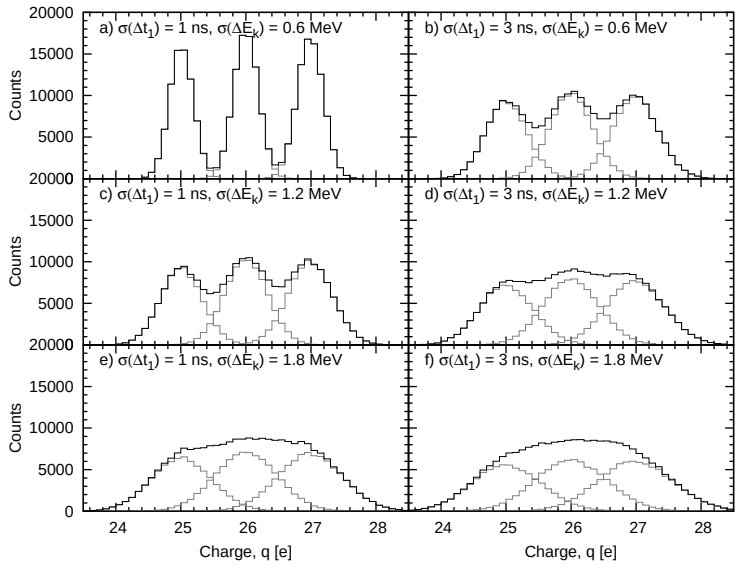

Figure 2.24: The charge spectra reconstructed from the focal plane information and ToF through MARA calculated with the second order Taylor polynome $\delta_K(x_{\mathrm{fp}}, \Delta x_{\mathrm{fp}}, \Delta t_1)$ for various kinetic energy resolutions (from top to bottom) and for two ToF resolutions (left and right). The gray lines show the individual charges the sum spectra drawn in black are consisting of. See labels in the panels for more information.

the charge of the ions can be at least partially identified which can be used further in the identification of the different reaction products. The absolute resolution in units of elementary charges depends also strongly on reaction kinematics and not only on detector resolutions.

2.4.7 Improving δ_m resolution by tracking

The main goal of the MARA ion optics is to provide mass per charge information of a recoil. Due to aberrations described in section 2.3.4 and shown in equation (2.10) the real m/q resolution is deteriorated from the first order value. The main aberrations are related to the energy deviation or the initial angle. However, the values of δ_K and a_0 can be calculated to some precision from observed quantities and therefore part of their contribution to the aberrations can be reduced.

Again the most convenient method to extract the improved m/q value is to use a fitted Taylor polynome. In principle, the estimated a_0 and δ_K discussed in previous sections and the equation (2.10) could be used to obtain the improved m/q value. Instead, a Taylor polynome $\delta_m(x_{\mathrm{fp}}, \Delta x_{\mathrm{fp}}, \Delta t_{1/2})$ has been fitted directly. In order to correct the tilted focal plane effect, a second or higher order polynome is required. It was observed that the third order polynome does not improve the fit further from the precision of the second order fit. The contributions of the detector position resolution, scattering and the ToF resolutions to the δ_m resolution are visualized in figure 2.25. The figure represents the contours of the standard deviations of values $(\delta_{m,\mathrm{est}} - \delta_m) \cdot 100$ % calculated for distribution (2.14) which was used also for fitting the polynome.

If we assume that the horizontal position can be detected with an accuracy of $\sigma(x_{\mathrm{fp}}) = 0.6$ mm, the scattering in the first detector is $\sigma(a_{\mathrm{fp}}) = 5$ mrad and the accuracy of $\sigma(\Delta t_2) = 0.4$ ns for the focal plane ToF, then the left column of figure 2.25 suggests $\sigma(\delta_m) \approx 0.3$ which translates to mass resolving power $\mathcal{R}_m = 100/(2.35 \cdot 0.3) \approx 140$ for the distribution (2.14). If the ToF through MARA is measured with fast detectors (scintillator and SED/MWPC) then the value of $\mathcal{R}_m \approx 170$ could be achieved.

Mass spectra of test distribution (2.2) expanded with neighbouring masses are shown in figure 2.26 as translated from the focal plane position spectra (thick gray line) and calculated from the position, angle and ToF with the Taylor polynomes (thin black line). See the figure caption for detailed information about the parameters. The comparison of subfigures (a) and (b) shows that the use of the ToF over MARA (Δt_1) instead of Δt_2 improves the mass resolution. This is due to better correction of the a_0-related aberrations in the case of Δt_1. In both cases the main correction compared to the position spectra x_{fp} comes from the correction of the tilted mass focal plane. When the horizontal

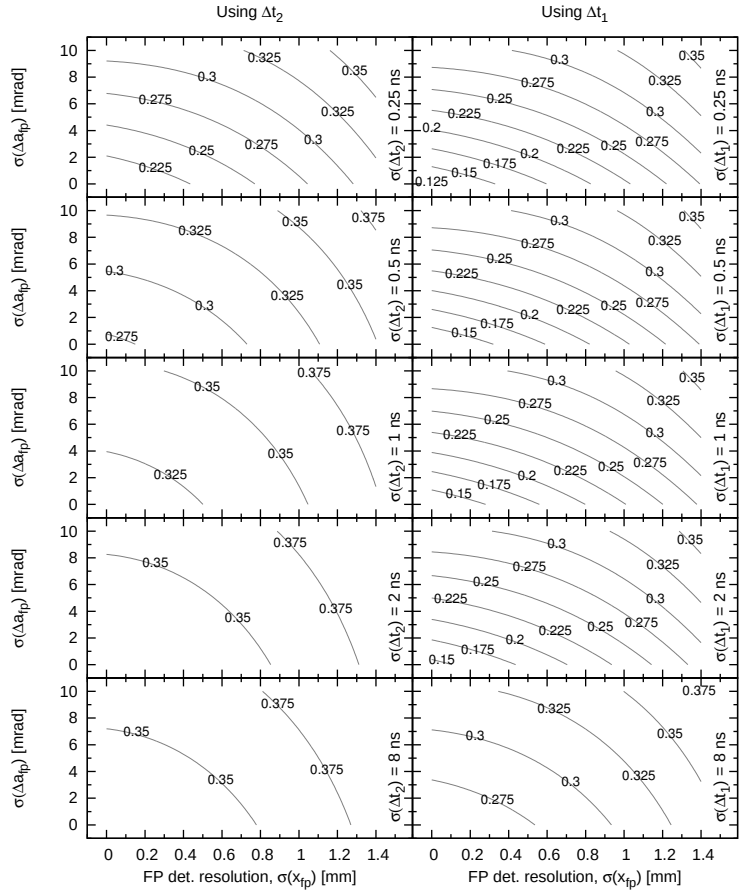

Figure 2.25: Standard deviation of the m/q ratio estimated with a second order Taylor polynome as a function of focal plane position resolution, $\sigma(x_{\mathrm{fp}})$, and scattering in the detector, $\sigma(\Delta a_{\mathrm{fp}})$, in per cents.

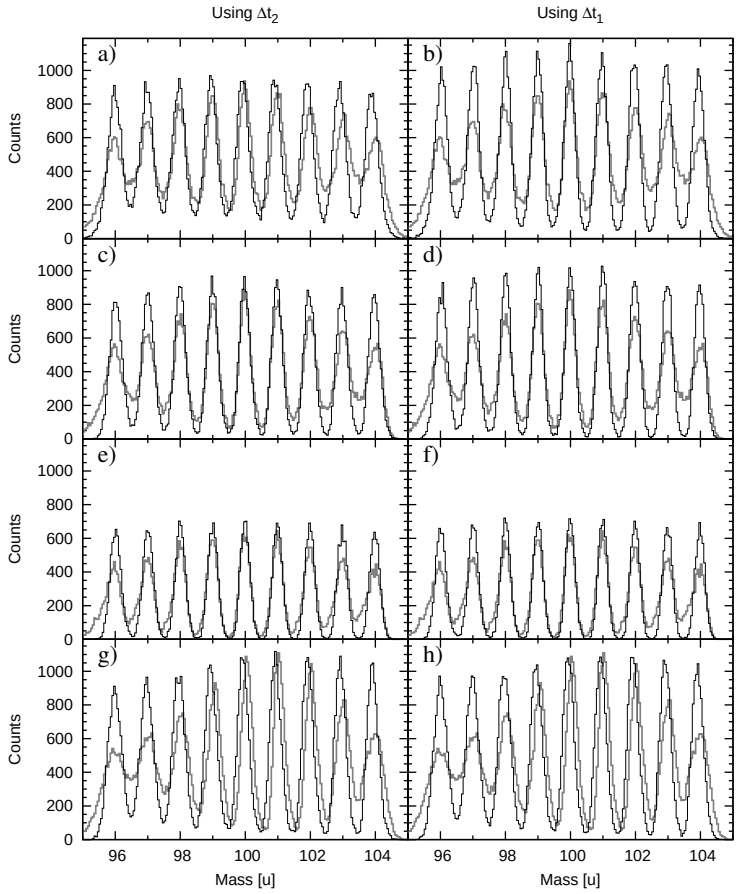

Figure 2.26: The mass spectra of distribution (2.2) expanded with neighbouring masses ($m \in \{96, 97, ..., 104\}$ u) having charge state $q = 26$. The spectra drawn in gray are obtained directly from the focal plane position spectra. The improved mass spectra calculated with a second order Taylor polynome are drawn in black. The left (right) column shows the results when Δt_2 (Δt_1) has been used. In all cases $\sigma(x_{\mathrm{fp}}) = 0.6$ mm, $\sigma(a_{\mathrm{fp}}) = 5$ mrad, $\sigma(\Delta t_2) = 0.4$ ns and $\sigma(\Delta t_1) = 0.2$ ns. Other conditions: a) and b) full acceptance with nominal settings, c) and d) horizontal acceptance limited to ± 35 mrad, e) and f) horizontal acceptance limited to ± 25 mrad, g) and h) extra hexapoles enabled with fields $B_{H1}/\chi_B = 0.04$ m^{-1} and $B_{H2}/\chi_B = -0.02$ m^{-1}.

angular acceptance is limited to ±35 mrad (subfigures (c and (d)) and further to ±25 mrad (subfigures (e) and (f)) the differences between position spectra and mass spectra improved by the tracking data are becoming smaller. The subfigures (g) and (h) show what happens if the hexapole corrections discussed in section 2.3.4 are added. For masses close to 100 (the reference) the system with hexapoles provides as good physical separation as the tracking can provide. The masses further away from $m = 100$ u are not separated mainly due to the tilted focal plane. The tracking based mass resolution is about the same with the nominal settings and with hexapoles added.

2.5 Optical elements

In this section technical descriptions of the MARA optical elements—the quadrupoles, dipole and deflector—are given. All elements are/will be manufactured by Danfysik A/S, Denmark. Danfysik is also the manufacturer of the power supplies of the quadrupoles and the dipole. F.u.G Elektronik GmbH, Germany, has manufactured the HV supplies of the deflector.

2.5.1 Quadrupole triplet

The quadrupole triplet consists of three quadrupoles: Q_1, Q_2 and Q_3. The quadrupoles Q_2 and Q_3 have identical design parameters and are larger than the first quadrupole, Q_1. The quadrupoles will be mounted on a common stand fabricated by the magnets' manufacturer. The stand provides fine alignment of the individual quadrupoles. One of the larger quadrupoles is shown in figure 2.27. Mirror plates are attached to the front of Q_1, to both sides of Q_2 and to the exit side of Q_3. The drift lengths between the quadrupoles may differ slightly from those given in table 2.3.

The quality of the quadrupoles has been checked according to the quality-assurance system of Danfysik. The received test reports state that the elements fulfil the specifications. The technical specification is given in table 2.4 and figure 2.28 shows the excitation curves measured by the manufacturer. The quality of the quadrupole field had been specified such that the strength of the other multipole components is less than 1%. The manufacturer has measured the harmonic content (i.e. multipole components) by using the fast rotating compansated coil technique. The sums of the measured coefficients $S = C_3 + C_4 + \cdots + C_{10} + C_{14}$ have been reported relative to C_2 (see equation (1.24)) at 50% B-field and at full field and are: Q_1, 0.12% (50%) and 0.10% (100%); Q_2, 0.59% (50%) and 0.56% (100%); Q_3, 0.59% (50%) and 0.54% (100%). The measurement radii were 40.00 mm and 60.00 mm for the small and the larger

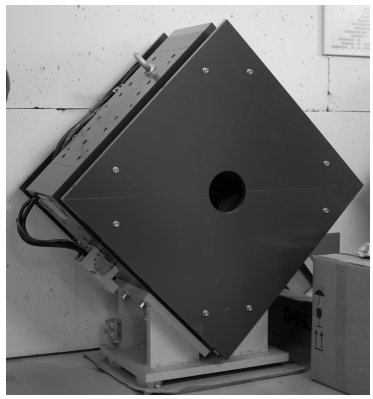

Figure 2.27: One of the larger MARA quadrupoles (Q_2/Q_3).

Table 2.4: Technical specification of the quadrupole magnets of MARA. The information is taken from the test reports provided by the manufacturer (Danfysik). To the appropriate extent the values are from the magnet test evaluations carried out by Danfysik with full powers: $I_{Q1} = 147$ A and $I_{Q2} = I_{Q3} = 251$ A.

	Q_1	$Q_{2,3}$
Serial number(s)	06056	06057, 06058
Power supply (type, Serial no.)	858, 1011743	858, 1103597/1103598
Width at beam line height	695 mm	1230 mm
Length along z-axis incl. mirror plates	398 mm	542 mm
Maximum field gradient	10 T/m	10 T/m
Aperture radius (G_0)	50.0 mm	75.0 mm
Effective length	250 mm	350 mm
Total weight, copper, iron [kg]	315, 64, 245	1485, 160, 1315
Pole profile and shape	facetted, square	facetted, square
Pole width·length at its root	100·218 mm^2	184·312 mm^2
Pole and yoke material	XC 06, St. 37	XC 06, St. 37
Coil type	Hollow conductor	Hollow conductor
Conductor dimensions (⌀)	7·4 mm^2	9·6.5 mm^2
Number of turns per coil	75	104
Current	147 A	251 A
Field gradient	∼10.6 T/m	∼10.2 T/m
Voltage	23.6 V	74.3 V, 74.0 V
Power	3.5 kW	18.6 kW
Pressure drop	5 bar	3 bar
Inlet temperature	18.5 °C	16.2, 16.5 °C
Tempereture rise	10.5 °C	30.8, 30 °C
Water flow	4.3 l/min	7.6 l/min,

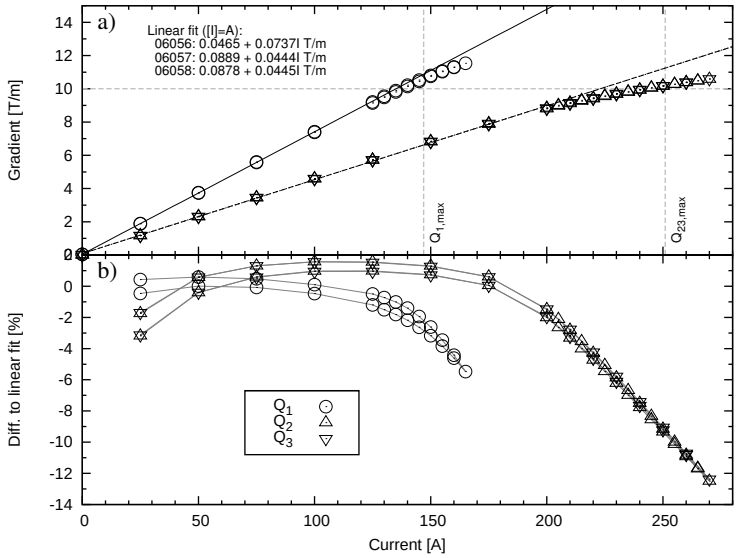

Figure 2.28: Gradients of the quadrupole magnets as a function of the current. Panel (a) shows the gradients versus the current in absolute scale. The linear fits have been performed to data points having current less than 80% of the nominal value. Panel (b) shows gradients relative to the fit as $(g(I)/g_{\mathrm{fit}}(I) - 1) \cdot 100\%$. Data are taken from the test reports.

quadrupoles, respectively. The values of the individual coefficients are given in the quality reports.

From figure 2.28 one can observe that the field strength due to hysteresis is on the order of 1%. Taking care of the quadrupole triplet solutions shown in figure 2.8, the maximum difference to the linear fit in the case of Q_1 and Q_2 is about 2% at currents of 147 A and 201 A, respectively. For Q_3 currents only up to about 85 A are needed and thus another linear fit limited to currents below 110 A should be used instead of the one shown in figure 2.28. The field strength at lower currents around 20–30 A in Q_3 needs to be measured before or during the commissioning of MARA.

The specified optical half lengths of the quadrupoles are 125 mm (Q_1) and 175 mm (Q_{23}) while the mechanical half lengths are 199 mm and 271 mm, respectively. This means that the quadrupoles extend mechanically 74 mm and 94 mm over the EFB. Therefore, the space available between the target and the entrance of Q_1 is about $(350 - 74) = 276$ mm. For comparison, the distance between the target position and the entrance surface of the mirror plate of the first quadrupole in RITU is about 335 mm. The first quadrupoles

in MARA and RITU have about the same width of 70 cm (measured along x/y-axis). In the current RITU setup the shortest distance from the Jurogam II germanium array and its frame to Q_1 is about 60 mm. Therefore, it should be possible to use Jurogam II also in front of MARA.

First order transfer matrix

The first order transfer matrix of the quadrupole triplet, from the target position to the exit of Q_3, is $\mathbf{Q}_{\text{triplet}} = \mathbf{Q}_3\mathbf{T}_{l_3}\mathbf{Q}_2\mathbf{T}_{l_2}\mathbf{Q}_1\mathbf{T}_{l_1}$. The multiplication with nominal settings given in table 2.3 yields

$$\mathbf{Q}_{\text{triplet,x}} = \begin{pmatrix} -1.042 & 1.255 & 0. & 0. \\ -0.9729 & 0.2117 & 0. & 0. \\ 0. & 0. & 1. & 0. \\ 0. & 0. & 0. & 1. \end{pmatrix} \tag{2.16}$$

$$\mathbf{Q}_{\text{triplet,y}} = \begin{pmatrix} 0.6697 & 0.8208 & 0. & 0. \\ -1.359 & -0.172 & 0. & 0. \\ 0. & 0. & 1. & 0. \\ 0. & 0. & 0. & 1. \end{pmatrix} \tag{2.17}$$

when the equations (1.19) and (1.33) are used.

2.5.2 Magnetic dipole

A photo of the MARA magnetic dipole is shown in figure 2.29. Figure 2.30 gives a closer look at the gap between the poles and shows the surface coils attached to the poles. The vacuum chamber, designed and manufactured in JYFL, is not shown in the figure but its dimensions in the horizontal plane can be seen in figure 2.2. The chamber can be placed inside the dipole by removing the upper part of the magnet. Special baffle plates or structures meant for decreasing the number of scattered primary beam particles can be easily attached to a set of pivots which are bonded inside the chamber close to the walls. A stand for the dipole has been fabricated by Danfysik. The stand enables position adjustment of the dipole within the range of 20 mm in all directions.

Part of the technical parameters of the dipole, taken from the quality assurance report delivered by Danfysik, are given in table 2.5. The excitation curve is shown in figure 2.31 with the linear fit to the data in the range $I = 0$–365 A. Panel (b) shows the relative difference of the magnetic field compared to the fit. At currents above $\sim$100 A, the hysteris produces a difference of about 1%.

The maximum current through the surface coils is 20 A which produces a gradient $|\partial B/\partial x| \approx 0.099$ T/m in the radial direction (x-axis). The B-field along

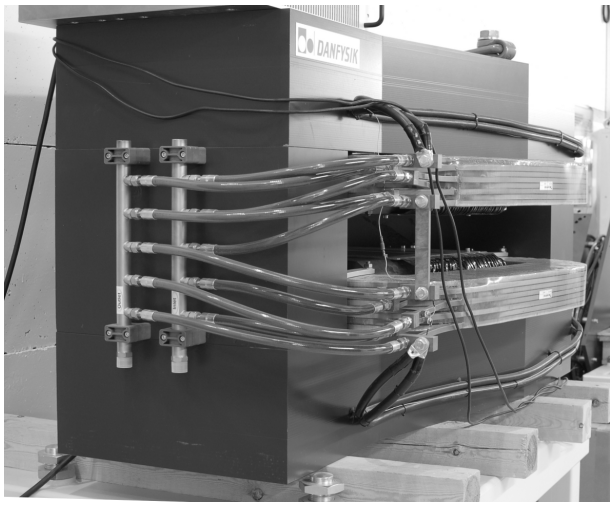

Figure 2.29: Photo of the magnetic dipole.

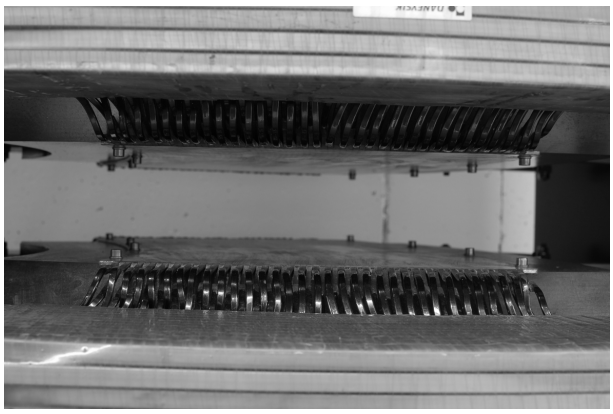

Figure 2.30: Surface coils of the magnetic dipole.

Table 2.5: Technical specification or realized parameters of the magnetic dipole (serial no. 08007). To the appropriate extent the values are from the magnet test evaluation carried by Danfysik with full power at $I = 430$ A which gives approximately field of $B = 1$ T (the nominal current to reach this field in specification is 456 A). The floor dimensions include the stand and are given along the optical coordinate-system axes.

Power supply (model, serial no.)	853, 0805568
Deflection angle and radius	40°, 1.0 m
Maximum field (nominal)	1 T
Weight: total, iron, copper	5595, 5173, 415 kg
Floor dimensions x·z·y (approximate)	1600·1100·1800 mm^3
Pole iron gap (excl. surface coils)	100 mm
Pole base width	520 mm
Pole and Yoke materials	XC06 and St37
Good field area (x- and y-directions)	±100, ±40 mm
Conductor	hollow, 11·11 mm^2, ⌀6 mm
Current	430 A
Maximum nominal B-field	∼1 T
Voltage, DC	46.4 V
Power	20.0 kW
Field homogeneity (meas. at $I = 430$ A)	$2.9 \cdot 10^{-4}$
Pressure drop	5.1 bar
Cooling water flow	20.2 l/min
Water temperature at inlet and outlet	17 and 30 °C
Surface coils:	
Number of conductors per pole	66
Width	331 mm
Maximum current	20 A
Max. field gradient in radial direction	0.099 T/m
Power supply (model, serial no.)	232, 10052237

the x-axis is tabulated in the test report for the range $x = -100 \ldots +100$ mm with 20 A current in the surface coils for the cases of 50% and 100% excitation in the main coils. According to the data, the errors of the field relative to the field at the optical axis are less than $1 \cdot 10^{-4}$ and thus the design goals are fulfilled.

First order transfer matrix

According to equation (1.25) the non-relativistic first order transfer matrix for a magnetic dipole having parameters $\phi_0 = 40°$, $\rho_0 = 1000$ mm and direction

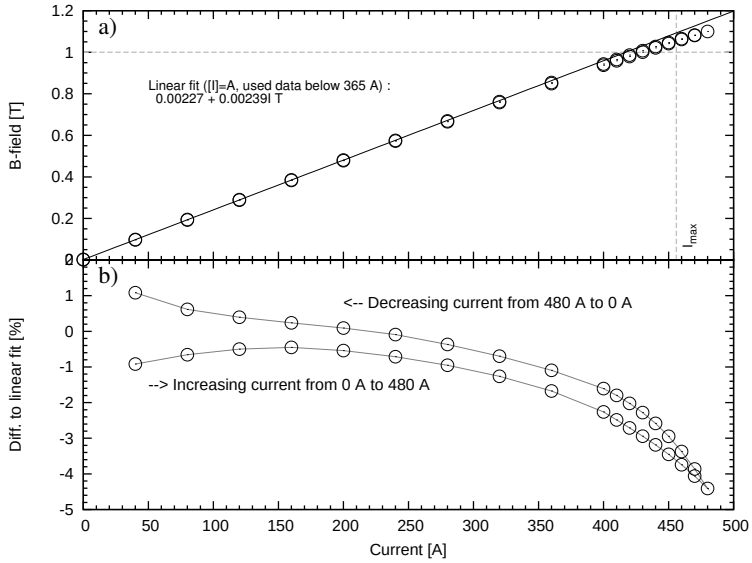

Figure 2.31: The excitation curve of the MARA dipole. Panel (a) shows the magnetic field flux density as a function of the current and a linear fit to the data in the range $I = 0$–365 A. Panel (b) shows the relative difference of the data to the linear fit.

$d = 1$ is

$$\mathbf{D}_{\mathrm{M,x}}(\varepsilon_1 = \varepsilon_2 = 0) = \begin{pmatrix} 0.7660 & 0.6428 & 0.1170 & 0.1170 \\ -0.6428 & 0.7660 & 0.3214 & 0.3214 \\ 0 & 0 & 1 & 0 \\ 0 & 0 & 0 & 1 \end{pmatrix} \tag{2.18}$$

in the horizontal direction.

The EFB's in the entrance and the exit of the MARA dipole have an angle $\varepsilon_1 = \varepsilon_2 = 8^\circ$ (specification) to the normal of the optical axis. The real inclination angles of the EFB's are 8.14° and 8.10° according to the test report. The drift length between the dipole and the focal plane would change about 1.7 cm in the calculations if the measured inclination angles are used instead of the specification. However, in this study, the nominal angle of 8° has been used. Equation (1.26) results in $f_1 = f_2 = -0.1405$ as the focal length of the thin lenses describing the inclined EFB in the horizontal direction for the entrance

and exit EFB. Combining this to (2.18) one obtains

$$\mathbf{D}_{\mathrm{M,x}} = \begin{pmatrix} 0.8564 & 0.6428 & 0.1170 & 0.1170 \\ -0.4148 & 0.8564 & 0.3378 & 0.3378 \\ 0 & 0 & 1 & 0 \\ 0 & 0 & 0 & 1 \end{pmatrix}. \tag{2.19}$$

Transformations of the (y, b) coordinates can be calculated with matrix

$$\mathbf{D}_{\mathrm{M,y}} = \mathbf{F}_{-f_2}\mathbf{T}_{l=\phi_0\rho_0}\mathbf{F}_{-f_1} = \begin{pmatrix} 0.9019 & 0.6981 & 0 & 0 \\ -0.2673 & 0.9019 & 0 & 0 \\ 0 & 0 & 1 & 0 \\ 0 & 0 & 0 & 1 \end{pmatrix}. \tag{2.20}$$

2.5.3 Electrostatic deflector

The electrostatic deflector of MARA needs more design and modelling than the MARA magnets before its parameters can be fully fixed. This is mostly because of its large physical size, unique design parameters and high voltage issues. Clearly, the price of such a tailor-made element is also relatively high. A lot of deflectors exist around world but the majority of them are part of small mass-analyser systems and only few are used in recoil mass spectrometers (table 2.1 lists almost all of them).

The presence of a half MV electric voltage over a 10–20 cm cap places demands on the surface smoothness and materials. The mass resolution can be achieved only if the co-operative action of the electrostatic deflector and the magnetic dipole cancels the energy dispersion at the focal plane. Therefore, the high electric field uniformity in an active volume is needed which translates to precise mechanics and alignment of the electrodes. An extra complication to the design and manufacturing is introduced by the required horizontal gap along the anode. This split anode enables a controlled collection of the primary beam. This is expected to reduce the level of unwanted background at the focal plane. In the preliminary design the gap will extend only from the middle of the anode to the close of its end in order to minimise its disturbance to the electric field.

Due to the fringing field the trajectory of a charged particle approaching the electric field of the deflector begins to bend already before it enters the volume between the electrodes. To take this into account the optical axis needs to be shifted at the entrance and exit. Another effect is that the bending of 20° will be achieved with electrodes that extend less than 20° as seen from the center of curvature. Of course, these effects occur also in a magnetic dipole but those elements are more standardised and can be ordered from a manufacturer

Table 2.6: Technical specification of the MARA deflector used in this thesis study. The values of some parameters may be slightly different in the real element.

High voltage supply:	
Manufacturer	F.u.G Elektronik GmbH, Germany
Model and serial no. (pos.)	HCH 250 - 250 000 pos, 13580-01-01 2005/04
Model and serial no. (neg.)	HCH 250 - 250 000 neg, 13580-01-02 2005/04
Physical dimensions (HxWxD)	1880x967x927 mm^2
Reach of the HV cable	> 7 m
Maximum current	1 mA
Optical parameters:	
Deflection angle (ϕ_0) and radius (ρ_0)	20°, 4.0 m
Vertical gap ($2G_0$)	140 mm
Maximum voltage (V)	$\pm$250 kV
Technical specification:	
Manufacturer (currently in design)	Danfysik A/S, Denmark
Floor dimensions (approximate)	round, diameter $\sim$1.7 m
Electrode height	400–500 mm
Electrode angular length	$\sim$19.0°
Vertical gap height in the anode	15 mm
Distance to entrance/exit shims	$\sim$100 mm

by listing the optical parameters. The deflector will be equipped with shunts which confine the fringing field. The distance between the shunts and electrodes defines the geometry of the electrodes (i.e. the angular extent). A shunt-electrode distance of $D = 10$ cm has been adopted in the following. The geometry for this distance has been derived with ray-tracing simulations in 2D. The effect of the split anode has been studied and is discussed later in this section.

The main optical parameters of the deflector are given in table 2.3 and also in table 2.6 which lists also some technical parameters. The radius of curvature, $\rho_0 = 4000$ mm, of the optical axis and the gap of 140 mm give $R_1 = 3930$ mm and $R_2 = 4070$ mm as the radii of curvature for the cathode and the anode, respectively. With these radii the equation (1.28) yields the electrical potential $V_{oa} = 8.7504 \cdot 10^{-3}$ V at the optical axis for the symmetric voltage $\pm V$ in the electrodes. For the standard reference particle (eq. (2.1)) the electric rigidity is $\chi_E = 7.68818$ MV according to (1.14). Since the change in potential energy for the reference particle when it is entering the deflector, $\Delta U = V_{oa} q_0$, is small compared to its kinetic energy, the rigidity can be assumed to be the same also inside the deflector, $\chi_E^* \approx \chi_E$. The actual change in kinetic energy is $\Delta E_k = 0.0306$ MeV which is small compared to the initial energy of 100 MeV. Equation (1.29) gives $V = 134.56$ kV as the voltage needed on the electrodes which is about 54% of the maximum.

According to the equation (1.31) the non-relativistic transfer matrix for the MARA deflector becomes

$$\mathbf{D}_{\mathrm{E,x}} = \begin{pmatrix} 0.8806 & 1.340 & -0.2388 & 0 \\ -0.1675 & 0.8806 & -0.3351 & 0 \\ 0 & 0 & 1 & 0 \\ 0 & 0 & 0 & 1 \end{pmatrix} \tag{2.21}$$

corresponding to the deflection angle $\phi_0 = 20^\circ$, radius of curvature $\rho_0 = 4000$ mm and direction $d = -1$. The transfer matrix in the vertical direction is simply the drift length matrix $T_{l=\phi_0\rho_0}$.

High voltage supplies and conditioning

The high voltages for the electrodes of the MARA deflector will be created with F.u.G high-voltage supplies. Some of their parameters are given in table 2.6. In order to reduce the capacitance of the system, the HV supplies are planned to be positioned around the deflector so that the distances to the electrodes are minimized. The total width of the vacuum tank and two HV supplies is about 3.7 m in minimum. For comparison, the width of the MARA cave is 8 m which leaves free space of about 2 m on both sides of the HV system. For security reasons the deflector area and the HV supplies need to be enclosed.

Contrary to the magnets, the raising of the electric field in the deflector may require a relatively long time. Spolaore et al. [Spo88] have studied the conditioning of electrode pairs: a) aluminum cathode and stainless steel anode and b) a pair of titanium electrodes. The distance between electrodes was $2G_0 = 15$ cm in their study. The first conditioning of the electrodes to the total voltage of $2V = 500$ kV took about 20–30 h depending on the electrode materials. A design of a compact HV multiplier stack closer to the electrodes of the LNL recoil mass spectrometer is described by Beghini et al. [Beg91]. The conditioning of electrodes is generally done so that the HV is increased with a constant rate $\Delta V/\Delta t$ while observing the current I. If the current exceeds some limit I_L then the HV is decreased, for example by one ΔV. In addition, if a larger discharge current limit, I_D, has been exceeded the HV is reduced more. The conditioning of CARP electrodes is described in [Mor92]. They use values $\Delta V = 30$ V, $\Delta t = 0.1$ s, $I_L = 50$ µA, $I_D = 150$ µA. In the case of a discharge they reduced the HV by 0.2%.

The HV supplies will be delivered to Danfysik in the spring at 2012, after the deflector has been fabricated. Probably the supplies will be tested first by Danfysik.

Ray tracing of a reference particle

The electric field of the deflector has been solved with the Comsol multiphysics analysis programme [COMSOL], which uses the *finite element method*. The geometry of the problem (i.e. the vacuum chamber, electrodes and shims) was drawn with QCad and imported to Comsol. The solution which is the solved electric potential at triangle mesh nodes and the mesh triangles itself were exported from Comsol to an ASCII file for later analysis.

A special tracking programme which traces a charged particle in the solved mesh has been compiled. Since the electric field can be calculated from the potential as $\boldsymbol{E} = -\boldsymbol{\nabla} V(\boldsymbol{r})$, it is constant inside a mesh triangle. This leads to the (non-relativistic) equation of motion

$$\boldsymbol{r}(t) = \boldsymbol{r_0} + \boldsymbol{v_0} t + \frac{1}{2}\frac{q\boldsymbol{E}}{m} t^2 \tag{2.22}$$

inside a triangle. The tracking proceeds triangle by triangle. This is done by calculating the intersections of the parabolic trajectory (2.22) and the three edges of the triangle where the particle is at that moment. The intersection point having smallest positive time t_1 is chosen to be the next starting point. The triangles have information about their neighbours and thus it is easy to change the current triangle according to the edge of the intersection. The new velocity is calculated as $\boldsymbol{v_1} = \boldsymbol{v_0} + q\boldsymbol{E}/m\, t_1$.

The electric potential of $V = 134.629$ kV calculated with equation (1.30) was used in the electrodes. This value gives the correct non-relativistic radius of curvature for the reference particle which has a kinetic energy of $E_k = 100$ MeV *inside* the deflector on the optical axis. In contrast to the earlier discussion, in the tracking simulation the reference particle was set initially on the optical axis in the middle of the deflector and then tracked backwards out from the deflector.

In the first step a suitable grid density and the tracking method were studied with the geometry shown in figure 2.32. It should be noted that the electric field in this step is solved for a 10° sector of the cylindrical condenser which means that Neumann boundary conditions have been applied to the left and righ boundaries of the mesh. The solved area extends from the angle of 80° (on the left in the figure) to 90° (on the right) as seen from the centre of curvature which is positioned at $P = (0, -4000)$ mm.

The solutions with five different mesh sizes have been studied in two ways. First the radial electric field along the optical axis was compared to the analytical solution of equation (1.27). Next the trajectory tracking precision was studied by tracking the reference particle initially positioned at the optical axis corresponding to the angle of 80° with the initial velocity pointing to the negative optical axis, until it reached the angle 90° (y-axis in figure 2.32). Then

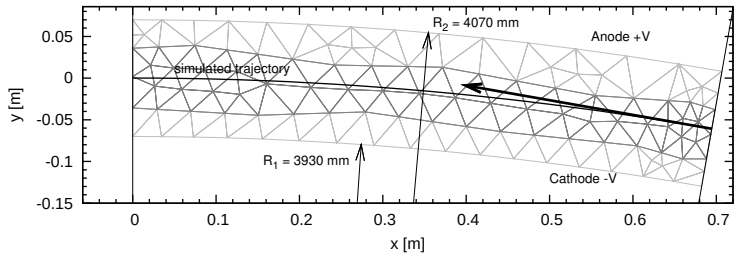

Figure 2.32: Trajectory of the reference particle between the electrodes of a sylindrical condencer. The starting point lies in the middle of the deflector on the optical axis and the initial velocity vector has been set parallel to the optical axis. The inner triangle mesh shown with darker gray visualizes the area where denser meshes have been used in other trajectory calculations.

the end positions of the reference particle and its velocity vector directions at the y-axis intersection of its trajectory were compared to the known trivial values for different mesh sizes. The results of these calculations are listed in table 2.7. The coarsest grid consisted of only 8 triangles but gives already good results. The maximum field deviation from analytical solutions is small and the end position deviates only 0.043 mm. However, this very coarse mesh gives an imprecise angle, 1.2 mrad, at the end.

Apart from the coarsest mesh case, the area was divided into two mesh regions in order to avoid the optical axis to be in the boundary of a triangle front which could cause numerical instability. These regions are shown in figure 2.32 with lighter and darker grays. The edges of the inner mesh region were drawn freehand in the CAD programme. According to the listed results, the two densest meshes could be used for the analysis of deflector geometries.

Fringing field and effective field boundary

In the ideal case the electric field would ramp up from zero to a full value in the beginning of the electrodes. The transfer matrix method describes elements of this kind. Luckily, the transfer matrix method can be still used if the electrodes are modified in such way that the element has an effective field boundary (EFB) at the position where the ideal field would begin. In the case of the electrostatic deflector it means that the electrodes need to be shortened because the fringing field extending from the area between electrodes already bends ions. Otherwise the ions would be bent more than designed. A long fringing field causes also the particle not to cross the EFB perpendicularly. This can be corrected by shifting the element perpendicularly to the optical axis.

Table 2.7: Comparison of different mesh densities. The *visited triangles* means the number of triangles coinciding with the optical axis in this case. The maximum field deviation has been calculated along the optical axis and is expressed relative to the analytic value. The end position and the angle refer to the error of position and angle at the point where the trajectory intersects with y-axis in figure 2.32. This figure shows the case of the second coarsest grid.

Average triangle area [mm^2]	Visited triangles	Max. field deviation [%]	End position	End angle
10855.1	8	0.0375	$-4.3 \cdot 10^{-5}$	$1.2 \cdot 10^{-3}$
539.903	39	-0.2115	$1.2 \cdot 10^{-4}$	$-3.4 \cdot 10^{-3}$
135.554	79	-0.0471	$9.6 \cdot 10^{-6}$	$-7.1 \cdot 10^{-5}$
33.9248	159	0.0039	$-1.1 \cdot 10^{-6}$	$4.2 \cdot 10^{-6}$
8.48348	319	0.0025	$1.4 \cdot 10^{-7}$	$-4.1 \cdot 10^{-6}$

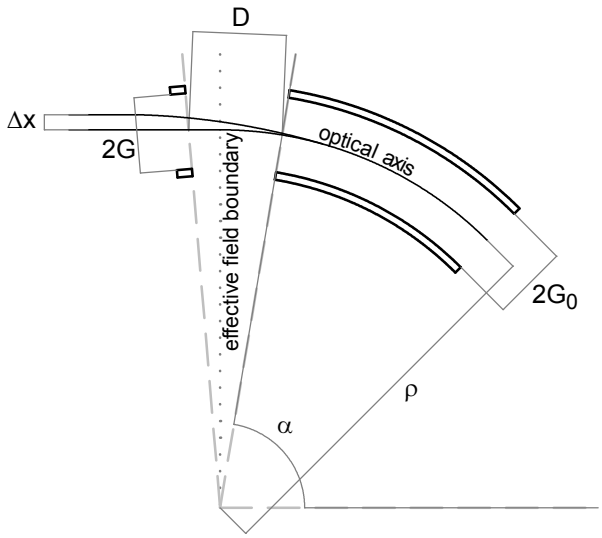

Figure 2.33: Exaggerated geometry of deflector electrodes, field shunts and optical axis.

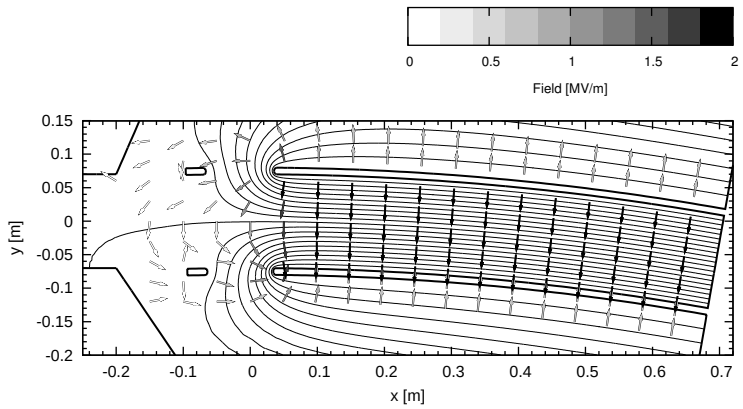

Figure 2.34: Potential contours (0, ±10%, ±20%, ..., ±90% of $V = 134629$ V) and some electric field vectors in the case of the electrode starting angle being $\alpha = 89.5^\circ$. The strength of the field is coded with the intensity of gray.

The goal of the particle tracking exercise was to find a geometry which produces the real bending angle of 20° with a fixed distance between the eletrodes and the field shunts. In this study this distance was fixed to a value of $D = 100.0$ mm. The gap between the shunts, $2G$, was fixed to be the same as the gap between the electrodes, $2G_0$. An exaggerated geometry of the problem is represented in figure 2.33. The location of the shunts and distance D are defined in the figure. The shunts are set on the slant with respect to the line of the effective field boundary. A More realistic geometry, equipotential contours, some electric field directions and the coordinate system of the particle tracking are shown in figure 2.34 in the case where the electrode starting angle is $\alpha = 89.5^\circ$.

The trajectory of the reference particle was traced for different electrode starting angles α ranging from 89° to 90°. The tracking was started at the optical axis in the middle of the deflector and the initial velocity was set in the direction of the negative optical axis. The tracing was stopped when the particle reached the left boundary of the mesh at $x = -0.3$ m. In figure 2.35 the a) angle and b) parallel shift of the particle at $x = -0.3$ m are presented as a function of electrode starting angle α. The angle of the particle relative to the negative x-axis at the end of the particle's trajectory seems to be directly proportional to α and diminishes at $\alpha \approx 89.5$. The shift, i.e. y-coordinate, at $x = -0.3$ m behaves also linearly and has a value of $\Delta x = 0.40$ mm when $\alpha = 89.5^\circ$. Based on these results the total angular length of the electrodes should be 19.0° if the shunt distance of $D = 100$ mm is chosen. The shift of 0.4 mm is insignificant and can be neglected according to sensitivity calculations which have been carried out.

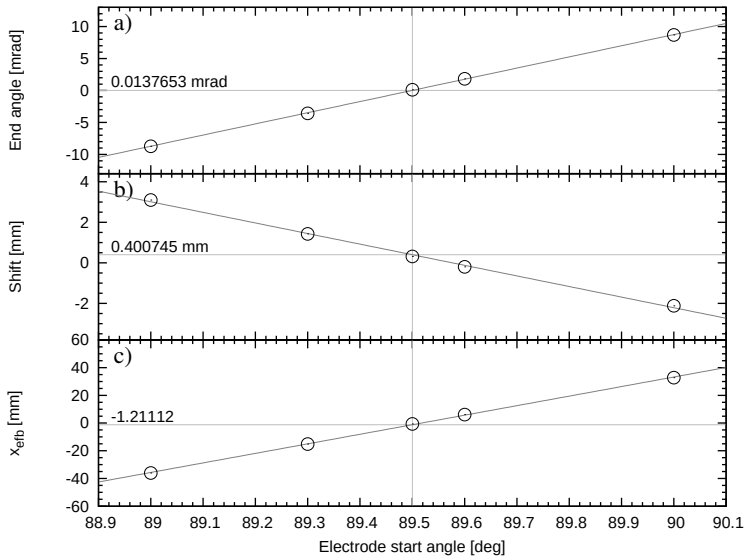

Figure 2.35: Results of the optimization of the angular length of the electrodes. a) The end angle of the reference particle ($\tan^{-1}(\Delta x/\Delta y)$, particle moving towards the negative x-axis), b) y coordinate at $x = -0.3$ m and c) the difference between the EFB and the designed EFB as a function of electrode start angle.

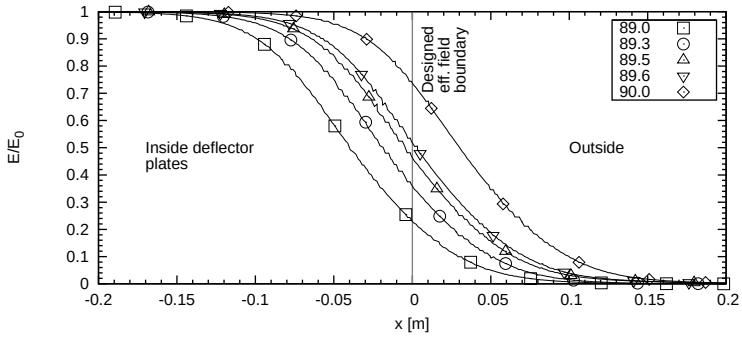

Figure 2.36: Perpendicular electric field, $E_\perp$, relative to the nominal field, E_0, along the optical axis with different electrode lengths. Contrary to other figures and the text, x is here relative to the designed EFB and measured along the trajectory.

The EFB position can also be integrated from the electric field component perpendicular to the optical axis, $E_\perp(x)$, and performing the integration from well inside the deflector to the ground potential outside the deflector along the optical axis. Let x_0 and x_1 be coordinates at the optical axis inside and outside the electric field, respectively. Then the coordinate of the effective field boundary x_{efb} is

$$x_{\mathrm{efb}} = x_0 + \int_{x_0}^{x_1} \frac{E_\perp(x)}{E_0} dx, \tag{2.23}$$

where E_0 is the magnitude of the electric field given by the equation (1.27) at the optical axis. The perpendicular field components for different electrode lengts are shown as a function of distance to the designed EFB (line $x = 0$ in figure 2.34) in figure 2.36. By choosing $x_0 = -0.2$ cm and $x_1 = 0.2$ cm one can observe that for $\alpha = 89.5^\circ$ equation (2.23) yields $x_{\mathrm{efb}} \approx 0$. The $x_{\mathrm{efb}}(\alpha_i)$ for different start angles is given in figure 2.35 (c). The difference $x_{\mathrm{efb}}(\alpha = 89.5) = -1.2$ mm is close to zero and can be approved. As a conclusion, the integration method and requiring the perpendicular end angle of the trajectory relative to the EFB produce the same result: $\alpha = 89.5^\circ$.

The values of α and the shift have been estimated also by using the equations and graphs given in [Wol87a]. Those yield $\alpha = 89.43^\circ$ and a shift of 0.42 mm which are sufficiently close to those obtained by particle tracking.

Split anode

The separation of the primary beam and fusion evaporation residues (recoils) takes place in the electric field of the deflector. The electric rigidity ratio between the primary beam and the recoil, $\chi_{\mathrm{E,beam}}/\chi_{\mathrm{E,recoil}}$ varies between 2.1–6.8 for the reactions listed in the section 2.8. The smallest ratio, about 2.0 when using a little bit thicker target than in the table, is obtained in the case of the inverse reaction ^{92}Mo+^{54}Fe. The corresponding magnetic rigidity ratio is about 1.2 for this reaction. The comparison of the magnetic and electric rigidity ratios confirms that the electric deflector is an ideal element for separation of the primary beam and the products.

The MARA deflector is long enough so that the primary beam will hit the anode which can be problematic. In order to avoid elastic scattering from the anode and also to protect the anode's surface it will be split horizontally into two pieces or at least a long slit will be provided for the beam. The dimensions of this gap and effects arising from the disturbed field will be discussed in the following. A slit anode is used at least in HIRA [Sin94] and in CARP [Mor92]. The problem is addressed also at FMA [Sew09a].

The geometry of the deflector and its surroundings are best represented in figure 2.2. The lowest $\chi_{\mathrm{E,beam}}/\chi_{\mathrm{E,recoil}}$ ratio corresponds to the smallest radius

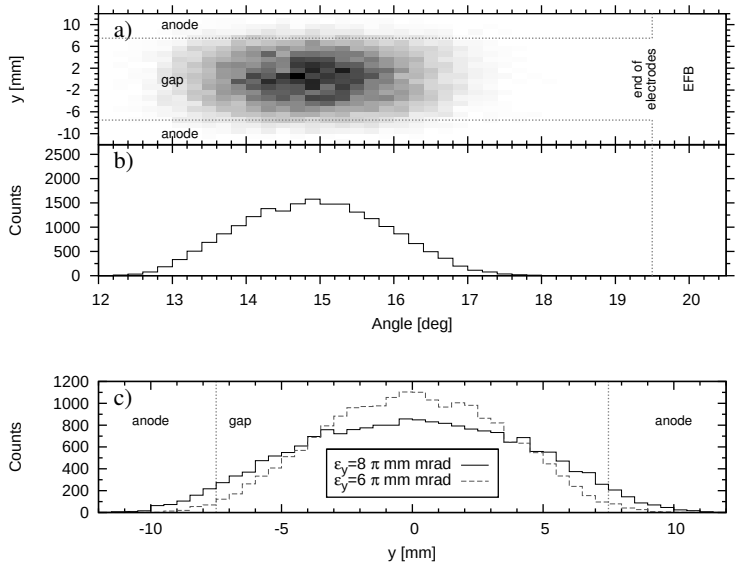

Figure 2.37: a) Spatial hit distribution of the ^{92}Mo beam at the anode as a function of the angular distance along the deflector and the vertical coordinate. Panels (b) and (c) show the one dimensional projections of (a). The emittances of $\varepsilon_x = \varepsilon_y = 8\ \pi$ mm mrad have been used with $|x_0|_{\max} = 1.0$ mm and $|y_0|_{\max} = 1.5$ mm. Additionally, the case with $\varepsilon_y = 6\ \pi$ mm mrad is shown for comparison in panel (c).

of curvature of a beam particle in the deflector, and hence the Mo beam in the ^{92}Mo+^{54}Fe reaction will hit closest to the deflector exit. The hit region of the Mo beam at the anode has been estimated with graphical inspection by using arcs of circles having radii of 8.0 m and initial full width of 20 mm for the parallel beam at the entrance EFB of the deflector. This inspection results in the hit region being between 13.6° and 16.4° (0° and 20° correspond to the entrance and exit EFB, respectively).

To get a more precise hit pattern, first order transfer matrices were used to transfer a ^{92}Mo beam from the ^{54}Fe target (thickness $d = 0.5$ mg/cm^2, thicker than in table 2.8) to the exit EFB of Q_3 and then ^{92}Mo particles were tracked in the electric field by using the methods described above until hitting the anode surface. The matrices were calculated with the GICOSY code in order to take the quadrupoles' fringing fields into account. In the simulation a beam emittance of $\varepsilon_x = \varepsilon_y = 8\ \pi$ mm mrad and a distribution shape similar to 2.2 were used with beam spot size $\pm 1.0 \cdot \pm 1.5$ mm^2 (horizontal and vertical minor radii). In addition to this distribution, two independent random numbers sampled from a Gaussian distribution having $\sigma = 1.3$ mrad were added to the horizontal and vertical angles in order to simulate the angular scattering in the

target. The sigma value of the scattering has been fitted from the distribution produced by the TRIM code. The energies of the beam particles were sampled from the uniform distribution $E_k \sim \mathcal{U}(465.3, 474.7)$ MeV and the charge states were selected from distributions described by equations (1.38) and (1.40). The results of this simulation are represented in figure 2.37 which shows that the beam will hit the anode in the range 12°-18°.

The height of the gap in the anode has been designed to be 15 mm. The FWHM value of the vertical hit distribution is 12 mm and about 7% of beam intensity will hit the electrode. If the vertical emittance of the beam is cut down to $\varepsilon_y = 6\ \pi\,\mathrm{mm\,mrad}$ by limiting the maximum angles to ±4 mrad then the HWHM will be 9.2 mm and only about 2% of the particles would hit the electrode. The vertical distribution in this smaller emittance case is also shown in figure 2.37 (c).

According to the simulation of the ^{92}Mo beam in this inverse kinematics reaction having the smallest rigidity difference compared to the product, the region from 18° until the end of the anode at 19.5° will not be reached by the beam particles. Therefore, it is possible to close the gap at the end which would enhance the mechanical strength of the anode.

In figure 2.38 the corresponding beam hit distribution is shown for the reaction ^{48}Ca+^{208}Pb used to produce ^{254}No. For this reaction the electric rigidity ratio is as large as 6.8. Thus the radius of curvature of the beam in the deflector will be around 27 m. The figure shows that the hit distribution extends from 9.8° to 13.4°. Both horizontal and vertical hit distributions are narrower in this case than in the inverse reaction examined but still a few percent of beam would hit the anode even if the vertical emittance is reduced. In the simulation, parameters $\varepsilon_x = \varepsilon_y = 8\ \pi\,\mathrm{mm\,mrad}$ (and $\varepsilon_y = 6\ \pi\,\mathrm{mm\,mrad}$), $d = 0.5\ \mathrm{mg/cm^2}$, $\sigma_{\mathrm{scatter}} = 1.8$ mrad and $E_k \sim \mathcal{U}(213.8, 218.2)$ MeV have been used.

In order to avoid scattering from the anode surface the demands on the beam alignment are crucial. The effects of misaligned beam have been studied briefly in the case of the ^{92}Mo beam. A nonzero horizontal incoming angle will move the centre of the horizontal hit distribution but will not affect the vertical distribution significantly. A vertical incoming angle will move the vertical distribution substantially: the addition of 2 mrad to the vertical angle would move the distribution by almost 3 mm vertically and increase the amount of particles hitting the anode by up to around 9% (2% for the aligned beam) if $\varepsilon_y = 6\ \pi\,\mathrm{mm\,mrad}$ is adopted. The vertical offset does not seem to have any significant effect on the vertical hit position.

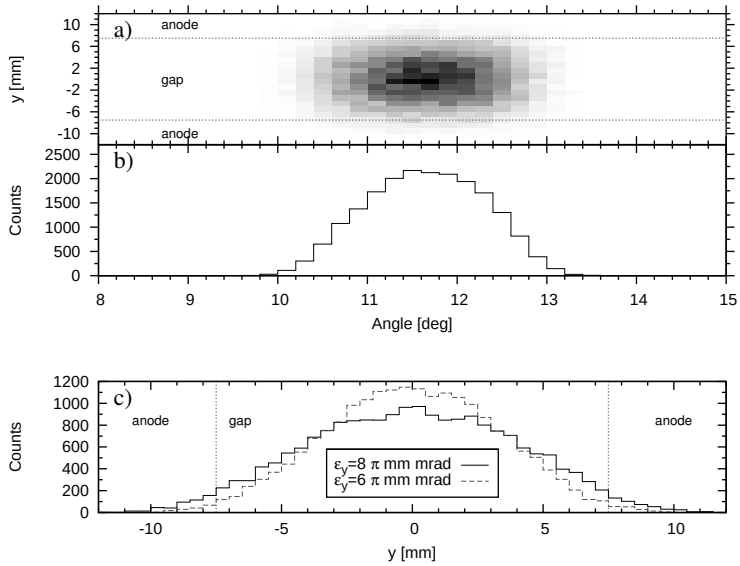

Figure 2.38: Spatial hit distribution of the ^{48}Ca beam on the anode as a function of the angular distance along the deflector and the vertical coordinate. Panels (b) and (c) show the one dimensional projections of (a). The emittances used are the same as in figure 2.37.

Sensitivity analysis and the split anode

The trajectories of the reference particles have been analysed over the chosen geometry ($\alpha = 89.5°$) with different electric field strengths. Due to the symmetry of the deflector the tracking through the whole deflector was performed by reflecting the particle at the mesh boundary on the right hand side in figure 2.34. The tracking was started and stopped 30 cm before and after the deflector EFB, respectively. Results, the end position and the end angle, for 9 different field deviations are presented in figure 2.39. It shows also the lines fitted into the data. Since the radius of curvature of a trajectory is proportional to the particle's energy (in E-field) and to the electric field strength, the change in the field is analogous to the corresponding change in the particle's energy. Therefore, also the matrix formalism can be used to calculate the presented slopes. The analogous transfer matrix in the horizontal direction is $\mathbf{T} = \mathbf{T}_l\mathbf{D}_E\mathbf{T}_l$ where $\mathbf{T}_l$ represents a drift length of $l = 30$ cm and $\mathbf{D}_E$ is the deflector transfer matrix (eq. (2.21)). The multiplication results in $(x|\delta_K) = -0.3393$ and $(a|x) = -0.3351$. These values are in close agreement with the fitted slopes.

The nominal dispersion of MARA is 8.1 mm/%. The dispersion value can be

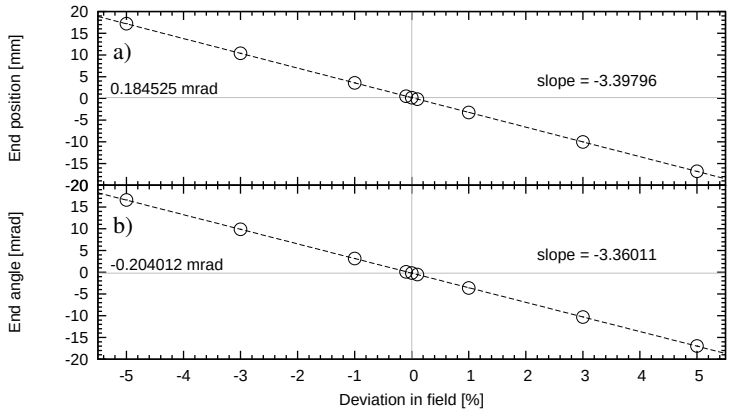

Figure 2.39: Effects of the relative difference in electric field on a) the position and b) the angle of the reference particle after the deflector. Data points have been calculated by tracking the particle (def. (2.1)) over the chosen deflector geometry surrounded by 30 cm drift lengths on both sides.

used to set the lower limit for the electric field homogeneity. The worst case is that the deviation of a real field from the ideal field is a function of the radius. Then the force acting on a particle is too weak or too strong over the deflector and the effect is accumulated. The transfer matrix describing the optical system from the point located 30 cm after the deflector exit EFB to the focal plane (in x-direction) is $\mathbf{T}_{l=0.5}\mathbf{D}_{\mathrm{M}}\mathbf{T}_{l=2.058}$. The interesting transfer coefficients are $(x|x) = 0.00278$ and $(x|a) = 2.407$. The latter is clearly dominating which means that the end position of a particle depends strongly on the angle after the deflector. The fitted slopes of figure 2.39 and transfer coefficients of $\mathbf{T}_{l=0.5}\mathbf{D}_{\mathrm{M}}\mathbf{T}_{l=2.058}$ yield together the estimate $\Delta x = -0.8097\Delta E/E_0$ m, where Δx is the horizontal shift of the particle at the focal plane caused by the relative deviation in the deflector field (this is naturally the same as the mass dispersion for non-relativistic particles). It means that a 1% deviation in the field corresponds to a shift of 8 mm. Therefore it can be concluded that in the active region of the deflector the radial component of the electric field should deviate less than 0.1% from the ideal value given by the equation (1.27). The active region extends vertically from $y = -50$ mm to $y = 50$ mm as shown in figure 2.5. Figure 2.40 presents the geometry which has been utilized to study the distortions of the electric field due to the split anode and the finite height of the electrodes.

The electric field with different electrode heights ($2L_1$ in figure 2.40) and radii of the shunt of the split anode (R_2) has been solved with the Comsol code. In all calculations the electrodes were 20 mm thick and had electrode roundings

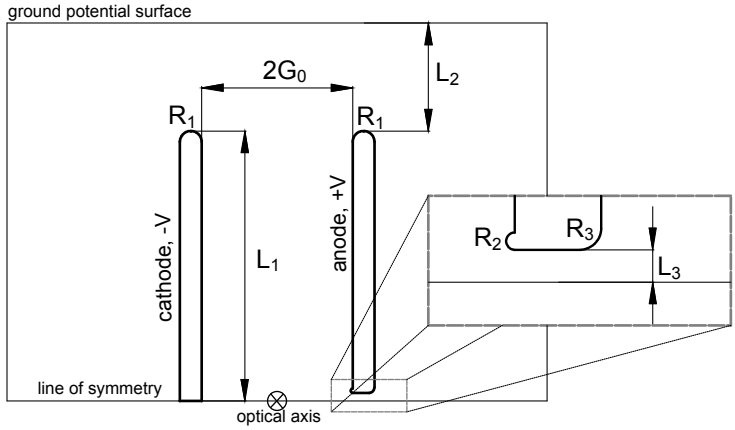

Figure 2.40: The cross sectional view of the deflector electrode geometry used in the electric field simulations. The optical axis is at the center of the line of symmetry and points towards the paper.

of $R_1 = 10$ mm. The distances from electrodes to the top and the bottom of the chamber being in the ground potential was fixed to $L_2 = 100$ mm.

The required electrode height was studied first. Figures 2.41 and 2.42 show the relative deviations of the radial field component, $E_x(r, y)$, from the ideal $E_{\text{ideal}}(r)$ and also the vertical component $E_y(r, y)$ values relative to $E_{\text{ideal}}(r = 4.0$ m). According to the results the minimum electrode height is $2L_1 = 40$ cm. However, a height of 50 cm would be a safer choice.

The field distortion caused by the split anode can be minimized by adding a suitable field shunt right below and above the gap as illustrated in figure 2.40. The effects of semicircle shaped shunts with varying radius R_2 have been calculated. The results are shown in figure 2.43 which suggests that the optimum radius is around $R_2 = 2$ mm. More precise calculations and optimisation will be carried out in collaboration with Danfysik A/S during the design phase of the deflector. It is clear that in any case the field distortion is too severe close to the gap and this area needs to be shielded.

The recoils whose electric rigidity is close to the rigidity of a reference particle will have trajectories parallel to the electrodes in horizontal direction. In vertical direction all trajectories are slowly focusing. Therefore a physical obstacle should be placed in the vacuum chamber between the Q_3 and the deflector so that the ions cannot enter the disturbed field area. However, the ions can enter this field area if they have larger electric rigidity than the reference particle has. Therefore a physical obstacle should be added also right after the deflector.

The vertical component of the electric field is not as important as the hor-

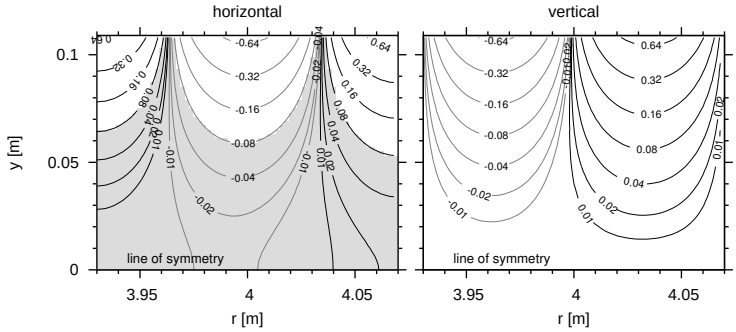

Figure 2.41: Relative deviation (in %) of the radial field component from an ideal field, $[E_x(r, y)/E_{\mathrm{ideal}}(r) - 1]$, (left subfigure) and the magnitude of the vertical component normalized by $E_{\mathrm{ideal}}(r = 4.0\ \mathrm{m})$ (right subfigure) in a geometry described by the parameters $R_1 = 10$ mm, $L_3 \equiv 0$, $L_1 = 200$ mm and $L_2 = 100$ mm. The gray area represents the region with acceptable deviation in the horizontal case.

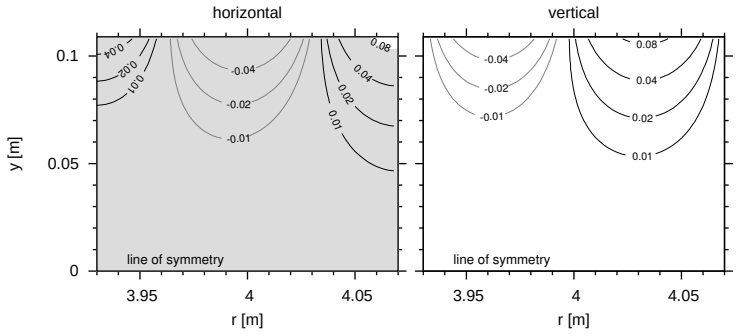

Figure 2.42: Same as figure 2.41 except for $L_1 = 250$ mm.

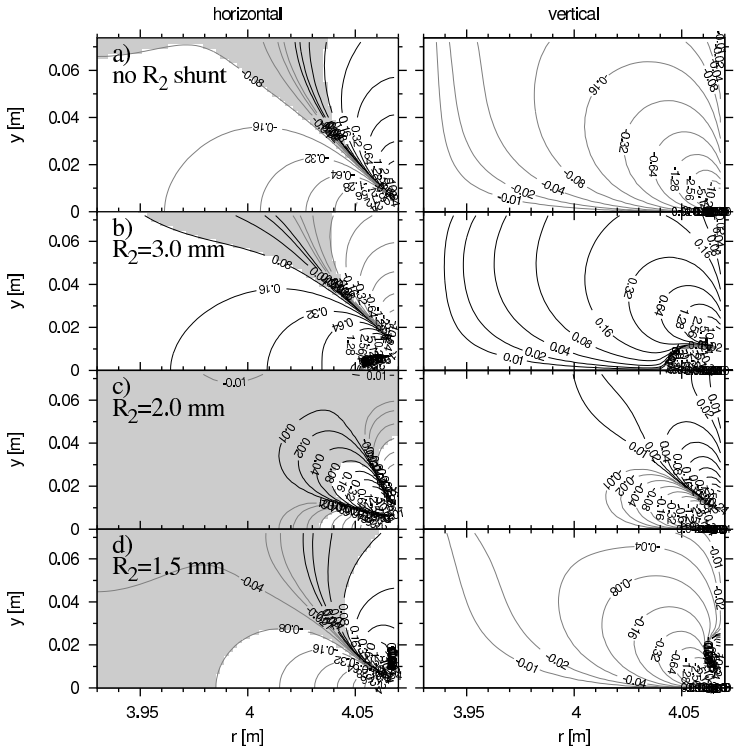

Figure 2.43: Effect of the radius of a semicircular field shunt near the anode gap on the goodness of the field. The half height of the electrodes is $L_1 = 250$ mm. See figure 2.41 for additional information about the graphical representation.

izontal component since it does not affect the resolving power. With non-relativistic kinematics a reference particle (energy E_k and mass m) needs the time $t = \sqrt{\phi_0^2 \rho_0^2 m/(2E_k)}$ to fly through the deflector (radius of curvature ρ_0 and deflection angle ϕ_0). Let the vertical field component be $E_y = fE_{\mathrm{ideal}}(r = \rho_0)$ where f is a dimensionless factor. This field causes a vertical shift of about $\Delta y \approx f\phi_0^2\rho_0/2$. For the MARA deflector this estimation yields $\Delta y = 0.24f$ m. The change in vertical velocity due to E_y is $\Delta v_y \approx \sqrt{2E_k/m} f\phi_0$. This leads to the change of $\Delta\beta \approx \Delta\tan(\beta) = f\phi_0 \approx 0.70f$ in the vertical angle. The relevant transfer coefficients in y-direction from the exit EFB of the deflector to the focal plane are $(y|y) = 0.5483$ and $(y|b) = 3.0594$. Those values have been calculated with the GICOSY code in order to take the horizontal gap of the magnetic dipole into account in fringing field matrices. Combining these, a vertical shift of

$$\Delta y_{\mathrm{fp}}(f) \approx 2.3f \text{ m} \tag{2.24}$$

at the focal plane caused by nonzero $E_y = fE_{\mathrm{ideal}}(r = \rho_0)$ is obtained. According to figure 2.43 (c) the maximum absolute value for f is less than 0.1% in the active region which translates to the maximum vertical shift of 2.3 mm at the focal plane.

Since the horizontal primary beam gap will extend only from about 9° to 18° (not decided yet) the effects of the gap on the mass resolution and spreading of the vertical image will be smaller than estimated here. In practice, this means that the shadowing obstacles around the deflector can be smaller than figure 2.43 (c) implies. However, it should be noted that the values of the contours in the figure are not linearly spaced.

There are many other studies that are not reported here to be done before fixing the design of the deflector. These are among others: 1) optimal distance between the electrode and the chamber in vertical direction (L_2), 2) analysis of maximum fields and 3) sensitivity analysis about misaligned electrodes. Some of these studies have been carried out and others will be performed for geometries to be suggested by Danfysik A/S.

2.6 Sensitivity analysis

The misplacement or misalignment of an optical element or elements can cause a significant effect on the performance of an entire optical system. It is also possible that the field strength in a quadrupole or in a sector field element deviates from the optimal. The so called *sensitivity analysis* should stress the most critical points where for example the alignment precision or field homogeneity requirements are important. The results of such a study can be exploited if for example the image of a set of particles with known rigidities is not centred at the focal plane in either direction.

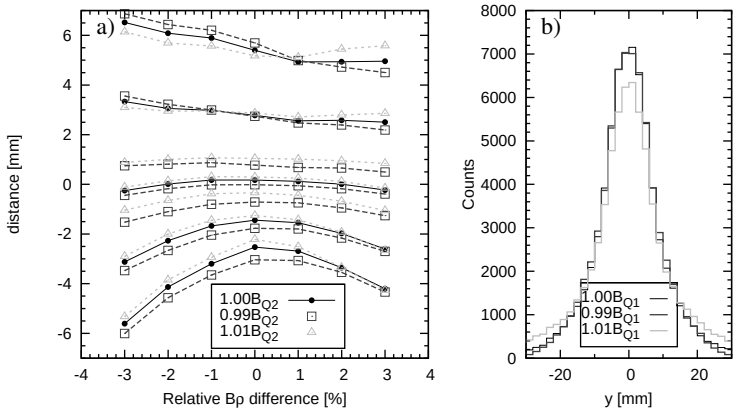

Figure 2.44: a) Position percentiles (1%, 10%, 31.7%, 50%, 68.3%, 90% and 99%) of mass peaks at z_{fp} as a function of magnetic rigidity and b) vertical position spectrum in cases where the field strength of Q_2 is changed by $\pm 1\%$. The percentiles 31.7% and 68.3% are not shown for the reference case. In (a) lines are drawn between the data points for given percentile to guide the eye.

A simple sensitivity analysis has been carried out for MARA elements one by one. The effects of different physical misalignments and slightly wrong field values on the mass resolution and vertical image size have been studied. In the analysis the standard reference particle (2.1) and the test distribution (2.2) have been used with the exeption of $\delta_K \sim \mathcal{U}(-0.07, 0.07)$ and $m \in \{97, 98, ..., 103\}$. In total 70000 particles were transported over MARA optics to the focal plane. The shapes of all mass peaks were analysed by determining the position of percentiles 1%, 10%, 31.7%, 50%, 68.3%, 90% and 99% of the ordered set of distances $x_i - \delta_m \mathcal{D}_m$.

First the effect of quadrupole field strengths being $\pm 1\%$ off were studied. It turned out that this offset in B_{Q1} does not affect the m/q resolution significantly. The $\pm 1\%$ offset in B_{Q2} or in B_{Q3} has a larger but still acceptable effect. Actually, the offset in B_{Q2} or in B_{Q3} seems to reduce the tail on one side of the peak and simultaneously increase the tail on the other side. The effect is opposite for an opposite change in field strength. The percentiles are shown in the case of Q_2 in figure 2.44.

The effect of a physically misaligned element has been analysed by introducing a sudden offset in one of the coordinates x, a, y or b just before the element. This is analogous to shifting (coordinates x and y) or tilting (coordinates a or b) of the rest of MARA. Some results are given below. The primary beam should be aligned in about 2 mrad presicion in x-direction. In y-direction the beam alignment is important only because the beam should pass the split anode.

The beam spot should be centered in sub-mm accuracy in x-direction. A shift of 1 mm in the beam's y-position did not cause practically any observable effect. The general observation from other misalignment tests is that the mass resolution is not degraded substantially for a misalignment of a few mrad in angle or 1 mm in position. However, some misalignments of this size can shift the position distribution in x- or y-direction. Due to the long focal length of the quadrupole triplet in vertical direction a misalignment in vertical position or angle can cause a significant shift of the vertical distribution at z_{fp}. In order to observe the misalignment in horizontal direction experimentally, the fields of the dipole elements must be set precisely to known rigidities of the particle used.

2.7 Simulated performance of MARA

In order to obtain a practical view of the performance of MARA for realistic experiments, a few fusion reactions have been simulated with the JIonO code. The behavior of cross-sections as a function of the projectile energy has been calculated with PACE4 excluding the reactions ^{24}Mg(^{40}Ca,3n)^{61}Ge and ^{208}Pb(^{48}Ca,2n)^{254}No. In those cases a constant cross-section across the target was assumed. The real yield of the fusion products can vary even a few orders of magnitude from results based on the PACE4 cross-sections. This concerns especially the weak xn channels. For the strongest channels the cross sections are assumed to be close to reality and thus the simulations can give useful information for example about background rates.

The methods of the simulation are described in section 1.5. The differential cross-section of a fusion product is naturally independent on the azimuth $\phi_0 \approx \tan^{-1}(b_0/a_0)$. However, this angle affects strongly an ion's hit position $(x_{\mathrm{fp}}, y_{\mathrm{fp}})$ at the focal plane. This fact was exploited in the simulations in order to enhance the statistics by transferring the same fusion product 100 times through MARA with random ϕ_0. The weights of the product were divided by 100.

Since most of the reactions have plenty of fusion evaporation channels open, the channel inclusion was automated in the simulation code. The code searched all active channels in PACE4 cross-section curves for the primary beam energy taking into account the energy loss of the beam in the target. The generation of the recoils for ion-optical calculations was also sped up by replacing the TRIM simulation of the target by sampling of the energy loss and scattering angle from independent Gaussian distributions. These distributions were calculated for multiple species in the populated region in the chart of nuclei with two energies. The mean value of the energy loss and standard deviations of energy loss and scattering angle were then linearly interpolated from this data set for an individual recoil. The validity of this approach has been tested against the

Table 2.8: Information about the simulated MARA reactions. The energy losses shown here are suggestive and have been calculated with SRIM/TRIM at the center of target. Δt_1 corresponds to the ToF from the target position to the focal plane ($s = 6.852$ m). For ^{254}No Δt_1 is calculated for $s = 6.15$ m. The rates reflect a beam intensity of $1 \cdot 10^{10}$ 1/s (i.e. 1.6 pnA).

Beam	^{40}Ca	^{54}Fe	^{92}Mo	^{40}Ca	^{48}Ca
Target	^{40}Ca	^{92}Mo	^{54}Fe	^{24}Mg	^{208}Pb
Main channel	2n	p4n	p4n	3n	2n
Main product	^{78}Zr	^{141}Ho	^{141}Ho	^{61}Ge	^{254}No
Int. barrier in CM/lab [MeV]	52.5/105	130./206	130./351	32.0/85.3	176/217
CN excitation at E_{int} [MeV]	38.3	31.5	31.5	37.6	24.2
Target thickness [µg/cm^2]	300	300	800	300	500
$E_{p,lab}$, E_{CM} [MeV]	117, 58.5	302, 190	502, 186	133, 55.5	221, 180
Beam ΔE [MeV/(mg/cm^2)]	18	15	40	19	9
Recoil ΔE [MeV/(mg/cm^2)]	31	36	58	37	7
Recoil energy after target [MeV]	48	102	265	71	37
Recoil energy FWHM [MeV]	7.3	12	23	12	3.3
Angular spread sigma [mrad]	26	24	15	29	35
Most abundant q-states	18, 19	28, 29	37, 38	19, 20	19, 20
Rel. abundancy of the q-states [%]	18, 19	16, 14	15, 14	20, 18	17, 17
Ref. particle: energy [MeV]	48	102	265	71	37
Ref. particle: mass [u]	78	141	141	61	254
Ref. particle: charge [e]	18.4	28.5	37.5	19.5	19.3
Ref. particle: Δt_1 [ns]	629	580.	360	458	1160*
Ref. particle: χ_E, χ_B	5.2, 0.48	7.2, 0.61	14, 0.74	7.4, 0.50	3.8, 0.72
Beam: $\bar{q}$ [e]	16.0	22.3	32.5	16.4	16.5
Beam: χ_E, χ_B	13.9, 0.60	27, 0.82	29, 0.92	15.5, 0.63	26, 0.89
Targetlike nuclei: E_k [MeV]	112	274	448	121	128
Targetlike nuclei: $\bar{q}$ [e]	16.0	29.1	23.6	11.4	30.1
Targetlike nuclei: χ_E, χ_B	13.9, 0.60	18.8, 0.79	38, 0.95	21, 0.68	8.5, 0.78
Production rate [kHz]	5.3	19	81	53	
FP rate (no slits) [kHz]	1.5	5.8	51	9.7	
FP rate (slits)	0.50	1.5	7.6	3.6	
Impl. rate (no slits)	0.78	3.3	33	4.6	
Impl. rate (slits)	0.17	0.64	4.6	2.8	
Transm. to FP/Impl. (no slits) [%]	60./30.	70./44	91/55	56/28	
Transm. to FP/Impl. (slits) [%]	30./29	27/26	27/26	28/27	

full TRIM approach in the case of a few channels and was found to be good.

The reactions studied in the following subsections should be understood to model predominantly ion optics rather than being reactions to be studied for nuclear structure. The reactions, simulation parameters and some of the results are shown in table 2.8. In a real experiment, different parameters (beam energy, target thickness, reference particle, slits and quadrupole settings) may be used. The main goal of the table is to give an overview of different fusion reactions and especially information about counting rates, required fields, transmission and rigidities of beam and target-like nuclei in comparison to those of a reference particle.

The rates in table 2.8 correspond to an initial beam intensity of $1 \cdot 10^{10}$ 1/s (i.e. 1.6 pnA). The height of the focal plane instrumentation including mass slits, transmission detector and implantation detector (DSSD) has been limited to

60 mm. The active width of the transmission detector was not limited but a width of 120 mm has been used for the DSSD. For all reactions, slits have been set to allow passing of two charge states.

For every recoil the charge state distribution was calculated with Schiwietz formulae (1.38) and (1.40) with parameters $Z_t = 6$ and $w = 0.9$. For some cases the reduced width w can be smaller than 0.9 but probably not more. For smaller w the relative abundancy of selected charge states would be higher. No carbon foil downstream from any target was used explicitly in the simulations except in the calculation of the charge state distribution. In real experiments a carbon foil placed downstream from the target will be used to reset the charge before MARA. This is important since the charge state of a recoil can be exceptionally high if the nuclear de-excitation of some isomeric state occurs after the target and causes the emission of an Auger electron cascade. The angular scattering in the reset foil increases slightly the virtual object size (i.e. beam spot size) which degrades the mass resolution. This is not taken into account in the following simulations.

2.7.1 A symmetric reaction: ^{40}Ca(^{40}Ca,2n)^{78}Zr

The symmetric reaction ^{40}Ca+^{40}Ca producing ^{78}Zr in the 2n channel has been simulated in order to study the separation properties of MARA for such a reaction. The overall fusion cross-section given by PACE4 drops from 180 mb down to about 50 mb along the target thickness. According to the measured total fusion cross-section [Tom82] the PACE4 values should be corrected by a factor 0.55–0.75 (reflecting the given errorbars). However, the uncorrected cross sections were used here.

Charge, energy and angular distributions of the ^{78}Zr and other fusion products after the 300 µg/cm^2 thick target are shown in figure 2.45. In reality, the lower limit for the thickness of the Ca target is probably more than 500 µg/cm^2. It can be seen from subfigures (b) and (c) that the distributions of the kinetic energy and the horizontal (and vertical) angle are narrower for ^{78}Zr than those for all recoils as expected. A little bit higher recoil energy and higher proton number of ^{78}Zr translate into a higher average charge state shown in subfigure (a). Clearly, if two charge states are to be collected, the reference particle should have a charge between 18–19 e in order to maximize the transmission of ^{78}Zr. These two charge states, 18 and 19, together represent 37% of all ^{78}Zr recoils. However, in a real experiment the collection of charge states 19 and 20 might be preferred because that would yield a lower background rate. As stated in table 2.8, the reference particle having parameters 48 MeV, 78 u and 18.4 e has been adopted.

Figure 2.46 shows the horizontal position distribution of the recoils at the mass

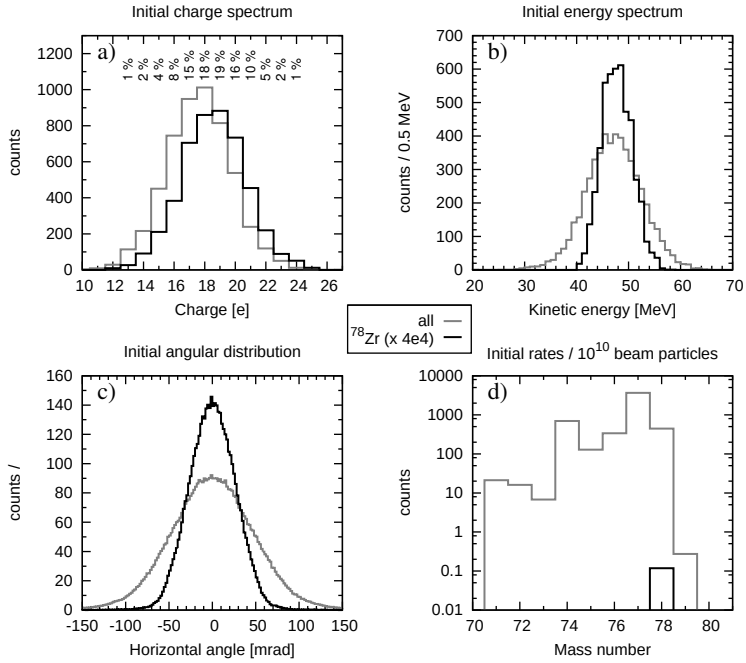

Figure 2.45: Distributions of a) charge, b) kinetic energy and c) horizontal angle (a) of ^{78}Zr (black line and multiplied by $4 \cdot 10^4$) and all relevant fusion products (gray line). Subfigure (d) shows the production rate of the recoils at the target as a function of mass number (note: ^{78}Zr counts are not multiplied). The percentage values in (a) show the relative abundancy of the individual charge states of ^{78}Zr. The number of counts reflects PACE4 cross-sections and beam intensity of $1 \cdot 10^{10}$ 1/s.

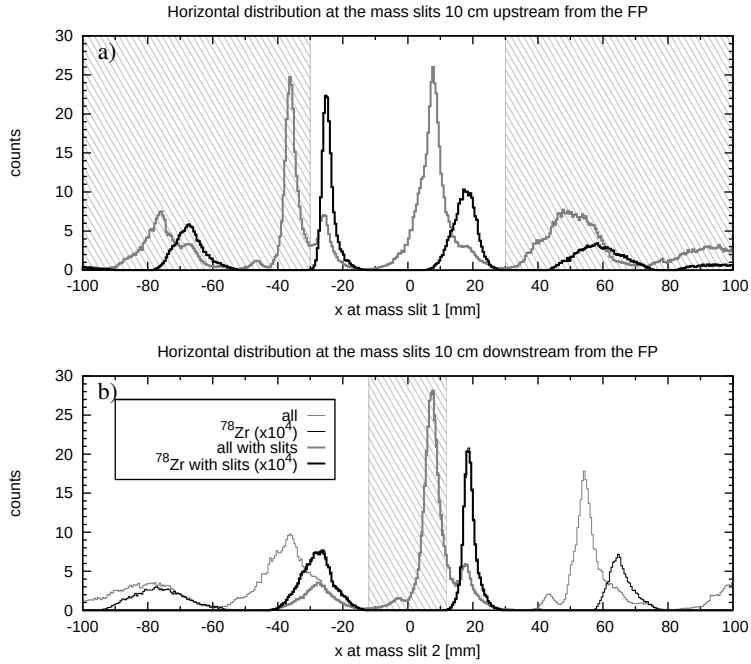

Figure 2.46: Horizontal position distributions at a) 10 cm upstream (MS_1) and b) 10 cm downstream (MS_2) from the focal plane. These are the positions where mass slits can be set. Thin lines in subfigure (b) represent recoils stopped at the first mass slits shown by (a). Recoils hitting the hatched region will be stopped.

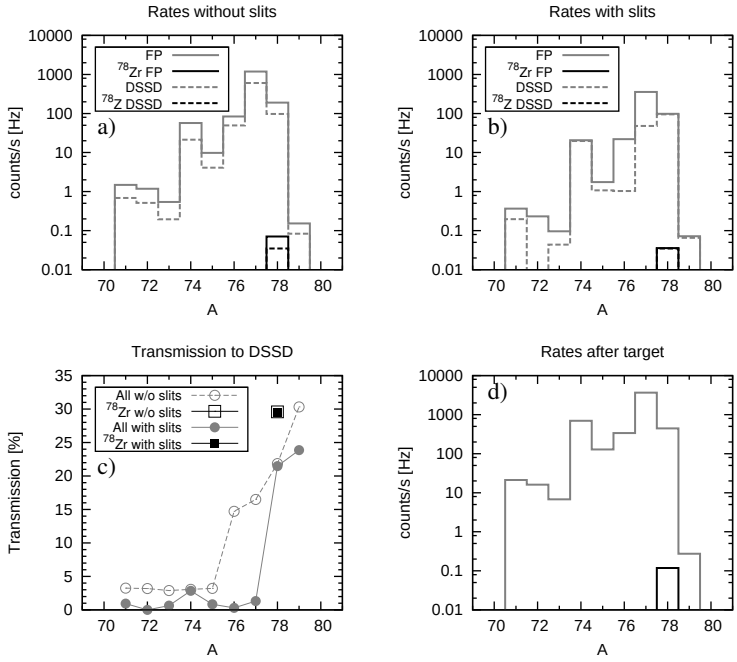

Figure 2.47: Rates at the focal plane detector and in the DSSD as a function of the recoil mass number for primary beam intensity $1 \cdot 10^{10}$ 1/s a) without and b) with the mass slits. Subfigure (c) shows transmission from the target to the DSSD in both cases. Subfigure (d) is the production rate and is shown for comparison.

slit positions a) 10 cm upstream and b) 10 cm downstream from the focal plane. The figure represents an option which allows charge states 18 and 19 of ^{78}Zr to be passed through the slits and which will cut most of the other masses. The ranges of the physical obstacles are hatched in the figure. A 60 mm wide aperture from -30 to 30 mm is opened at 10 cm behore the focal plane position (MS_1) and at 10 cm after the focal plane (MS_2) a 24 mm wide obstacle ranging from -12 to 12 mm has been set to block most of the recoils having $A = 77$ and $q = 18$ e. This peak consists mainly of ^{77}Rb recoils (channel 3p). Subfigure (b) shows with thinner lines also the recoils which are stopped at MS_1. According to the figure, this arrangement reduces the background rates at the implantation detector efficiently and most of the remaining background will be caused by pn and 2p channels.

The rates and the transmission of different masses are shown in figure 2.47. The effect of the slits on the rates can be seen by comparing subfigures (a) and (b). The largest drop in the DSSD rate, from 600 Hz down to 50 Hz, occurs for mass number 77 and is achieved with the obstacle shown in 2.46 (b). Panel

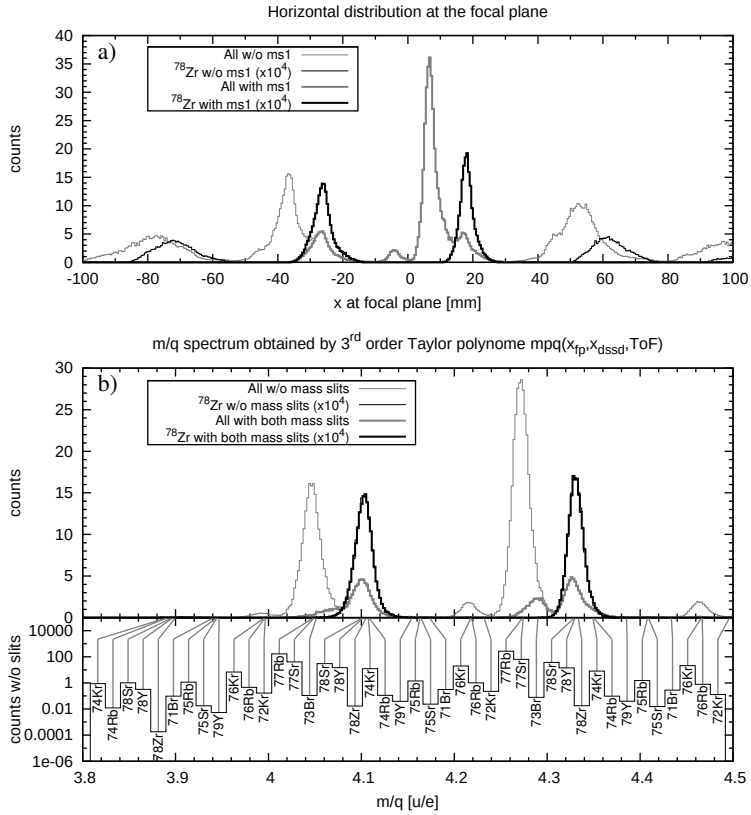

Figure 2.48: a) The horizontal distribution of recoils at the focal plane with and without the slits and b) calculated m/q spectrum with information about individual isotopes. Thin lines shows the spectra obtained without mass slits (MS_1).

(c) shows the transmission to the implantation detector with and without the slits. The slits reduce only little mass 78 but very efficiently masses 76 and 72. Mass 74 is not affected much since the m/q values are overlapping with those of ^{78}Zr. Mass 79 recoils are on purpose not obstructed with slits since the cross section is very small. However, it could be done as efficiently as the reduction of mass 77.

The horizontal distribution at the focal plane is shown in figure 2.48 alongside a corrected m/q spectrum. The panel below the m/q spectrum shows the rate of individual isotopes at the given m/q ratio. The m/q spectrum has been calculated with assumptions $\sigma(\Delta t_2) = 0.4$ ns (ToF over 40 cm), $\sigma(x_{\mathrm{fp}}) = 0.6$ mm and $\sigma(\Delta a_{\mathrm{fp}}) = 3$ mrad (see section 2.4.7). According to the m/q spectrum the neighbouring masses can be separated adequately. The mass resolving powers for the $m/q = 78/19$ peak of ^{78}Zr in figure 2.48 (b) are $\mathcal{R}_{68\%} =$

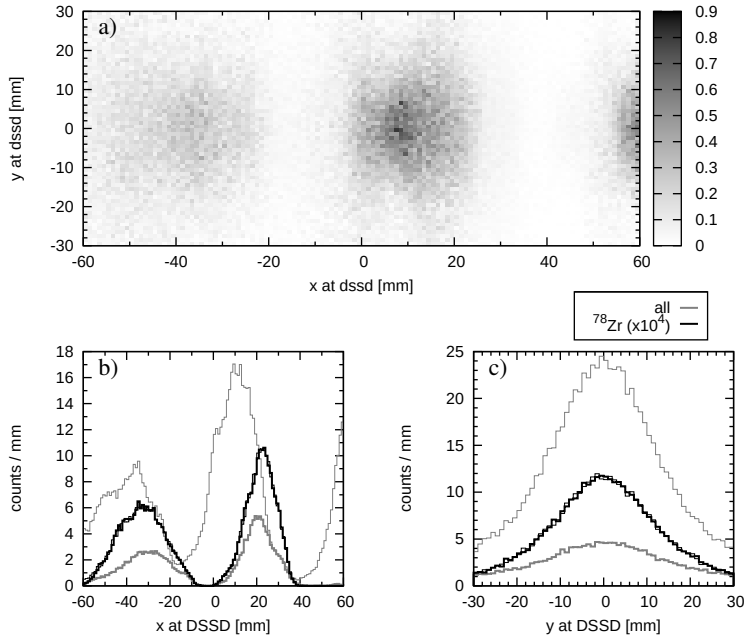

Figure 2.49: Position distribution at the DSSD. Thin lines correspond to the situation without the slits.

182 and $\mathcal{R}_{95\%} = 81$. For the rightmost peak, $m/q = 78/18$, these values are enhanced by about 20%.

Figure 2.49 visualizes the position distribution at the DSSD in both directions. It can be seen that a 12 cm wide DSSD would be enough for collection of two charge states. Due to the tilted focal plane and selected charge of the reference particle the two transmitted charge states of ^{78}Zr are not symmetrically around the optical axis in the horizontal direction. The FWHM of the image in vertical direction is about 2.6 cm and the detector height of 6 cm seems to be sufficient. The vertical image size at the focal plane (not shown) is only slightly smaller.

Method of double ToF

All isobars with $A = 78$ hit the same position at the focal plane and have the same m/q ratio as shown in figure 2.48 (b). In order to separate ^{78}Zr from ^{78}Y (pn) and ^{78}Sr (2p) the proton number must be extracted for individual recoils. This can be achieved for example by measuring the kinetic energy of a recoil before and after a degrader foil since the energy loss depends on Z. One

relatively accurate method to measure the energy—or in this case velocity—before and after the foil is to implement two subsequent time-of-flight systems around the degrader. Some results of applying such a system to the ^{40}Ca+^{40}Ca reaction are shown next.

Energy loss curves in carbon are presented in figure 2.50 for $A = 78$ isobars and ^{74}Kr as a function of incident kinetic energy. The energy loss curves are calculated with SRIM. The dE/dx values for ^{78}Zr are significantly lower than for ^{78}Y and ^{78}Sr. The difference between ^{78}Y or ^{78}Sr is much smaller than difference between ^{78}Zr and ^{78}Y. The most obvious reason for this is the way how the electron shells are filled as a function of Z. Usually a higher Z generates a higher energy loss value. Also with higher energies (i.e. $E_k/A > 1$ MeV/A) the energy losses behave more systematically. It should be noted also that in this case—as far as trusting SRIM results—the events having anomalously large energy-loss due to nuclear collisions do not cause additional background since the ^{78}Zr has the *lowest* energy loss values.

The principle of the double-ToF method has been tested for part of the recoils passing the slit system (2.46) and the DSSD aperture of 12·6 cm^2. Figure 2.51 shows results from the simulation where both time of flights have been measured over a distance of 40 cm before and after a carbon foil degrader with a thickness of 0.8 mg/cm^2 meaning that the implantation detector has been replaced by a transmission detector and the degrader. The first timing detector would be the normal transmission detector at the focal plane. Subfigure (a) shows the second ToF as a function of the first ToF while (b) shows the kinetic energy after the foil. The data do not include finite detector timing resolutions. A ToF resolution of $\sigma(\Delta t) \approx 0.2$ ns could be achieved with a pair of fast transmission detectors which is not probably good enough to separate ^{78}Zr from ^{78}Y in the figure's horizontal direction and thus a slightly longer drift length is probably needed.

The average separation between the mean values of the second ToF for a given first ToF value is large enough to be separated even with a DSSD being the third timing detector. However, the tail of the ^{78}Y recoil distribution is partly overlapping with ^{78}Zr recoils preventing a clear identification of ^{78}Zr. Probably better results could be achieved with a thinner degrader and a longer second drift length. In the case of this reaction, the maximum absolute energy difference between ^{78}Zr and ^{78}Y is achieved already with a degrader thickness ∼0.6 mg/cm^2 which would result in narrower lines relative to the line separation in the Δt_1-Δt_2 plot.

Compared to the normal DSSD position, slightly over 80% of the ^{78}Zr recoils hit inside the previously used DSSD area of 12·6 cm^2 if placed at the third detector position, 80 cm downstream from z_{fp}. The angular spreading of the recoils due to the degrader in addition to the normal divergence after the spectrometer's

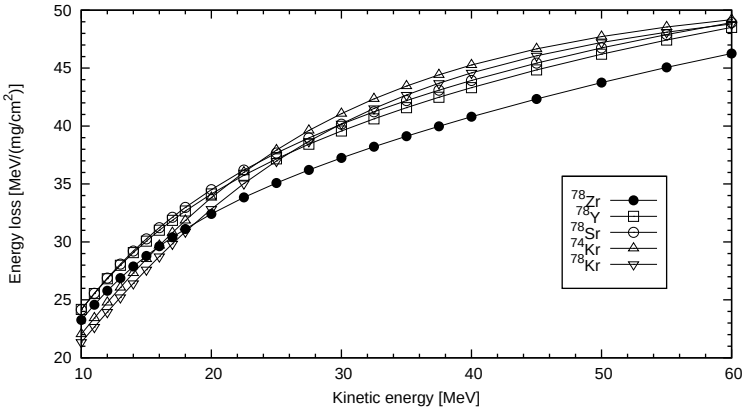

Figure 2.50: Energy loss curves in carbon for various species having overlapping m/q ratio with ^{78}Zr as a function of incident energy. Calculated with SRIM.

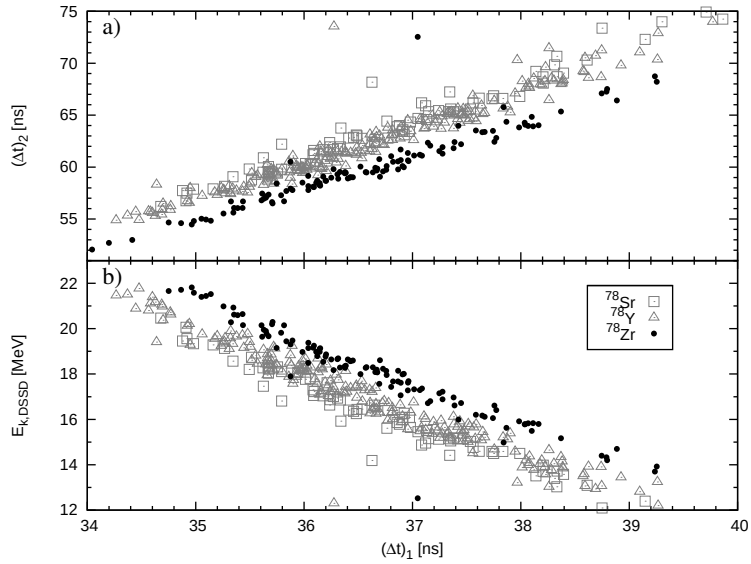

Figure 2.51: a) Second time of flight and b) kinetic energy after a 0.8 mg/cm^2 C-foil as a function of time of flight before the degrader. Finite detector resolutions are not taken into account. Flight paths have been 40 cm long for both ToF calculations. Calculated with TRIM.

focal plane sets the limits for usable drift lengths. In most cases the first detector should be as thin as possible especially if the following detector is not position sensitive. The second detector should have a good timing resolution since the same time measurement affects both time-of-flight values. The timing resolution of the last detector can be worse if the degrader is thick. In any case, the position measurement at the last detector cannot be used anymore for detection of the recoil angle at the focal plane. If this information is needed for improving m/q information the detector in the middle should be position sensitive. The incident angles increase only little the drift lengths and in this case affect the ToF resolutions less than for example the statistical energy loss variation. In most cases the placement of the first detector before the focal plane is not possible since the scattering will probably destroy the mass resolution even in the case of the thinnest transmission detector.

While the principle of the double-ToF method is quite straightforward, studies to optimize detector positions and degrader thickness in order to minimize the background events are strongly recommended for each reaction individually. It should be noted that the experimental energy loss can deviate from the one given by TRIM so that the double-ToF method would fail totally for this reaction. Probably the double-ToF method is most useful for the inverse kinematics reactions where recoils have typically more energy.

Vetoing charged particle channels

If there is a charged particle detector available around the target then the background channels including the evaporation of a charged particle can be partly vetoed in the analysis phase of an experiment. The best veto efficiency can be achieved for reactions where the nucleus under interest is produced in a pure neutron channel. In that case the recoil can be ignored if any charged particle has been observed at the target. The vetoing of the charged particle channels in the case of the reaction ^{40}Ca+^{40}Ca is discussed in the following.

Due to evaporation kinematics the angular distribution of the evaporated protons is a little forward directed. The most probable angle for an emitted proton is around $\theta = 62^{\circ}$ for both ^{78}Y and ^{78}Sr. The distributions have practically the same shape. Figure 2.52 shows the proton distributions of those ^{78}Y and ^{78}Sr recoils which have been transported up to the DSSD without the use of slits. According to the discussion in section 1.4.3 and to equation (1.62) the maximum change in the recoil angle caused by the evaporation of a proton is around 40 mrad which is less than the angular acceptance of MARA either in x- or y-direction. Therefore, the proton distributions of transmitted recoils shown in the figure have almost the same shape as those of all protons at the target. Due to the limited number of ions simulated in the target the distributions in the figure are not very smooth. In contrast, for channels including evaporation

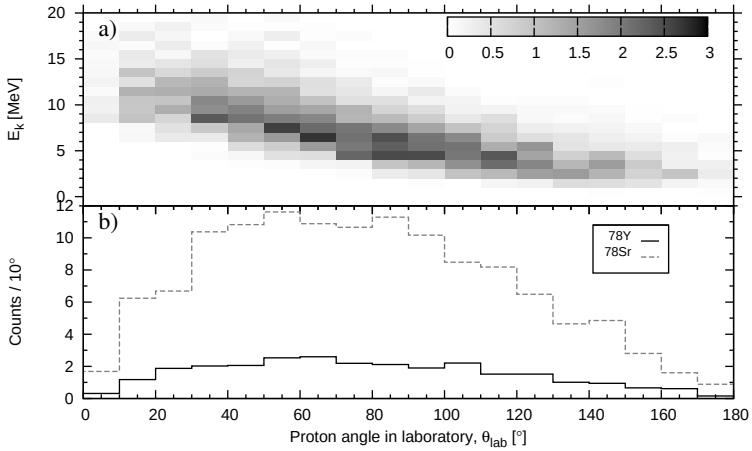

Figure 2.52: Distribution of evaporated protons from reactions ending in the production of ^{78}Y or ^{78}Sr. Only those protons belonging to recoils transmitted to the implantation detector (without slits) are taken into account. Counts correspond to $1 \cdot 10^{10}$ beam particles.

of α particles the θ_α distribution related to transmitted recoils differs significantly from the total distribution. For example only forward ($\theta_\alpha < 45^\circ$) and backward ($\theta_\alpha > 90$) emitted α particles will be seen for the transmitted ^{75}Sr (αn channel) while the most probable angle for θ_α is around 60°, same as for θ_p.

Figure 2.53 shows the effect of the detector length (symmetric opening angle of the detector seen from the target) on a) counting rate and b) vetoing efficiency. The latter subfigure shows also the efficiency in the case where the detector efficiency to observe a hitting event is $\varepsilon = 90\%$ (due to smaller active area for example). Since only one proton is emitted in the case of ^{78}Y the $\varepsilon = 90\%$ curve is just 90% of the $\varepsilon = 100\%$ curve. In the case of ^{78}Sr the efficiency to detect at least one proton is less sensitive to ε.

The LISA detector (see section 2.8.6) can cover around 80% of the solid angle which corresponds to the opening of 144° in θ. The detector is not set symmetrically since the forward angles are covered by a CD detector. Therefore, the LISA veto efficiency for ^{78}Sr is clearly more than 97–98% assuming that all the detectors are working. For ^{78}Y the efficiency is expected to be around 85–95%. Using these numbers the rate of the $A = 78$ recoils at the DSSD which are not vetoed is expected to be around 3–7 Hz per $1 \cdot 10^{10}$ primary-beam particles which can still be a few orders of magnitude more than the rate of the ^{78}Zr recoils.

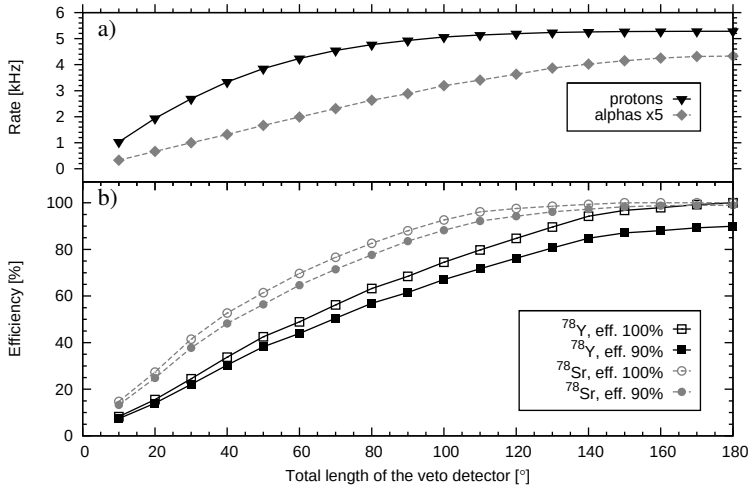

Figure 2.53: a) Proton and alpha particle rates in the reaction ^{40}Ca(^{40}Ca,2n)^{78}Zr and b) veto efficiency of the veto detector as a function of its length for two channels. The length of the detector is here the angle in which the detector is seen from the target. The center of the detector is at the position of the target. Rates correspond to a ^{40}Ca current of $1 \cdot 10^{10}$ 1/s.

2.7.2 A normal kinematics reaction: ^{92}Mo(^{54}Fe,p4n)^{141}Ho

The reaction ^{54}Fe+^{92}Mo producing the proton emitter ^{141}Ho in the p4n channel has been chosen as an example of a fusion reaction involving evaporation of a proton in addition to neutrons. The ^{141}Ho nucleus cannot be produced in n, 2n or 3n channels with stable projectile and target species. Also in channels 4n and 5n, the natural abundancies of needed species are too low in practice. The cross section is expected to be higher for the p4n channel than for the 6n channel. Evaporation of five particles requires high excitation energy and therefore E_{CM} needs to be well above the barrier ($E_{\mathrm{int,CM}} = 130$ MeV). In the simulation the ^{92}Mo (300 µg/cm^2) target was bombarded with 302 MeV ^{54}Fe projectiles. The primary beam loses about 5 MeV of its kinetic energy in the target and thus the collision energy and the excitation energy of the compound are $E_{\mathrm{CM}} = 187$–190 MeV and $E^* = 89$–92 MeV, respectively. The reaction is simulated also with inverse kinematics in the next section.

Ho isotopes 141 and 140 have been produced with this reaction for example at HRIBF at Oak Rigde [Ryk99]. They used a beam energy of 315 MeV, beam intensity of $8.1 \cdot 10^{10}$ and a 0.91 mg/cm^2 thick ^{92}Mo target. The recoil mass separator (RMS) was adjusted to collect mass 140 and part of mass 141 having charge state 27 to a DSSD. PACE4 estimates a cross-section of around 0.1 mb

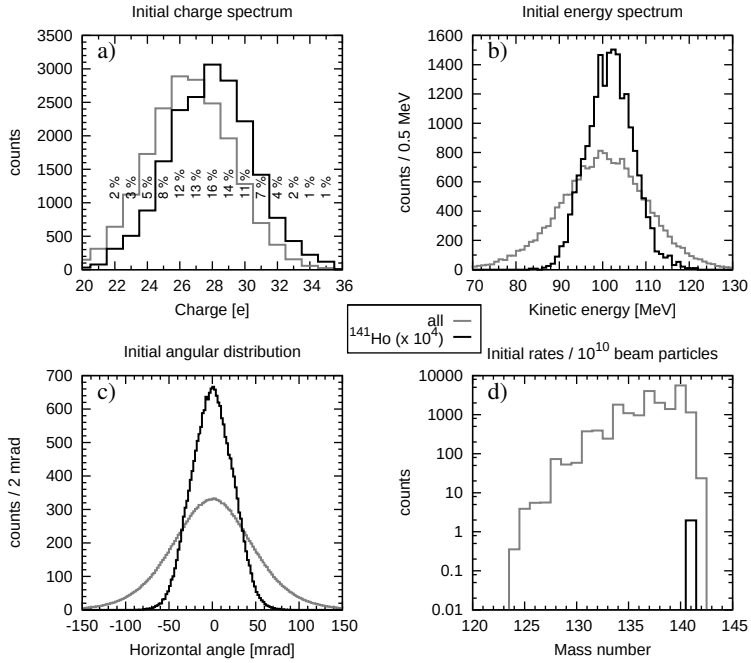

Figure 2.54: Distributions of a) charge, b) kinetic energy and c) horizontal angular distribution of ^{141}Ho (black line and multiplied by $1 \cdot 10^3$) and all relevant fusion products (gray line). Panel (d) shows the production rate of the recoils at the target as a function of mass number (note: ^{141}Ho counts are not multiplied). The counts reflect PACE4 cross-sections and a beam intensity of $1 \cdot 10^{10}$ 1/s.

for ^{141}Ho while [Ryk99] presents a number around 0.16 µb (smaller by factor of 600). The number of counts in the $A = 140$ peak in figure 1 of [Ryk99] (not sure whether the figure represents the whole experiment) and the given estimate of 3% transmission yields about 450 Hz as the production rate when normalized to the intensity and target of the current simulation while figure 2.54 (d) gives 5.5 kHz as the production rate of the $A = 140$ nuclei.

Figure 2.54 shows the charge, energy and angular distributions and the production rates of ^{141}Ho and other recoils. The ^{141}Ho recoils have significantly narrower energy and angular distributions than the other recoils. The total fusion rate is about 19 kHz for 1.6 pnA beam of ^{54}Fe which is about four times the rate (5.3 kHz) in the ^{40}Ca+^{40}Ca reaction due to higher excitation energy of the compound nucleus. The rates of the evaporated neutrons, protons and α particles are 22 kHz, 69 kHz and 18 kHz, respectively.

According to the PACE4 cross-sections the focal plane (and DSSD) rate originates from recoils having $A = 140$, 137 and 141. Figure 2.55 represents the slits

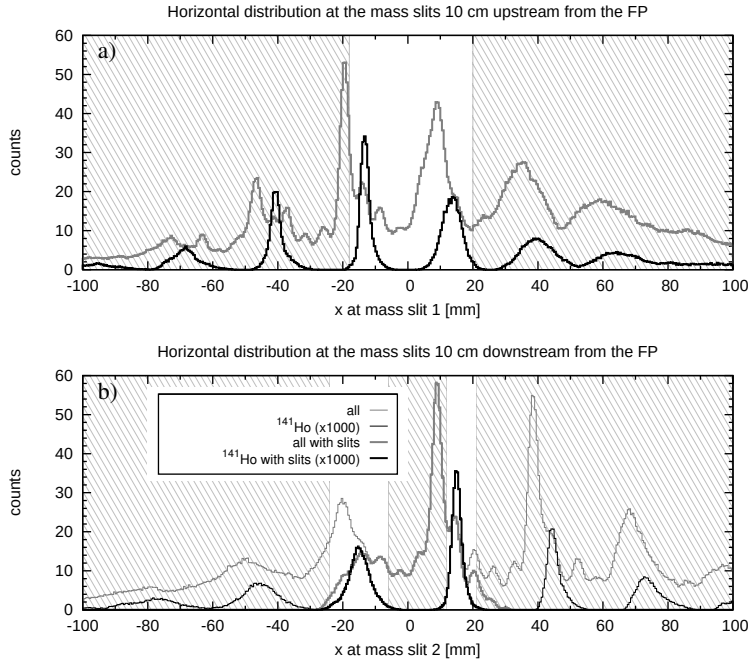

Figure 2.55: Horizontal position distributions at a) 10 cm upstream (MS_1) and b) 10 cm downstream (MS_1) from the focal plane where the mass slits can be set. Thin lines in (b) represent the situation without slits at MS_1.

adopted in the simulation. The situation differs from the case of the ^{40}Ca+^{40}Ca reaction where the production of $A = 79$ or $A = 75$ recoils was negligible compared to main channels. Here, a more advanced slit setup is found necessary to decrease the rate of the $A = 137$ peak on the right hand side of the $A = 141$ peak in the focal plane position spectrum. Figure 2.55 shows that the slits filter $A = 140$ recoils reasonably well but not so well the peak $A = 137$. If further decrease on rates is needed then an obstacle in the center at MS_1 position and a narrower right hand side slit in the MS_2 position has to be set. This would of course decrease the ^{141}Ho transmission. The slits drop the focal plane rate from 5.8 kHz to 1.5 kHz and the DSSD rate from 3.3 kHz to 0.64 kHz if the ^{54}Fe intensity of $1 \cdot 10^{10}$ 1/s is assumed. Transmission of masses is shown in figure 2.56. Transmission values of the ^{141}Ho recoils to the focal plane are as high as 70% without slits and 27% with slits. The corresponding values to the DSSD are 44% and 26%.

Figure 2.57 shows a) the position spectrum at the focal plane and b) the mass spectrum obtained with a third order Taylor polynome. The mass resolution is not enough to separate neighbouring masses as cleanly as in the ^{40}Ca+^{40}Ca

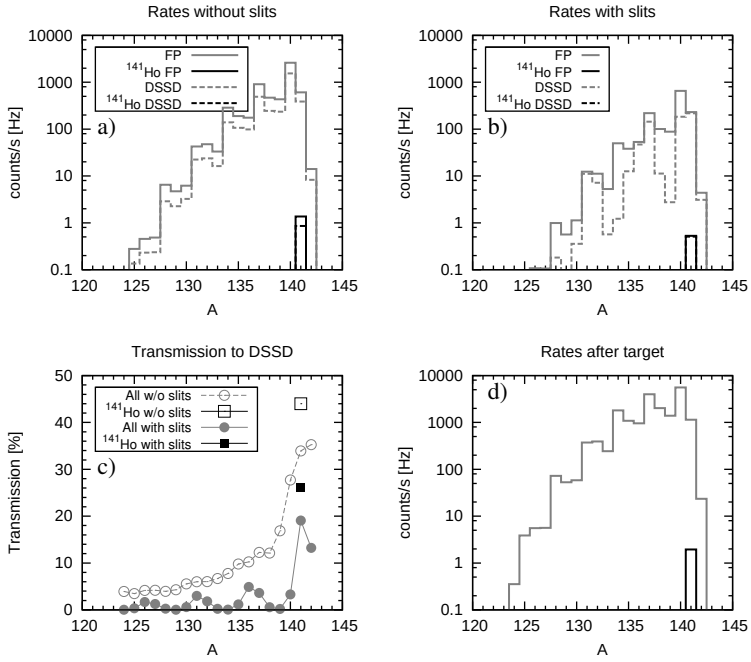

Figure 2.56: Rates at the focal plane detector and in the DSSD for the primary beam of $1 \cdot 10^{10}$ 1/s a) without and b) with the mass slits as a function of the recoil mass number. Subfigure (c) shows transmission from target to the DSSD in both cases. Subfigure (d) is the production rate and shown for comparison.

reaction. For comparison, the corrected mass spectrum seems to have slightly better resolution than shown for RMS in [Ryk99]. However, in that experiment the target had triple the thickness compared to this simulation. The effect of the limited horizontal acceptance of MARA has also been tested and for example by cutting the ^{141}Ho transmission to one third the neighbouring masses could be separated as cleanly as in the ^{40}Ca+^{40}Ca reaction.

Since the evaporation channel includes a proton, it is possible to get an accurate flight time over MARA, Δt_1, if a suitable detector is available at the target position. The mass resolution will be slightly enhanced if Δt_1 is used instead of Δt_2.

The two charge states of ^{141}Ho hit the DSSD in the range from -4.0 cm to $+3.5$ cm. The y-position distribution has a Gaussian shape with $\sigma = 1.1$ cm and only about 9% of ^{141}Ho recoils are outside ± 2.0 cm in y-direction.

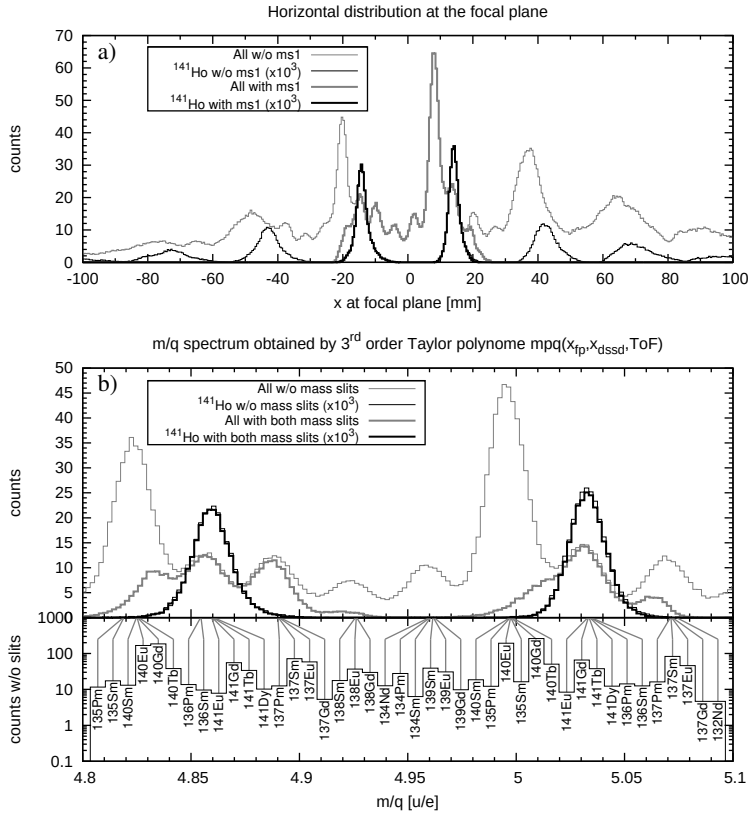

Figure 2.57: a) The horizontal distribution of recoils at the focal plane with and without the slits and b) calculated m/q spectrum with information about individual isotopes. The bottom panel shows only m/q combinations which generate at least a rate of 5 Hz. Counts represent a beam intensity of $1 \cdot 10^{10}$ 1/s.

2.7.3 An inverse kinematics reaction: ^{54}Fe(^{92}Mo,p4n)^{141}Ho

In the study presented in reference [Sew01a], ^{141}Ho has been produced in an inverse kinematics reaction in addition to normal kinematics. In the inverse kinematics part the 0.8 mg/cm^2 thick ^{54}Fe target was bombarded for five days with 502 MeV ^{92}Mo projectiles with a beam current of about 2.5 pnA. In the study, the proton decay of ^{141}Ho recoils which were mass separated with FMA and implanted to a DSSD, was utilized to tag the prompt γ rays belonging to ^{141}Ho (method of Recoil Decay Tagging, [Pau95]). The FMA separator was set to collect charge states 36 and 37.

A JIonO simulation has been performed for this inverse kinematics reaction to

see the differences compared to normal kinematics described in the previus section. In the simulation a beam of 502 MeV ^{92}Mo projectiles and a 0.8 mg/cm^2 thick ^{54}Fe target have been used as in the aforementioned experiment. According to TRIM the ^{92}Mo recoils have about 471 MeV kinetic energy after the target. The excitation energy of the compound nucleus is thus in the range 76–87 MeV. This is lower than in the previous simulation using normal kinematics. Now, most of the ^{141}Ho recoils are produced in the upstream part of the target and the production vanishes at beam energies lower than 480 MeV due to lack of statistics in PACE4 calculations. The chosen combination of the primary beam energy and target thickness gives an average energy of 265 MeV for ^{141}Ho recoils. The Schiwietz formula (1.38) gives $\bar{q} = 37.0$ as the average charge state after a carbon foil for that energy. Parameters $q = 37.5$, $E = 265$ MeV and $m = 141$ u were adopted for the reference particle. Its electrostatic rigidity becomes as high as $\chi_E = 14.1$ MV which is at the limits of MARA which is about 14.2 MV corresponding to $V = \pm 250$ kV on the deflector electrodes. Thus the higher excitation energy would require a thicker target or an energy degrader after the target.

The total rates and the transmission values of ^{141}Ho are given in table 2.8. The total rates at the focal plane and at the DSSD without slits are about 9–10 times as high as in the case of normal kinematics while the production rate is only four times as large. With slits $[-1.2, -0.8]$ cm and $[0.5, 1.5]$ cm at MS_1 and $[-1.6, -0.5]$ cm and $[0.9, 1.4]$ cm at MS_2 the rates are about 5–7 times as large.

In general, with inverse kinematics the width of the angular distribution of the fusion products is much narrower which translates to higher transmission of the products. This is also the case with the ^{141}Ho recoils although those had been created in the upstream part of the much thicker target (0.8 mg/cm^2 ^{54}Fe vs. 0.3 mg/cm^2 ^{92}Mo). However, due to the higher momentum in beam direction the transmission of other fusion channels is also significantly enhanced which leads to an increased rate at the focal plane detectors. The total widths of the angular distributions of the fusion evaporation residues are $\sigma = 46$ mrad and $\sigma = 25$ mrad for the normal and inverse kinematics, respectively. Also the energy distributions are narrower due to the higher momentum of the recoils which affects for example the width of the charge distribution and can therefore increase again the transmission. The charge distribution is also shifted towards higher values and therefore more peaks will fit into the focal plane detectors which can be a useful phenomenon. Smaller spread in energy and angle decrease also the absolute values of the aberrations at the focal plane and higher mass resolution can be expected. This gives an opportunity to use a different solution for quadrupoles, accompanied by limited horizontal acceptance, for increased mass resolution. This scheme has been studied and is discussed below.

The mass resolution was increased by using the quadrupole solution having

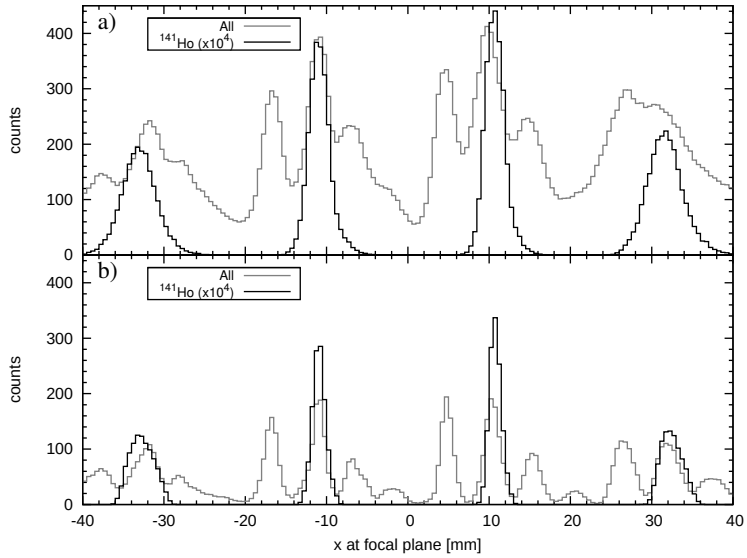

Figure 2.58: Horizontal position distributions at the focal plane a) with nominal MARA settings and b) with quadrupole settings having $B_{Q1}/\chi_B = 0.1$ m^{-1} and limited angular and energy acceptance (horizontal openings were $[-3.0, 3.0]$ cm at AP_1 and $[-3.0, 4.0]$ cm at AP_2). No mass slits have been set for this figure.

$B_{Q1}/\chi_B = 0.1$ m^{-1}. The rectangular aperture AP_1 located at the exit of Q_3 was set to $[-3.0, 3.0]$ cm in horizontal direction in order to decrease $(x|a^2)$ aberrations (see figure 2.8). Since the energy distribution of the ^{141}Ho recoils is narrower compared to all fusion products, the horizontal opening of the second aperture, AP_2, located 20 cm upstream from the dipole entrance was set to $[-3.0, 4.0]$ cm. This reduces energy related aberrations.

Figure 2.58 shows the focal plane position spectra in the case a) of the nominal MARA settings and b) of the high resolution settings described above. With the above mentioned mass slit settings, suppression factors higher than $1 \cdot 10^{-4}$ could be achieved for masses $A = \{139, 140, 142, 143\}$ if the high resolution settings are used. The resolving powers for the $m/q = 141/38$ peak at $x = -11$ mm in the figure have been calculated in both cases. They are a) $\mathcal{R}_{68\%} = 265$ and $\mathcal{R}_{95\%} = 115$ for the nominal settings and b) $\mathcal{R}_{68\%} = 403$ and $\mathcal{R}_{95\%} = 199$ for the high resolution settings.

Masses $A = \{137, 138\}$ have overlapping m/q peaks and cannot be separated physically. When applying the high resolution mode, the transmission to the focal plane and to the DSSD of charge states $q = \{37, 38\}$ of ^{141}Ho drops to 14% from about 26%. However, one can observe that the ratio of ^{141}Ho to

all products increases significantly. The vertical position distribution at the DSSD has a Gaussian shape with $\sigma = 1.1$ cm and 93% of the counts are inside $y \in [-2.0, 2.0]$ cm.

Peaks $m/q = 141/39$ at $x \approx -33$ mm and $m/q = 141/36$ at $x \approx 32$ mm are focused at the positions of the first and the second mass slit, respectively. Opticswise, it is possible to set mass slits to accept four charge states of $A = 141$ recoils and reject the neighbouring masses with a high suppression factor. All four charge peaks of Ho fit into a width of 10 cm at the DSSD and the charge peaks are still physically separated. For four charge states the total transmission of ^{141}Ho is around 25% which is about the same as achieved with nominal setting and two charge states.

2.7.4 An inverse kinematics reaction: ^{24}Mg(^{40}Ca,3n)^{61}Ge

The production of β^+ active ^{61}Ge via the inverse kinematics reaction ^{24}Mg(^{40}Ca, 3n)^{61}Ge has been simulated. The ground state of ^{61}Ge decays to the isobaric analog state (IAS) of ^{61}Ga via super-allowed Fermi β decay (with a branching ratio of 55(6)%) [Bla07, Hot87]. This IAS state decays by a prompt proton decay ($E_p = 3.17(3)$ MeV) to the ground state of ^{60}Zn. The half-life of ^{61}Ge is 44(6) ms.

The main parameters of the simulated reaction are given in table 2.8. The slits have been set to allow two charge states of ^{61}Ge to be implanted into the DSSD. The mass slits are visualized in figure 2.59 alongside the position spectra at slits. Figure 2.60 shows the focal plane position spectrum and the corrected m/q spectrum calculated with a Taylor polynome. According to the PACE4 cross-sections used in the simulation, the largest m/q peaks overlap with the selected ^{61}Ge peaks. The main background seems to come from ^{58}Ni produced in the α2p or the 4p2n channel. The PACE4 calculations did not give any ^{61}Ge events and therefore its cross-section was set as $\sigma(3n) = 1$ nb over the target. If the rate of ^{58}Ni needs to be decreased, one option is to choose ^{61}Ge charge states 18 and 17 instead of 20 and 19. The summed production rate of these lower charge states is about 20% less. However, the total rates with slightly adjusted slits from the settings shown in figure 2.59 and with an added obstacle in the first mass slits position would decrease the DSSD rate about 50% while the transmission of Ge drops only about 25%. If the fusion rate at the target is not a problem then it would be sensible to limit the horizontal angle and energy acceptance of MARA with apertures after the triplet and between the sector fields and increase the primary beam intensity.

The system has been simulated also with inclusion of the additional hexapole correction elements described in section 2.3.4. Settings $B_{H1}/\chi_B = 0.04$ m^{-1} and $B_{H2}/\chi_B = -0.02$ m^{-1} removed the tails of the m/q peaks perfectly. The

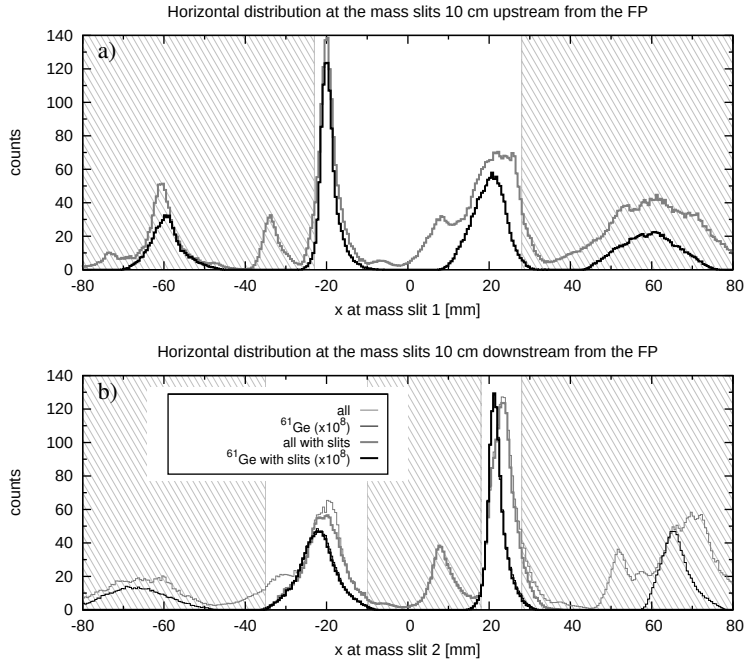

Figure 2.59: Horizontal position distributions of recoils from the reaction ^{40}Ca+^{24}Mg at mass slit positions a) MS_1 and b) MS_2. Thin lines in (b) represent recoils stopped at first mass slits shown by (a).

physical resolving powers for the left peak at the focal plane, $m/q = 61/20$, are $\mathcal{R}_{68\%} = 140$ and $\mathcal{R}_{95\%} = 64$. Without hexapoles (figure 2.60 (a)) the resolving powers of the same peak are $\mathcal{R}_{68\%} = 128$ and $\mathcal{R}_{95\%} = 51$. For comparison, the resolwing powers $\mathcal{R}_{68\%} = 192$ and $\mathcal{R}_{95\%} = 80$. are obtained for the corrected m/q spectrum of figure 2.60 (b). These values are better than in the case of hexapoles mainly since the tilt of the mass focal plane has been taken into account.

The same reaction with the same target thickness of 300 µg/cm^2 has been used for studies of the excited states of ^{61}Ga produced in the p2n channel [And05]. RMS at Oak Ridge National Laboratory has been utilized for mass identification of the fusion products in that study.

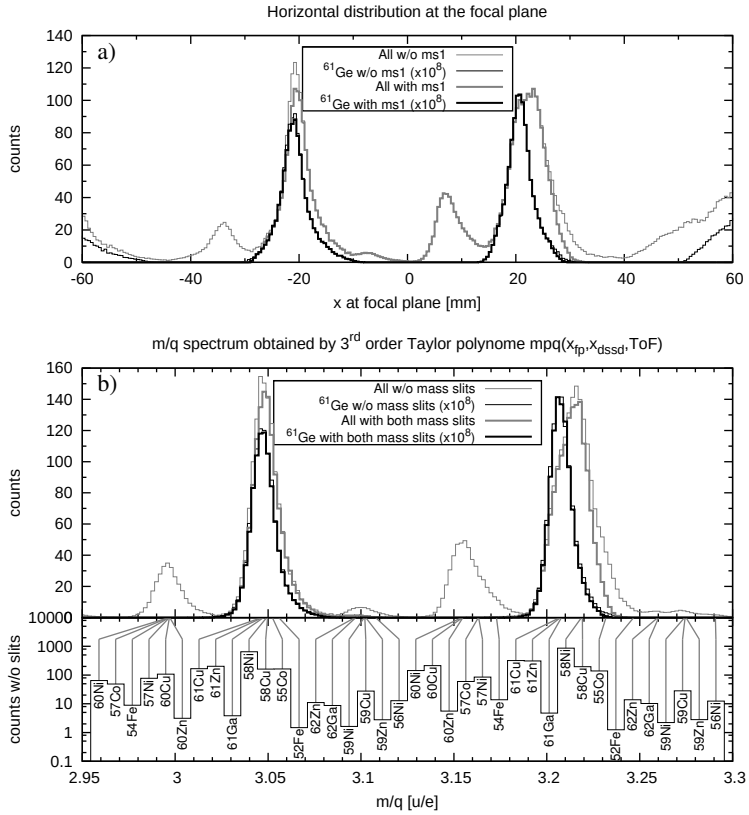

Figure 2.60: a) The horizontal position distribution at the focal plane of recoils originating from the ^{40}Ca+^{24}Mg reaction. b) Calculated m/q spectrum with information about individual species. Only m/q combinations which generate at least a rate of 1 Hz are included. Counts represent a ^{40}Ca beam intensity $1 \cdot 10^{10}$ 1/s.

2.7.5 Reaction ^{208}Pb(^{48}Ca,2n)^{254}No and the charge-plunger technique

It is known already beforehand that the RITU gas-filled recoil separator has a higher transmission for transfermium fusion-products than MARA. However, the ability of MARA to identify charge states can be used to extract additional information about life times of the isomeric states which decay through internal conversion. This can be achieved by using the *charge-plunger technique* [Ulf78]. It offers a unique possibility to measure life times of states having high conversion coefficients and low transition energies which excludes the use of the conventional plunger measurements observing variation in the Doppler shift of γ rays. Taking advantage of the charge-plunger technique with MARA

has been proposed by Peter Butler.

In the internal conversion of a γ-ray emission, a vacancy will be created in the innermost atomic shells—K, L or M. When another electron from an outer shell fills this vacancy some amount of energy is released which can be emitted as a photon or transferred to a second electron. The latter is called an Auger electron. Since the emission of the Auger electron leaves two vacancies in the electron cloud the process can continue and a large number of Auger electrons can be emitted. If this Auger cascade occurs in vacuum then the obvious result is an ion in a high charge state. Carlson et al. [Car66] have studied the average charge state as a function of the proton number in the cases where a sudden vacancy has been created in the innermost shells by x-ray irradiation. Their results suggest that in the nobelium region such a vacancy will cause average charge states ranging from 10^+ to 14^+. Metag et al. [Met76] have studied charge distribution of ^{240}Cm produced in the ^{239}Pu(α,3n) reaction and have observed charge states up to 45^+. They have found also that the average charge state, $\bar{q}$, depends on the number of consecutive converted decays of isomeric states. They estimate that a $\bar{q}$ of around 12^+, 19^+, 24^+, 29^+ and 33^+ is caused by 1, 2, 3, 4 and 5 consecutive decays, respectively. The FWHM of a single distribution is around 10. The average charge state of ^{254}No created in the reaction ^{208}Pb(^{48}Ca,2n) is already around 20^+ and therefore one can estimate that the shift in $\bar{q}$ introduced by one Auger cascade is around +4–5 charge units.

The principle of the charge-plunger technique is described by Ulfert et al. in [Ulf78] and is summarized in the following. A thin carbon foil is placed after an adjustable distance behind the target foil. If the isomer decays in between the foils then an anomalously high charge distribution caused by the Auger cascade will be reset at the carbon foil. If the decay occurs after the reset foil then the anomalous charge state distribution can be observed. Therefore, by comparing the charge state distributions and especially the mean charge state as a function of the reset foil distance, information about life times of isomeric states can be obtained.

The nucleus ^{254}No has been produced in many laboratories with this reaction and practically only one fusion channel is open. The reaction, where the 500 µg/cm^2 thick foil of doubly magic ^{208}Pb atoms is bombarded by also doubly magic 221 MeV ^{48}Ca ions, has been simulated with JIonO. These parameters are close to those used in a relatively recent study [Eec05] carried out with RITU. The results discussed in this section are based on 10000 reactions calculated in the target with a constant cross-section of 2 µb. This set of recoils were run 50 times through MARA optics with random directions. Since there is no clear need for mass resolving of the recoils, the focal plane distance from the dipole should be shortened in order to fit more charge states into the particle detectors and thus to increase the detection efficiency. Even higher transmis-

sion could be achieved by inverting the quadrupole triplet polarities but this would degrade the important charge-state resolution. In the simulation, the drift length after the dipole was shortened to 1.753 m (nominal being 2.058 m) by introducing a quadrupole component $n_1 = -0.1$ in the dipole. In addition, the focal plane instrumentation was moved 0.400 m upstream so that the implantation detector was at the optical focal plane. Therefore, the position of the first detector (SED or MWPC) was 0.400 m upstream from the focus. A quadrupole triplet solution having $B_{Q1}/\chi_B = 0.65$ m^{-1} (figure 2.8) was used to further increase the transmission. The reference particle was $m_0 = 254$ u, $E_{k,0} = 37$ MeV and $q_0 = 19.3$ as shown in table 2.8.

The energy loss and the angular scattering of the No recoils have been extrapolated from results of TRIM calculations carried out for several species between Pb and U.

Four charge states, $q = \{18, 19, 20, 21\}$ transmitted through MARA up to the implantation detector are shown in figure 2.61. A height of 8 cm is assumed for the first detector (6 cm in previous MARA simulations) and 6 cm for the DSSD. The effect of the detector widths on the collection efficiency can be estimated from the figure. It seems that it is possible to collect the four charge states with two parallel 6·6 cm^2 DSSD detectors if a suitable horizontal gap is left in between. If the normal height of 6 cm in the first detector is used the transmission drops by less than 1%.

Information about transmission as a function of a) initial charge state, b) energy, c) horizontal angle and d) position of the reaction in the target is given in figure 2.62. Transmission values of charge states 19^+ and 20^+ are about 70% while values about 50% are achieved for 18^+ and 21^+. Figure 2.62 (d) shows that evaporation residues originating from the exit side of the target have much higher probability to be transmitted than those which have travelled through the target. The total transmission probability suggested by the simulation is 38% with the described DSSD arrangement. The transmission of ^{254}No through RITU is discussed in section 3.2.

2.8 Instrumentation

The overview of MARA without auxiliary detectors is shown in figure 2.2. In this section the instrumentation of MARA is discussed. There is no decision made about the detector setup yet and therefore this discussion should be taken as suggestive.

MARA will be built next to the existing RITU gas-filled separator in the target hall in JYFL. Both separators are/will be in separated areas shielded by con-

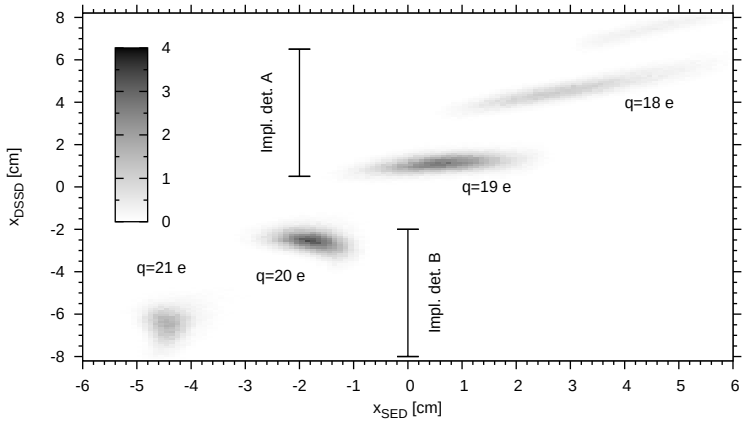

Figure 2.61: Hit positions of the No recoils in the first (x-axis) and second detector (y-axis).

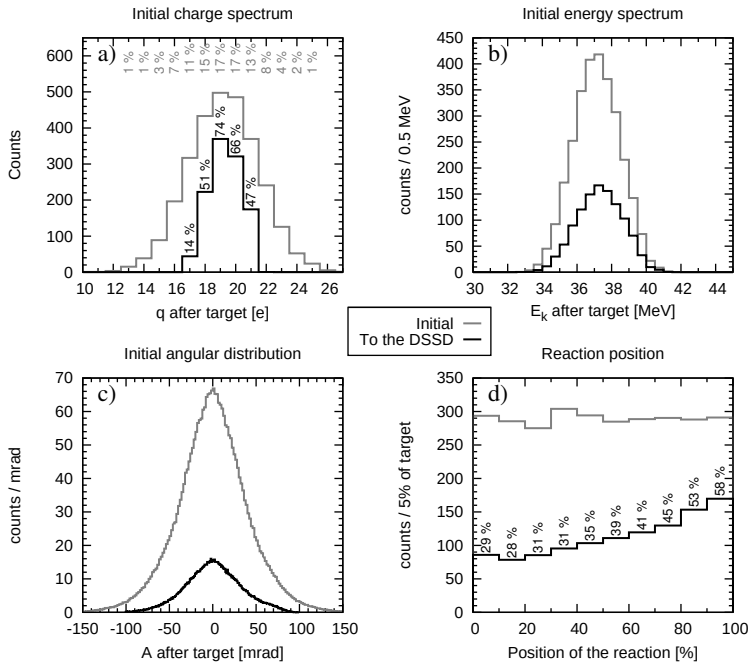

Figure 2.62: Number of produced and transmitted recoils as a function of a) initial charge state, b) energy, c) horizontal angle and d) position of the reaction in the target. The counts represent a total beam intensity of $1 \cdot 10^{15}$.

crete block walls and roofs. Since the detector requirements are very similar for both separators it should be possible to share the data acquisition system and some of the detectors. Experiments cannot be run simultaneously in both separators since the same K130 cyclotron is used for projectile acceleration. However, the separate experimental areas allow maintenance or preparation of a separator when the other one is in use.

An efficient data-acquisition (DAQ) system is essential in order to read and handle the physical events seen by the detectors. Since the observation of the rare physical processes requires practically always coincidences between different detectors the best way to maximize the sensitivity in an experiment is to collect and store data from all detector channels as independently as possible which means that one should not use a common trigger signal for data readout. Such a triggerless data aquisition or total data readout system (TDR) [Laz01] has been implemented for detectors used with RITU. It enables versatile conditions for coincidences to be set after or during an experiment.

2.8.1 Vacuum system

The rough disposition of three gate valves that divide MARA into three vacuum parts is shown in figure 2.2. The largest volume, composed of the deflector vacuum chamber and a tube through the triplet, is planned to be pumped with a large turbomolecular pump and a cryogenic pump. The most suitable place to connect the pumps is the bottom or top of the deflector chamber. A gate valve should be used also to separate the dipole and the focal plane chambers since the latter needs to be vented and pumped frequently. Turbomolecular pumps will be used for the pumping of both volumes. The vacuum system includes also several pressure gauges.

2.8.2 Aperture system

In addition to the m/q slits at the focal plane, adjustable apertures at least in two postitions are needed in order to increase the versatility of MARA to be better suited for different reactions. These can be used to limit the angular acceptance of MARA and to some extent also to limit the energy acceptance. Therefore, the absolute values of aberrations can be decreased which increases the mass resolving power. Possible places, at the exit of Q_3 and between the sector fields, are indicated in figure 2.2.

The rectangular aperture between Q_3 and the deflector is used to limit the angular acceptance in both directions. Let this aperture be named as AP_1. Figure 2.15 (a) shows that the horizontal aberration at the focal plane caused

by the initial horizontal angle, a_0, is almost the same for positive and negative a_0. However, four linear vacuum-feedthroughs, which enable independent adjustment of both sides in both directions, will be used for implementation of the aperture. Transfer matrices in 2.16 give $(x|a)_{\mathrm{AP}_1} = 1.255$ mm/mrad and $(y|b)_{\mathrm{AP}_1} = 0.8208$ mm/mrad. Therefore, the symmetric ± 35 mrad acceptance is achieved with AP_1 having a width of 88 mm and a height of 57 mm. The values of the transfer coefficients change for different solutions for the triplet.

The second aperture, AP_2, should be placed either at the entrance or at the exit of the magnetic dipole. In the simulations, AP_2 has been set 20 cm upstream from the entrance EFB of the dipole. The aperture is intended to be adjustable with two opposing linear feedthroughs and only in the horizontal direction. It can be used to partially control the aberrations involving the product $a\delta_K$. It should be noted that a recoil having a positive product $a_0\delta_{K,0}$ can be transmitted even if AP_2 is narrow.

Some of the primary beam particles hitting the surface around the split anode in the deflector can reach the focal plane by scattering from vacuum chamber walls. If this is causing severe background at the focal plane then the adjustable AP_2 can probably be found useful. The negative side of AP_2 can be pulled inwards also in a case where a strong population of fusion products are travelling too close to the split anode.

Both apertures, AP_1 and AP_2, should be understood to work together. The best view of their concurrent action can probably be obtained from figure 2.5. The work is going on to develop an easy-to-use graphical interface for the JIonO code which could support decision making before and during an experiment for example when the optimal aperture settings are considered.

2.8.3 General consideration about the focal plane area instrumentation

Figure 2.63 illustrates a qualitative sketch of MARA focal plane instrumentation in the case of using a DSSD for recoil implantation. The ion-optical coordinate system has been drawn in the figure. Only part of the vacuum chamber is shown. The mass slits, transmission detector, implantation detector and auxiliary detectors are discussed in more detail in the next subsections. The design of the focal plane instrumentation has not been started yet and only rough ideas will be presented.

In order to take full advantage of the adjustable focal length from the dipole to z_{fp} allowed by the surface coils (see section 2.3.1), the instrumentation at the focal plane is required to be easy to move along the optical axis. One solution would be to use a movable platform for the chambers and detectors and to

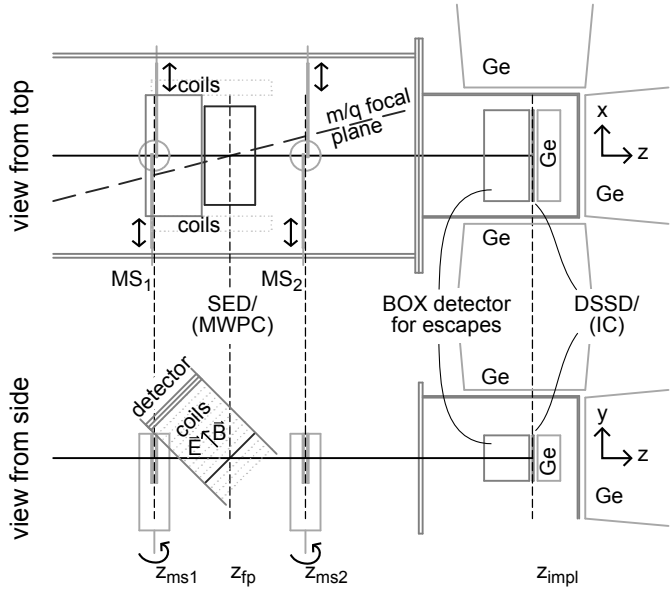

Figure 2.63: A qualitative sketch of MARA focal plane instrumentation. The active area of 12·6 cm has been adopted for the figure.

change the length of the vacuum tube after the dipole. In this case, one longer tube can be installed from the dipole up to the position corresponding to the shortest focal length and then a set of tubes with varying lengths could be used to cover the rest of the drift length.

The diversity of detector and slit setups at the MARA focal plane is clearly larger than in the case of RITU. This is mostly since MARA makes possible to run also inverse kinematics fusion reactions and it provides m/q separation. The first feature offers an opportunity to use for example an ionisation chamber instead of a Si-detector. The latter feature may require different kind of slit-detector combinations. Altogether, the focal plane instrumentation must be designed to be as modular as possible in order to allow versatile and efficient setups.

2.8.4 Mass slit system

Figure 2.63 shows a possible placement of the mass slit system and illustrates also the tilted m/q focal-plane. The simulations (section 2.7) have suggested that 6 cm is enough for the active height and 12 cm for the width. These dimensions are used also in the figure. Let us assume that a transmission detector is located at z_{fp}. In order to suppress neighbouring m/q peaks effectively, mass

slits must be implemented both before and after the focal plane. The corresponding profile planes are at $z_{\mathrm{ms1}} = z_{\mathrm{fp}} - 0.10$ m and $z_{\mathrm{ms2}} = z_{\mathrm{fp}} + 0.10$ m.

One possible implementation (shown in the figure) of the mass-slit system accepting two charge states is that both MS_1 and MS_2 consist of two linear vacuum feedthroughs and of one feedthrough combining linear and rotational movement. The first two feedthroughs move plates horizontally and set the horizontal opening of two slits. The width of the obstacle at the center can be adjusted by rotating the plate at the center. A width of 4.0 cm for the rotating plate seems to be suitable for most (or even all) experiments. The linear movement is needed for lifting the center plate away from the optical axis. This kind of slit system, albeit at one profile plane only, has been used with FMA at Argonne [Uus11]. According to the simulations, the optimal rotational axis of the center plate is not at the optical axis but in the negative x side for MS_1 and in the positive x side for MS_2. This fact needs to be taken into account when designing the mass slits.

If a transmission detector at the focal plane is based on a thin foil at 45° then the slit system needs to be moved farther off from the focal plane. This problem is indicated also in the figure. This may decrease the mass slit performance since at $z_{\mathrm{fp}} \pm 10$ cm the m/q focus is already at $x = 2.5$ mm which is more than the half separation of the neighbouring charge-state peaks in any of the simulated reactions.

Another solution for mass slits is the following. Two slits with fixed horizontal apertures are implemented on two separate plates. The position of an aperture is adjusted with a linear feedthrough. If both apertures begin 10 mm from the end of the plate the center obstacle can be adjusted within a range of 10–20 mm. This slit system would require change of the aperture plates for example if the peak widths needs to be changed. However, the focal plane vacuum chamber is vented and evacuated quite often. The m/q resolution can be estimated before an experiment and thus the fixed apertures would not be a problem. The free adjustment of the peak separation makes it possible to change the charge of the reference particle which may be needed for optimizing the yield.

2.8.5 Focal plane detector system

The most important instrumentation of a separator is evidently the focal plane detector system. Following requirements can be set on the MARA focal plane setup: a) position measurement of an arriving recoil at z_{fp}, b) detection of the angle, c) time-of-flight measurement to get the velocity, d) energy and/or energy loss measurement, e) Z identification and f) possibility to detect the decay of the recoil and to correlate this with the recoil. Clearly, the points a, b, c, and f require the presence of two detectors where the first position

sensitive transmission detector lies at the focal plane.

The requirements are similar to those at the RITU focal plane except for the strict need for position measurement at z_{fp}. Therefore the GREAT spectrometer [Pag03] is probably the best starting point for the design process of the focal plane detector system for MARA.

Transmission detector at $z_{\mathbf{fp}}$

The transmission detector would record the m/q ratio and time of the arriving recoil and thus can be exploited as a veto detector for decay events. To fulfill this, an efficiency close to 100% is needed. There are two options for a transmission detector: a multi-wire proportional counter (MWPC) or a thin foil acting as a source of electrons to be detected in a secondary electron detector ($\mathrm{Se}^-\mathrm{D}$). The latter is shown qualitatively in figure 2.63.

MWPC The position sensitive GREAT MWPC detector consists of three electrodes packed successively in a gas volume (typically a few hPa of isobutane) confined by thin Mylar windows. The center electrode, a metallized foil, is set to a positive voltage around 500 V and is surrounded by wire planes at ground potential. The wire separation (pitch) is 1 mm in both directions. The position of a recoil passage is given by a time-to-amplitude converter (TAC) using the time difference of signals coming from the fast anode (metallized foil) and slow wire planes read through delay lines. The disadvantage of using MWPC with MARA is the relatively high material thickness of the detector. The working principle of low-pressure gaseous detectors is presented for example in [Bre82].

$\mathrm{Se}^-\mathrm{D}$ The solution based on detection of secondary electrons (Se^-) is probably the best since the thickness of the material along the recoil's flight path is then minimized. The space consumption and rough working principle of this detector are shown in figure 2.63. The Se^- detector which has been used at the focal plane of VAMOS [Pul08] is described in detail in [Dro07]. The working principle of such a detector: the heavy ion creates multiple secondary electrons when it is passing through the foil. These are accelerated towards the position sensitive detector. At VAMOS a MWPC detector has been developed for this purpose because the more traditional choice, micro-channel plates (MCP), are limited in size and do not work very well in the same vacuum chamber with gaseous detectors. In addition to the acceleration voltage, a pair of coils on both sides are used to create a magnetic field parallel to electric field. This B-field enhances the position resolution of the device since the electrons are spiraling along the magnetic field lines. [Dro07]

If the emissive foil is used and it is set to a 45° angle relative to the optical axis then some space conflict between the $Se^{-}D$ and the mass slit system needs to be solved. In the VAMOS setup the foil is attached to a structure continuing mechanically to both directions, upwards and downwards, which would mean a space conflict with both mass slits. In principle there should not be an absolute necessity for that.

The size of 120·85 mm^2 (width·height) is a minimum for the emissive foil tilted 45° around the x-axis. The area is less than 20% of the area of the emissive foil at VAMOS which has a size of 400·150 mm^2. The VAMOS foil has three layers of material: 120 µg/cm^2 Mylar aluminized 30 µg/cm^2 on both sides. This translates to about 250 µg/cm^2 as total effective thickness when the factor $\sqrt{2}$ is taken to account. Since the foil to be used with MARA is much smaller, the total thickness could be reduced.

DSSD For most of the experiments the recoils will be implanted into a double-sided Si-strip detector (DSSD). Its advantage is that it gives position information, energy and time. If the lifetimes of studied nuclear species are short enough compared to the counting rate per pixel then the emissions of α particles, protons, conversion electrons or β particles can be observed at the same pixel enabling the correlation with the recoil. The implantation area in GREAT consists of two parallel 60·40 mm^2 DSSD's having strip width of 1 mm in both directions. Detectors having thicknesses 100, 300 and 700µm have been used. The optimal thickness of the detector depends on the experiment. For example proton activities are easier to observe with a thin detector due to the lower β background. In the case of β tagging, a thick detector is usually preferred. Information about β tagging experiments run with RITU can be found in [Ste06, Nar07a, Nar07b, Wad09].

In most of the experiments, two charge states fit inside about 10 cm horizontally at z_{impl} but leave a gap about 1 cm wide in between (see figures 2.49 and 2.61 for instance). One can take advantage of this feature if two parallel Si detectors are to be used. The gap between active regions of the GREAT Si detectors is about 5 mm. Contrary to this, the implantation station at the end of FMA utilizes only one DSSD having a size of 64·64 mm^2 (160·160 strips) [Sew09a]. However, in the case of FMA, the mass separation is lost quikly after the focal plane and all masses are focused to the same point at the DSSD. The clear advantage of the narrower implantation area is that the auxiliary detectors around the DSSD will have higher detection efficiencies.

If the DSSD is instrumented with digital electronics which provides traces (digital sampling of the pre-amplifier signal) to be collected, a fast decay after the implantation of a recoil could be searched for on top of the implantation signal. This is already possible with part of the GREAT DSSD channels.

Other detectors In RITU experiments a variety of decay modes has been utilized for recoil decay tagging (RDT [Pau95]). These are α and proton decay, spontaneous fission, β decay, isomeric γ decay and internally converted decay. The MARA focal plane instrumentation should be sensitive also to these events. Since most of the products are not α emitters, as opposed to RITU experiments, the other detectors will have even higher importance.

The GREAT planar Ge-detector is positioned right behind the implantation detectors inside the vacuum chamber. It is efficient for low energy γ-rays. In order to increase its efficiency for low energy γ-rays, a beryllium window is used at the face which is towards the DSSD. It has been utilized also for vetoing light particles, namely protons and α particles, which penetrate through the DSSD. The β particles in the β tagging experiments have been detected with the planar detector.

The high energy γ-rays emitted from implanted recoils are detected with clover Ge-detectors in GREAT. The actual GREAT clover detector is set on top of the vacuum chamber and other (clover) detectors can be installed on both sides and also behind the planar detector.

There is a set of Si PIN-diodes forming a *box detector* upstream from the DSSD in GREAT. It can be used to observe particles, typically α particles or conversion electrons, which escape from the implantation detectors. The box detector can therefore increase the total observation probability for α particles. One very important feature is that it enables GREAT to be sensitive for a fast decay occurring right after a recoil implantation causing a dead time for several µs in a DSSD strip.

The schematic positions of a planar Ge-detector and four clover detectors as well as the box detector are sketched also in figure 2.63. This layout is the same as that adopted in GREAT. For comparison, the FMA implantation station [Sew09a] resembles this but it has no planar Ge-detector. In addition, it has another Si-detector behind the DSSD. It has also plastic scintillators on three sides of the chamber for β detection.

Ionization chamber A description of the use of an ionization chamber (IC) for recoil Z identification at the focal plane of the Oak Ridge RMS is given in [Gro00]. The IC is useful in cases where recoils have a kinetic energy of 1 MeV/u at least. This means that inverse kinematics is required. The properly configured system has proven to be useful for Z idenfication up to $Z \approx 40$. For higher Z the centroid shift can be used for example for the identification of prompt γ-ray peaks [Gro00].

2.8.6 Auxiliary detectors around the target position

Gamma detector array

An efficient γ detector array coupled to MARA offers a powerful instrumentation for studies of nuclear structure. Majority of the experiments performed in the last decade with the RITU gas-filled separator have utilized the so called recoil gating or recoil decay tagging (RDT [Pau95]) methods in order to reduce the background in the prompt γ-ray measurement. The fundamental idea of the tagging or gating is to extract data from the Ge detectors temporally around the creation of an interesting fusion product. In recoil gating the arrival of a recoil at the focal plane is used to trigger the collection of data. In the RDT method the decay of a recoil is used for recoil identification. The same method has been used for example with the GAMMASPHERE array coupled to FMA [Sew01b].

The current Ge-detector array in front of RITU is *Jurogam II* (its details are given in the publication included in chapter 3). The Jurogam II array, or its successor, will be highly useful also in front of MARA. However, the moving of such an array is a demanding project and takes easily several months since the HV bias of each individual detector needs to be dropped before physical transportation. Due to neutron damages "activating" in the detectors when switching the HV off their annealing is essential before the HV can be raised again. Therefore, the array should be kept in the same place for at least 6–12 months. This needs to be taken into account when scheduling experiments.

Charged particle detectors

The Light Ion Spectrometer Array, LISA [LISA11], is a novel device developed to work simultaneously with the Jurogam II array. It is composed of an octaconal barrel Si-detector along the optical axis and of an annular CD shaped Si-detector downstream from the target. It can be used to detect evaporated protons and α particles and thus provides a tool to veto charged particle channels in the case where the interesting product is created in a pure neutron channel (see section 2.7.1). The LISA detectors are also able to observe fast proton decays from products having life times much shorter than the flight time through a recoil separator. LISA can be mounted to a separator within one working day. Additionally, it is on wheels and thus easy to use in front of either separator.

A project is going on to develop plastic scintillator detectors which could replace the LISA Si-detectors in case the position sensitivity is not needed. The advantage of a plastic detector, among others, is the faster timing signal which

could be exploited with MARA.

The observation of a fast proton originating from a weak fusion channel in the environment of high flux of evaporated protons and α particles can be extremely challenging. One option to detect at least part of the fast emissions would be an installation of a Si detector downstream from the target into the shadow of a mechnical barrier or collimator. Fusion products having a kinetic energy of 0.5 MeV/u travel approximately 1 cm/ns. Even if the gate valve in front of Q_1 is taken into account there is still potentially 15–20 cm space along the optical axis which can be exploited. This means that such a detector would be sensitive to life times ranging from a few ns up to around 50 ns depending on the recoil velocity. The problem is that the angle of a proton emission cannot be detected which means that the Doppler correction cannot be applied. However, in the case of one decay energy and simple lifetime and with decent statistics, both decay values can be extracted from the two dimensional (E, z) spectrum where E is the observed energy at a distance z from the target. Despite the lack of the event-based Doppler correction, the detector background level is expected to be low and even the information about hits and the hit distribution parallel to the optical axis could be essential for some experiments. This information could reveal a fast proton activity which could have otherwise caused one to conclude that no recoil is produced via the corresponding channel since the decayed recoil would not be detected at the focal plane.

Conversion electron spectrometer

The conversion electron spectrometer SAGE [Pap09] has been built to operate simultaneously with the Jurogam II array. This combination is unique tool to measure both conversion electrons and γ rays emitted from the same fusion evaporation residue. As the internal conversion factor increases with increasing proton number, SAGE is most useful at heaviest elements. However, in some cases it would be sensible to run these experiments with MARA (see for example section 2.7.5) and then use of SAGE with MARA can be preferred. For lighter products SAGE can be utilized for detection of E0 transitions which are always converted and thus cannot be observed with Ge detectors. SAGE is also easy to move between the separators.

2.8.7 Control system

The majority of the primary beam is transmitted through the split anode plate of the deflector to an appropriate Faraday cup between the sector field elements. The center of the horizontal distribution of the projectiles at the cup is related to the beam energy and in principle, after a suitable calibration, could be used

to measure the beam energy. One way to implement this would be a segmented and movable Faraday cup. The current reading from the cup can be used for normalization of the beam intensity or to control the intensity.

An extensive control system should be designed. The system should measure all vacuum gauges and states of the valves and vacuum pumps so that all information could be seen at the same place. The system, either manual or computer driven, should include interlocks to shield against human errors or for example power failures.

The currents in the magnets and especially the deflector voltage should be controlled by a computer for multiple reasons. First, the control software can be aware of different quadrupole settings which makes the optimization of an experiment easier. Second, the conditioning of the deflector HV (see section 2.5.3) can take a long time and automation of the procedure is necessary.

One advantage of the computer based control system (or readout) is that the parameters of the fields as well as the beam intensity and the pressure readings can be saved to an electronic logbook. An extensive and rigorous electronical logbook enables the experiment to be replicated. Some of the information could even be included to the data stream of an ongoing experiment which can be useful in the data analysis. Also more advanced interlocks can be set than in an analogue systems which can be cost-effective.

Chapter 3

Separation properties of the gas-filled recoil separator RITU

The absolute transmission of the RITU gas-filled recoil separator has been measured for several fusion evaporation reactions. The results and experimental techniques—as well as the main ion optical properties of RITU and its instrumentation—are presented in the article by J. Sarén et al. (Nucl. Instrum. and Meth. in. Phys. Res. A 654 (2011) 508) which is included in the next section in this thesis.

The experimental transmission studies described in the article suggest that the transmission of a fusion evaporation residue depends strongly on its initial angle after the target. With an assumption that the recoil will be transmitted if and only if it is inside the rectangular acceptance gate of $\pm 25 \cdot \pm 85$ mrad^2, the measured transmission values were reproduced with $\pm 20\%$ relative accuracy. This result has been applied to the reaction ^{208}Pb(^{48}Ca,2n)^{254}No and is discussed in section 3.2.

The methods presented in section 1.5 have been applied to the modelling of the transportation of ^{186}Hg recoils created in the reaction ^{40}Ar+^{150}Sm in gas-filled RITU. The results are compared to the experimental observations.

3.1 Absolute transmission and separation properties of the gas-filled recoil separator RITU

J. Sarén et al., Nucl. Instrum. and Meth. in. Phys. Res. A 654 (2011) 508

J. Sarén et al., Nucl. Instrum. and Meth. in. Phys. Res. A 654 (2011) 508

This page is not available in this electronic version. Publication is included in the printed version.

J. Sarén et al., Nucl. Instrum. and Meth. in. Phys. Res. A 654 (2011) 508

This page is not available in this electronic version. Publication is included in the printed version.

J. Sarén et al., Nucl. Instrum. and Meth. in. Phys. Res. A 654 (2011) 508

This page is not available in this electronic version. Publication is included in the printed version.

J. Sarén et al., Nucl. Instrum. and Meth. in. Phys. Res. A 654 (2011) 508

This page is not available in this electronic version. Publication is included in the printed version.

J. Sarén et al., Nucl. Instrum. and Meth. in. Phys. Res. A 654 (2011) 508

This page is not available in this electronic version. Publication is included in the printed version.

J. Sarén et al., Nucl. Instrum. and Meth. in. Phys. Res. A 654 (2011) 508

J. Sarén et al., Nucl. Instrum. and Meth. in. Phys. Res. A 654 (2011) 508

This page is not available in this electronic version. Publication is included in the printed version.

J. Sarén et al., Nucl. Instrum. and Meth. in. Phys. Res. A 654 (2011) 508

J. Sarén et al., Nucl. Instrum. and Meth. in. Phys. Res. A 654 (2011) 508

This page is not available in this electronic version. Publication is included in the printed version.

J. Sarén et al., Nucl. Instrum. and Meth. in. Phys. Res. A 654 (2011) 508

This page is not available in this electronic version. Publication is included in the printed version.

J. Sarén et al., Nucl. Instrum. and Meth. in. Phys. Res. A 654 (2011) 508

This page is not available in this electronic version. Publication is included in the printed version.

J. Sarén et al., Nucl. Instrum. and Meth. in. Phys. Res. A 654 (2011) 508

J. Sarén et al., Nucl. Instrum. and Meth. in. Phys. Res. A 654 (2011) 508

This page is not available in this electronic version. Publication is included in the printed version.

3.2 Transmission for the reaction ^{208}Pb(^{48}Ca, 2n)^{254}No

In section 2.7.5 the total transmission of 38% to the implantation detector at the MARA focal plane was obtained for ^{254}No recoils created in the reaction ^{48}Ca+^{208}Pb. The transmission value for the same reaction in the case of RITU is estimated to be 47(4)% for the MWPC if it is assumed that all recoils inside the rectangular acceptance gate of $\pm 24 \cdot \pm 83$ mrad^2 are transmitted. Furthermore, 32(6)% of the recoils would be observed at the DSSD if a DSSD efficiency of 70(10)% is assumed for the recoils observed at the MWPC.

In the experiment of Eeckhaudt et al. [Eec05], 55000 ^{254}No recoils were observed for the total ^{48}Ca dose of $6.6 \cdot 10^{16}$ at the target. The estimated efficiency of 32% and the cross-section of 2 µb give 61000 ^{254}No recoils which is in very close agreement with the experimental value since there are always some missing Si-strips in the detector and some of the recoils may have been outside of a coincidence gate.

The estimated transmission values 32(6)% for RITU and 38% for MARA cannot be compared directly. In the case of RITU, the 70(10)% DSSD efficiency is mostly due to wires and the angular spreading in the MWPC which is not taken into account in the case of MARA.

3.3 Modelling the reaction ^{150}Sm(^{40}Ar,4n)^{186}Hg

In order to understand the working principle of gas-filled separators better, the distribution of ^{186}Hg recoils created in the reaction ^{40}Ar+^{150}Sm has been transported through RITU. The modelling has been carried out using the methods discussed in section 1.5.3. The simulation presented here does not repreduce perfectly all the measured values shown in the included article but it seems to give a good qualitative description of the transportation properties related to the ^{186}Hg recoils.

There are many adjustable parameters which need to be applied to the simulation in order to reproduce the observed behaviour. The most important parameters are:

- $\overline{\Delta E}$, the mean energy loss of a recoil travelling 1 m in He gas at 1 hPa pressure. Its unit is MeV/(hPa m). This parameter affects mainly the time of flight (Δt) through RITU.
- $\sigma_{\Delta E}$, standard deviation of the energy loss. Values between zero and 0.1 MeV/(hPa m) have been tested and as a result no effect on image properties was found.

- $d_{\bar{q}}$, standard deviation of the Gaussian distribution representing the charge states.
- $f_{l,qq'}$. The mean free path between the charge-exchange collisions given by (1.53) is multiplied by $f_{l,qq'}$ in order to get a mean free path to be used in the simulation. This parameter controls the speed of image size growth when the pressure is decreased.
- $\sigma_{\Delta a,\mathrm{scat}}$, standard deviation of scattering for a recoil travelling 1 m in He gas at 1 hPa pressure. The scattering of a recoil after path length s is sampled independently for horizontal and vertical directions (coordinates a and b) from $\mathcal{G}(\sqrt{ps/(1\text{ m hPa})}\sigma_{\Delta a,\mathrm{scat}})$. This parameter controls the speed of image size growth when the pressure is increased.
- $\sigma_{\Delta a,\mathrm{mwpc}}$, standard deviation of scattering applied independently to the recoil's angular coordinates a and b at the position of the MWPC. This affects the image size at the DSSD.
- B_{Q1}, B_{Q2} and B_{Q3}, strenth of the B-field at the pole tips of RITU quadrupoles. Values $B_{Q1}/\chi_B = 0.3000$ m^{-1}, $B_{Q2}/\chi_B = 0.2015$ m^{-1} and $B_{Q1}/\chi_B = 0.2913$ m^{-1} have been used if it has not been mentioned otherwise.
- A reference particle having parameters 31 MeV, 186 u and 6.75 e has been used. With this reference particle, the horizontal distribution was within a few mm from the optical axis at the DSSD in all cases.

3.3.1 The energy loss of ^{186}Hg in He

The energy loss and the angular scattering of the ^{186}Hg recoils in the He gas has been calculated with TRIM. The calculation was performed at 1 hPa pressure for 2000 particles having an initial energy of 32 MeV. The resulting a) energy-loss and b) horizontal angle distribution are shown in figure 3.1. The mean energy loss given by the fit is 0.89 MeV/(hPa m) with a standard deviation of 0.076 MeV/(hPa m).

The experimental value for the energy loss has been determined by bracketing the energy loss value, $\overline{\Delta E}$, until the measured slope of 19.0 ns/hPa in the $(\Delta t)_{\mathrm{MWPC}}$ vs. pressure curve was obtained in the simulation. This slope is given by the linear fit in figure 7 (a) in the included article. The bracketing resulted in the value 0.714 MeV/(hPa m) which is slightly smaller than the value given by TRIM. The other simulation parameters were found to have a negligible effect on $(\Delta t)_{\mathrm{MWPC}}$.

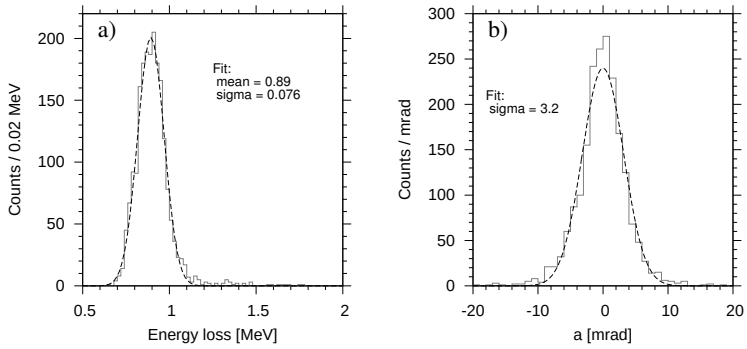

Figure 3.1: a) Energy loss and b) horizontal angle distribution of 2000 monoenergetic 32 MeV ^{186}Hg recoils after travelling 1 m in He gas at 1 hPa pressure. Calculated with TRIM. The dashed lines show the fits of Gaussian distributions.

3.3.2 Charge states and rigidities

The average charge states were calculated with equation (1.44). The effect of energy loss on average charge state measured at the center of the RITU dipole was observed to be small, only about 0.15 charge units, in the pressure range from 0.2 hPa to 1.6 hPa. With parameters $f_{l,qq'} = 1$, $\sigma_{\Delta a,\mathrm{scat}} = 0$ and $d_{\bar{q}} = 0.8$ the center of the horizontal distribution moved from -0.3 mm to 1.4 mm corresponding to a total change of about 0.2% in rigidity. It should be noted that the measured rigidity, which is based on RITU dispersion and dipole field strength, changes about 8% (see figure 8 (c) in the article) as a consequence of 0.4 units change in the average charge state (see figure 17 (b) in the article).

The constancy of the simulated (effective) rigidity is important because it proves that the observed density effect in $\bar{q}$ is real and not caused by the long mean free path between charge-exchange reactions. In a more advanced simulation study one should probably use the observed charge states. One implementation would be to use an equation like $\bar{q}(v,\tau) = \bar{q}_5(v) + \Delta\bar{q} + Q(\tau)$ where $\bar{q}_5$ refers to equation (1.44), $\Delta\bar{q}$ is an offset correction for $\bar{q}$ and $Q(\tau)$ is a function which increases as a function of mean free time, τ, between charge exchange collisions.

3.3.3 Reproducing the experimental image size and transmission

The most important goal of the simulations is to reproduce the behaviour of the experimental image size and transmission as a function of pressure. These experimental observations are shown in figure 8 in the article and also in figure 3.2. The qualitative behaviour of the horizontal image size is well understood and discussed for example in [Arm71]. At low pressures the mean free path, $l_{qq'}$, between charge exchanges is long and the image will be spread due to the width of the charge distribution. Therefore the slope depends strongly on $l_{qq'}$. As the pressure increases the scattering in the gas becomes more dominant. Clearly the slope at high pressures can be changed by altering the value of $\sigma_{\Delta a,\mathrm{scat}}$.

In the simulations, it was observed that the width of the image in vertical direction, $\sigma_y(p)$, depends significantly on $\sigma_{\Delta a,\mathrm{mwpc}}$ and $\sigma_{\Delta a,\mathrm{scat}}$. The former acts like an offset and the latter gives the slope. In principle, $\sigma_y(p)$ could be used to find the values for these parameters. However, if the $\sigma_y(p)$ behaviour is fully reproduced then the more important horizontal width as a function of pressures, $\sigma_x(p)$, seems to differ too much from the experiment.

The decreasing slope of $\sigma_x(p)$ at low pressures was studied first by setting $\sigma_{\Delta a,\mathrm{scat}}$ and $\sigma_{\Delta a,\mathrm{mwpc}}$ close to zero in order to get the right value for the factor $f_{l,qq'}$. With a charge state distribution width of $d_{\bar{q}} = 0.8$ units the value $f_{l,qq'} \approx 6$ seems to give the slope. However, the effect of too long $l_{qq'}$ on transmission to the MWPC is not strong enough which would indicate that a larger value for $f_{l,qq'}$ is needed. In any case, it seems that the charge exchange cross-sections estimated by equation (1.48) are about one order of magnitude too large in this case.

The effect of scattering in the He gas was studied next by adopting the parameters $d_{\bar{q}} = 0.8$ and $f_{l,qq'} = 6$ for the bracketing of $\sigma_{\Delta a,\mathrm{scat}}$. With value $\sigma_{\Delta a,\mathrm{scat}} \approx 0.004$ mrad the shape of the experimental $\sigma_x(p)$ curve is reproduced perfectly and so is the MWPC transmission curve excluding the data points at 0.2 hPa and 0.3 hPa. The simulation yields the same slope for $\sigma_y(p)$ as measured. The value $\sigma_{\Delta a,\mathrm{scat}} \approx 0.004$ mrad is close to the value given by the TRIM simulation (see figure 3.1).

In a last step the size of the scattering in the MWPC was varied. At values $\sigma_{\Delta a,\mathrm{mwpc}} \approx 45$ mrad the correct value for $\sigma_y(p \to 0)$ was obtained. This affects also σ_x and therefore the size of the mean-free-path factor was increased from the value presented above. After many cpu-time consuming iterations the parameters $\sigma_{\Delta a,\mathrm{mwpc}} \approx 40$ mrad, $f_{l,qq'} = 8$ and $\sigma_{\Delta a,\mathrm{scat}} = 4.0$ mrad were chosen. The simulated image width in both directions and the transmission values to the MWPC and DSSD calculated with these parameters are shown

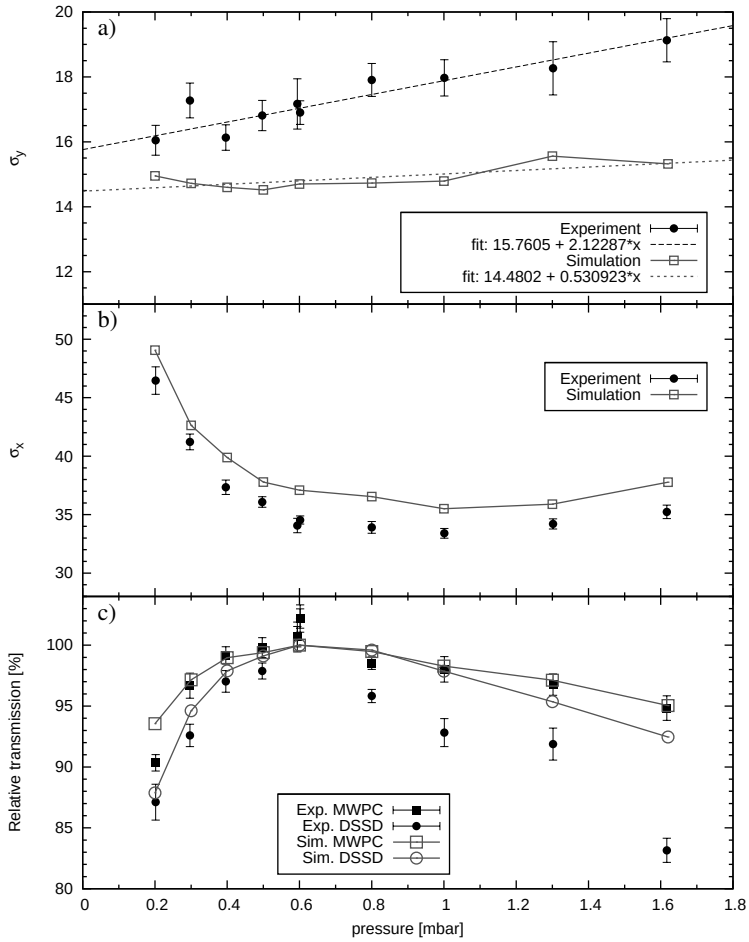

Figure 3.2: Experimental and simulated image widths at the DSSD of RITU in a) the vertical direction and b) the horizontal direction for the reaction ^{150}Sm(^{40}Ar,4n)^{186}Hg. Panel (c) shows the transmission to the MWPC and DSSD relative to maximum values around $p = 0.6$ hPa. The simulation parameters were $d_{\bar{q}} = 0.8$ charge units, $f_{l,qq'} = 8$, $\sigma_{\Delta a,\mathrm{scat}} = 4.0$ mrad, $\sigma_{\Delta a,\mathrm{mwpc}} = 40$ mrad and $\sigma_{\Delta E} = 0.1$ MeV/(hPa m).

in figure 3.2 alongside the measured results. The simulated data reproduce the measured data very well except that in vertical direction the simulated widths have slightly smaller absolute values while in the horizontal direction the simulated values are about 3 mm larger. The transmission to the DSSD seems to decrease slower in simulations than the experimental data at high pressures. It should be noted that the simulated MWPC-transmission curve is almost identical to the experimental curve. The highest absolute transmission value to the MWPC in the simulation (at around 0.6 hPa) is 50% while the maximum experimental transmission was 48%.

The effect of $d_{\bar{q}}$ has been tested also. As can be expected, it affects the shape and minimum value of the $\sigma_x(p)$ curve. The value $d_{\bar{q}} = 0.8$ charge units seems to fit best the experimental data. It was also noticed that the interplay between parameters $f_{l,qq'}$, $\sigma_{\Delta a,\mathrm{scat}}$ and $d_{\bar{q}}$ is quite complicated. If a more precise reproduction of the data is requested then one should probably include the more realistic average charge state discussed in section 3.3.2 to the simulation. One could also model the scattering and energy loss in He gas more accurately. This is more important at higher pressures since the probability for a recoil to encounter at least one collision having a large scattering angle increases with pressure and can be significant. It should be considered also that the ion-optical configuration of RITU is not identical to the one used in the calculations. For example the increased focusing in horizontal direction and defocusing in vertical direction would move the simulated curves closer to the observations.

The intensity maps in figure 3.3 show the positions of the charge exchange collisions in the vertical and horizontal directions alongside the RITU elements and focal plane detector positions.

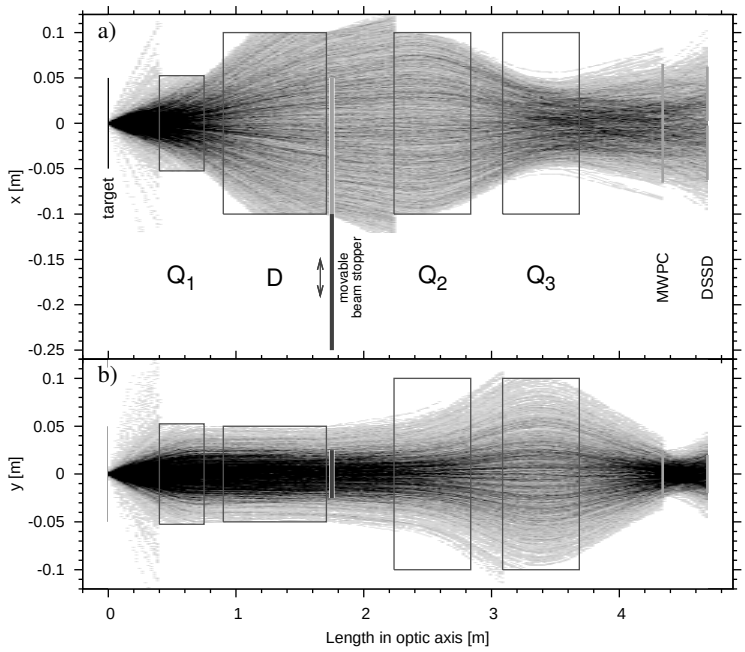

Figure 3.3: Number of charge-exchange reactions in a) horizontal direction and b) vertical direction in the case of the reaction ^{150}Sm(^{40}Ar,4n)^{186}Hg at 0.6 hPa He pressure. Simulation parameters are the same as in figure 3.2.

Bibliography

[And05] L.-L. Andersson, E. K. Johansson, J. Ekman, D. Rudolph, R. du Rietz, and C. Fahlander, *Identification of excited states in* $^{61}_{31}Ga_{30}$*: Mirror nuclei in the upper fp shell*, Phys. Rev. C 71 (2005) 011303-1

[Arm71] P. Armbruster, J. Eidens, J. W. Grüter, H. Lawin, E. Roeckl, K. Sistemich, *Are Gas-Filled Magnetic Separators a Useful Tool to Investigate Heavy Fast Recoils from Nuclear Reactions*, Nucl. Instr. and Meth. 91 (1971) 499

[Bas74] R. Bass, *Fusion of heavy nuclei in a classical model*, Nuclear Physics A 231 (1974) 45

[Beg91] S. Beghini, G. Bovo and A. Dal Bello, *A compact high voltage power supply for the LNL recoil mass spectrometer*, Nucl. Instr. and Meth. A 300 (1991) 328

[Bet72] H. D. Betz, *Charge States and Charge-Changing Cross Sections of Fast Heavy Ions Penetrating Through Gaseous and Solid Media*, Rev. Mod. Phys. 44 (1972) 465

[Bet83] The mathematical formulation has been adopted from [Pau89] which refers to H. D. Betz, Appl. At. Collis. Phys. 4 (1983) 1

[Bla07] B. Blanc et al., *Production cross-sections of proton-rich* ^{70}Ge *fragments and the decay of* ^{57}Zn *and* ^{61}Ge, Eur. Phys. J. A 31 (2007) 267

[Boh40] N. Bohr, *Scattering and Stopping of Fission Fragments*, Phys. Rev. 58, 654 (1940)

[Bre82] A. Breskin, *Progress in low-energy gaseous detectors*, Nucl. Instr. and Meth. 196 (1982) 11,

[Car66] Thomas A. Carlson, W. E. Hunt and Manfred O. Krause, *Relative Abundances of Ions Formed as the Result of Inner-Shell Vacancies in Atoms*, Phys. Rev. 151 (1966) 41

[Col00] A. J. Cole, *STATISTICAL MODELS FOR NUCLEAR DECAY, From Evaporation to Vaporization*, Fundamental and applied nuclear physics series, Institute of Physics Publishing, Bristol and Philadelphia, 2000

[Coh58] B. Cohen, C. Fulmer, *Fission-Fragment Mass Separator and the Nuclear Charge Distribution of Fission Fragments of a Single Mass*, Nucl. Phys. 6 (1958) 547

[COMSOL] Comsol Multiphysics, version 3.5, `http://www.comsol.com`

[CDav89] C. N. Davids and J. D. Larson, *The Argonne Fragment Mass Analyzer*, Nucl. Instr. and Meth. B 40/41 (1989) 1224

[BDav05] B. Davids, C. N. Davids, *Emma: A recoil mass spectrometer for ISAC-II at TRIUMF*, Nucl. Instr. and Meth. A 544 (2005) 565

[Dro07] A. Drouart, C. Mazur, Ph. Bourgeois, et al., *Very large emissive foil detectors for the tracking of low-energy heavy ions*, Nucl. Instr. and Meth. A 579 (2007) 1090

[Duc99] G. Duchene, F. A. Beck, P. J. Twin, G. de France, D. Curien, L. Han, C. W. Beausang, M. A. Bentley, P. J. Nolan, J. Simpson, *The Clover: a new generation of composite Ge detectors*, Nucl. Instr. and Meth. A 432 (1999) 90

[Hot87] M. A. C. Hotchkis, J. E. Reiff, D. J. Vieira, F. Blönningen, T. F. Lang, D. M. Moltz, X. Xu, and Joseph Cerny, *Beta-delayed proton decay of* ^{61}*Ge*, Phys. Rev. C 35 (1987) 315

[Eec05] S. Eeckhaudt, P. T. Greenlees, et al., *Evidence for non-yrast states in* ^{254}*No*, Eur. Phys. J. A 26 (2005) 227

[Eng79] H. A. Enge, *Magnetic Spectographs for nuclear reaction studies*, Nucl. Instr. and Meth. 162 (1979) 161

[Eng81] H. A. Enge, *Progress in recoil spectrometers for separation of fast nuclear reaction products*, Nucl. Instr. and Meth. 186 (1981) 413

[Enq03] T. Enqvist, P. Heikkinen, H. Kettunen, P. Kuusiniemi, M. Leino, A.-P. Leppänen, C. Scholey, J. Uusitalo, *The design of a new gas-filled separator at JYFL*, Nucl. Instr. and Meth. B 204 (2003) 138

[Ful58] C. Fulmer, B. Cohen, *Equilibrium Charges of Fission Fragments in Gases*, Phys. Rew. 109 (1958) 94

[Gav80] A. Gavron, *Statistical model calculations in heavy ion reactions*, Phys. Rev. C 21 (1980) 230

[Ghi88] A. Chiorso, S. Yashita, M. Leino, L. Frank, J. Kalnins, P. Armbruster, J.-P. Dufour and P. K. Lemmertz, *SASSY, A Gas-Filled Magnetic Separator for the Study of Fusion Reaction Products*, Nucl. Instr. and Meth. A 269 (1988) 192

[GICOSY] M. Berz, B. Hartmann, K. Lindemann, A. Magel, H. Weick, `http://www-linux.gsi.de/~weick/gicosy/`

[GICOSY manual] H. Weick et al. How to use GICOSY, Version November 2005

[Gre05] K. E. Gregorich, W. Loveland, D. Peterson, P. M. Zielinski, S. L. Nelson, Y. H. Chung, Ch. E. Düllmann, C. M. Folden III, K. Aleklett, R. Eichler, D. C. Hoffman, J. P. Omtvedt, G. K. Pang, J. M. Schwantes, S. Soverna, P. Sprunger, R. Sudowe, R. E. Wilson, and H. Nitsche, *Attempt to confirm superheavy element production in the* $^{48}Ca+^{238}U$ *reaction*, Phys. Rev. C 72 (2005) 014605

[Gro00] C. J. Gross, T. N. Ginter, D. Shapira, W. T. Milner, et al. *Performance of the Recoil Mass Spectrometer and its detector systems at the Holifield Radioactive Ion Beam Facility* Nucl. Instr. and Meth. A 450 (2000) 12

[GSL] M. Galassi et al., GNU Scientific Library Reference Manual, 3rd Ed., v 1.12 (2009)

[Ike97] H. Ikezoe, T. Ikuta, S. Mitsuoka, S. Hamada, Y. Nagame, I. Nishinaka, Y. Tsukada, Y. Oura and T. Ohtsuki, *The feature of the JAERI recoil mass separator*, Nucl. Instr. and Meth. B 126 (1997) 340

[Iwa97] N. Iwasa, H. Geissel, G. Münzenberg, C. Scheidenberger, Th. Schwab and H. Wollnik, *MOCADI, a universal Monte Carlo code for the transport of heavy ions through matter within ion-optical systems*, Nucl. Instr. and Meth. B 126 (1997) 284

[Nat07] S. Nath, *A Monte Carlo code to calculate transmission efficiency of HIRA*, Nucl. Instr. and Meth. A 576 (2007) 403

[Iwa11] N. Iwasa, H. Weick, H. Geissel, *New features of the Monte-Carlo code MOCADI*, Nucl. Instr. and Meth. B 269 (2011) 752

[Laz93] JINR report E7-93-274, Dubna 1993, vol. 2B497

[Laz01] I. H. Lazarus, et al., *The GREAT Triggerless Total Data Readout Method*, IEEE Trans. Nucl. Sci. 48 (2001) 567

[Lei95] M. Leino, J. Äystö, T. Enqvist, P. Heikkinen, A. Jokinen, M. Nurmia, A. Ostrowski, W. H. Trzaska, J. Uusitalo, K. Eskola, P. Armbruster, V. Ninov, *Gas-filled recoil separator for studies of heavy elements*, Nucl. Instr. and Meth. B 99 (1995) 653

[Lei03] M. Leino, *Gas-filled separators - An overview*, Nucl. Instr. and Meth. B 204 (2003) 129.

[Lei04] M. Leino, Private communication

[LISA11] LISA (Light Ion Spectrometer Array), `http://ns.ph.liv.ac.uk/~dod/LISA/home.html`, 30th of August 2011

[Mor92] S. Morinobu, I. Katayama, et al., *Performance of and experiments with the recoil separator CARP at RCNP*, Nucl. Instr. and Meth. B 70 (1992) 331

[Maz08] M. Mazzocco, D. Ackermann, M. Block, H. Geissel, F. Herfurth, F. P. Heßberger, S. Hofmann, N. Iwasa, K. Nishio, W. R. Plaß, C. Scheidenberger, H. Weick, M. Winkler, *MOCADI_FUSION: Extension of the Monte-Carlo code MOCADI to heavy-ion fusion-evaporation reactions*, Nucl. Instr. and Meth. B 266 (2008) 3467

[Met76] V. Metag, D. Habs, H. J. Specht, G. Ulfert and C. Kozhuharov, *Hyperfine Interactions and Charge Distributions of Actinide Ions Recoiling into Vacuum*, Hyp. Int. 1 (1976) 405

[Mün81] G. Münzenberg, W. Faust, F.P. Heßberger, S. Hofmann, W. Reisdorf, K. H. Schmidt, W. F. W. Schneider, H. J. Schtt, P. Armbruster, K. Güttner, B. Thuma, H. Ewald, and D. Vermeulen, Nucl. Inst. Meth. 186 (1981) 423

[Nar07a] B. S. Nara Singh, A.N. Steer, D.G. Jenkins, R. Wadsworth, et al., *Recoil Beta Tagging: Application to the study of odd-odd near proton drip line nuclei,* ^{74}Rb *and* ^{78}Y, Eur. Phys. J. Special Topics 150, 147148 (2007)

[Nar07b] B. S. Nara Singh, A. N. Steer, D. G. Jenkins, R. Wadsworth, et al., *Coulomb shifts and shape changes in the mass 70 region*, Phys. Rev. C 75 (2007) 061301(R)

[Nik68] V. S. Nikolaev and I. S. Dmitriev, *On the equilibrium charge distribution in heavy element ion beams*, Phys. Lett. A 28 (1968) 277

[Nin95] V. Ninov, P. Armbruster, F. P. Heßberger, S. Hofmann, G. Münzenberg, Y. Fujita, M. Leino, A. Lüttgen, *Separation of actinide-made transurania by a gas-filled magnetic separator*, Nucl. Instr. and Meth. A357 (1995) 486

[Oga91] Yu. Ts. Oganessian, Yu. V. Lobanov, A. G. Popeko, F. Sh. Abdullin, Yu. P. Kharitonov, A. A. Ledovskoy, Yu. S. Tsyganov, *The average equilibrium charge states of heavy ions with Z¿60*, Z. Phys. D 21 (1991) S357

[Pag03] R. D. Page, et al., *The GREAT spectrometer*, Nucl. Instr. and Meth. B 204 (2003) 634

[Pap09] P. Papadakis, R.-D. Herzberg, J. Pakarinen, et al., *Towards combining in-beam γ-ray and conversion electron spectroscopy*, AIP Conf. Proc. 1090 (2009) 14

[Pau95] E. S. Paul, P. J. Woods, T. Davinson, R. D. Page, P. J. Sellin, et al., *In-beam γ-ray spectroscopy above ^{100}Sn using the new technique of recoil decay tagging*, Phys. Rev. C 51 (1995) 78

[Pau89] M. Paul, B. G. Glagola, W. Henning, J. G. Keller, W. Kutschera, Z. Liu, K. E. Rehm, B. Schneck, R. H. Siemssen, *Heavy ion separation with a gas-filled magnetic spectrograph*, Nucl. Instr. and Meth. A 277 (1989) 418

[Pau98] S. D. Paul, C. Baktash, W. Satula, C. J. Gross et al., *Band structure in ^{79}Y and the question of T=0 pairing*, Phys. Rev. C 58 (1998) R3037

[Pul08] S. Pullanhiotan, M. Rejmund, A. Navin, W. Mittig, S. Bhattacharyya, *Performance of VAMOS for reactions near the Coulomb barrier*, Nucl. Instr. and Meth. A 593 (2008) 343

[Roz96] J. P. Rozet, C. Stéphan, D. Vernhet, *ETACHA: a program for calculating charge states at GANIL energies*, Nucl. Instr. and Meth. B 107 (1996) 67

[Roz09] J. P. Rozet, in collaboration with INSP (Paris), CNEA (Bariloche), IFR (Rosario), *Towards improvement of ETACHA for S3 ions*, contribution for S3 Workshop, June 2009, GANIL, Caen, France

[Ryd70] G. Ryding, H. D. Betz, A. Wittkower, *Influence of ionic excitation in heavy-ion charge-changing cross sections*, Phys. Rev. Lett. 26 (1970) 123

[Ryk99] K. Rykaczewski, et al., *Proton emitters ^{140}Ho and ^{141}Ho: Probing the structure of unbound Nilsson orbitals*, Phys. Rev. C 60 (1999) 011301

[Sar04] J. Sarén, *RITU:n kehittäminen ja kaasutäytteisiin separaattoreihin liittyvää ionioptiikkaa (Development of the RITU separator and ion optics related to gas-filled separators)*, master thesis, University of Jyväskylä, 2004

[Sew01a] D. Seweryniak, P. J. Woods, J. J. Ressler, et al., *Rotational Bands in the Proton Emitter ^{141}Ho*, Phys. Rev. C 86 (2001) 1458

[Sew01b] D. Seweryniak, P. J. Woods, J. J. Ressler, et al., *GAMMASPHERE+FMA: A journey beyond the proton drip-line* Nucl. Phys. A 682 (2001) 247c

[Sew09a] D. Seweryniak, *Fragment Mass Analyzer upgrades and X-array status*, ATLAS workshop of August 8-9, 2009, `http://www.phy.anl.gov/atlas/workshop09/Seweryniak.ppt`

[Sew09b] D. Seweryniak, *Nuclear structure around* ^{100}Sn, ATLAS workshop of August 8-9, 2009, `http://www.phy.anl.gov/atlas/workshop09/Seweryniak_2.ppt`

[Sew09c] D. Seweryniak, *Gas-filled separator for nuclear structure experiments at ATLAS*, ATLAS workshop of August 8-9, 2009, `http://www.phy.anl.gov/atlas/workshop09/Seweryniak_3.ppt`

[Spo85] P. Spolaore, J. D. Larson, C. Signorini, S. Beghini, X.-K. Zhu and H.-Z. Si, *A Recoil Mass Spectrometer for the XTU Tandem at LNL*, Nucl. Instr. and Meth. A 238 (1985) 381

[Spo88] P. Spolaore, G. Bisoffi, X. L. Guan, S. Beghini and C. Signorini, *High voltage insulation over large gaps in vacuum*, Nucl. Instr. and Meth. A 268 (1988) 397

[Sch01] G. Schiwietz, P. L. Grande, *Improved charge-state formulas*, Nucl. Instr. and Meth. B 175-177 (2001) 125

[Schla83] A. S. Schlachter, J. W. Stearns, W. G. Graham, K. H. Berkner, R. V. Pyle and J. A. Tanis, *Electron capture for fast highly charged ions in gas targets: An empirical scaling rule*, Phys. Rev. A 27 (1983) 3372

[Schmitt10] C. Schmitt, M. Rejmund, A. Navin, B. Lecornu, B. Jacquot, G. de France, A. Lemasson, A. Shrivastava, P. Greenlees, J. Uusitalo, K. Subotic, L. Gaudefroy, Ch. Theisen, B. Sulignano, O. Dorvaux, L. Stuttge, *New gas-filled mode of the large-acceptance spectrometer VAMOS*, Nucl. Instr. and Meth. A 621 (2010) 558

[Shi89] K. Shima, N. Kuno, M. Yamanouchi, *Systematics of equilibrium charge distributions of ions passing through a carbon foil over the ranges Z=4–92 and E=0.02–6 MeV/u*, Phys. Rev. A 40 (1989) 3557

[Shi92] K. Shima, N. Kuno, M. Yamanouchi, H. Tawara, Atomic Data and Nuclear Data Tables 51 (1992) 173

[Sin94] A. K. Sinha, N. Madhavan, J. J. Das, P. Sugathan, D. O. Kataria, A. P. Patro, G. K. Mehta, *Heavy ion reaction analyzer (HIRA): a recoil mass separator facility at NSC*, Nucl. Instr. and Meth. A 339 (1994) 543

[Ste06] A. N. Steer, D. G. Jenkins, R. Glover, B. S. Nara Singh, N. S. Pattabiraman, R. Wadsworth, et al., *Recoil-beta tagging: A novel technique for studying proton-drip-line nuclei*, Nucl. Instr. and Meth. A 565 (2006) 630

[Sub02] K. Subotić, Yu.Ts. Oganessian, V. K. Utyonkov, Yu. V. Lobanov, F. Sh. Abdullin, A. N. Polyakov, Yu. S. Tsyganov, O. V. Ivanov, *Evaporation residue collection efficiencies and position spectra of the Dubna gas-filled recoil separator*, Nucl. Instr. and Meth. A 481 (2002) 71

[Sub08] K. Subotić, P. Ujić, D. Dragosavac, I. Čeliković, D. Toprek, *ANAMARI simulation code for gas-filled separators and spectrometers*, Nucl. Instr. and Meth. B 266 (2008) 4209

[Tar08] O. B.Tarasov, D. Bazin, *LISE++: Radioactive beam production with in-flight separators*, Nucl. Instr. and Meth. B 266 (2008) 4657

[Tom82] E. Tomasi, et al., *Fusion excitation function of the ^{40}Ca+^{40}Ca system close to the threshold*, Nucl. Phys. A 373 (1982) 341

[Ulf78] G. Ulfert, D. Habs, V. Metag and H. J. Specht, *Lifetime measurements of nuclear levels with the charge plunger techique*, Nucl. Instr. and Methods 148 (1978) 369

[Uus11] J. Uusitalo, private communication, 2011

[Wad09] R. Wadsworth, B. S. Nara Singh, A. N. Steer, D. G. Jenkins, et al., *THE NORTHWEST FRONTIER: SPECTROSCOPY OF N≈Z NUCLEI BELOW MASS 100*, Acta Phys. Pol. B 40 (2009) 611

[Wol87a] H. Wollnik, *Optics of Charged Particles*, Academic Press inc, 1987

[Wol99] H. Wollnik, *Ion Optics in Mass Spectrometers*, J. Mass Spectrom. 34 (1999) 991

[Woo84] C. J. Woods, C. J. Sofield, N. E. B. Cowern, M. Murrell and J. Draper, *Comparison of charge-changing cross sections in gaseous and solid targets*, J. Phys. B: At. Mol. Phys. 17 (1984) 867

[Yer94] A. V. Yeremin, et al., *The kinematic separator VASSILISSA performance and experimental results*, Nucl. Instr. and Meth. A 350 (1994) 608

[Yer08] A. Yeremin, O. Malyshev, A. Popeko, A. Lopez-Martens, K. Hauschild, O. Dorvaux, *Project of the experimental setup dedicated for gamma and electron spectroscopy of heavy nuclei at FLNR JINR*, Nucl. Instr. and Meth. B 266 (2008) 4137x

[Zie04] SRIM/TRIM Version 2008, J. F. Ziegler, Nucl. Instr. and Meth. B 219 (2004) 1027

Appendix A

The MARA transfer coefficients

The transfer matrix coefficients of the nominal MARA configuration described in table 2.3 for the standard reference particle of definition (2.1) at the focal plane are given below. The listing is the output of a third order GICOSY calculation using calculation mode 2.

NON SYMPL. SYSTEM TRANSFER MATRIX AT PATH-LENGTH L= 6.852395102E+00 M

		X	A	Y	B	T
0		2.573631E-12	6.211097E-13	0.000000E+00	0.000000E+00	4.936808E-07
1	X	-1.603618E+00	6.721650E-01	0.000000E+00	0.000000E+00	-5.993106E-08
2	A	1.070551E-04	-6.236347E-01	0.000000E+00	0.000000E+00	-3.932183E-12
3	Y	0.000000E+00	0.000000E+00	-4.701572E+00	-7.287874E-01	0.000000E+00
4	B	0.000000E+00	0.000000E+00	-2.730753E-05	-2.126989E-01	0.000000E+00
5	G	8.095978E-01	3.369391E-01	0.000000E+00	0.000000E+00	2.485493E-07
6	D	-8.833697E-05	2.595446E-01	0.000000E+00	0.000000E+00	-2.704780E-07
7	XX	1.033187E+01	4.097264E+00	0.000000E+00	0.000000E+00	3.660366E-07
8	XA	-9.733210E+00	-3.956786E+00	0.000000E+00	0.000000E+00	-3.565379E-07
9	XY	0.000000E+00	0.000000E+00	-2.755309E+01	-1.186156E+01	0.000000E+00
10	XB	0.000000E+00	0.000000E+00	5.333762E+00	2.073214E+00	0.000000E+00
11	XG	-2.454971E+00	-1.535664E+00	0.000000E+00	0.000000E+00	-8.844702E-09
12	XD	8.145571E-02	-1.954937E-01	0.000000E+00	0.000000E+00	1.561191E-08
13	AA	2.288660E+00	9.334135E-01	0.000000E+00	0.000000E+00	1.372358E-07
14	AY	0.000000E+00	0.000000E+00	1.313038E+01	5.662429E+00	0.000000E+00
15	AB	0.000000E+00	0.000000E+00	-2.314677E+00	-9.527811E-01	0.000000E+00
16	AG	1.963136E+00	1.319630E-01	0.000000E+00	0.000000E+00	5.774542E-10
17	AD	1.150976E+00	-5.141020E-01	0.000000E+00	0.000000E+00	6.265202E-08
18	YY	-1.367136E+01	-5.396769E+00	0.000000E+00	0.000000E+00	4.988235E-07
19	YB	4.477728E+00	1.777482E+00	0.000000E+00	0.000000E+00	2.113461E-07
20	YG	0.000000E+00	0.000000E+00	6.604987E+00	-2.047221E-01	0.000000E+00
21	YD	0.000000E+00	0.000000E+00	1.434640E+00	-2.396098E+00	0.000000E+00
22	BB	-3.946719E-01	-1.882798E-01	0.000000E+00	0.000000E+00	9.906632E-08
23	BG	0.000000E+00	0.000000E+00	6.282228E+00	6.749928E-01	0.000000E+00
24	BD	0.000000E+00	0.000000E+00	7.431771E+00	1.087076E+00	0.000000E+00

25	GG	-6.074837E-01	-2.565950E-01	0.000000E+00	0.000000E+00	-5.266091E-08
26	GD	-8.105605E-01	-3.176151E-01	0.000000E+00	0.000000E+00	-1.255356E-07
27	DD	1.093621E-01	-2.028865E-01	0.000000E+00	0.000000E+00	2.309968E-07
28	XXX	-6.253366E+00	2.139188E+00	0.000000E+00	0.000000E+00	5.018755E-07
29	XXA	-1.036499E+01	9.967998E+00	0.000000E+00	0.000000E+00	-1.700014E-06
30	XXY	0.000000E+00	0.000000E+00	-1.474968E+02	-2.630854E+01	0.000000E+00
31	XXB	0.000000E+00	0.000000E+00	-7.966278E+01	-4.417276E+00	0.000000E+00
32	XXG	-1.160248E+01	-5.058226E+00	0.000000E+00	0.000000E+00	-1.451505E-07
33	XXD	-1.293582E+01	-4.609550E+00	0.000000E+00	0.000000E+00	-5.863779E-07
34	XAA	9.332420E+00	8.430611E-01	0.000000E+00	0.000000E+00	1.104851E-06
35	XAY	0.000000E+00	0.000000E+00	2.886282E+01	1.809989E+01	0.000000E+00
36	XAB	0.000000E+00	0.000000E+00	7.663975E+00	-9.183250E-01	0.000000E+00
37	XAG	-4.057946E+00	-1.292451E+00	0.000000E+00	0.000000E+00	-2.255671E-07
38	XAD	-4.148467E+00	-2.419239E+00	0.000000E+00	0.000000E+00	1.939938E-07
39	XYY	-4.791958E+01	1.096467E+01	0.000000E+00	0.000000E+00	5.310368E-07
40	XYB	1.394714E+01	3.723856E+01	0.000000E+00	0.000000E+00	4.564734E-07
41	XYG	0.000000E+00	0.000000E+00	9.390764E+01	3.972252E+01	0.000000E+00
42	XYD	0.000000E+00	0.000000E+00	7.880098E+01	3.032952E+01	0.000000E+00
43	XBB	6.437851E-01	9.902187E+00	0.000000E+00	0.000000E+00	-5.361285E-08
44	XBG	0.000000E+00	0.000000E+00	4.014491E+01	1.696497E+01	0.000000E+00
45	XBD	0.000000E+00	0.000000E+00	4.314776E+01	1.881618E+01	0.000000E+00
46	XGG	4.196048E+00	1.805540E+00	0.000000E+00	0.000000E+00	-5.199063E-08
47	XGD	3.551861E+00	6.246612E-01	0.000000E+00	0.000000E+00	1.534022E-08
48	XDD	-7.401899E-02	-7.741271E-01	0.000000E+00	0.000000E+00	9.265863E-08
49	AAA	-6.704312E+00	1.778681E+00	0.000000E+00	0.000000E+00	-3.922887E-07
50	AAY	0.000000E+00	0.000000E+00	-1.122535E+02	-1.309070E+01	0.000000E+00
51	AAB	0.000000E+00	0.000000E+00	-7.398953E+01	-6.198975E+00	0.000000E+00
52	AAG	4.618236E+00	1.834061E+00	0.000000E+00	0.000000E+00	2.014002E-07
53	AAD	4.774271E+00	2.263539E+00	0.000000E+00	0.000000E+00	2.820070E-08
54	AYY	-3.487793E+01	3.291972E+01	0.000000E+00	0.000000E+00	-2.155745E-06
55	AYB	-7.717393E+01	2.793252E+01	0.000000E+00	0.000000E+00	-2.999800E-06
56	AYG	0.000000E+00	0.000000E+00	-2.452959E+01	-1.052956E+01	0.000000E+00
57	AYD	0.000000E+00	0.000000E+00	-1.323343E+01	-4.239184E+00	0.000000E+00
58	ABB	-2.503623E+01	1.036422E+01	0.000000E+00	0.000000E+00	-8.856700E-07
59	ABG	0.000000E+00	0.000000E+00	-2.229292E+01	-9.421587E+00	0.000000E+00
60	ABD	0.000000E+00	0.000000E+00	-2.445886E+01	-1.054330E+01	0.000000E+00
61	AGG	-5.773765E-01	1.818128E-01	0.000000E+00	0.000000E+00	1.732826E-08
62	AGD	6.247644E-01	3.284576E-01	0.000000E+00	0.000000E+00	5.699773E-08
63	ADD	-8.098768E-01	4.194897E-01	0.000000E+00	0.000000E+00	-1.072651E-07
64	YYY	0.000000E+00	0.000000E+00	4.218535E+01	1.128212E+02	0.000000E+00
65	YYB	0.000000E+00	0.000000E+00	-6.967056E+02	-1.139465E+02	0.000000E+00
66	YYG	7.216713E+01	2.832991E+01	0.000000E+00	0.000000E+00	-1.565074E-06
67	YYD	6.165513E+01	2.491626E+01	0.000000E+00	0.000000E+00	-1.810026E-06
68	YBB	0.000000E+00	0.000000E+00	-3.362003E+02	-2.045657E+01	0.000000E+00
69	YBG	2.981358E+01	1.153796E+01	0.000000E+00	0.000000E+00	-8.371459E-07
70	YBD	3.310322E+01	1.264257E+01	0.000000E+00	0.000000E+00	-1.037770E-06
71	YGG	0.000000E+00	0.000000E+00	-3.430677E+00	2.411804E+00	0.000000E+00
72	YGD	0.000000E+00	0.000000E+00	1.529500E+01	1.092766E+01	0.000000E+00
73	YDD	0.000000E+00	0.000000E+00	1.685031E+01	1.044826E+01	0.000000E+00
74	BBB	0.000000E+00	0.000000E+00	-8.588411E+01	-8.161539E+00	0.000000E+00
75	BBG	-6.838075E+00	-2.816466E+00	0.000000E+00	0.000000E+00	-2.535217E-08
76	BBD	-7.157117E+00	-2.909362E+00	0.000000E+00	0.000000E+00	-1.422459E-07
77	BGG	0.000000E+00	0.000000E+00	-3.626265E+00	8.028504E-01	0.000000E+00
78	BGD	0.000000E+00	0.000000E+00	7.305159E+00	5.680293E+00	0.000000E+00
79	BDD	0.000000E+00	0.000000E+00	3.626776E+00	3.911995E+00	0.000000E+00
80	GGG	5.458404E-01	2.340168E-01	0.000000E+00	0.000000E+00	2.150676E-08
81	GGD	7.276337E-01	3.020561E-01	0.000000E+00	0.000000E+00	8.626406E-09
82	GDD	9.404183E-01	3.603448E-01	0.000000E+00	0.000000E+00	8.984746E-08
83	DDD	-2.924739E-01	1.186138E-01	0.000000E+00	0.000000E+00	-2.234451E-07